eman ta zabal zazu

Universidad del País Vasco

Euskal Herriko Unibertsitatea

SUSTAINABLE MULTIFUNCTIONAL MATERIALS WITH TAILORED MAGNETIC AND ELECTRICAL PROPERTIES FOR ELECTRONICS APPLICATIONS

Memoria para optar al Grado de Doctor por la Universidad del País Vasco (UPV/EHU)
presentada por

Mikel Rincón Iglesias

Leioa, septiembre 2022

eman ta zabal zazu

Universidad del País Vasco

Euskal Herriko Unibertsitatea

SUSTAINABLE MULTIFUNCTIONAL MATERIALS WITH TAILORED MAGNETIC AND ELECTRICAL PROPERTIES FOR ELECTRONICS APPLICATIONS

BCMATERIALS

BASQUE CENTER FOR MATERIALS, APPLICATIONS & NANOSTRUCTURES

ehugroup

Mikel Rincón Iglesias

PhD Thesis

Supervisors:

Senentxu Lanceros-Méndez

Erlantz Lizundia Fernández

Leioa, Septiembre 2022

Abstract

The global framework of digitalisation, related to the concepts of Industry 4.0 and the internet of things, aims to interconnect any process and object in the different facets of society. For this purpose, ubiquitous sensing and communication technologies are necessary. In this regard, significant efforts in research rely on developing flexible electronics. Thus, lightweight, flexible, stretchable, efficient, low cost and simple fabrication materials are demanded for the development of sensors and actuators, among others. Therefore, a wide range of materials with the ability to respond to the application of external stimuli need to be studied for the concretisation of such technological needs. In this framework, composite materials based on polymers and nanometric functional fillers represent a suitable way to accomplish these characteristics and technical requirements. Among the plethora of functional responses that the addition of fillers can achieve in polymer matrices, electrical conductivity and magnetic activity are pursued in the present work. These two functionalities are the basis of a variety of electronic components, sensors and actuators.

Contrary to the previous industrial revolutions, the ongoing one is aware of the environmental issues that could entail basing the electronic advancements on non-degradable and synthetic materials. Thus, it is encouraged sustainable development built on biodegradable and natural-resourced materials. Likewise, printing technologies arise as a commercially viable and more sustainable fabrication technology for electronic devices and sensors that tackle traditional technologies' limitations. Thus, materials based on biodegradable and natural-based polymers and functional fillers and additives processed by solution-based technologies compatible with additive manufacturing procedures have been developed in the thesis.

Principally, naturally-sourced polysaccharides including cellulose, ι-carrageenan and agarose have been employed as matrices, but biodegradable synthetic polyesters such as polylactic acid (PLA), polycaprolactones (PCL), polybutylene succinate (PBSu), and poly(butylene adipate-co-terephthalate) (PBAT), have also been used.

Among these polymers, cellulose, the biosphere's most widely available natural polymer, has been predominantly employed. Three water-soluble cellulose derivatives were used as matrices for magneto-active free-standing films and electro-mechanical bending actuators in a simple and environmentally benign synthesis. Magnetically active films based on methyl cellulose (MC), hydroxypropyl cellulose (HPC), and sodium carboxymethyl cellulose (NaCMC), combined with cobalt ferrite ($CoFe_2O_4$) nanoparticles (up to 50 wt.%) were

fabricated by the doctor blade technique using solely water as solvent and subsequently tested for their suitability as screen-printing ink. Similarly, the ionic liquid 2-hydroxy-ethyl-trimethylammonium dihydrogen phosphate ([Ch][DHP]) was employed to develop sustainable electro-mechanical bending actuators based on the previously used cellulose derivatives (MC, HPC, and NaCMC) and cellulose nanocrystals (CNCs). In this case, samples were processed by the solvent casting method. IL incorporation in the cellulosic matrix was found to increase the electrical conductivity and electro-mechanical bending. The morphological, mechanical, and physicochemical properties have been analysed in both cases. In addition, magnetic and dielectric properties are assessed for the nanocomposites comprising $CoFe_2O_4$, and the conductivity and electro-mechanical performance have been evaluated for the samples combined with [Ch][DHP]. Based on the obtained magneto-activity and electro-mechanical actuation performance, respectively, their simple processability, and their renewable nature, the fabricated materials represent a step forward in developing sustainable printable functional materials of high practical relevance.

Similarly, free-standing mesoporous membranes based on CNCs and either $CoFe_2O_4$ nanoparticles or graphite at concentrations up to 20 wt.% via a soft-templating process. Morphological and adsorption-desorption isotherms reveal highly-porous interconnected 3D structure, where the thermal stability is enhanced by the addition of filler. The obtained magnetically active or electrically conducting nanohybrids were suitable for fabricating sensors, recoverable catalysts for water purification, actuators, and other devices from natural origin where porous structures can be taken to advantage.

Next, the role of the CNCs in the composite was changed, using them as a filler to enhance the mechanical and electrical properties of ι-carrageenan, a polysaccharide obtained from algae. Again, free-standing nanocomposites with a CNC concentration of up to 20 wt.% were made by the doctor blade method using water as solvent. Uniaxial tensile testing shows a marked increase in Young's modulus without loss in ductility until high concentrations of CNCs are added. Such an increase indicates that CNCs are homogeneously dispersed within the matrix, as well as the presence of a strong carrageenan-CNC interface. Finally, the CNC incorporation enhances the real dielectric constant ε' and the AC conductivity values as a consequence of the additional carrageenan-CNC interfacial contributions to the dielectric response.

Analogously, biodegradable magnetic nanocomposites based on a series of biodegradable polyesters were prepared by doctor blade casting. PLA, PCL, PBSu, and PBAT have been combined with Fe_3O_4 nanoparticles up to 10 wt.%, producing nanocomposite films with tuneable mechanical properties ranging from stiff and brittle to soft and ductile. The influence on crystallinity by the inclusion of Fe_3O_4 was analysed by DSC. Adding magnetic activity to biodegradable polymers in a solutions-based fabrication method based opens new avenues for developing functional devices, replacing unreliable conventional systems made from petroleum-derived materials.

Finally, there were synthesised novel hybrid core-shell nanorods based on magnetite and gold Fe_3O_4@Au). The nanomaterials were then incorporated into an agarose hydrogel to obtain anisotropic magnetic and optical properties for magneto- and photo-thermal anisotropic transductions. Highly monodisperse ferrimagnetic Fe_3O_4 nanorods with tunable size were synthesised by a solvothermal method by varying the amount of hexadecylamine capping ligand. A gold shell was coated onto the Fe_3O_4 nanorods, leading to an optical response in the near-infrared region. The nanorods were introduced and oriented in an agarose hydrogel to fabricate free-standing anisotropic materials, providing a proof of concept for the applicability of these materials for anisotropic magneto- and photo-thermia applications. The strongly gelling upon cooling and shear-thinning behaviour of agarose enabled the fabrication of magnetically active continuous hydrogel filaments upon injection. These developed multifunctional nanohybrid materials represent a base for advanced sensing, biomedical, or actuator applications with anisotropic response.

Overall, the present work represents in a contribution to the development of electrically and magnetically responsive materials compatible with additive manufacturing technologies, for a next generation of sustainable electronics, being a needed contribution to the ongoing technological transitions.

Table of Contents

1. Introduction

1.1. Context

1.1.1. Industry 4.0 and Internet of things

At the Hannover Messe Trade Fair in 2011, the term "Industry 4.0", a strategic plan for transforming the manufacturing process, was coined. The fourth industrial revolution was thereby defined by connectivity, intelligence, and flexible automation.[1] This concept matched perfectly with the previous idea of the "Internet of Things" (IoT) introduced by Kevin Ashton, director of the Auto-ID Center at Procter and Gamble (P&G) in 1999.[2] The IoT aims to expand the conventional mobile and internet networks to any object of the real world during its whole lifecycle, i.e., IoT proposes to connect *anytime, anywhere* with *anything* and *anyone*.[3] Both concepts together promise to interconnect products and services where the manufacturing machines interact instantly with the products being processed to achieve smooth, cooperative, and efficient manufacturing processes, evolving into Smart Factories.[4] Therefore, total connectivity/interactivity has the potential to influence directly on many societal facets significantly, as represented in **Figure 1.1**. The European Research Cluster on the Internet of Things (IERC) identified that the IoT applications would cover "smart" environments/spaces in domains like transportation, building, city, lifestyle, retail, agriculture, factory, supply chain, emergency, health care, user interaction, culture and tourism, environment, and energy, among others.[5,6]

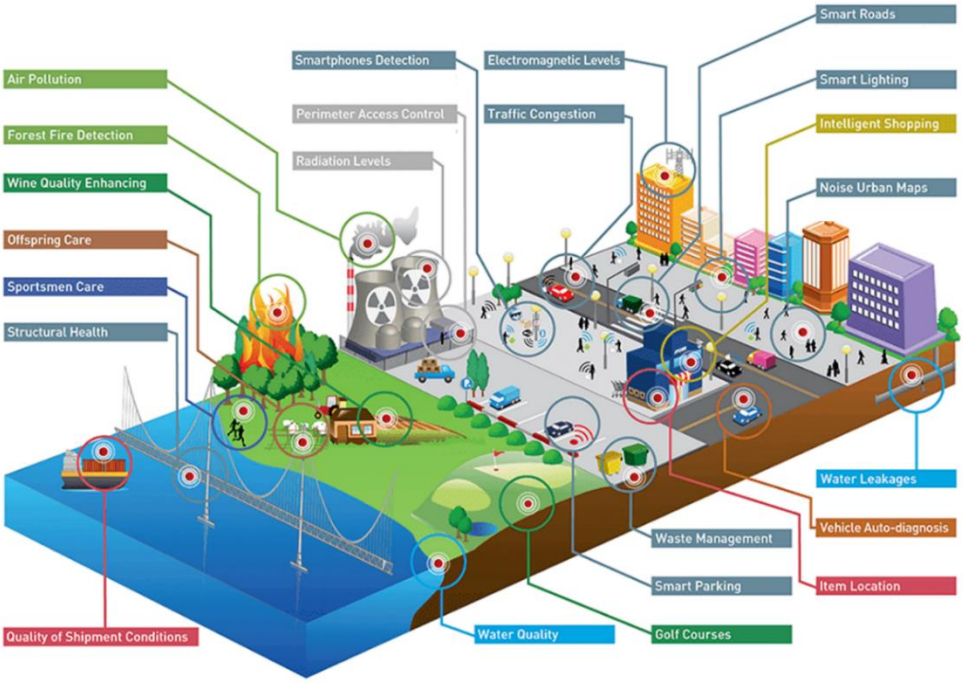

Figure 1.1. Graphical representation of IoT applications in different industrial and societal facets.[7]

This level of connectivity requires new technological advances in digital areas such as machine learning, artificial intelligence, and cloud computing, on the one hand, together with physical advancements in responsive materials, nanotechnology, and additive manufacturing, on the other hand. Hence, it is possible to develop new sensors that gather information, data storage systems, antennas, and energy harvesters, among others.[8] According to Cisco Annual Internet Report, 29.4 billion of all global network devices will be in use by 2023, being 50 % dedicated to *machine-to-machine* (M2M) connections (**Figure 1.2)**.[9] The high demand for components and devices to build a ubiquitous network requires advanced responsive materials. Moreover, integrating the devices in clothes, machines, tools, vehicles, or buildings requires lightweight, flexible, stretchable, efficient, low-cost, and accessible fabricating materials.

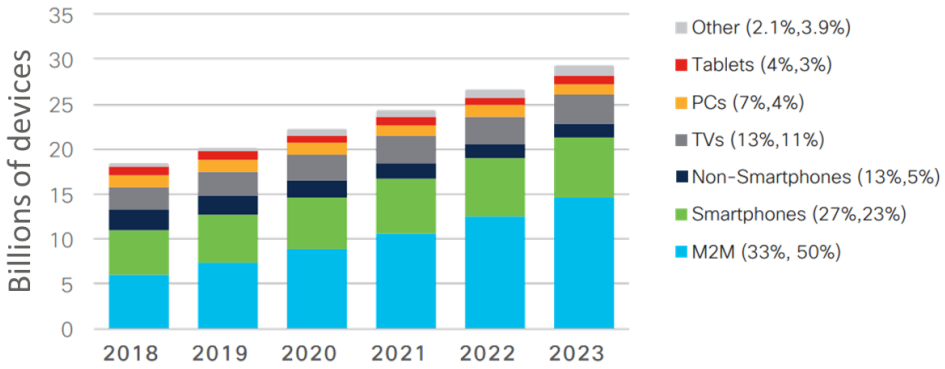

Figure 1.2. Global devices and connections growth expected from 2018 to 2023 by Cisco.[9]

In this global framework, flexible electronics is the most promising technology that assembles these characteristics. The reinforced epoxy circuit board is substituted by a thinner and lighter polymeric film of thickness in a typical range of 25-200 μm with the functional layers deposited onto them.[10] Flexible definition has been referred to bendable, conformally shaped, elastic, lightweight, non-breakable, roll-to-roll manufacturable, or large-area of fabrication materials.[11] The born of flexible electronics is considered to be located in the 1960s when the first flexible solar cell arrays were obtained by thinning single crystal silicon wafer cells to ~100 μm and then assembling them on a plastic substrate to provide flexibility and use them in extra-terrestrial satellites. In materials science research, the flexible term can be considered a conformally shaped material that can be bent considerably without losing its function.[12] Thus, the most widely used substrates for flexible electronics are thermoplastic polymer foils such as polyethylene terephthalate (PET), polyethylene naphthalate (PEN),

polycarbonate (PC), polyethersulphone (PES), polyarylates (PAR), polycyclic olefin (PCO), and polyimide (PI).[13] These materials are excellent substrates because of their mechanical properties, easy processing, and high oxygen and water penetration resistance.[14]

Although these polymers are insulating materials that withstand mechanical deformation or strain, they do not respond to other stimuli and therefore, must be partnered with another material to be useful in sensors, actuators, or distinct electronic components. The active components selectively and reversibly respond to external stimuli, such as temperature, pressure, electric and magnetic fields, pH, or light.[15,16] In this sense, hybrid or composite nanomaterials based on polymers have also received increasing attention, given their high versatility and tunability for specific applications.[17–19]

1.1.2. Responsive materials for flexible electronics

The mixture between polymers and active fillers is a practical pathway for fabricating responsive films, fibres, membranes, or printable inks.[20] Often, responsive materials take advantage of nano- and micro-composite systems conjugating polymers' mechanical and binding properties and specific active functionalities of metallic and ceramic nano-micro-fillers, metal organic frameworks (MOFs), ionic liquids, and carbon-based materials.[21] The combined properties and functionalities of the different components lead to multifunctional materials with increased efficiency and integration capabilities.[22,23]

The development of nanostructured materials initiated the optimisation of their processability. Traditional integration of microelectronics on a rigid substrate and metallic thin films processed at high temperatures did not satisfy the demand for using flexible substrates. Instead, nanostructured materials, which are possible to process in solution, can be cast by various solution methods depicted in **Figure 1.3**, such as spin-coating, spraying, dip-coating, blade-coating (doctor-blade technique), and metering-rod techniques.[24–26]

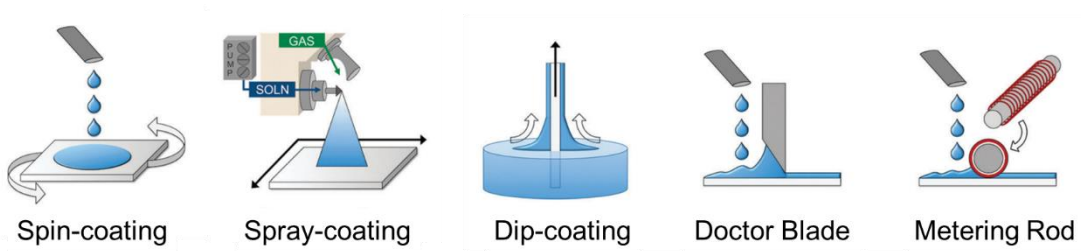

Figure 1.3. Representations of solution deposition methods.[26]

Nevertheless, these solution-phase methods are commonly used for laboratory demonstrations but are hard to be scaled up with the desired pattern. Therefore, additive manufacturing and printing technologies arise to enable processing large areas with industrialised potential.[27] Initial targets of printed electronics were the display and lighting industries. However, printing is currently a commercially viable fabrication technology for electronic devices and sensors.[28,29] Both industry and academia are using inkjet printing, screen printing, and gravure printing together with the aforementioned film processing technologies and other hybrid printing methods opening new opportunities to tackle the limitations of the traditional technologies.[8] The integration of these technological advances into smart factories for manufacturing systems is in constant evolution to produce high-quality goods and services.[27]

At this point, the awareness of the previous industrial revolutions' consequences related to the current environmental issues poses some questions. For example, how will these new materials and processing methods contribute to sustainable development?; how will the waste of the new materials be managed?

1.1.3. Sustainability concerns

It is currently known that the success of ubiquitous technology involves consequences concerning sustainability. The extent of waste associated with electrical and electronic devices and equipment (e-waste) is increasing enormously. For instance, in 2019, a total amount of 53.6 million metric tons (Mt) of e-waste was generated worldwide, which means a real growth of 9.2 Mt since 2014, considering that only 17.4 % of this was officially documented as adequately collected and recycled (**Figure 1.4**).[30,31]

The e-waste problem can be partially ascribed to non-degradable synthetic polymers for the fabrication of electronic devices. The use of these materials in flexible electronics aggravates the global problem of the accumulation of plastic waste. By 2015, the total plastic waste accumulation was estimated at around 6300 Mt, where 79 % was unmanaged finishing in landfills or natural environments.[32] More precisely, 8 Mt of plastics are discarded into the ocean annually (recently anticipated to increase by an order of magnitude by 2025).[33]

Therefore, given the severity of the plastic waste and the contribution of e-waste, there is an urgent need to develop sustainable materials for constructing newly flexible electronics that are eco-friendly, and biodegradable.[34]

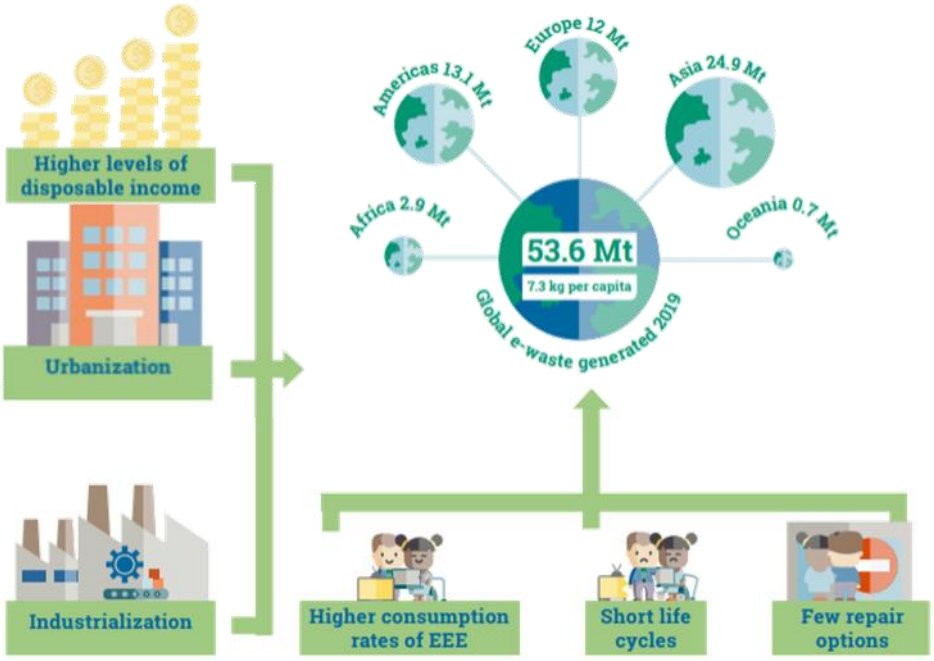

Figure 1.4. Representation of the e-waste generated in 2019.[30]

In this regard, strong scientific and technological efforts are being carried out to replace traditional petroleum-based synthetic polymers with renewable materials or biopolymers to reduce the environmental footprint.[35,36] Biopolymers are polymers that biodegrade and should include, among their properties, renewability, sustainability, and non-toxicity. According to their origin, they can be classified as natural sourced and synthetic biopolymers.[37] Nature provides a wide range of renewable and readily available materials, including polysaccharides such as cellulose, chitin/chitosan, carrageenans, alginate, hyaluronates, and starch.[38] These natural polymers can be sourced from primary renewable resources but can also be found in low-value organic wastes. For instance, cellulose can be extracted from agricultural and forestry residues, starch can be obtained from potato peels, collagen is a high-value fish byproduct, and carrageenans and alginate are produced by red seaweed and brown seaweed, respectively.[39] In the case of synthetic biodegradable polymers, their origin and properties will be discussed later more deeply.

Completely sustainable development requires the extraction of natural resources at rates that do not risk long-term supplies. Thus, the exploitation of renewable resources to develop new materials should not harm food production or result in deforestation and loss of biodiversity. In addition, the rate of residues generation can´t surpass the capacity of the natural environment to assimilate them.[40] Typically, biodegradable polymers are biodegraded

or composted under certain conditions. Thus, these materials should be clearly identified to take advantage of their biodegradability and avoid contributing to the accumulation of plastic in natural environments.

In this scenario, the work developed during this thesis aims to contribute positively to society by developing sustainable composite materials. Biopolymers have mostly been employed as matrices comprising inorganic or organic responsive fillers. Usually, matrices based on polysaccharides were selected, but synthetic biodegradable polymers were also studied and compared to obtain a better understanding and availability of sustainable materials. Depending on the mechanical, thermal, or functional properties and their solubility in appropriate solvents, a manufacturing technique and a specific application can be developed. Among the plethora of activities that the addition of fillers can perform, electrical conductivity and magnetic activity are sought after in these materials. These two functionalities are the basis of a large variety of electronic devices, including sensors and actuators.

1.2. Sustainable responsive materials

Among the existing biopolymers available to fabricate responsive composite materials, extensive attention relapses on the combination of active fillers with polysaccharides, molecules composed of long chains of monosaccharide units linked by glycosidic bonds in the linear or branched configuration. Considering all available polysaccharides, cellulose, the most abundant biomaterial in the biosphere, emerges as one of the most promising, as demonstrated by the increasing number of scientific publications during the last two decades. Mainly, cellulose-based materials have been investigated during the thesis due to their abundance, strength, biocompatibility, processability, degradability, low cost, hydrophilicity, high sorption capacity, alterable optical appearance, and easiness of being chemically modified.[41]

1.2.1 Cellulose

The exploitation of cellulose has been known since the dawn of civilisation, from clothing and paper to building materials. Still, in recent decades, it has drawn much attention to the extraction of its nanostructured materials and nanofibers to employ their improved properties

on innovative high-value applications with new and advanced functionalities.[42]

Cellulose is a natural fibrous polymer and the main component of plant cell walls. Thus, it has diverse starting materials. It is mainly extracted from plants on a large scale, such as wood, cotton, bamboo, and cereal, or is generated from tunicates and bacteria. Natural cotton fibres typically contain up to 98 % cellulose, and wood can have cellulose contents ranging from 10 % to more than 90 %, depending on the type of wood and material.[43] Chemically, it is a high molecular weight homopolymer of β-1,4-linked anhydro-D-glucose units in which every unit is corkscrewed 180° with respect to its neighbours, and the repeat segment is frequently taken to be a dimer of glucose, known as cellobiose (**Figure 1.5a)**.[44]

On the one hand, as represented in **Figure 1.5b**, the high density of hydroxyl groups can form intramolecular hydrogen bonding with the adjacent rings of their chain, leading to more stable glycosidic linkage motifs and linear-chain configuration. On the other hand, inter-chain hydrogen bonds can occur between the neighbouring polymer chains and promote their parallel stacking to be assembled into elementary fibrils. Therefore, microfibers can be created with two differentiated regions: crystalline (highly ordered) and amorphous (disordered) structures similar to those represented in **Figure 1.5c**.[45] These two regions' distribution is conditioned by raw materials and pretreating techniques. Cellulose fibres can be processed into various morphologies, such as cellulose nanofibres (CNF) and cellulose nanocrystal (CNC) using different treatments.[46] CNCs are rod-like rigid crystals of the crystalline regions of cellulose fibres, with lengths between 100 nm and several micrometres and widths of 5–70 nm. They are obtained by the removal of amorphous sections of a purified cellulose source by mild acid hydrolysis using sulphuric acid, often followed by ultrasonic treatment. During the process, the acid induces the cleavage of glycoside bonds of the amorphous regions of the cellulose fibres, which leads to the dissolution of amorphous cellulose, remaining the CNC.[47]

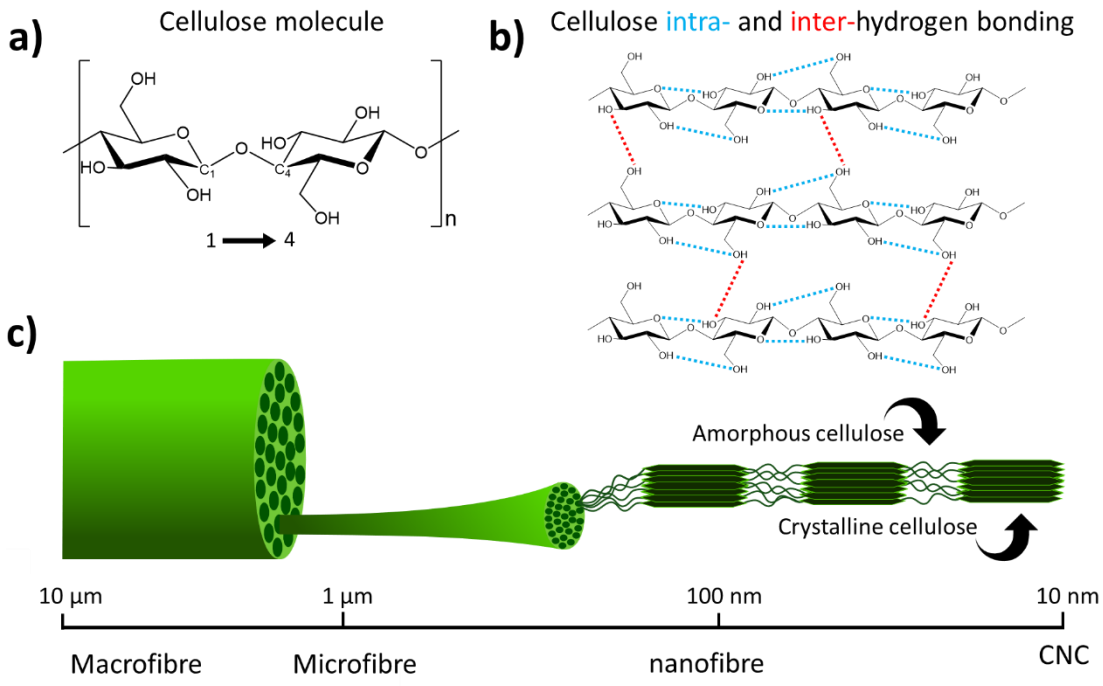

Figure 1.5. schematic representation of different cellulose structures. a) cellulose repetitive unit, showing 1→4 linkage. b) The molecular structure of cellulose chains linked by intra- (blue) and inter- (red) hydrogen bonding. c) Supramolecular structure of cellulose macrofibres, microfibres, nanofibers, and nanocrystals. The scale line indicates the order of magnitude of the diameter of the structures. Inspired from references [43] and [45].

During hydrolysis, sulfuric acid reacts with the surface hydroxyl groups of CNCs via an esterification process and yields negatively charged sulfate groups ($–OSO_3^-$) that promote uniform dispersion of the crystals in water via electrostatic repulsions. CNCs tend to adopt configurations that minimise the existing electrostatic interactions when the water phase is continuously removed. Interestingly, concentrated suspensions self-organise into liquid crystalline arrangements, similarly to what occurs in non-flocculating suspensions of other rod-like particles, such as poly(tetrafluoroethylene) whiskers, tobacco mosaic viruses, DNA fragments, or crystallites extracted from other polysaccharides such as chitin.[48] This self-organisation from suspensions was observed by polarised optical microscopy, revealing the appearance of "fingerprint" patterns, indicative of a chiral-nematic ordering. The chiral nematic structure remains after complete water evaporation resulting in iridescent films of CNCs reflecting left-handed circularly polarised light in a narrow wavelength band determined by the chiral nematic pitch and the refractive index of the film.[48]

1.2.1.1. Mechanical properties

The mechanical properties of individual CNC are conditioned by different factors such as anisotropy, defects in the nanocrystals, or crystallinity percentage. Theoretical calculations and indirect experimental measurements using atomic force microscopy (AFM), X-ray diffraction analysis (XRD), inelastic X-ray scattering, Raman scattering, etc., were used to calculate the elastic properties of CNC. The theoretical tensile strength of CNCs was found to be 7.5–7.7 GPa, higher than that of steel wire, carbon nanotubes, and Kevlar®-49, as can be compared in **Table1.1**. Further, Young's Modulus ranges between 130 and 250 GPa.[49,50] As CNCs are anisotropic, where the cellulose chains in a monoclinic crystalline structure align parallel to the long axis of the CNC, this leads to a higher Young's modulus (E) for the axial direction of the CNC (E=100–220 GPa), compared with transversal direction (E=10–50 GPa).[51] Nevertheless, the CNC films are usually brittle due to their crystalline nature. In addition, the ineffective load transfer caused by porosity and weak CNC-CNC interfaces within the film yields lower Young´s modulus (E= 6 GPa, for CNC extracted from woods; E= 5–10 GPa for CNC from tunicates) than those of the individual CNC.[52,53] Still, the use of cellulose films as an innovative material to develop chiroptical luminescent sensors, energy-storage devices such as lithium-ion batteries, and water-activated shape memory materials has been increasingly popular during the last decade.[54]

Table 1.1. Properties of cellulose compared with several reinforcements: density (ρ), tensile strength (σ_f), elastic modulus in the axial direction (E_A), and elastic modulus in the transverse direction (E_T).[51]

Material	ρ (g cm^{-1})	σ_f (GPa)	E_A (GPa)	E_T (GPa)
Kevlar-49 fibre	1.44	3.6-4.1	124-130	2.5
Carbon fibre	1.78	1.5-5.5	150-500	-
Steel wire	7.85	4.1	210	-
Clay nanoplatelets	-	-	170	-
Carbon nanotubes	-	11-63	270-950	0.8-30
Boron nanowhiskers	-	2-8	250-360	-
Crystalline Cellulose	1.55	7.5-7.7	110-220	10-50

The excellent mechanical properties of individual CNC gave rise to their use in composite manufacturing as a reinforcement phase in polymer matrix composites.[55] Helbert, Cavaillé, and Dufresne were pioneers in fabricating nanocomposite films of poly (styrene-co-butyl acrylate) and CNC up to 30 wt.% by solvent casting. The nanocomposite's *E* increased two

orders of magnitude when comprising a 5 wt.% and close to 1000 times higher than the pure polymer for samples at 30 wt.%.[56] Since then, CNC has been employed as filler with many polymers. Moreover, the reinforcing effect of CNCs in biopolymers attracts particular interest due to the preservation of full renewability. Hence, both synthetic and natural polymers, such as polylactic acid (PLA),[57] polycaprolactones (PCL),[58] polybutylene succinate (PBSu),[59] polyvinyl alcohol (PVA)[59], cellulose derivatives,[60,61] chitosan,[62] or starch[63] have been combined with CNC to improve their properties. In general, adding a small amount of CNCs, in the range of 0.5–5 wt.%, improves the mechanical properties, characterised by a significant increase of *E*, and tensile strength. Typically, CNCs form a percolating network within the polymer matrix in which the stress is assumed to be transferred through crystal/crystal and crystal/polymer matrix interactions. However, high loadings (≥10 wt.%) result detrimental to the material, usually due to the formation of large aggregates of CNCs, a product of their strong hydrogen bonding property, leading to a premature fracture of the material.[64]

1.2.1.2. Thermal stability

The thermal properties of CNCs are typically studied attending to their onset of thermal chemical degradation measured by thermogravimetric analysis (TGA). Typically, the onset of thermal degradation of CNCs occurs in the range of 200–300 °C, which mainly depends on the particle origin, and surface modification. The CNC hydrolysis with other acids such as hydrochloric, hydrobromic, citric, or phosphoric supposes a different surface charge, and colloidal and thermal stability of the CNCs.[55] Camarero Espinosa *et al.* compared thermal stabilities of sulfonated (S-CNC), phosphorylated (P-CNC), and non-functionalised (with their hydroxyl groups) (H-CNCs) from cotton. Sulfonates groups catalysed the start of thermal degradation with an onset at around 150 °C, with a slow decomposition rate, reaching the maximum decomposition temperature at 500 °C. P-CNCs and H-CNCs had lower charge content, promoting CNC-CNC interactions and remain more aggregated in composites but have higher thermal stability. Both started to decompose at 220 °C. However, the decomposition process was slower for H-CNCs, where the maximum decomposition temperature was 350 °C, in comparison to 325 °C for the P-CNCs.[65]

Interestingly, the addition of CNC into several matrices such as natural rubber,[66] or starch,[67] increases the thermal stability of the polymer matrix with increasing CNCs concentration in the nanocomposite. The increase in the thermal stability associated with the

CNC is usually ascribed to the generation of large CNC-matrix interphase, where the large surface area of the nanofiller restricts the chain mobility, producing a delay in the scission of the polymer chains and the escape of byproducts. Furthermore, the influence of the addition of cellulose nanofiller on the thermal transitions of the polymer matrices has been investigated. However, controversial results have been found regarding the glass transition (T_g) and melting (T_m) temperatures of polymers, as contrary effects are found depending on the fabrication process, the nature of the polymeric systems, and CNC characteristics.[52,68,69]

1.2.2. Cellulose derivatives

Because of the strong intramolecular and intermolecular interactions via hydrogen bonds, pure cellulose is insoluble in cold or hot water. Thus, the facility to modify cellulose is advantageous in synthesising water-soluble cellulose derivatives by substituting the -OH groups in each anhydroglucose unit. These cellulose derivatives can be divided into two main groups according to the functionality of the bonded oxygen, cellulose esters, and cellulose ethers. Particularly in the formed ethers, properties such as water retention capacity, pseudoplasticity, film formation, complexation, and surface activity, among others, facilitate the processing of cellulose-based materials and make them suitable for the fabrication of flexible materials by different printing techniques. The most studied cellulose ethers are gathered in **Table 1.2**, where the substituents' possible positions are represented in **Figure 1.6**. In this thesis, it was considered three of the most studied cellulose derivatives in the literature: Methyl cellulose (MC), hydroxypropyl cellulose (HPC), and sodium carboxymethyl cellulose (NaCMC).[70]

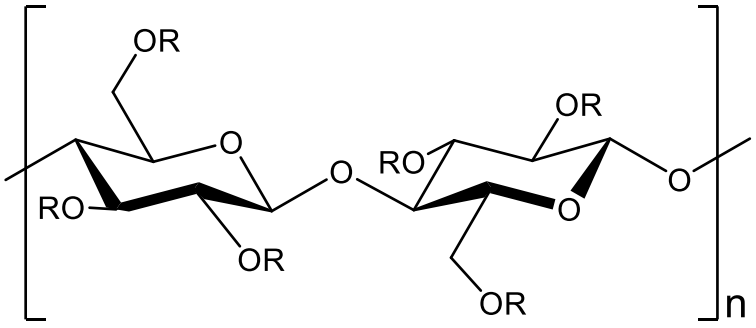

Figure 1.6. Structure of cellulose derivatives (R=H or R from Table 1.2)[70]

Table 1.3. Substituents of water-soluble cellulose ethers (CM= carboxymethyl, HE= hydroxyethyl, HP= hydroxypropyl, M= methyl, SE= sulphoethyl, C= cellulose in a limited DS range)[70]

Cellulose ether	–R
Carboxymethyl cellulose (NaCMC)	$–CH_2COONa$
Sulfoethyl cellulose (SEC)	$–CH_2CH_2SO_3Na$
Methyl cellulose (MC)	$–CH_3$
Ethyl cellulose (EC)	$–CH_2CH_3$
Hydroxyethyl cellulose (HEC)	$–CH_2CH_2OH$
Hydroxypropyl cellulose (HPC)	$–CH_2CH_2CH_2OH$
Cyanoethyl cellulose (CyEC)	$–CH_2CH_2CN$

MC is the most straightforward cellulose derivative extensively used in the food industry, cosmetics, gels, and adhesives,[71,72] as a result of its lower critical solution temperature (LCST) of 29 °C, which acts as viscosity-controller (above 29 °C an increase in the viscosity is achieved).[73] HPC is a water-soluble cellulose ether with many applications in the fields of food, medicine, construction, and smart materials.[41,74,75] It shows good film-forming capacity, is highly transparent, presents good resistance to oil and fats, and shows an LCST of 41 °C in water.[76] As HPC has been used as a stabilising agent to improve the dispersibility of inorganic nanoparticles (NPs) into polymeric matrices, NPs dispersed in HPC typically show a homogeneous distribution.[77] NaCMC is an anionic cellulose derivative produced at an industrial scale. Thanks to its low-cost, renewability, biodegradability/biocompatibility, high viscosity, transparency and hydrophilicity, it has been used for applications as varied as tissue engineering, food industry, textile, paper industry, or water treatment.[78] In particular, many works have focused on developing NaCMC-based hydrogels as their numerous hydroxyl and carboxylic groups allow an efficient water binding. Notably, despite the fact that all these three derivatives are water-soluble, they can keep their morphology and do not become sticky when exposed to humidity, allowing their use in industrial applications.

As nanocomposite development results in an efficient route to obtain hybrid properties tailored for specific functional responses, cellulose derivatives have been reinforced with NPs as varied as graphene oxide,[79] bentonite,[78] attapulgite,[80] ZnO,[81] ZnS,[82] halloysite nanotubes,[83] montmorillonite,[84] carbon dots,[85] and carbon nanotubes.[86] Overall, improved thermal, barrier, mechanical, electrical, or catalytic properties were obtained.

1.2.3. Synthetic biodegradable polymers

Although natural polymers are an excellent option to tackle the plastic problem associated with e-waste, biodegradable synthetic polymers offer the additional advantage of providing materials with tailored physico-chemical and mechanical properties and higher reproducibility and uniformity.[87] In addition, some of the monomers of biodegradable polymers can be obtained from renewable resources (either natural feedstock or bacterial fermentation), limiting the dependence on fossil resources. Specifically, biodegradable polyesters have gained attention in the last years towards sustainability both in fundamental research and in the actual market because of their capacity to hydrolytically cleavage of ester groups.[88] In terms of biodegradation, a process of three steps can occur at a molecular level in soil, water, or human beings. The first is the deterioration, where the polymer's mechanical, chemical and physical properties begin to be modified. The second step involves the fragmentation of high molar mass macromolecular chains to oligomers and monomers. This results in polar functional chain ends and monomers accompanied by the loss of specific polymer properties, such as molar mass and strength. This step can take place due to hydrolysis (with or without enzymatic catalysis) or oxidation, where critical factors are the chemical structure of the polymer backbone and the environment in which the polymer is being disposed and/or used. In the third step occurs the mineralisation of the oligomers with polar chain ends by microorganisms. Ultimately, carbon dioxide (CO_2), methane, water, and biomass are formed (**Figure 1.7**).[89] These biodegradable polymers mainly include aliphatic polyesters such as PLA, PCL, PBSu, poly(butylene succinate-co-adipate) (PBSA), and other aliphatic copolyesters and aliphatic-aromatic copolyesters such as poly(butylene adipate-co-terephthalate) (PBAT). In this thesis, magnetoactive materials have been developed based on magnetite as filler and PLA, PBSu, PCL, and PBAT as matrices; which main synthesis routes and their characteristic mechanical and thermal properties are discussed in the following.

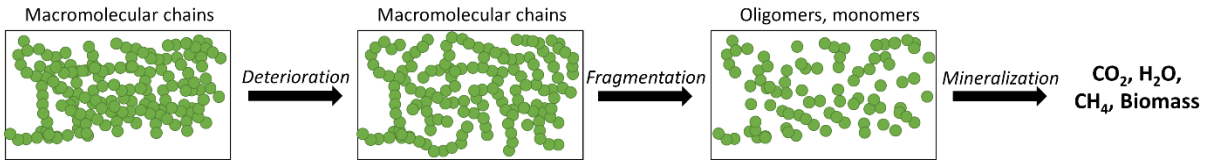

Figure 1.7. Scheme of the stages during the biodegradation process. Figure inspired from references [89] and [90].

1.2.3.1. Polylactic acid

Polylactic acid, PLA, can be synthesised from natural resources. Its monomer, lactic acid (the most widely occurring carboxylic acid in nature), is made by the bacterial fermentation of carbohydrates such as corn, sugarcane, potatoes, and other biomass. High-molecular-weight PLA can be synthesised using three different routes: direct condensation polymerisation, azeotropic dehydrative condensation, and ring-opening polymerisation of lactide. Among these routes, direct condensation polymerisation is the least expensive method, but low-molecular-weight PLA is obtained due to the difficulty in removing the water from the reaction media. It presents L-, D-, and DL-lactide isomers, which depend on the pendent methyl group on the alpha carbon atom. The original L-lactic acid is the natural and biologically important isomer, while D-form can be produced by some microorganisms or by racemisation. DL-lactide is a blend of D-lactide and L-lactide, which can vary the percentage of the stereoisomers.[89] The homopolymer of L-lactide (PLLA) is a semicrystalline polymer with a reference value of T_m= 157–180°C and a T_g= 55–65°C.[89] It is a slow-crystallising material, where its crystallinity strongly depends on processing conditions such as cooling rate and annealing status. PLLA exhibits higher strength (∼60 MPa) and modulus (∼3 GPa) than many *commodity* polymers.[91] For instance, HDPE has a specific strength and modulus of 20 MPa and 1 GPa, while polypropylene (PP) shows a typical strength and modulus of 30 MPa and 1.5 GPa, respectively. However, PLA is a brittle polymer that exhibits a standard tensile strain at a break of less than 6 % and limits its use in many applications.[92]

1.2.3.2. Poly(butylene succinate)

Poly(butylene succinate), PBSu, is mainly synthesised by polycondensation between succinic acid and 1,4-butanediol (BD). The reaction proceeds in two steps. First, esterification occurs between the diacid and the diol, and then polycondensation occurs under high temperatures to form high-molecular-weight PBSu.[92] The monomers can be obtained from both fossil or renewable resources, whereas succinic acid and BD can be derived from the fermentation method to produce bio-based PBSu. It is a semicrystalline polymer with a T_g range from −45 °C to −10 °C and a T_m from 90 °C to 120 °C. The tensile yield stress ranges 30–35 MPa with Young's modulus of 300–500 MPa.[93] The flexibility of the materials depends on the degree of crystallinity. Thermal stability is influenced by the content of

residual carboxylic acid terminals, which dominates the water sensitivity and the molecular structure of polymer chains. It is considered to be the potential alternative to PE and PP.[94]

1.2.3.3. Polycaprolactone

Polycaprolactone, PCL, is a petroleum-based semicrystalline linear aliphatic polyester composed of hexanoate repeating units. It is synthesised by ring-opening polymerisation (ROP) of ε-caprolactone in the presence of metal alkoxides (tin octoate, aluminium isopropoxide) instead of condensation usually employed for the synthesis of polyesters.[88] PCL has good water, oil, solvent, and chlorine resistance.[95] It presents a T_g of -60 °C and a low T_m of 57−60 °C, making it suitable for biomedical applications, but it is a drawback for high-temperature applications. High molecular weight PCL polymer has elastomeric behaviour with a tensile stress of 12–30 MPa and a break extension of 400–900%.

1.2.3.4. Poly(butylene adipate-co-terephthalate)

Poly(butylene adipate-co-terephthalate), PBAT is the most widely used aliphatic-aromatic copolyester, usually known under the brand name Ecoflex® (developed by BASF). It can be produced by polycondensation reaction of 1,4-butanediol with both adipic and terephthalic acids (or butylene adipate). The polymerisation requires long times reaction, high vacuum, and high temperature.[92] Apparently, higher concentrations of terephthalic acid (from 31 mol.% to 48mol.%) increase the tensile strength (from 8 MPa to 12 MPa). Still, the higher chain stiffness due to the inclusion of aromatic groups leads to a severe decrease in the elongation at break (from 650 % to 180 %). Likewise, the Tg increases by 40 ºC from -61ºC, and the Tm rises from 79 ºC to 137 ºC.[96] As PBAT is a compostable polymer, it has been mainly used in packaging and agricultural applications.[97]

1.2.4. Electrically and ionically conductive fillers

Advances in polymer composites have been focused on the fabrication of conductors, including electrical and ionic ones. Indeed, conducting materials with high electrical conductivity and good compatibility with biopolymers have been combined to fabricate biocompatible conductors. Various conducting materials, including electron-conductive materials (e.g., metal-based and carbon-based nanomaterials, conducting polymers) and ion-

conductive fillers (ionic liquids and salts), have been investigated as conductive components combined with natural biopolymers. The electrical properties of a polymer-based conductive composite material rely on the intrinsic conductivity of conductive components, the compatibility of the counterparts, and the dispersion of active material in the polymeric network.[98] Metal-based nanomaterials are typically based on gold (Au) and silver (Ag) with various shapes: spherical NPs, nanowires, nanorods, and flakes, as they exhibit high electrical conductivity. However, silver nanomaterials are susceptible to oxidation, leading to their low long-term stability for practical applications where the fabrication process involves water as solvent. Moreover, stabilising ligands can hinder the close contact of metal nanomaterials leading to inefficient conduction of percolation networks.[99]

Thus, carbon-based nanomaterials such as carbon nanotubes (CNTs), graphene, and graphene oxide (GO), or other carbon allotropes such as graphite and carbon black (CB) have been developed for conductors. They perform good electrical conductivity, superior chemical stability, and facile functionalisation. However, CNTs and graphene's hydrophobic feature makes them difficult to disperse within hydrophilic natural biopolymers. Besides, graphite has a mild hydrophilic character, with a water contact angle lower than 90º, which can help in the development of conductive materials in aqueous and hydrophilic solutions.[100] Currently, graphite is less trendy than carbonaceous nanosized materials, but it is the most common form of naturally occurring polymorphs of crystalline carbon. It has been important in catalysis, electrochemistry, gas adsorption, and solid lubrication.[101] Graphite is anisotropic, with electrical and thermal conductivity along the layers (due to the in-plane metallic bonding) but results in a poor electrical and thermal conductor perpendicular to the layers (due to the weak van der Waals forces between the layers). Therefore, the carbon layers can easily separate with respect to one another, enabling the use of graphite as a good lubricant and pencil material.[102] Indeed, its electrical conductivity allowed it to develop lightweight, high safety, high flexibility, and environmental benign electrochemical electrodes,[103] humidity sensors,[104] and electric brushes by a simple pencil-drawing onto cellulose papers.[105]

In the framework of sustainable conductors, ionic liquids (ILs) have emerged as a novel class of chemical compounds for developing advanced (multi)functional materials with outstanding potential in applications in several areas.[105] ILs are typically defined as liquid electrolytes composed only of ions with a relatively low melting temperature (<100 °C). They can include a vast number of organic cations and organic or inorganic anions. ILs are characterised by their efficient interplay between their ions' hydrogen bonding, and

coulombic and van der Waals interactions. These compounds present unique characteristics such as negligible vapour pressure, nonvolatility, relatively high viscosity, high chemical and thermal stability, electrochemical stability with an electrochemical window between 4 and 6 V, nonflammability, and overall, high ionic conductivity ($\approx 10^{-3}$–10^{-2} S cm^{-1}).[106] Additionally, they have been demonstrated as green solvents to dissolve natural biopolymers, such as protein and polysaccharides, with dense network structures induced by inter- and intramolecular interaction.[107] In fact, their high solubility enables to replace volatile and toxic organic solvents in organic reactions, catalysis, extraction, and separation, promoting the development of green chemistry and clean technologies.[108]

Different responsive materials have been reported based on combining polysaccharides as matrices and ILs as active additives. Quaternized chitosan cross-linked with glutaraldehyde and synthesised gemini-type basic morpholine ionic liquid ([Nbmd][OH]) were employed to develop an exchange membrane. The addition of the IL improved the thermal stability and ionic conductivity with the content of OH^- groups (1.37×10^{-2} S cm^{-2}).[109] A biocompatible, biodegradable, highly transparent, and flexible, solid-state electrolyte has recently been developed by combining levan polysaccharide and choline-based water-soluble ionic liquid. Levan is a polysaccharide of fructose molecules connected by 2,6 beta glycosidic linkages. Large specific capacitance (≈40 μF cm−2) at a low operation voltage range was observed when it was utilised in organic transistors.[109] Furthermore, ionic electroactive polymer (EAP) actuators have been reported based on silk fibroin (SF), which derives from silkworm and is composed of glycine, alanine, and serine amino acids. In this case, the use of ILs choline dihydrogen phosphate ([Ch][DHP]) and 1-n-butyl-3-methylimidazolium tricyanomethanide ([Bmim][$C(CN_3)$]) lead to a bending effect of SF films when an electric field is applied.[110] The mechanism of these bendable actuators can be explained as an electric-double-layer capacitor. When a voltage is applied between two electrodes, the cations and anions in the matrix-electrolyte are transferred to the cathode and anode layers, respectively. The ion transportation is most likely to result in the swelling of the cathode layer and the shrinkage of the anode layer due to the larger size of the cation than the anion, resulting in a bending displacement toward the anodic side.[111]

1.2.5. Magnetic fillers

Magneto-responsive materials integration in the IoT environment is particularly interesting

due to their non-contact activation, non-local modulation, and in some cases, fast switching.[112,113] They allow the fabrication of antennas, artificial muscles, inductors, transformers, sensors, and actuators, among others. They usually arise from the combination of magnetic NPs and polymeric matrices. In these systems, the effect of an external magnetic field over magnetic particles triggers a physical change in the structure of the polymer.[113] Depending on the mechanical and physico-chemical properties, for example, elastomeric matrices can lead to magnetorheological elastomers (MREs), where the modulus of the material change under an external magnetic field.[114] For different applications, small particle sizes and tailorable magnetisation are preferred to incorporate them into a matrix, as they become easily processable and highly functional.[115] Beside enabling device miniaturisation, the physical properties of nanometric magnetic particles can vary notably from their bulk counterparts.[116]

The most used materials that provide the magnetic properties to the NPs are iron (Fe), cobalt (Co), or nickel (Ni), their oxides, and some other elements combining several metals, such as materials based on copper, zinc, manganese, strontium, and barium. Among these elements, in the last five years, superparamagnetic iron oxide NPs (SPIONs), and in particular magnetite (Fe_3O_4), maghemite (γ-Fe_2O_3), and metallic substituted ferrites (MFe_2O_4 (M= Co, Cu, Ni, Mn, Mg, etc.) have attracted almost completely the attention due to their biocompatibility, chemical stability, low cost, and unique magnetic properties.[117] Magnetic materials can be divided into soft and hard magnetic materials depending on how easily they are demagnetised, which reflects in the behaviour of the hysteresis loops, as presented in **Figure 1.8a-c**.[118] The study of these hysteresis loops is important in designing and optimising magnetic and electromagnetic components and devices. Soft magnetic materials are known for rapid magnetism reversal with low retentivity and coercivity, thus being useful in electrical apparatus that requires small energy dissipation. Otherwise, a much higher retentivity and coercivity, resulting in higher remanent magnetisation, is needed in permanent magnets and memory devices, where demagnetisation must be difficult to induce.[119,120]

According to the magnetic behaviour of the magnetisation as a function of the applied magnetic field, magnetic materials can be classified into different types (**Figure 1.8d–h**).[121,122] Diamagnetic materials produce a magnetic dipole in the opposite direction to the applied magnetic field.[123] Conversely, if a material presents a random magnetic dipole orientation in the absence of an external magnetic field and the magnetic moments are aligned in the field's presence, the material is called paramagnetic.[124] A ferromagnetic

material already has a magnetic dipole orientation and, consequently, permanent magnetisation in the absence of an external magnetic field, maintaining it in the presence of a magnetic field up to saturation and exhibiting long-range order. Ferrimagnetic and antiferromagnetic materials, similarly to ferromagnetic materials, show aligned magnetic dipoles in the absence of a magnetic field; however, they also contain adjacent non-oriented antiparallel magnetic dipoles capable of reducing or cancelling the neat magnetisation, respectively.[123,124] Finally, another specific type of magnetism is called superparamagnetism. This form of magnetism appears in nanoscale ferromagnetic or ferrimagnetic NPs below a critical size, and their response to an external magnetic field is like a paramagnetic material; however, the response of a superparamagnetic material is much larger.[123]

In one of the most well-known applications of magnetoactive materials, rare earths, such as samarium (Sm), terbium (Tb), neodymium (Nd), or dysprosium (Dy), have been used in the development of magnets due to their high magneto-activity and efficient performance. However, the use of rare earths encompasses significant global problems, such as political and economic challenges, due to the limited availability and the high demand for these materials for technological applications. In terms of sustainability, the increase in mining activities implies hazardous consequences associated with environmental issues, including their presence as traces in waters and wastewaters.[112] Thus, ferrites and other less sparse elements, such as Ni and Co, have been employed in the last decade to tackle the problematic issues that arise due to rare earths.[125] Additionally, ferrites have been introduced in magneto-active materials since they present a wide range of suitable magnetic properties, as they are, in general, soft magnetic materials allowing the reversibility of the response at low fields.

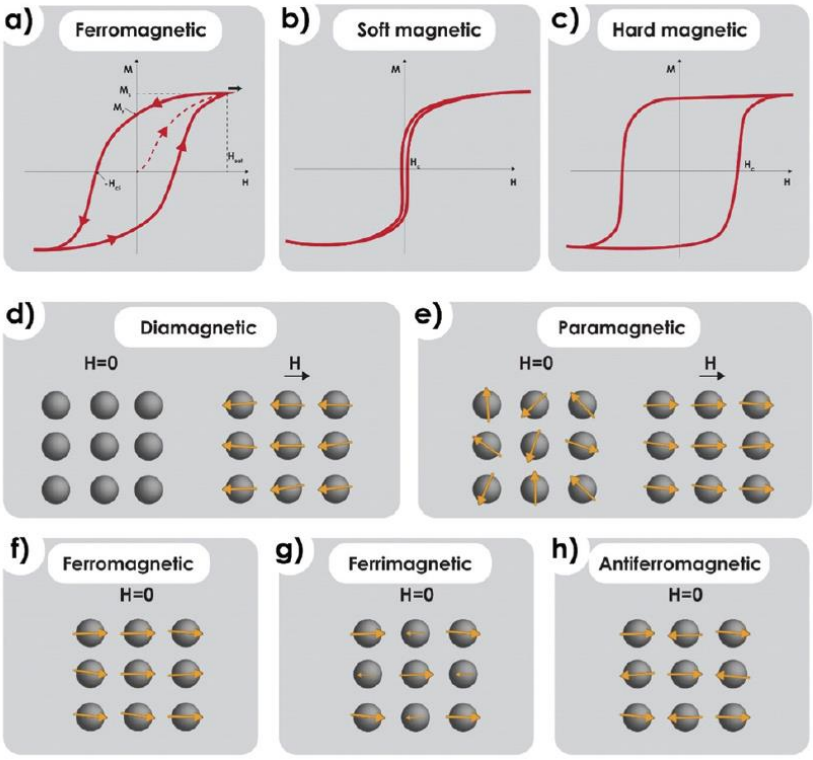

Figure 1.8. (a) Hysteresis loop for a ferromagnetic material. Representative hysteresis loops of (b) soft magnetic materials and (c) hard magnetic materials. (d–h) Arrangements of the magnetic dipoles for five different types of magnetic materials, both in the absence and in the presence of an external magnetic field.[126]

Among all the magnetic iron oxides currently available, cobalt ferrite ($CoFe_2O_4$) display outstanding properties as present high saturation magnetisation, small coercivity, and low toxicity. However, Co is considered a critical raw material because its production is concentrated in a few countries, leading to geopolitical instability and supposing environmental risk.[127] To avoid this issue, Fe_3O_4 or γ-Fe_2O_3 also present suitable magnetic performance with similar properties and easiness to be synthesised by different methods, such as co-precipitation, thermal decomposition, sol-gel method, or solvothermal/hydrothermal synthesis.[128,129] These NPs have shown a great potential to develop multifunctional materials when incorporated into polymeric matrices such as poly(vinylidene fluoride) (PVDF) and its copolymers.[128,130,131] However, in the framework of this thesis, biodegradable hybrid materials emerge as a sustainable alternative to replace the existing electroactive materials such as PVDF and its copolymers,[132] which apart from being based on petrochemical resources typically require the use of chlorinated solvents such as dimethyl formamide (DMF).[133] Particularly, embedding magnetic NPs into soft biopolymeric matrices has attracted great attention as they allow the fabrication of sustainable multifunctional free-

standing materials and devices.[134] In this sense, the incorporation of nanofillers within a host matrix enables combining in a synergetic way the intrinsic properties of the matrix (such as mechanical adaptability) with the functional properties of the fillers.[126] Given the broad range of magnetic fillers and polymeric matrices, these materials can be tailored for many applications, particularly in soft actuators, sensors, or electronics components.

Furthermore, ferrites can be easily functionalised. The combination of materials with different structures and functionalities leads to a hybrid material with multifunctional features enabling diverse tasks to be performed simultaneously.[135] Several heterostructures have been generated to take advantage of each component's benefits. For instance, multiple morphologies (core-shell, yolk-shell, core-satellite, or Janus) multicomponent magnetic NPs have been synthesised for a plethora of applications related to the IoT, such as viruses, bacteria or health-related substances detection, organic pollutants and heavy metals sensors, electrode-based sensors or point of care devices, among others.[136]

1.3. Printing technologies

Currently, different methods are available for the fabrication of electrically and magnetically active materials (either composites or monoliths), including gas flow sputtering,[137] layer-by-layer,[138] solvent casting,[129] spin coating,[139] or melt-mixing.[140] Several of those traditional approaches result expensive, non-scalable, involve time-consuming processes and/or do not allow the fabrication of well-defined shapes with accuracies below the millimetre. Moreover, the resulting materials are difficult to assemble onto mechanically flexible substrates, which are increasingly being demanded for emerging applications such as flexible and wearable devices.[141,142] During the last decade, additive manufacturing technologies are emerging as high-throughput routes which allow to overcome the issues mentioned above.[143,144] The versatility of printing technologies in processing lightweight microdevices of active elements onto flexible substrates with the desired shape, large areas, high throughput, and environmentally friendly processes, make them a key tool for developing electro- and magneto-active polymeric devices. Conventionally, 2D electronics, sensors, and actuators are manufactured mainly on rigid substrates by processes where expensive equipment that expend large amounts of energy is required, such as electroless plating, photolithography, and vacuum deposition.[145146] Printing methods are classified into contact and non-contact methods, as depicted in **Figure 1.9**. Screen, flexographic, or gravure

printings are some of the 2D printing contact techniques. They employ a screen or a roller in the printing setup that contacts with the substrate and the ink in the deposition moment.[147,148] Among these techniques, screen-printing technology offers the possibility of scaling up the fabrication process, with printing speeds that can reach 20 $m \cdot min^{-1}$ for flat-bed printers or even 150 $m \cdot min^{-1}$ for rotary printers.[149] Additionally, screen-printing results in a cost-effective approach in which samples with desired shapes can be accurately fabricated onto mechanically flexible substrates using a predefined pattern.[143,150] All these requisites and advantages make this technique ideal for printing the water-soluble linear chain polysaccharides studied in this thesis.

The inks required for screen-printing should present specific rheological properties, i.e., preferably exhibiting a shear-thinning behaviour.[151,152] Inks should be highly viscous to avoid undesired flow when no shear forces are applied. However, it should present lower viscosity upon applying external forces to allow it to pass through the mesh. After printing, the ink transfers its form into a several micrometres thick wet layer which should keep its shape again to avoid undesired spreading issues resulting in inaccurately printed patterns (**Figure 1.9a**). Nowadays, silver-based inks are among the most widely used in 2D printing processes as they can produce electrically-conducting traces with reliable mechanical properties.[153,154] On the contrary, fewer examples have dealt with the 2D printing of magnetic materials. Accordingly, the development of printing processes in which magnetically active inks are used, could open novel avenues for the development of magnetic responsive devices.

Other contact techniques employed in the industry are flexography and gravure printing. These consist of multiple feed roller systems which supply ink to a transfer roller and the print is made onto a flexible substrate. To rapidly differentiate them, in flexography **(Figure 1.9b)**, the transfer roller is the one that contains the setoff pattern. In gravure printing (**Figure 1.9c)**, the feeding roller is the patterned one, giving the ink only in the pattern regions to the transfer roller. These techniques are not employed as often for printing responsive materials as screen-printing is. The main disadvantage of contact methods is that mold and pattern have to be physically fabricated and have poor reusability.[155,156]

In this framework, using aqueous dispersions as inks for printing would enable the replacement of electronic components fabricated through expensive/non-sustainable methods by a simple and fast approach that relies on the use of solvents (principally water), polysaccharides, and ferrites. Additionally, printing substrates based on renewable resources may help to further alleviate the pressure on petroleum-based products by acquiring circular-

economy practices.[157] Thanks to its low cost, hydrophilicity,[158] mechanical flexibility,[159] chemical compatibility,[160], and disintegration under composting conditions,[161] cellulose can be used as an eco-friendly substrate to develop multifunctional materials and devices through 2D printing techniques.[162,163] Interestingly, the cellulose derivatives used in this thesis typically show remarkable shear-thinning properties.[164,165] Given the chemical similarities, it is expected that they should perfectly adhere to the paper substrate once magnetic cellulose-derivative inks are printed.[166]

Nevertheless, non-contact printing methods avoid these drawbacks of contact techniques because they use a head or a nozzle to deposit the ink directly onto the substrate or above the previous layer of the printed material in additive manufacturing, but still represent some drawbacks in reproducibility and versatility of the inks. The most prevalent techniques are inkjet printing, aerosol jet, fused deposition modelling (FDM), and 3D dispensing (**Figure 1.9 d-g**).[13167] However, for the scope of this thesis, only the techniques that involve printing in a solution state are considered.

Inkjet and aerosol jet printing are similar 2D-printing techniques. For example, in inkjet printing, drops of very low viscosity and volatile ink are ejected to print a digital pattern directly. Some problems can be derived from the magnetic components of the printing, and the generation of agglomerates can clog the nozzle. Thus, this technique wasn´t an alternative for printing the materials developed during the thesis.[25168] However, aerosol jet printing is more versatile than inkjet printing, as it allows the printing of diverse materials with different aspect ratios in a wide range of viscosities (1-1000 mPa s) at high lateral resolution patterns (∼10 μm). Then the formulation of the ink can be tuned.[169147] Regarding solvent-based printing techniques for the fabrication of 3D structures, dispensing or direct printing technique allows the continuous extrusion of high viscosity ink in the form of filament through a nozzle. They are widely used to print 3D structures of ceramics and functional metallic particles with a polymer as a binder in the absence of high temperatures.[170–172]

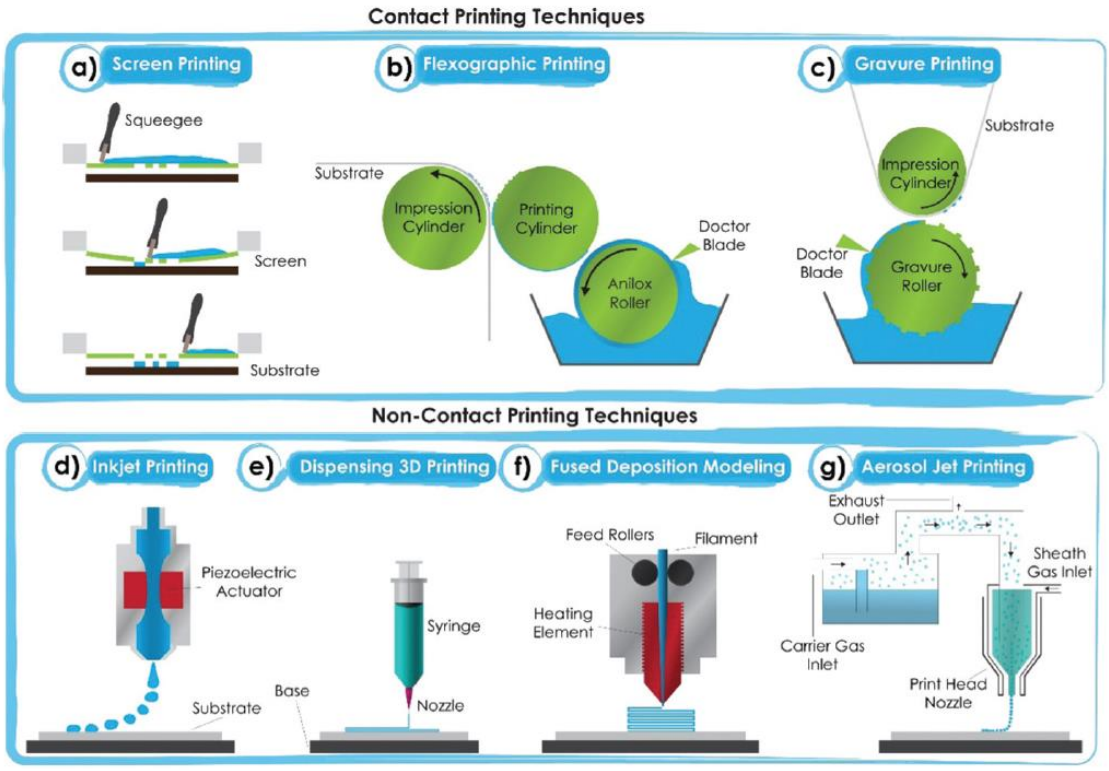

Figure 1.9. Schematic representations of the main contact (a–c) and non-contact (d–g) printing techniques that allow the printing of magnetic nanocomposites.[126]

Overall, the main parameters to consider are the ink's rheological properties, the nanoparticles' size, wettability of the ink with the substrate, temperature, the printing speed and the distance of the screen/roller/nozzle from the substrate. In addition, shear stress for contact systems has to be considered as well.

1.4. Objectives and methodology

In this scenario, the principal objective of the present thesis is the development of sustainable multifunctional materials suitable for printed electronics. Therefore, composites based on a polymeric matrix and a functional fillers and additives with tailored magnetic and electrical properties have been developed, considering their subsequent suitability for fabricating sensors and actuators by printing technologies. Besides, renewable sourced and biodegradable polymers have been employed to substitute the traditionally used non-degradable plastics.

This document is structured in nine chapters, where six chapters describe the preparation, characterization and evaluation of the materials developed. Chapter 1 (current chapter)

introduces an overview of the topic, providing a context that allows further comprehension of the subsequent works' motivation. Chapter 2 gathers the materials and characterization methods employed during the thesis with the aim of favours the reading of the following chapters.

The subsequent chapters describe laboratory works developed. Principally, cellulose-based materials have been employed as matrices (Chapters 3, 4, 5). First, three water-soluble cellulose derivatives: methyl cellulose (MC), hydroxypropyl cellulose (HPC), and sodium carboxymethyl cellulose (NaCMC), are employed as suitable matrices for multifunctional materials. Chapter 3 shows the preparation and characterization of free-standing magnetic films based on these matrices and cobalt ferrite ($CoFe_2O_4$) nanoparticles. The composites are processed by doctor blade using water as solvent. The influence on mechanical, dielectric and magnetic properties is evaluated upon the addition of different concentrations of filler. In addition, the suitability of these materials as inks for fabricating sensors and actuators by screen-printing technique is evaluated.

In this line, the cellulose derivatives are also employed in Chapter 4. Additionally, cellulose nanocrystals (CNC) are introduced as a matrix. Instead of using particles as filler, they are combined with the ionic liquid 2-hydroxy-ethyl-trimethylammonium dihydrogen phosphate ([Ch][DHP]) for developing free-standing films processed by solvent casting. There, mechanical properties and electrical and electro-mechanical performance of the materials with different ionic liquid content are evaluated to develop a bending actuator.

Due to the versatility of cellulose, multifunctional materials based on a CNC matrix presenting a porous structure are prepared in Chapter 5 for developing sensors/actuators that benefit from their porosity. Mesoporous CNCs' membranes with magnetic properties and electrical conductivity upon the incorporation of $CoFe_2O_4$ nanoparticles and graphite are fabricated through a soft-templating process. Porous structure, magnetic properties and electrical conductivity of the composites at different fillers' concentrations are assessed.

A final work using CNCs is developed in Chapter 6, where entirely natural resourced materials with tailored mechanical and electrical properties are prepared. Free-standing nanocomposites based on ι-carrageenan as matrix and CNCs as filler are fabricated by doctor blade casting. Thermal, mechanical, and electrical properties of the nanocomposites are evaluated.

After using natural-resourced matrices, in Chapter 7, different biodegradable synthetic

polyesters are employed as matrices for developing magnetic nanocomposites. The prepared nanocomposites are based on polylactic acid (PLA),[57] polycaprolactones (PCL),[58] polybutylene succinate (PBSu), and poly(butylene adipate-co-terephthalate) (PBAT) combined with Fe_3O_4 nanoparticles. The influence of the content of filler on the crystallinity, mechanical and magnetic properties, and biodegradation is evaluated and compared.

Finally, to control the direction in advanced sensing, biomedical, or actuator applications, Fe_3O_4@Au core-shell nanorods are synthesized in Chapter 8. Then they are incorporated into an agarose hydrogel to obtain anisotropic magnetic and optical properties. The composite hydrogels' optical, mechanical, and magnetic properties are evaluated. A proof of concept for the applicability of these materials for anisotropic magneto- and photo-thermia applications is shown.

The final chapter of this thesis is dedicated to the presentation of the conclusions of the developed works.

1.5. References

1 M. Ammar, A. Haleem, M. Javaid, S. Bahl and A. S. Verma, Implementing Industry 4.0 technologies in self-healing materials and digitally managing the quality of manufacturing, *Mater. Today Proc.*, 2022, **52**, 2285–2294.

2 K. Ashton, That 'Internet of Things' Thing, *RFID J.*

3 Y. Zhan, Y. Mei and L. Zheng, Materials capability and device performance in flexible electronics for the Internet of Things, *J. Mater. Chem. C*, 2014, **2**, 1220–1232.

4 A. M. Qazi, S. H. Mahmood, A. Haleem, S. Bahl, M. Javaid and K. Gopal, The impact of smart materials, digital twins (DTs) and Internet of things (IoT) in an industry 4.0 integrated automation industry, *Mater. Today Proc.*

5 O. Vermesan and P. Friess, River Publishers Series in Communication, 2014.

6 Harald Sundmaeker ... [et al.], *Vision and challenges for realising the Internet of Things vol. 2*, 2010.

7 P. Brodowicz, Dominika P Pospieszny and Z. Grzymata, *Eco-cities: Challenges, Trends and Solutions*, 2015, vol. 7.

8 A. Kumar, Methods and Materials for Smart Manufacturing: Additive Manufacturing, Internet of Things, Flexible Sensors and Soft Robotics, *Manuf. Lett.*, 2018, **15**, 122–125.

9 C. Annual and I. Report, *White paper Cisco public*, 2018.

10 K. Jain, M. Klosner, M. Zemel and S. Raghunandan, Flexible electronics and displays: High-resolution, roll-to-roll, projection lithography and photoablation processing technologies for high-throughput production, *Proc. IEEE*, 2005, **93**, 1500–1510.

11 A. Kamyshny and S. Magdassi, Flexible and Stretchable Medical Devices, *Flex. Stretchable Med. Devices*.

12 W. S. Wong and A. Salleo, Eds., Springer US, Boston, MA, 2009, vol. 11.

13 A. Kamyshny and S. Magdassi, Conductive nanomaterials for 2D and 3D printed flexible electronics, *Chem. Soc. Rev.*, 2019, **48**, 1712–1740.

14 A. Laskarakis and S. Logothetidis, Investigation of the optical anisotropy of PET and PEN films by

VIS-FUV to IR spectroscopic ellipsometry, *Appl. Surf. Sci.*, 2006, **253**, 52–56.

15 A. B. Shodeinde, A. C. Murphy, H. F. Oldenkamp, A. S. Potdar, C. M. Ludolph and N. A. Peppas, Recent Advances in Smart Biomaterials for the Detection and Treatment of Autoimmune Diseases, *Adv. Funct. Mater.*, 2020, **30**, 1909556.

16 C. Mendes-Felipe, J. Oliveira, I. Etxebarria, J. L. Vilas-Vilela and S. Lanceros-Mendez, State-of-the-Art and Future Challenges of UV Curable Polymer-Based Smart Materials for Printing Technologies, *Adv. Mater. Technol.*, 2019, **4**, 1800618.

17 S. Mohapatra, T. A. Nguyen and P. Nguyen-Tri, Noble metal-metal oxide hybrid nanoparticles: Fundamentals and applications, *Noble Met. Oxide Hybrid Nanoparticles Fundam. Appl.*, 2018, 1–674.

18 M. Benelmekki, Designing Hybrid Nanoparticles, *Des. Hybrid Nanoparticles*, 2015, 1–68.

19 S. F. Javier Requera, Kim Hyewon, Advances in Janus Nanoparticles, *Chim. Int. J. Chem.*, 2013, **67**, 811–818.

20 D. Gao, J. Lv, P. S. Lee, D. Gao, J. Lv and P. S. Lee, Natural Polymer in Soft Electronics: Opportunities, Challenges, and Future Prospects, *Adv. Mater.*, 2021, 2105020.

21 D. M. Correia, L. C. Fernandes, P. M. Martins, C. García-Astrain, C. M. Costa, J. Reguera and S. Lanceros-Méndez, Ionic Liquid–Polymer Composites: A New Platform for Multifunctional Applications, *Adv. Funct. Mater.*, 2020, **30**, 1909736.

22 R. D. Farahani, M. Dubé and D. Therriault, Three-Dimensional Printing of Multifunctional Nanocomposites: Manufacturing Techniques and Applications, *Adv. Mater.*, 2016, **28**, 5794–5821.

23 J. Kim and X. Jia, Previews From Space to Battlefield: A New Breed of Multifunctional Fiber Sheets for Extreme Environments, *Matter*, 2020, **3**, 602–604.

24 W. Yang, E. J. W. List-Kratochvil and C. Wang, Metal particle-free inks for printed flexible electronics, *J. Mater. Chem. C*, 2019, **7**, 15098–15117.

25 D. Li, W.-Y. Lai, Y.-Z. Zhang, W. Huang, D. D. Li, -Y W Lai, Y.-Z. Zhang and W. Huang, Printable Transparent Conductive Films for Flexible Electronics, *Adv. Mater.*, 2018, **30**, 1704738.

26 R. M. Pasquarelli, D. S. Ginley and R. O'hayre, Solution processing of transparent conductors: from flask to film, *This J. is Cite this Chem. Soc. Rev*, 2011, **40**, 5406–5441.

27 U. Männl, C. Van Den Berg, B. Magunje, M. Härting, D. T. Britton, S. Jones, M. J. Van Staden and M. R. Scriba, Nanoparticle composites for printed electronics, *Nanotechnology*, 2014, **25**, 6.

28 S. Fu, Z. Sun, P. Huang, Y. Li and N. Hu, Some basic aspects of polymer nanocomposites: A critical review, *Nano Mater. Sci.*, 2019, **1**, 2–30.

29 M. Yiu-Wing and Y. Zhong-Zhen, *Polymer Nanocomposites*, Woodhead Publishing, 2006.

30 V. Forti, C. P. Baldé, R. Kuehr and G. Bel, *The Global E-waste Monitor 2020: Quantities, flows, and the circular economy potential*, .

31 H. Ismail and M. M. Hanafiah, A review of sustainable e-waste generation and management: Present and future perspectives, *J. Environ. Manage.*, 2020, **264**, 110495.

32 R. Geyer, J. R. Jambeck and K. L. Law, Production, use, and fate of all plastics ever made, *Sci. Adv.*, 2017, **3**, e1700782.

33 J. R. Jambeck, R. Geyer, C. Wilcox, T. R. Siegler, M. Perryman, A. Andrady, R. Narayan and K. L. Law, Plastic waste inputs from land into the ocean, *Science*, 2015, **347**, 768–771.

34 L. Lan, J. Ping, J. Xiong and Y. Ying, *Sustainable Natural Bio-Origin Materials for Future Flexible Devices*, John Wiley & Sons, Ltd, 2022, vol. 9.

35 M. Hong and E. Y-X Chen, Future Directions for Sustainable Polymers, *Trends Chem.*, 2019, **1**, 148–151.

36 J. A. Shatkin and B. Kim, Cellulose nanomaterials: life cycle risk assessment, and environmental health and safety roadmap, *Environ. Sci. Nano*, 2015, **2**, 477–499.

37 K. K. Sadasivuni, D. Ponnamma, J. Kim, J. J. Cabibihan and M. A. AlMaadeed, *Biopolymer Composites in Electronics*, Elsevier, 2016.

38 M. Muthu, H. F. Wu, J. Gopal, I. Sivanesan and S. Chun, Exploiting Microbial Polysaccharides for Biosorption of Trace Elements in Aqueous Environments—Scope for Expansion via Nanomaterial Intervention, *Polym.*, 2017, **9**, 721.

39 Erlantz Lizundia, Francesca Luzi and Debora Puglia, Organic waste valorisation towards circular and sustainable biocomposites, *Green Chem.*, 2022, **24**, 5429–5459.

40 R. A. Sheldon and M. Norton, Green chemistry and the plastic pollution challenge: towards a circular economy, *Green Chem.*, 2020, **22**, 6310–6322.

41 X. Qiu and S. Hu, 'Smart' materials based on cellulose: A review of the preparations, properties, and applications, *Mater.*, 2013, **6**, 738–781.

42 D. Trache, M. H. Hussin, M. K. M. Haafiz and V. K. Thakur, Recent progress in cellulose nanocrystals: sources and production, *Nanoscale*, 2017, **9**, 1763–1786.

43 M. Jian, Y. Zhang and Z. Liu, Natural Biopolymers for Flexible Sensing and Energy Devices, *Chinese J. Polym. Sci*, **2020**, 459–490.

44 S. J. Eichhorn, A. Dufresne, M. Aranguren, N. E. Marcovich, J. R. Capadona, S. J. Rowan, C. Weder, W. Thielemans, M. Roman, S. Renneckar, W. Gindl, S. Veigel, J. Keckes, H. Yano, K. Abe, M. Nogi, A. N. Nakagaito, A. Mangalam, J. Simonsen, A. S. Benight, A. Bismarck, L. A. Berglund and T. Peijs, Review: current international research into cellulose nanofibres and nanocomposites, *J Mater Sci*, 2010, **45**, 1–33.

45 Y. Liang, Y. Li, H. Wang, J. Zhou, J. Wang, T. Regier and H. Dai, Co3O4 nanocrystals on graphene as a synergistic catalyst for oxygen reduction reaction, *Nat. Mater.*, 2011, **10**, 780–786.

46 J. George and S. N. Sabapathi, Nanotechnology, Science and Applications Dovepress Cellulose nanocrystals: synthesis, functional properties, and applications, *Nanotechnol. Sci. Appl.*, 2015, **8**, 45–54.

47 D. Klemm, F. Kramer, S. Moritz, T. Lindström, M. Ankerfors, D. Gray and A. Dorris, Nanocelluloses: A New Family of Nature-Based Materials, *Angew. Chemie Int. Ed.*, 2011, **50**, 5438–5466.

48 Y. Habibi, L. A. Lucia and O. J. Rojas, Cellulose nanocrystals: Chemistry, self-assembly, and applications, *Chem. Rev.*, 2010, **110**, 3479–3500.

49 M. Mariano, N. El Kissi and A. Dufresne, Cellulose nanocrystals and related nanocomposites: Review of some properties and challenges, *J. Polym. Sci. Part B Polym. Phys.*, 2014, **52**, 791–806.

50 J. George and S. N. Sabapathi, Cellulose nanocrystals: synthesis, functional properties, and applications, *Nanotechnol. Sci. Appl.*, 2015, **8**, 45–54.

51 R. R. Lahiji, X. Xu, R. Reifenberger, A. Raman, A. Rudie and R. J. Moon, Atomic force microscopy characterization of cellulose nanocrystals, *Langmuir*, 2010, **26**, 4480–4488.

52 R. J. Moon, A. Martini, J. Nairn, J. Simonsen and J. Youngblood, Cellulose nanomaterials review: structure, properties and nanocomposites, *Chem. Soc. Rev.*, 2011, **40**, 3941–3994.

53 A. B. Reising, R. J. Moon and J. P. Youngblood, Effect of particle alignment on mechanical properties of neat cellulose nanocrystal films, *J-for*, 2012, **2**, 32–41.

54 D. Klemm, E. D. Cranston, D. Fischer, M. Gama, S. A. Kedzior, D. Kralisch, F. Kramer, T. Kondo, T. Lindström, S. Nietzsche, K. Petzold-Welcke and F. Rauchfuß, Nanocellulose as a natural source for groundbreaking applications in materials science: Today's state, *Mater. Today*, 2018, **21**, 720–748.

55 F. A. dos Santos, G. C. V. Iulianelli, M. I. B. Tavares, F. A. dos Santos, G. C. V. Iulianelli and M. I. B. Tavares, The Use of Cellulose Nanofillers in Obtaining Polymer Nanocomposites: Properties, Processing, and Applications, *Mater. Sci. Appl.*, 2016, **7**, 257–294.

56 W. Helbert, J. Y. Cavaillé and A. Dufresne, Thermoplastic nanocomposites filled with wheat straw cellulose whiskers. Part I: Processing and mechanical behavior, *Polym. Compos.*, 1996, **17**, 604–611.

57 E. Lizundia, E. Fortunati, F. Dominici, J. L. Vilas, L. M. León, I. Armentano, L. Torre and J. M. Kenny, PLLA-grafted cellulose nanocrystals: Role of the CNC content and grafting on the PLA bionanocomposite film properties, *Carbohydr. Polym.*, 2016, **142**, 105–113.

58 H. Y. Mi, X. Jing, J. Peng, M. R. Salick, X. F. Peng and L. S. Turng, Poly(ε-caprolactone) (PCL)/cellulose nanocrystal (CNC) nanocomposites and foams, *Cellulose*, 2014, **21**, 2727–2741.

59 T. Kim, H. Jeon, J. Jegal, J. H. Kim, H. Yang, J. Park, D. X. Oh and S. Y. Hwang, Trans crystallization behavior and strong reinforcement effect of cellulose nanocrystals on reinforced poly(butylene succinate) nanocomposites, *RSC Adv.*, 2018, **8**, 15389–15398.

60 C. Echeverria, P. L. Almeida, G. Feio, J. L. Figueirinhas and M. H. Godinho, A cellulosic liquid crystal pool for cellulose nanocrystals: Structure and molecular dynamics at high shear rates, *Eur. Polym. J.*, 2015, **72**, 72–81.

61 M. El Achaby, N. El Miri, A. Aboulkas, M. Zahouily, E. Bilal, A. Barakat and A. Solhy, Processing and properties of eco-friendly bio-nanocomposite films filled with cellulose nanocrystals from sugarcane bagasse, *Int. J. Biol. Macromol.*, 2017, **96**, 340–352.

62 H. Zhang, J. Jung and Y. Zhao, Preparation and characterization of cellulose nanocrystals films incorporated with essential oil loaded β-chitosan beads, *Food Hydrocoll.*, 2017, **69**, 164–172.

63 A. M. Slavutsky and M. A. Bertuzzi, Water barrier properties of starch films reinforced with cellulose nanocrystals obtained from sugarcane bagasse, *Carbohydr. Polym.*, 2014, **110**, 53–61.

64 E. Fortunati, D. Puglia, F. Luzi, C. Santulli, J. M. Kenny and L. Torre, Binary PVA bio-nanocomposites containing cellulose nanocrystals extracted from different natural sources: Part I, *Carbohydr. Polym.*, 2013, **97**, 825–836.

65 S. C. Espinosa, T. Kuhnt, E. J. Foster and C. Weder, Isolation of Thermally Stable Cellulose Nanocrystals by Phosphoric Acid Hydrolysis, *Biomacromolecules*, 2013, **14**, 1223–1230.

66 P. M. Visakh, S. Thomas, K. Oksman and A. P. Mathew, Crosslinked natural rubber nanocomposites reinforced with cellulose whiskers isolated from bamboo waste: Processing and mechanical/thermal properties, *Compos. Part A Appl. Sci. Manuf.*, 2012, **43**, 735–741.

67 M. Neus Angles and A. Dufresne, Plasticized starch/tuniein whiskers nanocomposites. 1. Structural analysis, *Macromolecules*, 2000, **33**, 8344–8353.

68 A. P. Mathew and A. Dufresne, Morphological investigation of nanocomposites from sorbitol plasticized starch and tunicin whiskers, *Biomacromolecules*, 2002, **3**, 609–617.

69 M. A. S. Azizi Samir, F. Alloin, J. Y. Sanchez and A. Dufresne, Cellulose nanocrystals reinforced poly(oxyethylene), *Polymer*, 2004, **45**, 4149–4157.

70 C. Clasen and W. M. Kulicke, Determination of viscoelastic and rheo-optical material functions of water-soluble cellulose derivatives, *Prog. Polym. Sci.*, 2001, **26**, 1839–1919.

71 P. L. Nasatto, F. Pignon, J. L. M. Silveira, M. E. R. Duarte, M. D. Noseda and M. Rinaudo, Methylcellulose, a Cellulose Derivative with Original Physical Properties and Extended Applications, *Polym.*, 2015, **7**, 777–803.

72 T. L. Rogers and D. Wallick, Reviewing the use of ethylcellulose, methylcellulose and hypromellose in microencapsulation. Part 1: materials used to formulate microcapsules, *Drug Dev. Ind. Pharm.*, 2012, **38**, 129–157.

73 C. Nowald, A. Penk, H.-Y. Chiu, T. Bein, D. Huster and O. Lieleg, A Selective Mucin/Methylcellulose Hybrid Gel with Tailored Mechanical Properties, *Macromol. Biosci.*, 2016, **16**, 567–579.

74 C. G. Otoni, A. S. Carvalho, M. V. C. Cardoso, O. D. Bernardinelli, M. V Lorevice, L. A. Colnago, W. Loh and L. H. C. Mattoso, High-Pressure Microfluidization as a Green Tool for Optimizing the Mechanical Performance of All-Cellulose Composites, *ACS Sustain. Chem. Eng.*, 2018, **6**, 12727–12735.

75 T. Chatterjee, K. P. O'Donnell, M. A. Rickard, B. Nickless, Y. Li, V. V Ginzburg and R. L. Sammler, Rheology of Cellulose Ether Excipients Designed for Hot Melt Extrusion, *Biomacromolecules*, 2018, **19**, 4430–4441.

76 J. Gao, G. Haidar, X. Lu and Z. Hu, Self-Association of Hydroxypropylcellulose in Water, *Macromolecules*, 2001, **34**, 2242–2247.

77 A. T. Qureshi, W. T. Monroe, M. J. Lopez, M. E. Janes, V. Dasa, S. Park, A. Amirsadeghi and D. J. Hayes, Biocompatible/bioabsorbable silver nanocomposite coatings, *J. Appl. Polym. Sci.*, 2011, **120**, 3042–3053.

78 S. Saber-Samandari, S. Saber-Samandari, S. Heydaripour and M. Abdouss, Novel carboxymethyl

cellulose based nanocomposite membrane: Synthesis, characterization and application in water treatment, *J. Environ. Manage.*, 2016, **166**, 457–465.

79 A. Abdulkhani, M. Daliri Sousefi, A. Ashori and G. Ebrahimi, Preparation and characterization of sodium carboxymethyl cellulose/silk fibroin/graphene oxide nanocomposite films, *Polym. Test.*, 2016, **52**, 218–224.

80 W. Wang and A. Wang, Nanocomposite of carboxymethyl cellulose and attapulgite as a novel pH-sensitive superabsorbent: Synthesis, characterization and properties, *Carbohydr. Polym.*, 2010, **82**, 83–91.

81 E. Lizundia, A. Urruchi, J. L. Vilas and L. M. León, Increased functional properties and thermal stability of flexible cellulose nanocrystal/ZnO films, *Carbohydr. Polym.*, 2016, **136**, 250–258.

82 J. F. Luna-Martínez, D. B. Hernández-Uresti, M. E. Reyes-Melo, C. A. Guerrero-Salazar, V. A. González-González and S. Sepúlveda-Guzmán, Synthesis and optical characterization of ZnS–sodium carboxymethyl cellulose nanocomposite films, *Carbohydr. Polym.*, 2011, **84**, 566–570.

83 K. Suppiah, P. L. Teh, S. Husseinsyah and R. Rahman, Properties and characterization of carboxymethyl cellulose/halloysite nanotube bio-nanocomposite films: Effect of sodium dodecyl sulfate, *Polym. Bull.*, 2019, **76**, 365–386.

84 S. Rimdusit, S. Jingjid, S. Damrongsakkul, S. Tiptipakorn and T. Takeichi, Biodegradability and property characterizations of Methyl Cellulose: Effect of nanocompositing and chemical crosslinking, *Carbohydr. Polym.*, 2008, **72**, 444–455.

85 E. Lizundia, T.-D. Nguyen, J. L. Vilas, W. Y. Hamad and M. J. MacLachlan, Chiroptical luminescent nanostructured cellulose films, *Mater. Chem. Front.*, 2017, **1**, 979–987.

86 V. Gautam, K. P. Singh and V. L. Yadav, Preparation and characterization of green-nano-composite material based on polyaniline, multiwalled carbon nano tubes and carboxymethyl cellulose: For electrochemical sensor applications, *Carbohydr. Polym.*, 2018, **189**, 218–228.

87 M. Flieger, M. Kantorová, A. Prell, T. Řezanka and J. Votruba, Biodegradable plastics from renewable sources, *Folia Microbiol.*, 2003, **48**, 27–44.

88 A. Larrañaga and E. Lizundia, A review on the thermomechanical properties and biodegradation behaviour of polyesters, *Eur. Polym. J.*, 2019, **121**, 109296.

89 S. Agarwal, Biodegradable Polymers: Present Opportunities and Challenges in Providing a Microplastic-Free Environment, *Macromol. Chem. Phys.*, 2020, **221**, 2000017.

90 T. Rigotti De Castro, · Dayana, C. De Macedo, · Daiane, M. De, G. Chiroli, · Robson Couto Da Silva and S. M. Tebcherani, The Potential of Cleaner Fermentation Processes for Bioplastic Production: A Narrative Review of Polyhydroxyalkanoates (PHA) and Polylactic Acid (PLA), *J. Polym. Environ.*, 1234, **30**, 810–832.

91 J. Chen, C. Deng, R. Hong, Q. Fu and J. Zhang, Effect of thermal annealing on crystal structure and properties of PLLA/PCL blend, *J. Polym. Res.*, 2020, **27**, 1–11.

92 L. Jiang and J. Zhang, Biodegradable and Biobased Polymers, *Appl. Plast. Eng. Handb. Process. Mater. Appl. Second Ed.*, 2017, 127–143.

93 M. J. Mochane, S. I. Magagula, J. S. Sefadi and T. C. Mokhena, A Review on Green Composites Based on Natural Fiber-Reinforced Polybutylene Succinate (PBS), *Polym.*, 2021, **13**, 1200.

94 M. Jawaid, M. Sapuan, S. Othman and Y. Alothman, *Green Energy and Technology Green Biocomposites Design and Applications*, 2017.

95 M. Flieger, M. Kantorová, A. Prell, T. Řezanka and J. Votruba, Biodegradable Plastics from Renewable Sources, *Rev. Folia Microbiol*, 2003, **48**, 27–44.

96 U. Witt, R. J. Müller and W. D. Deckwer, Biodegradation behavior and material properties of aliphatic/aromatic polyesters of commercial importance, *J. Environ. Polym. Degrad.*, 1997, **5**, 81–89.

97 F. V. Ferreira, L. S. Cividanes, R. F. Gouveia and L. M. F. Lona, An overview on properties and applications of poly(butylene adipate-co-terephthalate)–PBAT based composites, *Polym. Eng. Sci.*, 2019, **59**, E7–E15.

98 C. Wang, T. Yokota and T. Someya, Natural biopolymer-based biocompatible conductors for

stretchable bioelectronics, *Chem. Rev.*, 2021, **121**, 2109–2146.

99 S. Choi, S. I. Han, D. Kim, T. Hyeon and D. H. Kim, High-performance stretchable conductive nanocomposites: materials, processes, and device applications, *Chem. Soc. Rev.*, 2019, **48**, 1566–1595.

100 A. Kozbial, F. Zhou, Z. Li, H. Liu and L. Li, Are Graphitic Surfaces Hydrophobic?, *Acc. Chem. Res.*, 2016, **49**, 2765–2773.

101 E. H. L. Falcao and F. Wudl, Carbon allotropes: beyond graphite and diamond, *J. Chem. Technol. Biotechnol.*, 2007, **82**, 524–531.

102 D. D. L. Chung, Review: Graphite, *J. Mater. Sci.*, 2002, **37**, 1475–1489.

103 B. Yao, L. Yuan, X. Xiao, J. Zhang, Y. Qi, J. Zhou, J. Zhou, B. Hu and W. Chen, Paper-based solid-state supercapacitors with pencil-drawing graphite/polyaniline networks hybrid electrodes, *Nano Energy*, 2013, **2**, 1071–1078.

104 H. Zhao, T. Zhang, R. Qi, J. Dai, S. Liu and T. Fei, Drawn on Paper: A Reproducible Humidity Sensitive Device by Handwriting, *ACS Appl. Mater. Interfaces*, 2017, **9**, 28002–28009.

105 G. Zheng, L. Hu, H. Wu, X. Xie and Y. Cui, Paper supercapacitors by a solvent-free drawing method, *Energy Environ. Sci.*, 2011, **4**, 3368–3373.

106 D. M. Correia, L. C. Fernandes, M. M. Fernandes, B. Hermenegildo, R. M. Meira, C. Ribeiro, S. Ribeiro, J. Reguera and S. Lanceros-Méndez, Ionic Liquid-Based Materials for Biomedical Applications, *Nanomater.*, 2021, **11**, 2401.

107 P. Kuberský, T. Syrový, A. Hamáček, S. Nešpůrek and L. Syrová, Towards a fully printed electrochemical NO2 sensor on a flexible substrate using ionic liquid based polymer electrolyte, *Sensors Actuators B Chem.*, 2015, **209**, 1084–1090.

108 K. Dong, X. Liu, H. Dong, X. Zhang and S. Zhang, Multiscale Studies on Ionic Liquids, *Chem. Rev.*, 2017, **117**, 6636–6695.

109 D. Wang, Y. Wang, H. Wan, J. Wang and L. Wang, Synthesis of gemini basic ionic liquids and their application in anion exchange membranes, *RSC Adv.*, 2018, **8**, 10185–10196.

110 A. Reizabal, D. M. Correia, C. M. Costa, L. Perez-Alvarez, J. L. Vilas-Vilela and S. Lanceros-Méndez, Silk Fibroin Bending Actuators as an Approach Toward Natural Polymer Based Active Materials, *ACS Appl. Mater. Interfaces*, 2019, **11**, 30197–30206.

111 X. Liu, B. He, Z. Wang, H. Tang, T. Su and Q. Wang, Tough Nanocomposite Ionogel-based Actuator Exhibits Robust Performance, *Sci. Reports 2014 41*, 2014, **4**, 1–7.

112 E. L. Afonso, L. Carvalho, S. Fateixa, C. O. Amorim, V. S. Amaral, C. Vale, E. Pereira, C. M. Silva, T. Trindade and C. B. Lopes, Can contaminated waters or wastewater be alternative sources for technology-critical elements? The case of removal and recovery of lanthanides, *J. Hazard. Mater.*, 2019, **380**, 120845.

113 A. D. B. L. Ferreira, P. R. O. Nóvoa and A. T. Marques, Multifunctional Material Systems: A state-of-the-art review, *Compos. Struct.*, 2016, **151**, 3–35.

114 J. D. Carlson and M. R. Jolly, MR fluid, foam and elastomer devices, *Mechatronics*, 2000, **10**, 555–569.

115 A. G. Díez, C. R. Tubio, J. G. Etxebarria and S. Lanceros-Mendez, Magnetorheological Elastomer-Based Materials and Devices: State of the Art and Future Perspectives, *Adv. Eng. Mater.*, 2021, **23**, 2100240.

116 N. A. Frey, S. Peng, K. Cheng and S. Sun, Magnetic nanoparticles: synthesis, functionalization, and applications in bioimaging and magnetic energy storage, *Chem. Soc. Rev.*, 2009, **38**, 2532–2542.

117 J. Kudr, Y. Haddad, L. Richtera, Z. Heger, M. Cernak, V. Adam and O. Zitka, *Nanomater.* , 2017, 7.

118 E. Pellicer, E. Rossinyol, M. Cabo, A. Lopez-Ortega, M. Estrader, S. Surinach, M. Dolors, J. Nogues and J. Sort, *Oxide-Matrix Based Nanocomposite Materials for Advanced Magnetic and Optical Functionalities*, IntechOpen, 2011.

119 H. W. F. Sung and C. Rudowicz, Physics behind the magnetic hysteresis loop—a survey of misconceptions in magnetism literature, *J. Magn. Magn. Mater.*, 2003, **260**, 250–260.

120 F. Fiorillo, C. Appino and M. Pasquale, in *The Science of Hysteresis*, eds. G. Bertotti and J. Mayergoyz,

2006, vol. 3, pp. 1–190.

121 M. Reis, *Fundamentals of Magnetism*, Elsevier Inc., 2013.

122 M. Henini, *Principles of Electronic Materials and Devices*, 2nd edn., 2002, vol. 33.

123 A. G. Kolhatkar, A. C. Jamison, D. Litvinov, R. C. Willson and T. R. Lee, Tuning the Magnetic Properties of Nanoparticles, *Int. J. Mol. Sci.*, 2013, **14**, 15977–16009.

124 U. Jeong, X. Teng, Y. Wang, H. Yang and Y. Xia, Superparamagnetic Colloids: Controlled Synthesis and Niche Applications, *Adv. Mater.*, 2007, **19**, 33–60.

125 H. Tahanian, M. Aliahmadi and J. Faiz, Ferrite Permanent Magnets in Electrical Machines: Opportunities and Challenges of a Non-Rare-Earth Alternative, *IEEE Trans. Magn.*, 2020, **56**, 3.

126 K. J. Merazzo, A. C. Lima, M. Rincón-Iglesias, L. C. Fernandes, N. Pereira, S. Lanceros-Mendez and P. Martins, Magnetic materials: A journey from finding north to an exciting printed future, *Mater. Horizons*, 2021, **8**, 2654–2684.

127 A. B. Botelho Junior, S. Stopic, B. Friedrich, J. A. S. Tenório and D. C. R. Espinosa, Cobalt Recovery from Li-Ion Battery Recycling: A Critical Review, *Met.*, 2021, **11**, 1999.

128 P. Martins, C. M. Costa, G. Botelho, S. Lanceros-Mendez, J. M. Barandiaran and J. Gutierrez, Dielectric and magnetic properties of ferrite/poly(vinylidene fluoride) nanocomposites, *Mater. Chem. Phys.*, 2012, **131**, 698–705.

129 E. Lizundia, A. Maceiras, J. L. Vilas, P. Martins and S. Lanceros-Mendez, Magnetic cellulose nanocrystal nanocomposites for the development of green functional materials, *Carbohydr. Polym.*, 2017, **175**, 425–432.

130 P. Martins, C. M. Costa, J. C. C. Ferreira and S. Lanceros-Mendez, Correlation between Crystallization Kinetics and Electroactive Polymer Phase Nucleation in Ferrite/Poly(vinylidene fluoride) Magnetoelectric Nanocomposites, *J. Phys. Chem. B*, 2012, **116**, 794–801.

131 P. Martins, C. M. Costa, M. Benelmekki, G. Botelho and S. Lanceros-Mendez, On the origin of the electroactive poly(vinylidene fluoride) β-phase nucleation by ferrite nanoparticles via surface electrostatic interactions, *Cryst. Eng. Comm.* , 2012, **14**, 2807–2811.

132 Y. Zong, T. Zheng, P. Martins, S. Lanceros-Mendez, Z. Yue and M. J. Higgins, Cellulose-based magnetoelectric composites, *Nat. Commun.*, 2017, **8**, 38.

133 P. Martins, A. C. Lopes and S. Lanceros-Mendez, Electroactive phases of poly(vinylidene fluoride): Determination, processing and applications, *Prog. Polym. Sci.*, 2014, **39**, 683–706.

134 S. Wu, W. Hu, Q. Ze, M. Sitti and R. Zhao, Multifunctional magnetic soft composites: a review, *Multifunct. Mater.*, 2020, **3**, 42003.

135 S. Rittikulsittichai, A. G. Kolhatkar, S. Sarangi, M. A. Vorontsova, P. G. Vekilov, A. Brazdeikis and T. Randall Lee, Multi-responsive hybrid particles: thermo-, pH-, photo-, and magneto-responsive magnetic hydrogel cores with gold nanorod optical triggers, *Nanoscale*, 2016, **8**, 11851–11861.

136 Y. W. Jun, J. S. Choi and J. Cheon, Heterostructured magnetic nanoparticles: Their versatility and high performance capabilities, *Chem. Commun.*, 2007, 1203–1214.

137 M. Bedenbecker, R. Bandorf, H. Luethje, G. Braeuer and H. H. Gatzen, Development and fabrication of magnetic thin films, *Microsyst. Technol.*, 2006, **12**, 655–658.

138 W. Lin, W. Sun, J. Yang, Q. Sun and Z. Shen, Fabrication of Magnetic Thin Films by a Layer-by-Layer Self-Assembly Approach, *J. Phys. Chem. C*, 2009, **113**, 16884–16895.

139 R. P. Ummer, R. B, C. Thevenot, D. Rouxel, S. Thomas and N. Kalarikkal, Electric, magnetic, piezoelectric and magnetoelectric studies of phase pure (BiFeO3–NaNbO3)–(P(VDF-TrFE)) nanocomposite films prepared by spin coating, *RSC Adv.*, 2016, **6**, 28069–28080.

140 S. Biswas, G. P. Kar and S. Bose, Engineering nanostructured polymer blends with controlled nanoparticle location for excellent microwave absorption: a compartmentalized approach, *Nanoscale*, 2015, **7**, 11334–11351.

141 J. Bae, M. K. Song, Y. J. Park, J. M. Kim, M. Liu and Z. L. Wang, Fiber Supercapacitors Made of Nanowire-Fiber Hybrid Structures for Wearable/Flexible Energy Storage, *Angew. Chemie Int. Ed.*,

2011, **50**, 1683–1687.

142 W. Zeng, L. Shu, Q. Li, S. Chen, F. Wang and X.-M. Tao, Fiber-Based Wearable Electronics: A Review of Materials, Fabrication, Devices, and Applications, *Adv. Mater.*, 2014, **26**, 5310–5336.

143 J. Oliveira, V. Correia, H. Castro, P. Martins and S. Lanceros-Mendez, Polymer-based smart materials by printing technologies: Improving application and integration, *Addit. Manuf.*, 2018, **21**, 269–283.

144 H. P. Voisin, K. Gordeyeva, G. Siqueira, M. K. Hausmann, A. R. Studart and L. Bergström, 3D Printing of Strong Lightweight Cellular Structures Using Polysaccharide-Based Composite Foams, *ACS Sustain. Chem. Eng.*, 2018, **6**, 17160–17167.

145 O. Sarapulova, V. Sherstiuk, V. Shvalagin and A. Kukhta, Photonics and Nanophotonics and Information and Communication Technologies in Modern Food Packaging, *Nanoscale Res. Lett.*, 2015, **10**, 1–8.

146 H. Sirringhaus, T. Kawase, R. H. Friend, T. Shimoda, M. Inbasekaran, W. Wu and E. P. Woo, High-resolution inkjet printing of all-polymer transistor circuits, *Science*, 2000, **290**, 2123–2126.

147 J. Dai, O. Ogbeide, N. Macadam, Q. Sun, W. Yu, Y. Li, B. L. Su, T. Hasan, X. Huang and W. Huang, Printed gas sensors, *Chem. Soc. Rev.*, 2020, **49**, 1756–1789.

148 L. Dai, T. Cheng, C. Duan, W. Zhao, W. Zhang, X. Zou, J. Aspler and Y. Ni, 3D printing using plant-derived cellulose and its derivatives: A review, *Carbohydr. Polym.*, 2019, **203**, 71–86.

149 R. Faddoul, N. Reverdy-Bruas and A. Blayo, Formulation and screen printing of water based conductive flake silver pastes onto green ceramic tapes for electronic applications, *Mater. Sci. Eng. B*, 2012, **177**, 1053–1066.

150 D. Li, W.-Y. Lai, Y.-Z. Zhang and W. Huang, Printable Transparent Conductive Films for Flexible Electronics, *Adv. Mater.*, 2018, **30**, 1704738.

151 M. Schneider, E. Koos and N. Willenbacher, Highly conductive, printable pastes from capillary suspensions, *Sci. Rep.*, 2016, **6**, 31367.

152 G. Siqueira, D. Kokkinis, R. Libanori, M. K. Hausmann, A. S. Gladman, A. Neels, P. Tingaut, T. Zimmermann, J. A. Lewis and A. R. Studart, Cellulose Nanocrystal Inks for 3D Printing of Textured Cellular Architectures, *Adv. Funct. Mater.*, 2017, **27**, 1604619.

153 A. J. Kell, C. Paquet, O. Mozenson, I. Djavani-Tabrizi, B. Deore, X. Liu, G. P. Lopinski, R. James, K. Hettak, J. Shaker, A. Momciu, J. Ferrigno, O. Ferrand, J. X. Hu, S. Lafrenière and P. R. L. Malenfant, Versatile Molecular Silver Ink Platform for Printed Flexible Electronics, *ACS Appl. Mater. Interfaces*, 2017, **9**, 17226–17237.

154 F. Hoeng, A. Denneulin, N. Reverdy-Bruas, G. Krosnicki and J. Bras, Rheology of cellulose nanofibrils/silver nanowires suspension for the production of transparent and conductive electrodes by screen printing, *Appl. Surf. Sci.*, 2017, **394**, 160–168.

155 F. C. Krebs, Fabrication and processing of polymer solar cells: A review of printing and coating techniques, *Sol. Energy Mater. Sol. Cells*, 2009, **93**, 394–412.

156 K. Suganuma, *Introduction to printed electronics (SpringerBriefs in electrical and computer engineering)*, 2014.

157 J. M. M. Dolores Hidalgo Barrio and F. C. E. Marroquín, Management of biodegradable waste in the circular economy framework, *DYNA*, 2018, **93**, 132.

158 M. A. Lucchini, E. Lizundia, S. Moser, M. Niederberger and G. Nyström, Titania-Cellulose Hybrid Monolith for In-Flow Purification of Water under Solar Illumination, *ACS Appl. Mater. Interfaces*, 2018, **10**, 29599–29607.

159 T. Liu, W. Wu, K.-N. Liao, Q. Sun, X. Gong, V. A. L. Roy, Z.-Z. Yu and R. K. Y. Li, Fabrication of carboxymethyl cellulose and graphene oxide bio-nanocomposites for flexible nonvolatile resistive switching memory devices, *Carbohydr. Polym.*, 2019, **214**, 213–220.

160 E. Lizundia, T. D. Nguyen, J. L. Vilas, W. Y. Hamad and M. J. MacLachlan, Chiroptical, morphological and conducting properties of chiral nematic mesoporous cellulose/polypyrrole composite films, *J. Mater. Chem. A*, 2017, **5**, 19184–19194.

161 E. Lizundia, U. Goikuria, J. L. Vilas, F. Cristofaro, G. Bruni, E. Fortunati, I. Armentano, L. Visai and L.

Torre, Metal Nanoparticles Embedded in Cellulose Nanocrystal Based Films: Material Properties and Post-use Analysis, *Biomacromolecules*, 2018, **19**, 2618–2628.

162 D. Ha, Z. Fang and N. B. Zhitenev, Paper in Electronic and Optoelectronic Devices, *Adv. Electron. Mater.*, 2018, **4**, 1700593.

163 Y. Zhang, L. Zhang, K. Cui, S. Ge, X. Cheng, M. Yan, J. Yu and H. Liu, Flexible Electronics Based on Micro/Nanostructured Paper, *Adv. Mater.*, 2018, **30**, 1801588.

164 L. Huang, X. Du, S. Fan, G. Yang, H. Shao, D. Li, C. Cao, Y. Zhu, M. Zhu and Y. Zhang, Bacterial cellulose nanofibers promote stress and fidelity of 3D-printed silk based hydrogel scaffold with hierarchical pores, *Carbohydr. Polym.*, 2019, **221**, 146–156.

165 A. I. Cernencu, A. Lungu, I.-C. Stancu, A. Serafim, E. Heggset, K. Syverud and H. Iovu, Bioinspired 3D printable pectin-nanocellulose ink formulations, *Carbohydr. Polym.*, 2019, **220**, 12–21.

166 K. Xie, A. Gao, M. Li and X. Wang, Printing properties of the red reactive dyes with different number sulfonate groups on cotton fabric, *Carbohydr. Polym.*, 2014, **101**, 666–670.

167 S. C. Ligon, R. Liska, J. Stampfl, M. Gurr and R. Mülhaupt, Polymers for 3D Printing and Customized Additive Manufacturing, *Chem. Rev.*, 2017, **117**, 10212–10290.

168 M. Vural, A. Pena-Francesch, J. Bars-Pomes, H. Jung, H. Gudapati, C. B. Hatter, B. D. Allen, B. Anasori, I. T. Ozbolat, Y. Gogotsi and M. C. Demirel, Inkjet Printing of Self-Assembled 2D Titanium Carbide and Protein Electrodes for Stimuli-Responsive Electromagnetic Shielding, *Adv. Funct. Mater.*, 2018, **28**, 1–10.

169 E. W. C. Phuah, W. L. Hart, H. Sumer and P. R. Stoddart, Patterning of biomaterials by aerosol jet printing: A parametric study, *Bioprinting*, 2020, **18**, e00081.

170 Y. Zhang, D. Zhai, M. Xu, Q. Yao, J. Chang and C. Wu, 3D-printed bioceramic scaffolds with a Fe3O4/graphene oxide nanocomposite interface for hyperthermia therapy of bone tumor cells, *J. Mater. Chem. B*, 2016, **4**, 2874–2886.

171 A. Quintanilla, J. Carbajo, J. A. Casas, P. Miranzo, M. I. Osendi and M. Belmonte, *Catal. Today*, 2019.

172 C. R. Tubío, J. A. Nóvoa, J. Martín, F. Guitián, J. R. Salgueiro and A. Gil, Broadband terahertz ZnO photonic crystals fabricated by 3D printing, *Ceram. Int.*, 2019, **45**, 6223–6227.

2. Experimental Part

The purpose of this chapter is to provide a comprehensible overview of the materials, and characterisation techniques that have been used in this thesis. However, to favour the comprehension of each work, the synthesis of nanoparticles and fabrication of composites are described in the corresponding chapters.

2.1. Materials

2.1.1. Natural sourced polymers

Cellulose derivatives: HPC powder with a M_w of 100.000 g mol^{-1} (191884-100G), MC powder with a viscosity of 400 cP (M0262-100G), and NaCMC with a M_w of 250.000 g mol^{-1} and a degree of substitution of 1.2 (419281- 100G) were supplied by Sigma Aldrich. These materials, which chemical structures are depicted in **Figure 2.1**, were employed as matrices for the composites prepared in Chapters 3 and 4.

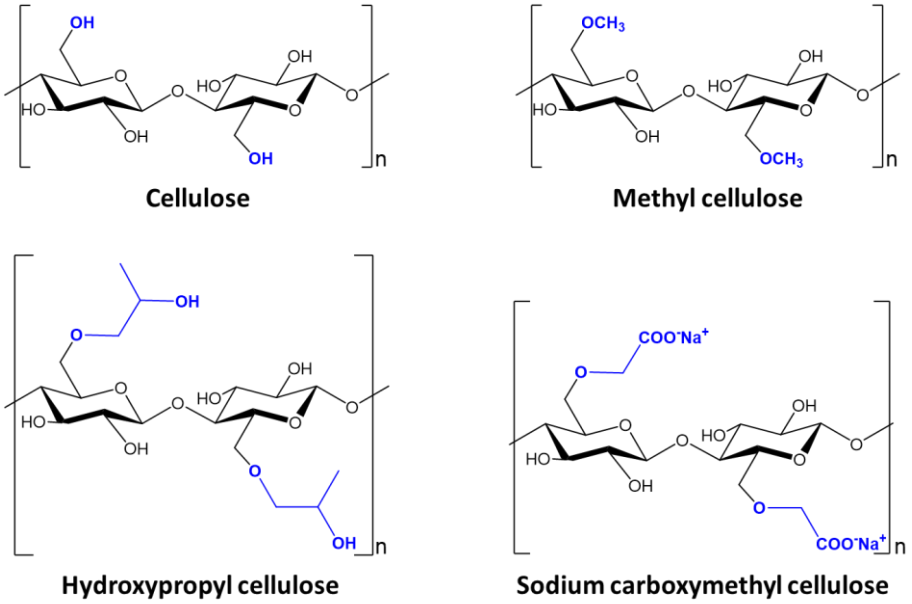

Figure 2.1. Molecular structure of the cellulose derivatives in regard to original cellulose: methyl cellulose, hydroxypropyl cellulose, and sodium carboxymethyl cellulose.

CNC synthesis: microcrystalline cellulose with an average particle size of 20 µm (310697-500G), sulphuric acid (95–97%, 30743-1L, Sigma-Aldrich, St. Louis, MO, USA). Due to their versatility, the synthesised CNCs have been employed in Chapters 4 and 5 as matrices and in Chapter 6 as filler.

CNC membranes: synthesised CNCs and tetramethyl orthosilicate (TMOS, 1.023 $g \cdot mL^{-1}$, 341436-25 G), glucose (d-(+)-Glucose, G5767-500 G) were used for the preparation of mesoporous membranes in Chapter 5.

Carrageenan: ι-carrageenan (C1138-100G) has been supplied by Sigma-Aldrich. It was the matrix used for the nanocomposites prepared in Chapter 6 (**Figure 2.2**).

Agarose: Agarose, D1 low electroendosmosis (EEO) was purchased from Condolab and employed as hydrogel in Chapter 8 (**Figure 2.2**).

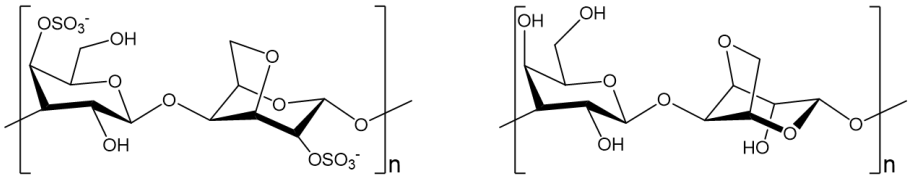

Figure 2.2. Molecular structure of natural resourced polymers: ι-carrageenan and agarose.

2.1.2. Biodegradable synthetic polyesters

PLLA with a number-average molecular weight (M_n) of 120.000 $g \cdot mol^{-1}$ has been supplied by Corbion (Amsterdam, Netherlands). **PCL** with a (M_n) of 80.000 $g \cdot mol^{-1}$ was purchased from Sigma-Aldric. **PBSu** and **PBAT** biopolyesters were offered in pellets from Natureplast (France) under commercial name PBE 003 and PBE 006, respectively. They have a Melt Flow Index (190°C; 2.16 kg) of 4–6 g $(10\ min)^{-1}$ and a density of 1.26 $g \cdot cm^{-3}$ according to the data provided by the manufacturer. These polymers were studied in Chapter 8, being their molecular structures shown in **Figure 2.3**. Chloroform (>99.8%, 11352878), purchased from Alfa Aesar™ was used as solvent. Phosphate buffered saline (PBS) tablets were also purchased from Sigma Aldrich.

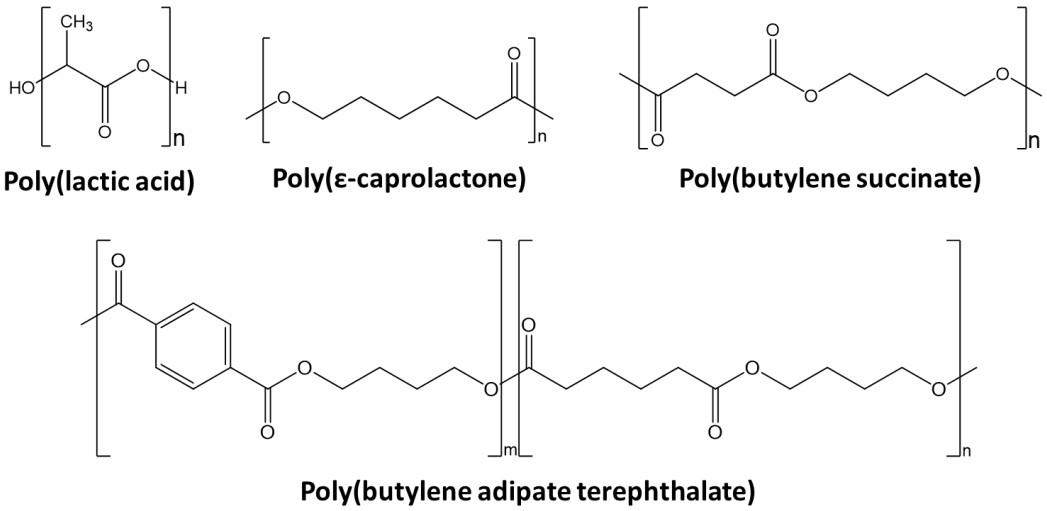

Figure 2.3. Chemical structures of biopolymers: PLA, PCL, PBSu, and PBAT.

2.1.3. Functional fillers and additives

Magnetic fillers: different ferrites have been selected as magnetic nanofillers along the PhD Thesis. Cobalt ferrite ($CoFe_2O_4$) spherical nanoparticles of 35−55 nm in diameter, were employed in Chapters 3 and 5. Magnetite (Fe_3O_4) nanopowder of 50−100 nm average particle size was used in the composites described in Chapter 7. Both ferrites were purchased from Nanostructured & Amorphous Materials Inc.

In addition, core-shell magnetite nanorods, coated with gold (Chapter 8), were synthesised using: Oleic acid (90%, 364525-1L), hexadecylamine (HDA) for synthesis grade (8222030500), iron (0) pentacarbonyl (195731-50G), 1-octanol for synthesis grade (8209311000), formaldehyde (37 wt.% in H2O, F1635-25ML), polyvinylpyrrolidone powder (average M_w ~55,000 $g \cdot mol^{-1}$), and K_2CO_3 purchased from Sigma Aldrich. (3-aminopropyl) triethoxysilane, 98% (APTES, A10668), chloroform (>99.8%, 11352878), and hydrogen tetrachloroaurate(III) hydrate (HAuCl4, 99.9%, 12325.06) were purchased from Alfa Aesar™. Absolut ethanol, EPR Ph.Eur., ≥ 99.5% V/V (ETHA-9TP-5K0) was purchased from Labbox.

Electrically conductive fillers: apart from synthesised and modified CNCs, graphite flakes (332461-2.5KG) were supplied by Sigma Aldrich (Chapter 5) were used for electroactive nanocomposites.

Ionic liquid: the IL 2-hydroxyethyl-trimethylammonium dihydrogen phosphate ([Ch][DHP]) (purity higher than > 98%) [Ch][DHP] was acquired from Iolitec (Heilbronn, Germany) (Chapter 4).

2.1.4. Screen-printing substrates and set-up

During the process of screen-printing, explained in more detail in Chapter 3, three different cellulosic fabrics were used as a substrate, including Whatman® filter paper Grade 4 (termed as Substrate 1), GE Healthcare Whatman™ Grade 1 Chr chromatography paper (termed as Substrate 2) and Albet LabScience general use filter paper (termed as Substrate 3). Substrate characteristics are given in **Table 2.1**. Furthermore, two screen mesh densities were used, named Screen 1 (180 threads cm^{-1}, 27 μm threads thickness and 28.55 μm dot size) and Screen 2 (120 threads cm^{-1}, 30 μm threads thickness and 53.33 μm dot size). A semi-automatic DX-3050P vertical electronic drive screen printing instrument from Shenzhen Dstar Machine Co. was used for the printing process.

Table 2.1. Cellulosic substrate main characteristics. [a]Porosity values have been calculated taking into account the apparent density of the membranes and the bulk density of cellulose (set at 1.5 $g \cdot cm^3$). Porosity* values have been supplied by the providers.

	Substrate 1	Substrate 2	Substrate 3
Thickness	205 μm	180 μm	170 μm
Pore size (particle retention)	20-25 μm	11 μm	7-12 μm
Porosity[a]	70.1 %	67.8 %	76.0 %
Porosity*(s/300mL/sq.in)	15	22	19
Basis weight	92 $g \cdot m^{-2}$	87 $g \cdot m^{-2}$	61 $g \cdot m^{-2}$

2.2. Characterisation methods

2.2.1. Morphological characterisation

Scanning electron microscopy (SEM) enables the observation and characterisation of bulk morphologies of heterogeneous organic and inorganic materials from nanometre (nm) to micrometre (μm) scale. The high depth of focus of the SEM makes it the ideal imaging tool to observe features such as sample roughness, fracture surface, pores, voids, size and

distribution of fillers and obtain an overall view of their compatibility with the matrix.[1] Typically, in composites area, surface and cross-sectional micrographs of the material are analysed to be compared with mechanical and physicochemical properties.

The morphologies of both fracture and top surfaces of nanocomposites were evaluated using a HitachiS-4800 field-emission scanning electron microscope (FESEM) at an acceleration voltage of 5 kV. In general, the samples examined in a SEM must be electrically conductive to minimise charge build up on the sample caused by the electron beam and avoid the degradation of the sample and distortion of the image.[2] Before imaging, the samples were sputtered with a 10 nm-thin gold layer by magnetron sputtering (Scancoat Six SEM Sputter Coater, HHV, Bangalore, India).

Energy dispersive X-ray spectroscopy (EDX) enables the chemical characterisation using a SEM. With this technique, an elemental mapping can be obtained to evaluate the elemental distribution across the surface of the sample. Briefly, an electron beam of uniform energy stimulates the atoms, which generates X-rays with specific energies, which are characteristic of the emitting element. This allows the elemental composition of the sample to be determined. Furthermore, the intensity of the X-ray signal at any energy level is proportional to the concentration of that element in the path of the electron beam.[3] SEM coupled with EDX analyses were performed on a DSM 982 Gemini instrument (Zeiss).

Transmission Electron Microscopy (TEM) has an unparalleled ability to provide structural and chemical information over a range of length scales from hundreds of nanometers down to the level of atomic dimensions. It is a powerful technique for evaluation of nanostructures such as particles, fibers, and thin films, and imaging of atoms.[4,5] The used nanoparticles, were characterised size, shape and aggregation.

Images were acquired in a JEOL JEM-1400 PLUS instrument operating at 100 kV. Further, just for the synthesised magnetite nanorods, a High-resolution TEM (HR-TEM) was performed in Thermo Fisher Talos-F200 TEM working at 200 kV. Magnetite nanoparticles were deposited on a carbon-coated TEM grid. For CNC (organic nanoparticles) A droplet of aqueous a suspension at 0.1 mg mL^{-1} of CNC was negatively stained with 1% uranyl acetate ($UO_2(CH_3COO)_2$) for 1 min before analysis. The nanoparticle morphological features were analysed with the Image J software package.

2.2.2. Physicochemical characterisation

Fourier transform infrared spectroscopy (FTIR) is an essential characterisation technique to elucidate the structure of matter at the molecular scale. It is typically used, in polymer composite materials, to analyse the chemical composition, in terms of functional groups, and the bonding arrangement of constituents.[6,7] The FTIR spectroscopy measurements in attenuated total reflection (ATR) mode of the produced films and membranes were performed with a Jasco FT/IR-6100 spectrometer equipped with diamond ATR optics. IR spectra were collected after 64 scans taken in the range 4000−600 cm^{-1} with a resolution of 2 cm^{-1}.

X-ray diffraction (XRD) is a nondestructive technique that provides information on structures, phases, preferred crystal orientations (texture), and parameters such as average grain size, crystallinity, tension, and crystal defects.[8] The experimental peaks of a crystalline sample can be determined by matching with the position and intensities of a reference peak from standard database.

XRD patterns were measured using a Bruker D8 Advance diffractometer equipped with a Cu tube, Ge (111) incident beam monochromator (λ = 1.5406 Å) (fixed slit 1 mm), and a Sol-X energy-dispersive detector. The sample was mounted on a zero-background silicon wafer embedded in a generic sample holder. Data were collected from 6 to 60° 2θ (step size = 0.02 and time per step = 100 s, total time 60 h) at room temperature.

Nevertheless, in the characterisation of synthesised magnetite nanorods (Chapter 9), it was found that both maghemite (γ-Fe_2O_3) and magnetite (Fe_3O_4) are reverse spinel structures. The resulting XRD spectrum of both compounds are approximately similar, therefore XRD is not the best method to distinguish between the two species.[9] Accordingly, nanorods were further characterised by X-ray photoelectron spectroscopy (XPS).

For **X-ray photoelectron spectroscopy (XPS)** the energies of emitted photoelectrons are characteristic not only of the particular element, but also of its oxidation state. Thus, the results obtained from XPS measurements provide information that is complementary to XRD and HRTEM analysisis.[10] Measurements were performed in the SPECS instrument (Berlin, Germany) equipped with an analyser Phoibos150 1D-DLD and monochromatic radiation source Al Kαα (1486.7 eV). A first quick wide scan was carried out to determine the present elements (step energy 1 eV, dwell time 0.1 s, pass energy 80 eV) and them a detailed analysis was performed for the different elements (step energy 0.08 eV, dwell time 0.1 s, pass energy

30 eV) with an electron outgoing angle of 90º. The spectrometer was previously calibrated with Ag (Ag 3d5/2, 368.26 eV). The spectra were fit with the software Casa XPS 2.3.16, which models the Gauss-Lorentzian contributions after a background subtraction (Shirley). Concentrations were calculated correcting the values with the relative atomic sensitivity factors (Scofield).

Zeta-potential measurements are performed using DLS, which determines particle stability based on an electrostatic repulsion between NPs. Surface charge was determined by Zeta-potential measurements using a Malvern Zetasizer Nano-ZS.

Elemental Analysis was measured in a quadrupole mass spectrometer with Inductively Coupled Plasma (ICP) source (Q-ICP-MS), model XSeries-II (Thermo). An internal standard was introduced by adding 100 µL of Yttrium at 500 ppb. The measured selected isotopes to perform the quantification were ^{57}Fe and ^{197}Au. Nanoparticle samples (typically 50 µL) were added to 100 µL of aqua regia (1:3 HNO_3:HCl, trace analysis grade), and left for digestion for 1 hour. The sample was then diluted with milli-Q water to 10 mL (further diluted if necessary) and measured by ICP.

2.2.3. Thermal properties

Typically, the applicability of composite materials is related to their thermal behavior, regardless of their composition. The thermogravimetric analysis (TGA) and differential scanning calorimetry (DSC) are the two most common procedures used to assess the thermal properties of a wide range of composite materials.[8]

Differential scanning calorimetry (DSC) measures the differences in heat exchange between an analysed sample and a reference. It is typically used to determine phase transitions of polymers: i) The glass transition temperature (T_g), ii) melting temperature (T_m), and iii) crystallisation temperature (T_c). Obtained thermograms of semicrystalline polymers typically present the shape of the scheme depicted in **Figure 2.4** These parameters are mostly used in practice to establish the operating temperatures of nanocomposite materials and predict their mechanical behavior at different temperatures.[11] For example, below the T_g, the molecular chains of an amorphous polymer or the amorphous portions of a semicrystalline polymer are frozen in place showing brittle behavior, while above the T_g the higher mobility of the polymeric chains confers flexibility and rubber-like behavior to the material. As the temperature slowly increases above the T_g, the chains have enough mobility to reorganise and

the microstructure crystallises (T_c) below the melting temperature. Often, this process is referred to as cold crystallisation (T_{cc}). Finally, at higher temperatures, the crystalline phase absorbs energy enough to break intermolecular bonding where the polymer melts (T_m).[12,13] Further, integrating the areas of crystallisation and melting peaks the latent heat of theses transitions is obtained and therefore the degree of crystallinity of the polymeric portion of composites can be calculated.[14] Samples prepared in Chapters 6 and 7 were measured with a 822e Mettler Toledo DSC under nitrogen flow in the ranges of 30-150ºC (Chapter 6) and 25–200 ºC (Chapter 7) at a rate of 10 ºC·min^{-1} for both cooling and heating. under a nitrogen flow of 50 mL·min^{-1}.

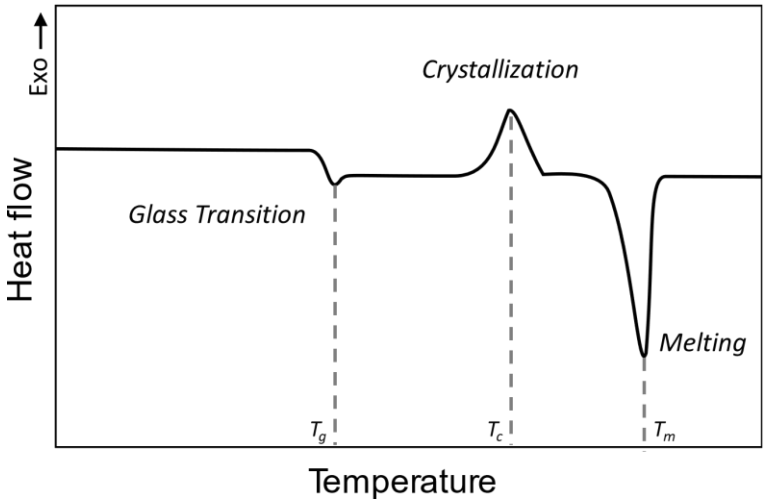

Figure 2.4 Schematic representation of a DSC thermogram displaying the typical thermal transitions of a semicrystalline polymer.

Thermogravimetric analysis (TGA) is a thermal analysis technique that involves measuring the change in mass of a sample as a function of time at a specific temperature or temperature profile under a controlled atmosphere. TGA is frequently used in nanocomposites research and testing to measure the degradation temperatures (stability), the moisture absorption, the amount of organic and inorganic compounds, and solvent residues by plotting the sample weight loss as a function of temperature.[8,15] The samples are transferred to open ceramic crucibles and analysed using a PerkinElmer TGA 4000 thermobalance operating at a heating rate of 10 °C min^{-1} under a nitrogen flow of 50 mL min^{-1}.

2.2.4. Optical properties

Ultraviolet-visible (UV-Vis) spectroscopy is a spectroscopic technique whose wavelengths are in the ultraviolet (100–400 nm), visible (400–750 nm) and near infrared (750–1400 nm) range. This technique allowed to analyse different properties of the fabricated materials. Nanocomposite films (Chapter 3 and 6) were evaluated by UV−Vis in transmittance mode according to the ASTM D1746-15 standard (Standard Test Method for Transparency of Plastic Sheeting), which determines the optical transparency as the transmittance (%) in the 540−560 nm range.[16] The samples, were measured in the 200–800 nm range with a sampling interval of 1 nm and 25 accumulations. However, in the synthesis of core-shell nanorods (Chapter 8), UV-Vis of the nanorod aqueous solutions were evaluated in absorbance mode to control of the shape and the thickness of the gold shell. A Cary 60 (Agilent) with a wavelength range of 300–1100 nm was employed. The processed films were fixed empty vertical holder for the measurements, while standard Macro cuvette were used for aqueous solutions.

Photothermia measurements presented in the Chapter 8 were performed with a homemade setup, where the sample is placed behind a 1x1 cm mask and irradiated with an LED light using a 10 W LED at 735 nm and an aspheric collimating lens. The current of the LED was controlled with a power source to obtain a final irradiance of 0.2 $W \cdot cm^{-2}$. The temperature was measured from the top using a thermal camera (Flir E4) and evaluated with the Flir tools+ software package. Light intensity was measured using a power sensor behind the sample (S425, Thorlabs).

The temperature variation was measured as a function of time (dT / dt) at the initial linear slope (t ≈ 1 min) in order to evaluate power dissipation, i.e. the SAR ($W \cdot g^{-1}$) per mass of the active element, gold. The SAR was then calculated using the following formula:

$$SAR = \frac{c_{gel}\, M_{gel}}{M_{Au}} \frac{dT}{dt} \tag{2.1}$$

where c_{gel} is the specific heat that was taken as the specific heat of water (4.185 $KJ \cdot Kg^{-1} \cdot K^{-1}$), M_{gel} is the sample mass that is approximately the water mass, and M_{Au} is the mass of nanorods' Au.

2.2.5. Mechanical properties

Uniaxial tensile tests: allows to study the behaviour of a material under mechanical solicitations. Stress-strain measurements can be used to forecast the stress that can withstand a fabricated material before being deformed or broken when in use. The main mechanical properties analysed are Young's modulus (E), maximum tensile stress or yield stress (σ_y), and elongation at break (ε_b), which depend on the temperature, surface state, applied forces, and the speed of deformation.[17] Experiments were carried out on an AGS-X universal testing machine from Shimadzu at 1 mm min^{-1}, except for the nanocomposites based on PCL and PBAT (studied in Chapter 8) that were performed at 3 mm min^{-1} due to their highly ductile behavior. Typically, before conducting the tests, specimens were exposed to relative humidity (RH) of 50 % and 20 ºC for 24 h. Typically five specimens of each film with 10 mm of width setting the gauge length at 30 mm.

2.2.6. Magnetic properties

The **vibrating-sample magnetometer (VSM)** is an instrument used to measure the magnetic characteristics of magnetic materials. In a VSM, a sample is located in a copper coil with an applied field and vibrated perpendicular to the magnetic moment. The field is recorded by measuring a variation in voltage. The VSM provides reliable information about the magnetic moment of MNPs and its composites as a function of field, crystal orientation, temperature and aggregation.[9] Magnetic hysteresis, also known as a hysteresis loop, represents the magnetisation of a material as a response to an applied external magnetic field (H). **Figure 2.5** shows a typical hysteresis loop of a ferromagnetic material. When an external magnetic field is applied, the magnetisation follows the pathway up to the saturation (M_s), where the magnetic dipole moments are aligned in the direction of the applied magnetic field. When H is reduced to zero, some remanent magnetisation remains in the material (M_r). By applying the magnetic field in the opposite direction, the magnetisation of the material goes to zero under the coercive field ($-H_c$). As the magnetic field increases in the opposite direction, the magnetisation reaches saturation as before but in the opposite direction ($-M_s$). The loop continues with an equal but opposite residual magnetisation ($-M_r$) and coercivity (H_c). The area of the hysteresis loop is directly related to the energy dissipated upon reversal of the applied magnetic field.[18]Magnetic hysteresis loops were measured at room temperature

using a MicroSense EZ7 vibrating sample magnetometer (VSM) with a maximum range between −1.8 and 1.8 T.

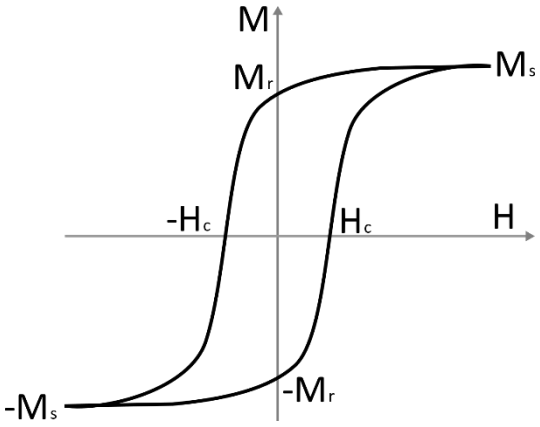

Figure 2.5. Representation of a magnetic hysteresis loop of a ferromagnetic material.[18]

The **AC Magnetometry** was employed in Chapter 8 to quantify the Specific Absorption Rate (SAR) by computing the hysteresis loops' area. The SAR is the absorbed energy per unit of nanoparticle mass. This parameter depends on the physicochemical properties of the nanoparticles such as composition, size, shape, crystallinity, and saturation magnetisation, among others. It was performed by using a homemade AC magnetometer.[19] Briefly, it consists of an air−core inductor part of a resonant circuit fed by a power amplifier. The dynamic magnetisation, M(t), is obtained by a pick-up coil system composed of two coils wound in opposite directions. The device is capable of working in a wide frequency range (100kHz-1MHz) with large field intensities: up to 90 mT at low frequencies and up to 30 mT at high frequencies.

The SAR values obtained in Chapter 8 were extracted by computing the area (*A*) enclosed by the loops, multiplied by the number of loops per second (frequency) and normalised by the sample concentration (mass per unit volume of the colloidal sample):

$$SAR\left(\frac{W}{g}\right) = \frac{f}{c}A = \frac{f}{c}\mu_0 \oint M\ dH \tag{2.2}$$

2.2.7. Electrical properties

Dielectric properties of polymer nanocomposites with high dielectric constants provide the combined advantages of high electrical energy storage density and can improve ionic conductivity and processing properties. Measuring this property of the fabricated materials

provides an insight of the potential of such composites for possible sensing (e.g., capacitive) application.[20]

Dielectric properties were obtained by measuring the capacity (C) in a frequency range of 100 Hz to 1 MHz at an applied voltage of 0.5 V, and the dielectric losses (tan δ) using an automatic Quadtech 1929 Precision LCR meter. The real part of the dielectric constant (ε') was extracted from the capacity (*C*) measurements taking into account the thickness (*d*) and area (*A*) of the samples according to Equation (2.3).[21] Meanwhile, the dielectric losses (tan δ) is calculated applying Equation (2.4), where ε'' is the imaginary part of the dielectric constant. The real part of the conductivity was obtained through the following Equation (2.5), where ε_0 (8.85×10^{-12} $F \cdot m^{-1}$) is the permittivity of free space and $\omega = 2\pi\nu$ is the angular frequency.

$$\varepsilon' = \frac{C \cdot d}{A} \tag{2.3}$$

$$tan\ \delta = \frac{\varepsilon''}{\varepsilon'} \tag{2.4}$$

$$\sigma' = \varepsilon_0 \omega \varepsilon'' \tag{2.5}$$

The **volume electrical conductivity** of the films was obtained by measuring the current–voltage (I–V) characteristic curves at room temperature applying voltages different voltages' ranges between -10 and 10 V using an automated Keithley 487 picoammeter/voltage source (Keithley Instruments, Beaverton, OR, USA). Prior to the electrical properties' measurements, circular gold electrodes of 5 mm diameter were coated in both sides by magnetron sputtering (Scancoat Six SEM Sputter Coater, HHV, Bangalore, India). The electrical conductivity (σ) was evaluated from the I-V slope by applying the Equation (2.6):[22]

$$\sigma = {}^{1}\Big/\left(R \cdot {}^{A}\Big/_{L}\right) \tag{2.6}$$

being *R* the resistance, *A* the electrode area and *L* the thickness of the samples.

Electrical conductivity of the surface was measured through the four-point probe method, consisting in four electrical probes in a line with equal spacing between each of the probes, using an Ossila Four-Point Probe System as it has been proven useful to determine the electrical conductivity of the samples prepared in Chapter 5.[23] Conductivity values were obtained by applying voltages up to 10 V using samples of 20 x 5 mm. Conductivity values

were extracted from resistance results following the Equation (2.6). Reported values represent the average and standard deviation over 20 measurements.

Electro-mechanical bending response is evaluated in Chapter 4, a procedure similar to the one presented by Dias et al. was used:[24] In short: samples with 12 mm x 2 mm were gold coated by magnetron sputtering onto both sides. The needles of the sample holder were connected to an Agilent 33220A function generator and an oscilloscope PicoScope 4227. All the samples were analysed by a square wave signal with different peak voltages (2, 3, 5, 8 and 10 Vpp) at a frequency of 100 mHz.

2.2.8. Viscosity of the inks

The **Viscosity** of the inks was evaluated at different shear stresses. The viscosity describes the resistance of an ink to flow at a certain shear because of internal friction and is defined as the ratio between shear stress and shear rate. This characterisation allows to predict the suitability of an ink for a determined printing technique. Among the different printing technologies, screen-printing has been used in the present work. Measurements were carried out using a Brookfield DV2T Touch Screen Viscometer using cone-plate geometry with a CPA-52Z cone (3° cone angle, 1.2 cm cone radius).

2.2.9. Porous structure

N_2 adsorption-desorption isotherms are a common method for determining the specific surface area and pore size distribution of microporous and mesoporous materials. It is based on the adsorption of N_2 on an adsorbent of interest at constant temperature, typically 77 K. The surface adsorption capacity of nitrogen in an adsorptive depends on the nitrogen relative pressure.[14] Isotherms of mesoporous materials are typically evaluated with the Brunauer-Emmet-Teller (BET) method to obtain the accessible surface area, as will be employed in Chapter 5. Porosity and surface area are important factors in membrane research since they disclose the membrane's structural properties. The permeability of a membrane is determined by the number of pores, their size distribution, and, most critically, its continuity (together with the hydrophilicity of the membrane material).[25]

Nitrogen sorption experiments were carried out on a Quantochrome Autosorb-iQ-C-XR at 77K, with nitrogen (99.999%) and helium (99.999%) provided by PanGas AG, Switzerland. Before the measurement, the samples were degassed in vacuum at 60 °C for 24 h.

2.3. References

1 J. Goldstein, D. Newbury, P. Echlin, E. Lifshin, L. Sawyer and J. Michael, *Scanning Electron Microscopy and X-Ray Microanalysis*, 2003.

2 M. de Assumpcão Pereira-da-Silva and F. A. Ferri, Scanning Electron Microscopy, *Nanocharacterization Tech.*, 2017, 1–35.

3 N. Scoutaris, K. Vithani, I. Slipper, B. Chowdhry and D. Douroumis, SEM/EDX and confocal Raman microscopy as complementary tools for the characterisation of pharmaceutical tablets, *Int. J. Pharm.*, 2014, **470**, 88–98.

4 D. J. Smith, in *Nanocharacterisation*, Royal Society of Chemistry, 2015, vol. 2015-Janua, pp. 1–29.

5 B. J. Inkson, Scanning electron microscopy (SEM) and transmission electron microscopy (TEM) for materials characterisation, *Mater. Charact. Using Nondestruct. Eval. Methods*, 2016, 17–43.

6 M. R. Sanjay, P. Madhu, M. Jawaid, P. Senthamaraikannan, S. Senthil and S. Pradeep, Characterisation and properties of natural fiber polymer composites: A comprehensive review, *J. Clean. Prod.*, 2018, **172**, 566–581.

7 R. Bhargava, S. Q. Wang and J. L. Koenig, FTIR Microspectroscopy of Polymeric Systems, *Adv. Polym. Sci.*, 2003, **163**, 137–191.

8 K. El Bourakadi, R. Bouhfid and A. el K. Qaiss, in *Cellulose Nanocrystal/Nanoparticles Hybrid Nanocomposites*, Woodhead Publishing, 2021, pp. 27–64.

9 L. Rashidi, in *Magnetic Nanoparticle-Based Hybrid Materials*, Woodhead Publishing, 2021, pp. 3–32.

10 A. Shavel, B. Rodríguez-González, M. Spasova, M. Farle and L. M. Liz-Marzán, Synthesis and Characterization of Iron/Iron Oxide Core/Shell Nanocubes, *Adv. Funct. Mater.*, 2007, **17**, 3870–3876.

11 M. R. Kessler, *Advanced Topics in Characterisation of Composites*, Trafford Publishing, 2004.

12 B. Wunderlich, *Thermal analysis*, Academic Press, 1st edn., 1990.

13 M. K. Singh and A. Singh, Thermal characterisation of materials using differential scanning calorimeter, *Charact. Polym. Fibres*, 2022, 201–222.

14 C. Schick, Differential scanning calorimetry (DSC) of semicrystalline polymers, *Anal. Bioanal. Chem. 2009 3956*, 2009, **395**, 1589–1611.

15 T. Y. Inan, Thermoplastic-based nanoblends: Preparation and characterisations, *Recent Dev. Polym. Macro, Micro Nano Blends Prep. Characterisation*, 2017, 17–56.

16 *Standard Test Method for Transparency of Plastic Sheeting*, ASTM International, 2015.

17 J. Davis, *Tensile Testing*, ASM International, 2nd edn., 2004.

18 F. Fiorillo, C. Appino and M. Pasquale, in *The Science of Hysteresis*, eds. G. Bertotti and J. Mayergoyz, 2005.

19 I. Rodrigo, I. Castellanos-Rubio, E. Garaio, O. K. Arriortua, M. Insausti, I. Orue, J. Á. García and F. Plazaola, Exploring the potential of the dynamic hysteresis loops via high field, high frequency and temperature adjustable AC magnetometer for magnetic hyperthermia characterisation, *Int. J. Hyperth.*, 2020, **37**, 976–991.

20 T. I. Yang and P. Kofinas, Dielectric properties of polymer nanoparticle composites, *Polymer (Guildf).*, 2007, **48**, 791–798.

21 E. Lizundia, A. Maceiras, J. L. Vilas, P. Martins and S. Lanceros-Mendez, Magnetic cellulose nanocrystal nanocomposites for the development of green functional materials, *Carbohydr. Polym.*, 2017, **175**, 425–432.

22 L. C. Fernandes, D. M. Correia, N. Pereira, C. R. Tubio and S. Lanceros-Méndez, Highly Sensitive Humidity Sensor Based on Ionic Liquid–Polymer Composites, *ACS Appl. Polym. Mater.*, 2019, **1**, 2723–2730.

23 S. Liu, T. Yu, Y. Wu, W. Li and B. Li, Evolution of cellulose into flexible conductive green electronics: a smart strategy to fabricate sustainable electrodes for supercapacitors, *RSC Adv.*, 2014, **4**, 34134–34143.

24 J. C. Dias, M. S. Martins, S. Ribeiro, M. M. Silva, J. M. S. S. Esperança, C. Ribeiro, G. Botelho, C. M. Costa and S. Lanceros-Mendez, Electromechanical actuators based on poly(vinylidene fluoride) with [N1 1 1 2(OH)][NTf2] and [C2mim] [C2SO4], *J. Mater. Sci.*, 2016, **51**, 9490–9503.

25 K. S. W. Sing, Adsorption methods for the characterisation of porous materials, *Adv. Colloid Interface Sci.*, 1998, **76**–**77**, 3–11.

3. Water-Soluble Cellulose Derivatives as Suitable Matrices for Magnetically Active Materials

A simple and environmentally benign route is followed to prepare magnetically active materials based on three cellulose derivatives: MC, HPC, and NaCMC, combined with $CoFe_2O_4$ nanoparticles. First, free-standing films with homogeneously dispersed nanoparticles are fabricated by mechanical agitation followed by doctor blade casting. Mechanical, physicochemical, optical, magnetic and dielectric properties of the material are analysed. Then, the suitability of the magnetic mix as screen-printing ink was tested. The renewable character of the hosting matrices and the fabrication methods that solely use water as a solvent provide novel insights into the processing of renewable, magnetically active and mechanically flexible materials with tailorable geometries.

3.1. Introduction

Cellulose presents a considerable potential to develop added-value materials for novel multifunctional devices as it combines low density and compostability [1] with high strength and stiffness.[2] Unfortunately, the strong inter- and intramolecular hydrogen bonding make cellulose non-soluble in many organic solvents and water, which difficults its processability and thus limits its potential application.[3] In this sense, modifying cellulose to make it water-soluble would enable its processing through printing technologies.[4] More precisely, cellulose derivatives have shown remarkable film-forming properties,[5] making this group of materials attractive for the development of multifunctional materials.

Among the existing cellulose derivatives, methyl cellulose (MC), hydroxypropyl cellulose (HPC) and sodium carboxymethyl cellulose (NaCMC) are some of the most commercially relevant ones. These cellulose ethers are obtained through the modification of the bonded oxygen onto the −OH groups of each anhydroglucose unit through a two-step process. The first step involves treating cellulose under mild alkali conditions (usually with sodium hydroxide). To obtain MC, a subsequent treatment with methyl chloride is required (dimethyl sulphate or methanol could also be used), replacing the hydroxyl groups with methoxy groups[6]. At the same time, HPC is produced after propylene oxide treatment (55 °C, 210 min)7. NaCMC is obtained after treating alkali cellulose with sodium monochloroacetate in an aqueous ethanolic medium[8] to introduce carboxymethyl groups (-CH_2COOH) into the 2, 3 and 6 hydroxyl groups of cellulose.[910]

Accordingly, this work aimed to fabricate and characterise a series of multifunctional materials based on cellulose derivatives and study their printability onto paper substrates. Nanocomposite films based on MC, HPC and NaCMC as a matrix and $CoFe_2O_4$ as a magnetic filler have been prepared by mechanical agitation followed by doctor blade casting. Interestingly, the approach here used only requires the use of water as a solvent. The morphology, optical properties, mechanical behaviour, magnetic and dielectric properties of nanocomposites with concentrations up to 50 wt. % are investigated.

Subsequently, these materials were employed as screen-printable magnetic inks to fabricate thin, flexible, biocompatible and biodegradable magnetically active structures with relatively improved lateral resolution below the millimetre. These structures can be potentially created directly on “paper-based” substrates, such as cardboard. The magnetic nanoparticles embedded in porous cellulose structure could also enable the possibility of

future incorporation of electrolytes, resulting in a multifunctional device capable of transporting ions and at the same time being magnetically active. The rheological properties of water-soluble cellulose derivatives/cobalt ferrite formulations are evaluated to gain insights into the printability of the inks. The effect of different printing parameters has been assessed. Additionally, three paper substrates with pore sizes varying from 7 to 25 μm are used. Finally, it is demonstrated that the fabricated patterns present enough magnetisation to be used in actuator and sensor applications.

3.2. Experimental

3.2.1. Sample preparation and characterisation

3.2.1.1. Free-standing films

Contrarily to the *in-situ* synthesis processes where a precursor material is typically reduced under relatively harsh conditions to yield the desired compound,[11] here is described the fabrication of hybrid materials through simple aqueous mixing of MC, HPC and NaCMC and $CoFe_2O_4$ of 35-55 nm. 40 μm thick films of three cellulose derivatives/$CoFe_2O_4$ nanocomposites with nanoparticle concentrations from 5 to 50 wt. % are fabricated by the doctor blade technique (**Scheme 3.1**). The first step involves nanoparticle dispersion and cellulose derivative dissolution in water. $CoFe_2O_4$ was dispersed using an ultrasound bath for 6 h, while cellulose derivative was dissolved in distilled water with a Teflon™ mechanical stirrer for the same time. In order to ensure a sufficiently low viscosity, the concentrations of cellulose derivative in water were optimized to be 2.5 wt./v %, 10 wt./v % and 4 wt./v % for MC, HCP and NaCMC, respectively. Then, dispersed nanoparticles were incorporated into the cellulose derivative solution and the resulting mixture was mechanically stirred for 1 h.

Finally, the mixtures were deposited with the doctor blade technique onto clean glass substrates, allowing water evaporation at room temperature. Very importantly, the drying temperature remains below the LCST of MC and HPC, avoiding undesired thermally induced phase changes which result in poor mechanical performance.[12,13] Neat films were also prepared for comparison. Overall, the reported approach results in an energetically-efficient straightforward method that enables a homogeneous dispersion of $CoFe_2O_4$ nanoparticles with no need for complex grafting steps. The materials specifications are compiled in Section 2.1.1 of Chapter 2.

The physicochemical properties were analyzed by FTIR measurements, morphological properties were evaluated by FESEM, the transparency of the films was measured by UV−Vis spectroscopy, mechanical properties were obtained from uniaxial tensile testing, and magnetic properties of the films were measured with a VSM. The dielectric properties were analyzed after measuring the capacity and the dielectric losses according to Equations (2.3) and (2.4).

3.2.1.2. Screen-printed films

On the other hand, the samples set at 50 wt.% of cobalt ferrite were printed through screen-printing as depicted in **Scheme 3.1**. Such concentration offers a good balance between a proper adhesion of the ink to the cellulose substrates fibres (given by the presence of cellulose derivative acting as a binder) and enough magnetisation saturation response [14]. Once the ink is obtained, it is forced through the screen mesh towards a microporous cellulosic substrate upon applying pressure using a squeegee. Two screens named Screen 1 and Screen 2, presenting a pattern of parallel lines with three different line widths, were utilised for printings onto three cellulosic substrates termed Substrate 1, Substrate 2, and Substrate 3. Printings were developed using a semi-automatic instrument, where the cellulosic substrates were set at 10 mm, while the squeegee angle concerning the screen was set at 30 °. For all the samples, the printing speed was optimised at 13.6 $cm \cdot s^{-1}$. Finally, printed features were dried at room temperature for 1 h. The main characteristics of the materials employed in the printing process are compiled in Section 2.1.4 of Chapter 2.

The viscosity of prepared formulations (inks) were evaluated using a cone-plate viscometer. The morphology of the top surface of the printed patterns was firstly evaluated using a 400x USB digital microscope. For further accuracy, FESEM was also used. A SEM coupled with EDX analyses were performed. Finally, Magnetic properties were measured using a VSM. The equipment specifications and measurements conditions are compiled in section 2.2 of Chapter 2.

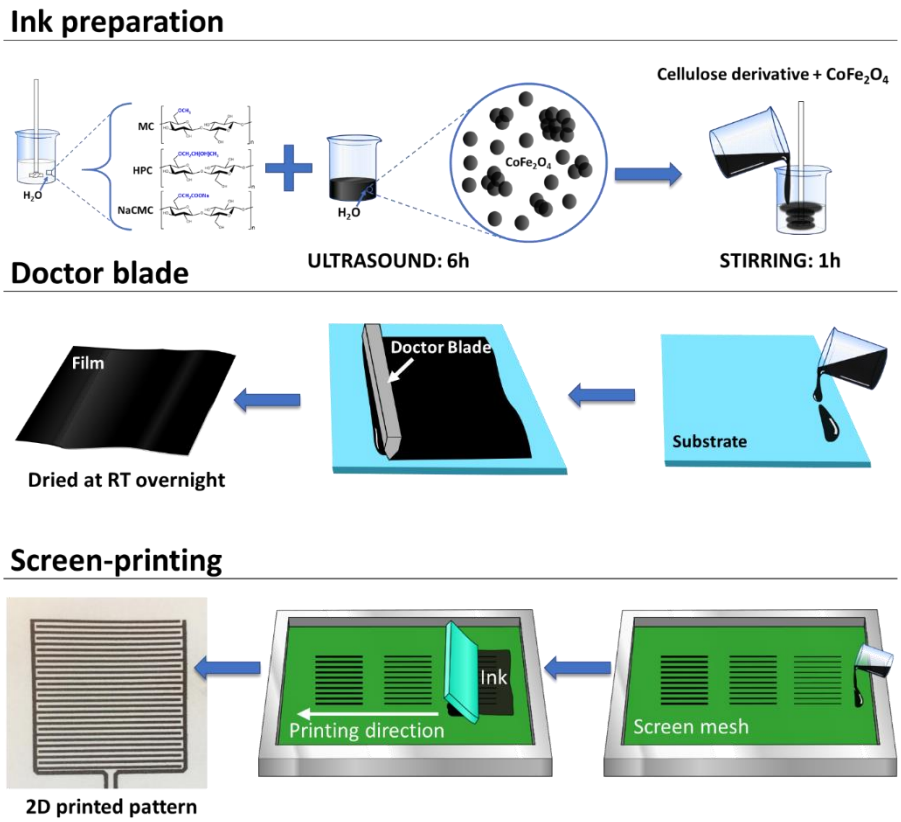

Scheme 3.1. Schematic diagram showing the preparation of methyl cellulose (MC), hydroxypropyl cellulose (HPC) and sodium carboxymethyl cellulose (NaCMC) composites (up) and their subsequent fabrication through the doctor blade method (middle) and screen-printing technique (below).

3.3. Results and discussion

The main purpose of developing a free-standing film was to study the intrinsic properties of the material having similar conditions to a working device. Once the prepared nanocomposites' characteristic properties were examined, printing technologies' fabrication process was tested and optimised. Therefore, in this Section, the prepared nanocomposites' characteristic properties are considered first, followed by the results regarding the composite ink's printability and the printed pattern's properties.

3.3.1. Physicochemical characterisation and morphology

The FTIR spectra in **Figure 3.1a** show that pure MC displays main absorption peaks at 3458 cm^{-1} (O-H stretching), 2902 cm^{-1} (C-H stretching), 1646 cm^{-1} (C-O stretching from the glucose moiety), 1455-1251 cm^{-1} (C-H bending) and 1065 cm^{-1} (C-O stretching from

asymmetric oxygen bridge) and 947 cm^{-1} (O-CH_3 stretching).[16] On the other side, neat HPC film shows a characteristic broad band at 3440 cm^{-1} due to the –OH groups and narrower bands centred at 2972, 1652, 1376 and 1056 cm^{-1} arising from the C–O–C asymmetric valence vibration, C=C stretch, –CH_2 vibration and –C-OH groups respectively.[12] Finally, NaCMC presents a broad peak at 3420 cm^{-1} as a result of the –OH stretching and intra/intermolecular hydrogen bonds and a weaker absorption band at 2913 cm^{-1} due to the C-H stretching. The narrower peaks at 1605, 1422 and 1128 cm^{-1} are ascribed to the asymmetrical and symmetrical stretching of carboxyl methyl ether and the >CH–O–CH_2 stretching, respectively.[17,18] Overall, in **Figure 3.1b-d,** no band displacement is observed upon adding cobalt ferrite for all the three hosting matrices, suggesting no intermolecular interactions between MC-HPC-NaCMC and $CoFe_2O_4$ exists. Further, no significant variations are observed due to increasing filler concentration for the different cellulose derivatives.

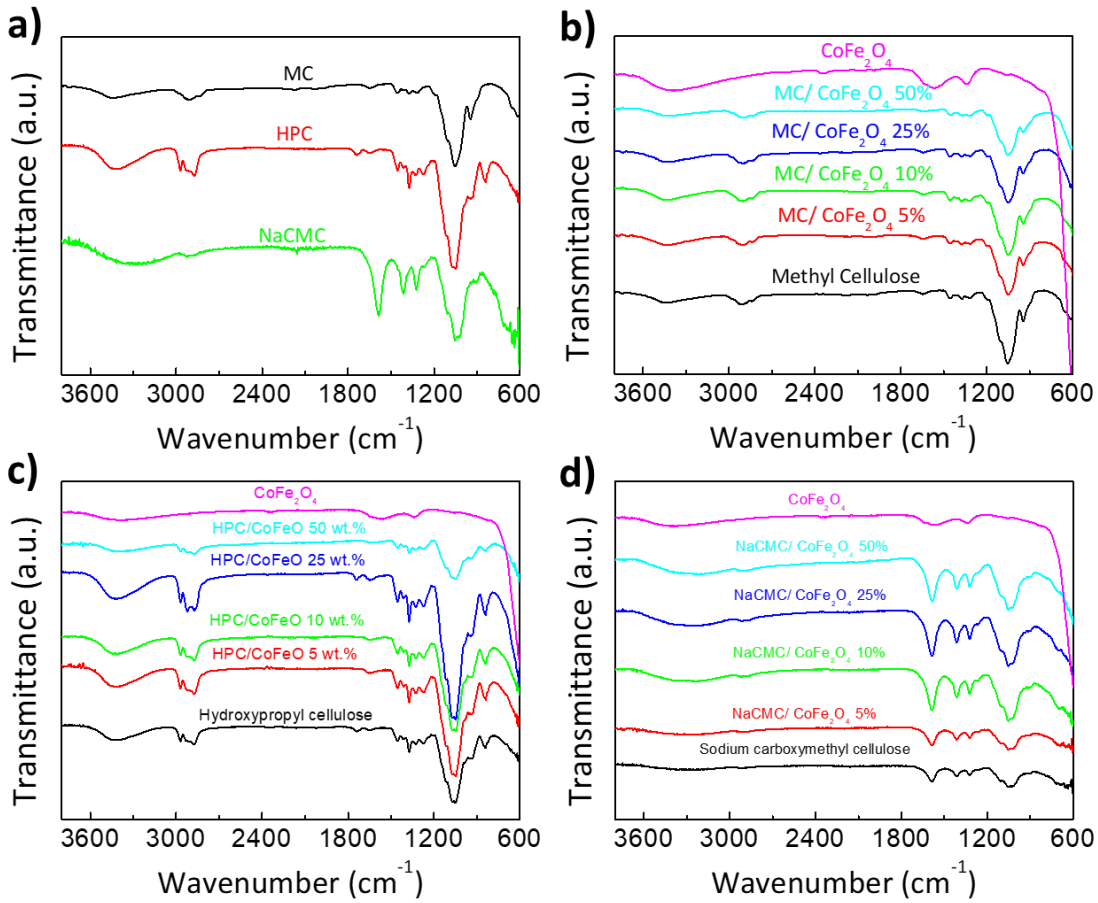

Figure 3.1. FTIR spectra in the 3800–600 cm^{-1} region of a) neat methyl cellulose (MC), hydroxypropyl cellulose (HPC) and sodium carboxymethyl cellulose (NaCMC) films and FTIR of b) MC/$CoFe_2O_4$, c) HPC/$CoFe_2O_4$, d) NaCMC/$CoFe_2O_4$ nanocomposite films for concentrations up to 50 wt.%.

It is well established that the properties of materials are dependent on their morphological structure.[19] This is even more evident in the case of polymer nanocomposites, where aggregation effects may lead to poor properties such as inefficient stress transfer across the filler-matrix interface,[20] or non-electrically conducting materials due to the agglomeration of conductive fillers which do not form a percolated network.[21] Accordingly, the morphology of the fabricated nanocomposites has been assessed by FESEM. **Figure 3.2a** shows representative FESEM images of film surfaces for NaCMC/$CoFe_2O_4$ nanocomposites when increasing the loading of nanoparticles. Neat NaCMC presents a crack-free homogeneous surface with no irregularities, highlighting the potential of the fabrication procedure here used to develop low roughness substrates. Independently of the concentration, $CoFe_2O_4$ nanoparticles are observed as bright spots randomly embedded within the darker NaCMC matrix. The higher the concentration, the larger the bright regions in the FESEM micrographs. FESEM images in **Figure 3.2b-d** indicate that NaCMC/$CoFe_2O_4$ and MC/$CoFe_2O_4$ nanocomposite films, at a loading of 50 wt.%, also show good nanoparticle dispersion in surface. Furthermore, the cross-section images show that the cobalt ferrite incorporation does not substantially modify the structure. However, HPC/$CoFe_2O_4$ nanocomposites show a more aggregated structure at this concentration on the surface. All the samples present a relatively rough surface characteristic of a ductile fracture.[22] No voids as a result of filler debonding can be found in these images, suggesting good physical compatibility between the $CoFe_2O_4$ filler and organic hosting matrix[22], underlining that inorganic nanoparticles are well intercalated through the whole thickness of the film. These observations indicate that nanoparticles are homogeneously dispersed in the matrices despite the large concentrations prepared here.

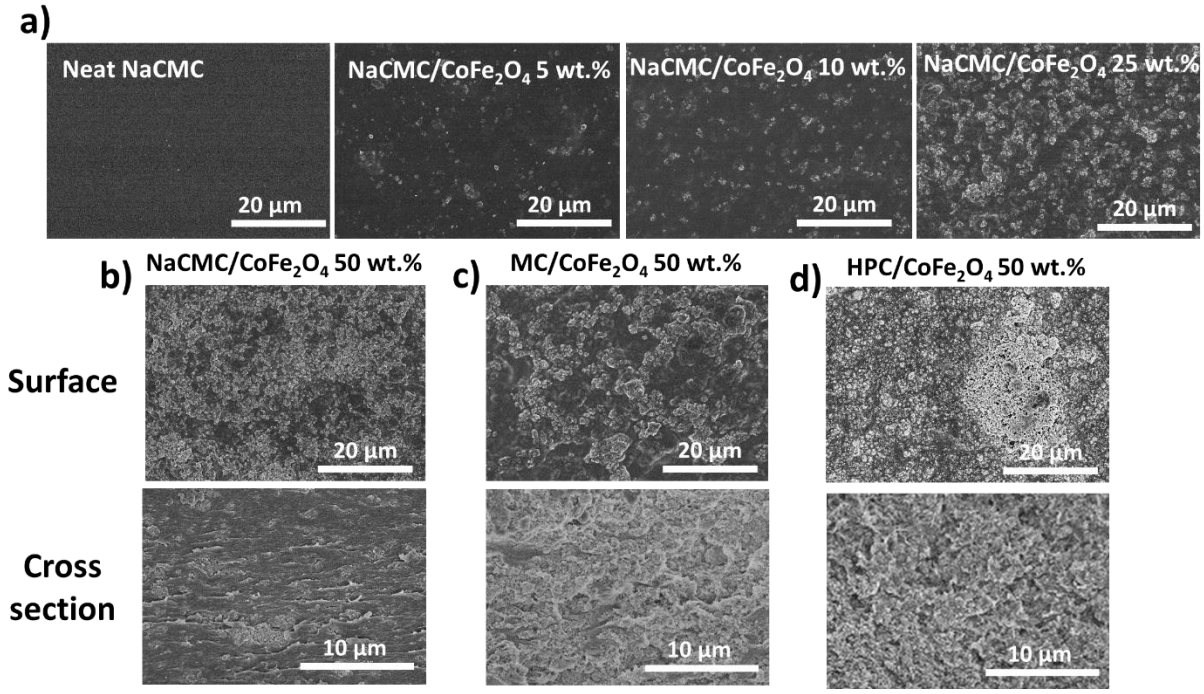

Figure 3.2. Representative field emission scanning electron microscopy (FESEM) images of film surfaces for NaCMC/$CoFe_2O_4$ nanocomposite films with different $CoFe_2O_4$ concentration a): 0 wt.%, 5 wt.%, 10 wt.%, and 25 wt.% and surface and cross-sectional images of b) NaCMC, c) MC, and d) HPC comprising 50 wt.% of $CoFe_2O_4$.

3.3.2. Optical properties

The optical properties of the nanocomposite films were evaluated by ultraviolet-visible (UV-Vis) spectroscopy in transmittance mode. **Figure 3.3a** displays the transmittance (%) of the neat films within the λ=200-800 nm region, while Figure **3.3b-d** shows the corresponding transmittance for three cellulose derivatives/$CoFe_2O_4$ films (**Figure 3.3e** provides their macroscopic appearance). Neat MC, HPC and NaCMC films present optical transparency of 84%, 88% and 91%, respectively, according to the ASTM D1746-15 standard (Standard Test Method for Transparency of Plastic Sheeting),[23] which determines the optical transparency as the transmittance (%) in the 540–560 nm range. Such high optical transmittance values make all three MC, HPC and NaCMC potential candidates for flexible electronics, transistors, optical sensors or touch screens.[24–26] The incorporation of $CoFe_2O_4$ nanoparticles within the 3 matrices yields optically black films where the amount of transmitted photons through the nanocomposite films is markedly decreased, showing transmittance values of nearly 0.5 % for concentrations exceeding 5 wt.%.[15]

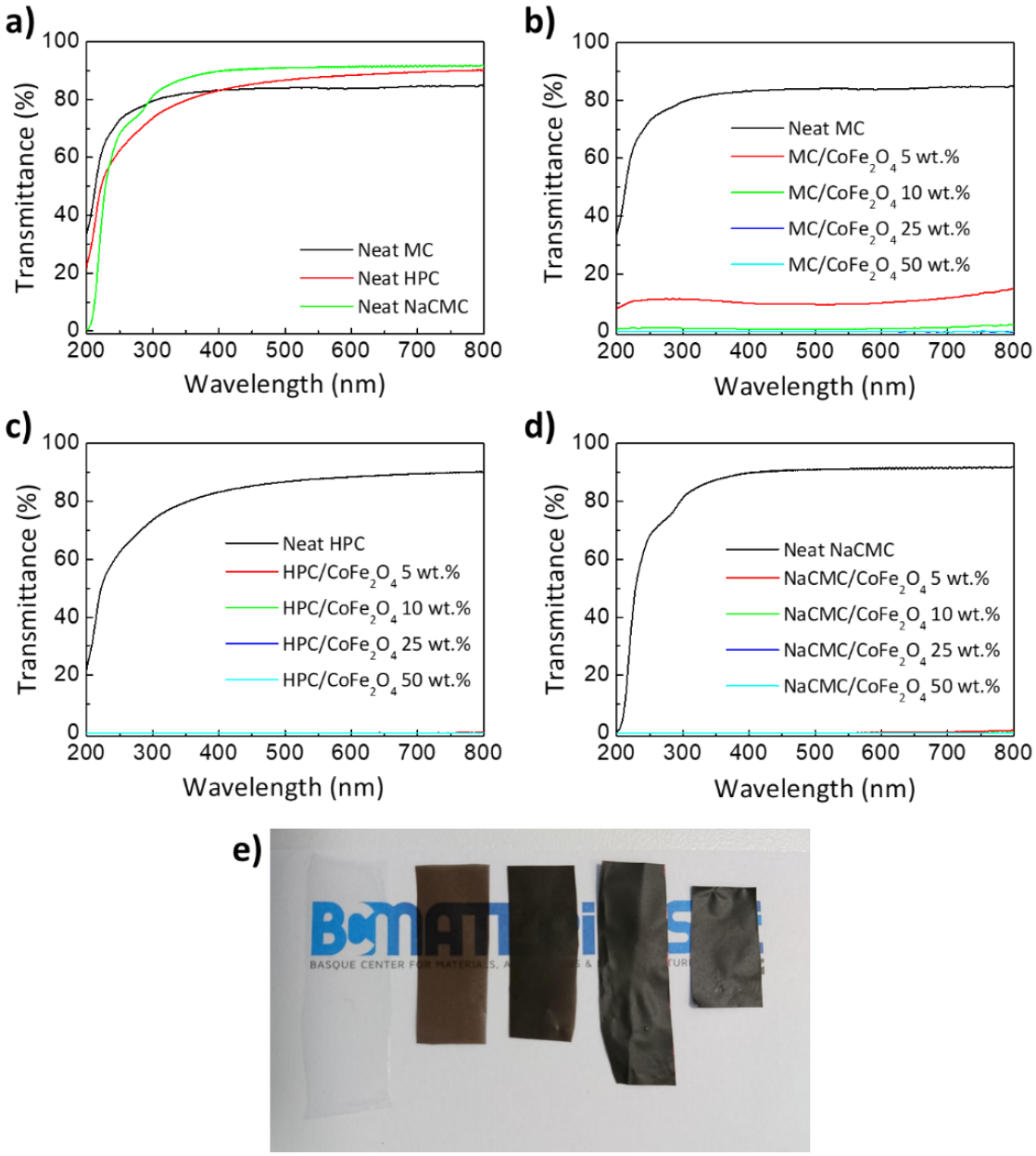

Figure 3.3. UV-Vis transmittance spectroscopy for neat films (a) and for MC/$CoFe_2O_4$ (b) HPC/$CoFe_2O_4$ (c) and NaCMC/$CoFe_2O_4$ (d) nanocomposite films. Optical photographs show the macroscopic appearance of MC/$CoFe_2O_4$ nanocomposite films with $CoFe_2O_4$ concentrations of 0, 5, 10, 25 and 50 wt.%.

3.3.3. Mechanical properties

Interestingly, prepared films keep mechanical flexibility, so they can be easily folded, as depicted in **Figure 3.4**, even at loadings as high as 50 wt.%. Although these observations denote the excellent suitability of these materials for flexible electronic applications, it is necessary to quantify the mechanical properties of the films.

Figure 3.4. Optical photographs showing the bendability of NaCMC/$CoFe_2O_4$ 25wt.% nanocomposite films.

In particular, the determination of tensile properties such as Young´s modulus (E), maximum tensile stress (σ_y) and elongation at break (ε_b) can be used to predict the capacity of fabricated materials to withstand applied stresses when in use. Accordingly, the mechanical properties of the materials have been evaluated by uniaxial tensile tests. **Figure 3.5** shows the representative stress-strain curves for all the obtained compositions, while **Table 3.1** summarises the main mechanical property values. Obtained data deviation may arise from the susceptibility of the prepared materials to moisture.[27]

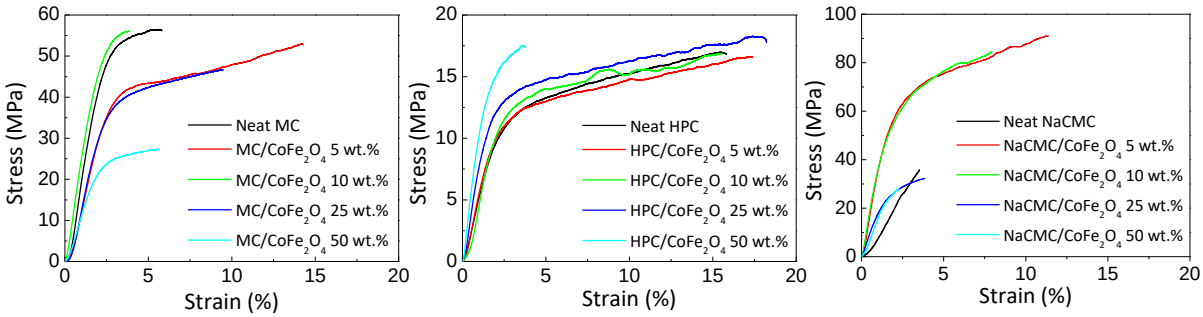

Figure 3.5. Representative stress-strain curves for MC/$CoFe_2O_4$, HPC/$CoFe_2O_4$ and NaCMC/$CoFe_2O_4$ nanocomposites.

Neat MC and NaCMC present a semi-brittle behaviour characterised by a E of 2620 ± 390 and 1120 ± 140 MPa and a ε_b of 5.4 ± 1.2 and 2.3 ± 0.9 %, respectively.[28–30] On the contrary, neat HPC shows a semi-ductile behaviour with a modulus of 600 ± 40 MPa and an elongation at break of 12.9 ± 3.6 %.[12,27] Young´s modulus and tensile strength generally tend to increase with the addition of cobalt ferrite for HPC and NaCMC-based hybrids. At the same time, E does not show any improvements when $CoFe_2O_4$ nanoparticles are incorporated into MC.

The *E* increase is particularly marked in the case of NaCMC, where it increases from 1120 ± 140 MPa to a maximum value of 3500 ± 320 MPa for its 5 wt.% counterparts.

Table 3.1. Table showing main representative parameters of tensile test for all the prepared nanocomposites. *E*: Young´s modulus; ε_y: elongation at yield; σ_y: yield stress; ε_b: elongation at break; σ_b: stress at break.

	wt.%	*E* (MPa)	ε_Y (%)	σ_y (MPa)	ε_b (%)	σ_b (MPa)
MC	0	2620 ± 390	3.4 ± 0.2	55.6 ± 2.7	5.4 ± 1.2	54.5 ± 7.8
	5	1600 ± 180	3.7 ± 0.9	38.7 ± 2.7	14.6 ± 1.6	50.2 ± 4.7
	10	2660 ± 180	3.4 ± 0.1	55.0 ± 3.5	3.7 ± 0.2	55.0 ± 3.6
	25	2210 ± 160	2.8 ± 0.3	40.0 ± 3.2	9.3 ± 1.2	48.6 ± 2.4
	50	1120 ± 200	2.6 ± 0.5	22.4 ± 1.0	5.1 ± 0.4	25.9 ± 1.0
HPC	0	600 ± 40	3.3 ± 0.4	12.7 ± 0.7	12.9 ± 3.6	16.4 ± 2.1
	5	510 ± 20	3.1 ± 0.4	12.3 ± 1.1	16.9 ± 1.7	16.4 ± 0.9
	10	320 ± 60	3.0 ± 0.3	12.6 ±0.3	16.6 ± 1.0	15.0 ± 1.7
	25	640 ± 70	2.8 ± 0.4	13.5 ± 0.3	17.0 ± 3.8	18.1 ± 1.1
	50	880 ± 50	1.9 ± 0.3	14.5 ± 1.1	5.6 ± 1.4	17.7 ± 0.5
NaCMC	0	1120 ± 140	-	-	2.3 ± 0.9	22.1 ± 10.0
	5	3500 ± 320	3.0 ± 0.1	66.4 ± 3.6	11.3 ± 1.3	91.3 ± 2.9
	10	3360 ± 240	2.7 ± 0.4	61.0 ± 6.1	7.8 ± 1.0	79.2 ± 7.1
	25	1620 ± 120	1.8 ± 0.2	24.0 ± 1.3	3.9 ± 1.4	31.2 ± 4.5
	50	1970 ± 220	-	-	2.0 ± 0.3	29.1 ± 1.9

Interestingly, adding cobalt ferrite does not necessarily decrease the ductility of the resulting material as typically observed for polymer composites, where the presence of particles leads to premature fracture due to stress concentration effects in filler-rich regions.[29] Indeed, for all three matrices, the presence of low amounts (i.e. 5 and 10 wt.%) of nanoparticles results in increased elongation at break values. This may be due to decreased hydrogen bonding between MC, HPC or NaCMC chains as a result of the "screening" effect of added nanoparticles, which reduce chain rigidity to enhance the overall ductility.

There is a given concentration in which further increase of nanoparticle content does not contribute to improving the mechanical performance of the resulting composite. Such critical concentration is detrimental to the material's mechanical properties, which has been reported for diverse cellulose derivative composite materials.[31,32] This behaviour has been ascribed to

nanoparticle aggregation that may decrease the effective filler-matrix interactions and create weak points in the material, although no cavities were observed through FESEM analyses.[33]

Experimentally obtained data can be compared with theoretical predictions according to the modified Halpin-Tsai model:[34,35]

$$\frac{E_C}{E_m} = \left(\frac{3}{8}\right)\left(\frac{1+2\rho\eta_L V_{CoFe2O4}}{1-\eta_L V_{CoFe2O4}}\right) + \left(\frac{5}{8}\right)\left(\frac{1+2\eta_T V_{CoFe2O4}}{1-\eta_T V_{CoFe2O4}}\right) \quad (3.1)$$

$$\eta_L = \frac{E_r - 1}{E_r + 2\rho} \qquad \eta_T = \frac{E_r - 1}{E_r + 2}$$

Where E_c and E_m are Young´s modulus of the composite and matrix, respectively, ρ is the $CoFe_2O_4$ nanoparticle aspect ratio (set at 1 due to its spherical shape), $V_{CoFe2O4}$ is its volume fraction within the nanocomposite and E_R is defined as the ratio between Young´s modulus of the filler and the matrix. $CoFe_2O_4$ volume fractions are extracted from the weight fraction of both components and their densities, assuming a density of 5.30 g·cm^{-3} for $CoFe_2O_4$ (obtained from the supplier) and 1.62 g·cm^{-3},[36] 0.50 g·cm^{-3} and 1.59 g·cm^{-3},[29] for MC, HPC and NaCMC respectively (obtained from the supplier).

Figure 3.6 compares the predicted Young´s modulus values according to Equation 3.1 with the experimentally obtained results. Overall, experimental values remain below-predicted data in the MC/$CoFe_2O_4$ while fitting markedly well for the HPC/$CoFe_2O_4$ system and remain above the theoretical predictions for NaCMC/$CoFe_2O_4$ nanocomposites. Those results suggest a poor MC-$CoFe_2O_4$ interface, which results more noticeable as the cobalt ferrite concentration increases (a more significant mismatch between theoretical and experimental results is found).[37,38] On the contrary, the homogeneous nanoparticle distribution and the effective stress transfer through the HPC-$CoFe_2O_4$ interfaces result in a perfect fit between the modified Halpin-Tsai prediction and the experimental results. Finally, a strong electrostatic interaction between the negatively charged carboxylate groups of NaCMC and the positive cobalt ferrite yields a remarkable modulus enhancement.[39] However, after reaching a maximum value, *E* decreases with further nanofiller addition, which can be attributed to the aggregation effect of cobalt ferrite.

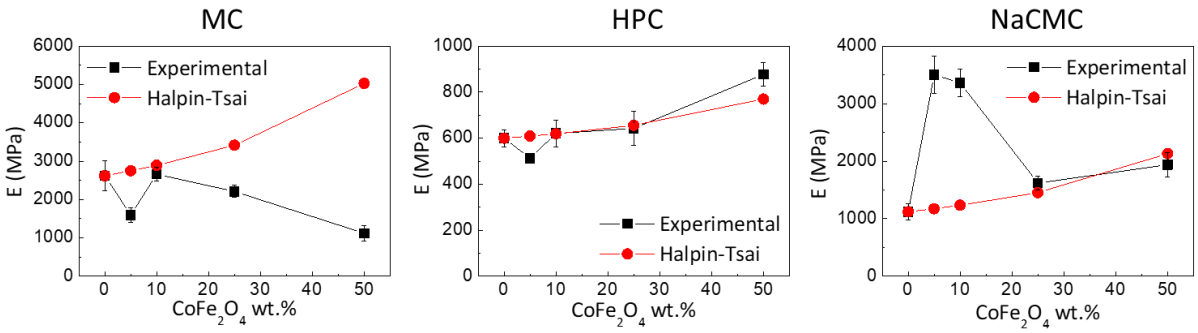

Figure 3.6. Experimental data and fitting results of MC/$CoFe_2O_4$, HPC/$CoFe_2O_4$ and NaCMC/$CoFe_2O_4$ nanocomposites determined according to the modified Halpin-Tsai model.

3.3.4. Magnetic and dielectric properties

The magnetic properties at room temperature of the fabricated materials have been investigated using a vibrating sample magnetometer (VSM) to explore the potential of such materials for magnetic applications. **Figure 3.7a-c** depicts hysteresis loops for prepared nanocomposites in the -1.8 to 1.8 T range, while their magnetisation saturation is shown in **Figure 3.7d**. The magnetisation increases with the applied magnetic field until saturation with coercivity values of 0.27, 0.23 and 0.25 MC/$CoFe_2O_4$, HPC/$CoFe_2O_4$ and NaCMC/$CoFe_2O_4$ nanocomposites, respectively, similarly to the results previously obtained for CNC/$CoFe_2O_4$ nanocomposites.[15] This coercivity arises from the ferromagnetic behaviour of $CoFe_2O_4$, which shows a blocked magnetic moment at room temperature.[40] The magnetisation hysteresis curves indicate that cobalt ferrite nanoparticles remain randomly distributed within their corresponding matrices. Magnetisation saturation (*Ms*) shows a nearly linear increase with $CoFe_2O_4$ concentration to yield maximum values of 23.3, 26.6 and 27.0 emu·g^{-1} for MC/$CoFe_2O_4$, HPC/$CoFe_2O_4$ and NaCMC/$CoFe_2O_4$ nanocomposites containing 50 wt.% of nanoparticles respectively (for comparison, the *Ms* of pure $CoFe_2O_4$ at a 1.5 T of an applied magnetic field is ~53 emu·g^{-1}).[40] Such saturation magnetisation values remain above from those previously obtained under similar external fields for NaCMC/maghemite composites (13.9 emu·g^{-1}),[11] the 8.5 emu·g^{-1} obtained for cellulose nanocrystal/$CoFe_2O_4$ composites having 20 wt.% of ferrite nanoparticles,[15] or the 10 emu·g^{-1} achieved for CMC/Fe_3O_4 with a filler concentration of 30 wt.%.[39] The linear increase of *Ms* with $CoFe_2O_4$ concentration for HPC and NaCMC-based nanocomposites suggests that nanoparticles remain finely dispersed within all the three cellulose derivatives (the lower *Ms* value for MC/$CoFe_2O_4$ nanocomposites indicates particle aggregation).[40]

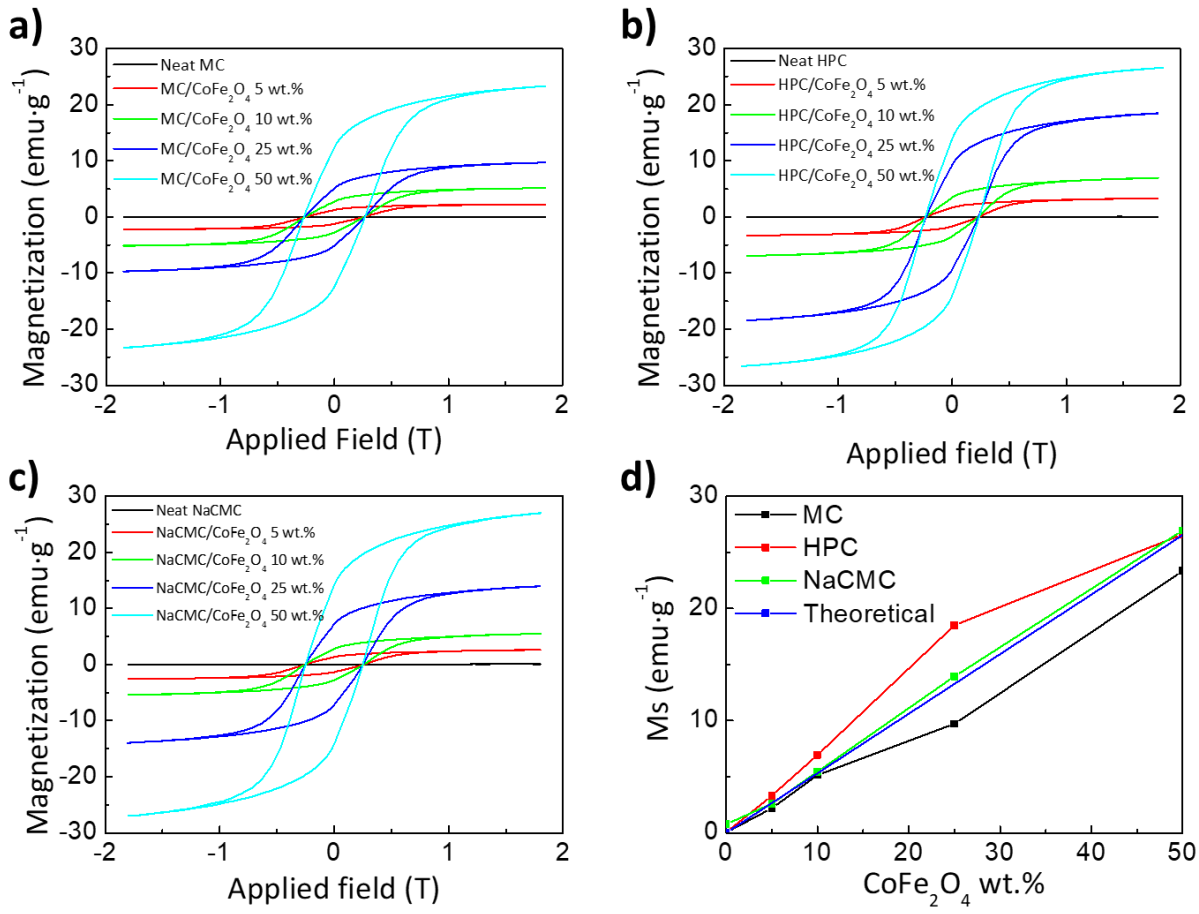

Figure 3.7. Room temperature hysteresis loops for MC/$CoFe_2O_4$ (a), HPC/$CoFe_2O_4$ (b), and NaCMC/$CoFe_2O_4$ and magnetization saturation (M_s) for all the studied compositions (b).

The dielectric behaviour at room temperature of the fabricated materials has been evaluated in order to investigate the potential of such composites for possible sensing (e.g. capacitive) applications. It should be considered that due to their inherent hygroscopic behaviour, the dielectric properties of fabricated materials markedly depend on the moisture content and also on the presence of tiny air bubbles in the films (it results in rather challenging to obtain completely solid films due to the high viscosity of the dissolutions before casting and doctor blade procedure). In this sense, the real part of the dielectric constant (ε′) and the corresponding dielectric loss values (tan δ) of neat polymers is shown in **Figure 3.8a** and **3.8b,** respectively, while the ε′ and the tan δ values measured at 1 kHz for all the studied compositions are summarised in **Figure 3.8c** and **3.8d** respectively. The ε′ continuous decrease with the frequency for all the neat polymers (MC, HPC and NaCMC) is attributed to the fact that upon frequency increase, the dipoles cannot follow the applied field and reorient in the direction of the applied field during each cycle. A particularly high

dielectric loss peak is achieved at around $5 \cdot 10^3$ Hz for NaCMC, which is explained in terms of energy dissipation via charge flow across the material. Neat MC and HPC display ε´ values of 12.6 ± 0.5 and 10.6 ± 0.8, respectively, while neat NaCMC shows an impressive ε´ of 729 ± 191. The high values of MC and HPC can be ascribed to the combined effect of the segmental motion of the main chains via the glycosidic bonds and to the presence of moisture/air bubbles in the film, which increase interfacial contributions.[41] Very interestingly, the high ε´ of neat NaCMC indicates that carboxymethylation increases the contribution of the orientational polarisation due to the dipole moment of $–CH_2OCH_2COONa$ over $–CH_2OH$ group,[42] though the main contribution of this substantial increase is associated to increased conductivity, as indicated by the high dielectric losses.

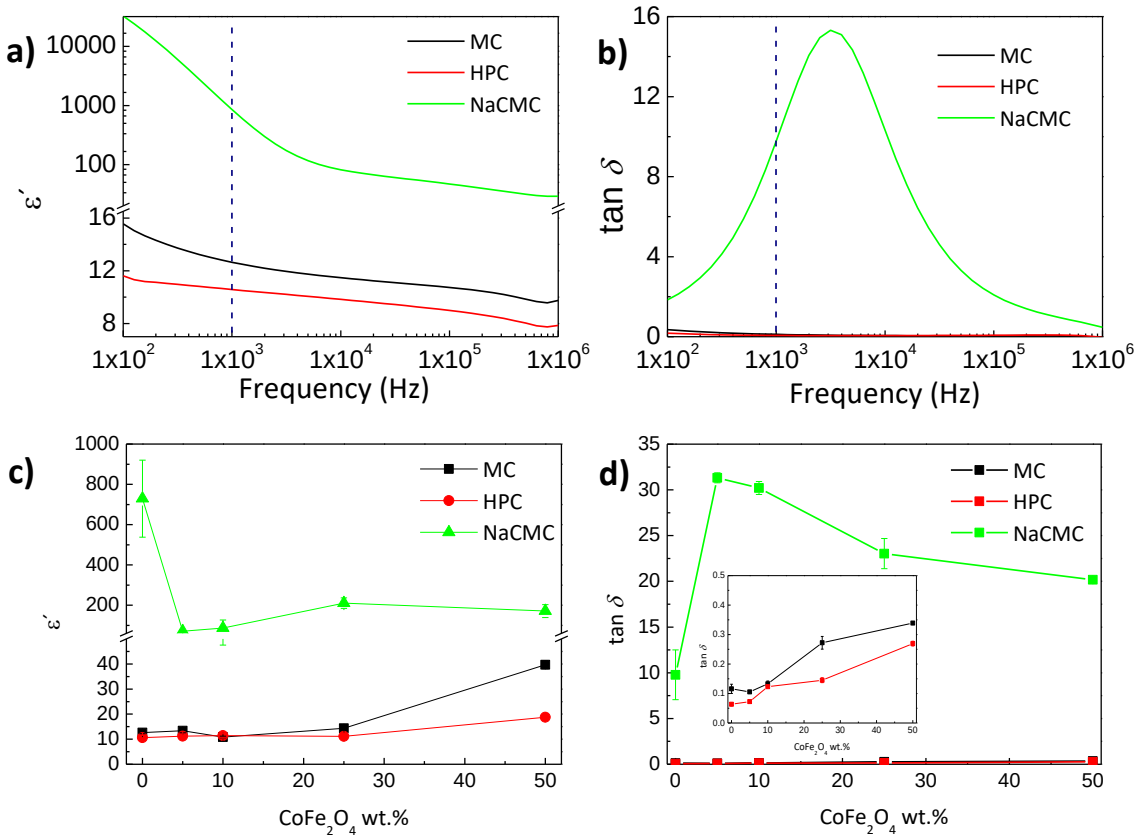

Figure 3.8. The real part of the dielectric constant (a) and the tan δ dielectric loss values (b) as a function of frequency for neat polymers; and the real part of the dielectric constant (c) and the tan δ dielectric loss values (d) measured at 1 kHz for all the studied compositions.

The inclusion of intermediate $CoFe_2O_4$ concentrations within the cellulosic matrices is observed to slightly lower the dielectric response of hybrid films while concentrations exceeding 25 wt. % tend to increase ε´ values.[43] This behaviour is ascribed to the hindering

effect provided by the rigid cobalt ferrite nanoparticles, which restrict the dipolar dynamic of the whole composite material.[44] On the contrary, the further addition of magnetic nanoparticles increases the overall ionic conductivity. It provides new interaction regions which enhance interfacial polarisation contributions (Maxwell-Wagner contributions), leading to an overall increase in the dielectric constant.[45] Dielectric losses in polymeric materials are associated with an energy transfer to phonon dissipation in the form of heat upon applying an electric field. The dielectric losses show a similar trend as that observed for ε′, keeping values below 0.3 for MC and HPC-based nanocomposite films, similarly to the results previously obtained for PVDF/$CoFe_2O_4$.[40] On the contrary, the dielectric losses are quite large for NaCMC based films, indicative of a strong conductivity.

Finally, **Figure 3.9** summarises the dependence of the electrical conductivity (σ) on cobalt ferrite concentration for all the studied composites, which is computed as:

$$\sigma = 2\pi f \cdot \varepsilon_0 \cdot \varepsilon'' \tag{3.2}$$

where f represents the frequency (Hz), ε_0 accounts for the vacuum permittivity (8.854x10^{-12} F·m^{-1}), and ε′′ ($\varepsilon'' = \varepsilon' \cdot tan\,\delta$) is the imaginary part of the permittivity. MC and HPC are basically insulating materials with σ values of $8.15 \cdot 10^{-10}$ and $3.73 \cdot 10^{-11}$ S·cm^{-1}, while NaCMC shows a conductivity of $4.43 \cdot 10^{-6}$ S·cm^{-1}. A general conductivity increase is observed upon $CoFe_2O_4$ addition due to increased interfacial effects.[46]

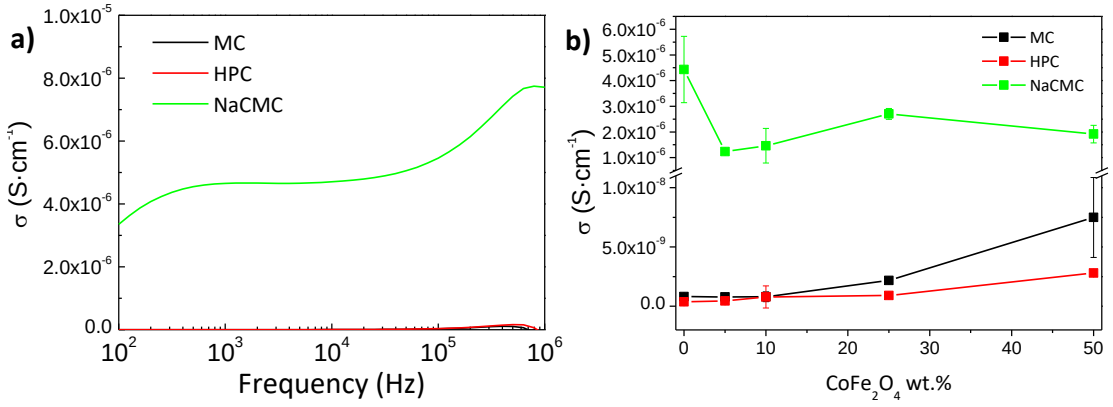

Figure 3.9. Electrical conductivity of neat MC, HPC and NaCMC films as a function of frequency (a) and obtained electrical conductivity values at 1 kHz for MC/$CoFe_2O_4$, HPC/$CoFe_2O_4$ and NaCMC/$CoFe_2O_4$ nanocomposite films as a function of cobalt ferrite nanoparticles (b).

After evaluating the suitability of these composite materials for magnetoactive flexible electronic devices, their printability was studied by screen-printing. Thus, from now on, the formulated mixtures are referred to as inks.

3.3.5. Ink rheology

Regarding the use of studied composites as ink for screen-printing, the rheological properties of the prepared formulations at a concentration of 50 wt.% were firstly evaluated at different applied shear stresses. As observed in **Figure 3.10**, all three nanocomposite inks with different cellulose-based matrices showed shear-thinning behaviour, which is advantageous for inks and paints to be applied by means of printing technologies.[47] Interestingly, the obtained shear-thinning character is also preferred for other applications which involve injectable dispersions using syringes, opening new opportunities in the biomedical field.[48] The formulation based on MC displayed the lowest viscosity values (lower than 1000 mPa·s over the whole measured shear-rate range), being below the recommended limit for screen-printing (1.000-10.000 mPa·s).[4,49] The viscosities of the formulations based on HPC and NaCMC exceeded 1.000 mPa·s, which are values in accordance with the screen-printing process. At lower shear rates, the NaCMC formulations showed the highest viscosity values of all three formulations.

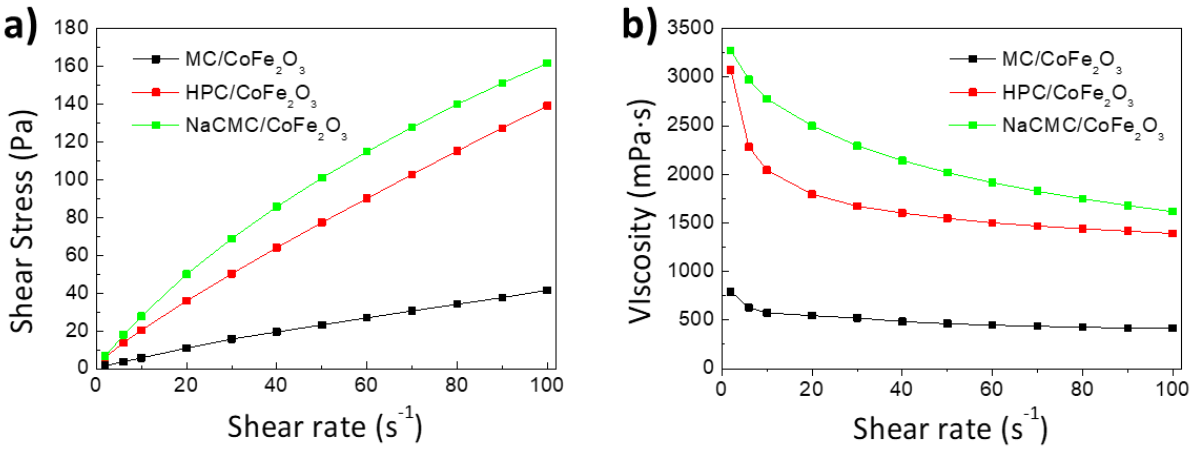

Figure 3.10. Shear stress (a) and viscosity (b) as a function of applied shear rate for the prepared nanocomposite inks (all of them having 50 wt.% of cobalt ferrite nanoparticles).

Apart from the relative concentration of each cellulose derivative, considering the chemical nature of the cellulose derivative in each formulation, the differences in viscosity characteristics may be related to the molecular weight, length and polarity of each derivative's substitutes, which contribute to the increasing interaction between the polymer chains [49]. Another factor, which might influence the viscosity of the prepared inks, is the degree of dispersion of the cobalt ferrite nanoparticles. The presence of larger and not well-

dispersed aggregates may also contribute to increased viscosity and, at the same time, lead to a less homogenous distribution of nanoparticles. The measured shear-stress/shear-rate curves were further evaluated through the Ostwald-de Waele power law model (Equation 3.3):[50]

$$\tau = c \cdot D^p \tag{3.3}$$

where τ stands for shear stress, D for shear rate, c for a "flow coefficient", and p for the "power-law index". These values were used to quantify the pseudoplasticity of each prepared formulation (**Table 3.2**) [51]. It is observed that both HPC/$CoFe_2O_4$ and NaCMC/$CoFe_2O_4$ show lower p values and higher c values than MC/$CoFe_2O_4$, resulting in higher pseudoplasticity and making them more suitable for screen-printing in comparison with MC-based ink. HPC and NaCMC possess longer substituents (hydroxypropyl group in HPC) or higher polarity groups (Na+ ion and carboxymethyl group in NaCMC), suggesting higher intermolecular interaction than in the case of the MC-based ink.

Table 3.2. *c* and *p* values for all three cellulose derivatives extracted according to Ostwald-de Waele's model.

Cellulose derivative	*c* ($Pa \cdot s^p$)	*p*
MC	0.86	0.841
HPC	3.31	0.813
NaCMC	4.09	0.807

3.3.6. Printing process

The prepared inks were screen printed onto the three microporous cellulosic substrates using two screen mesh densities. First, a visual (naked-eye) inspection was performed to determine whether or not obtained samples were printed satisfactorily. **Figure 3.11** shows optical photographs of the three printed patterns with both screen meshes using MC/$CoFe_2O_4$, HPC/$CoFe_2O_4$, and NaCMC/$CoFe_2O_4$ ink and Substrate 2, with medium pore size of the three substrates used. It can be observed that the obtained patterns using the so-called Screen 2 are more uniform than the ones achieved with Screen 1, which displays lines with gaps for the three prepared inks, suggesting the presence of areas that have not been completely covered during the printing process. These gaps of full ink coverage of printed magnetic ink, which are even more noticeable when the smallest pattern is used, arising from the smaller size of the opened dots of Screen 1 mesh retaining more ink and preventing it from going through the mesh (dot size of 28.55 μm in comparison with 53.33 for the Screen 2).

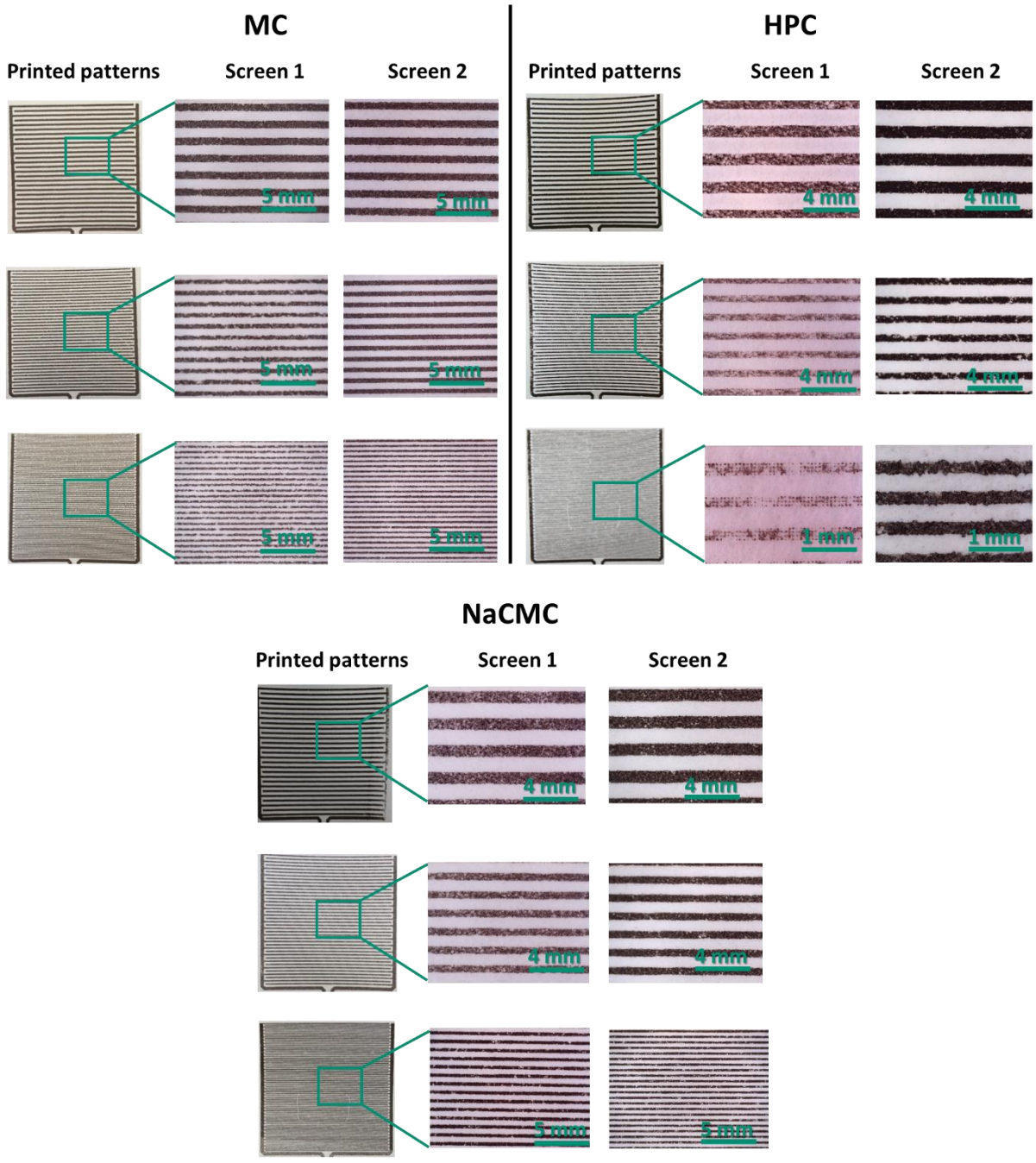

Figure 3.11. Optical photographs showing the macroscopic appearance of 3 printed patterns with Screen 1 and 2 using MC/$CoFe_2O_4$, HPC/$CoFe_2O_4$, NaCMC/$CoFe_2O_4$ inks onto Substrate 2.

Table 3.3 shows the measured width of the printed lines and photolytic patterns (based on the results from ImageJ software). Equation 3.4 was used to compare the deviation of the prints achieved with MC/$CoFe_2O_4$, HPC/$CoFe_2O_4$ and NaCMC/$CoFe_2O_4$ inks from the original pattern, expressed in parentheses.

$$\%\ Deviation = \frac{photolite\ width - printed\ line\ width}{photolite\ width} \cdot 100 \qquad (3.4)$$

As can be expected, the deviation of the dimension of the printed line from the photolith film is lower for Screen 1 than Screen 2, comprising 1-6 % and 1-9 %, respectively. The width obtained with Screen 2 is equal to or higher than the original pattern, while the width obtained with Screen 1 remains larger (or wider) than the original one, except the achieved with HPC/$CoFe_2O_4$ that is smaller for all the three printed patterns. The bigger dots of the Screen 2 mesh allow an easier diffusion of the ink through the screen, spreading the ink breadthways within the porous substrates. Interestingly, the deviation of the printing patterns remains below 10% for all the ink formulations and used screens.

Table 3.3. Measured photolith film and printed line widths in Substrate 2 for all the three used patterns using MC/$CoFe_2O_4$, HPC/$CoFe_2O_4$ and NaCMC/$CoFe_2O_4$ ink formulations. Deviations between printing and photolith film are expressed in parentheses. Statistics are based on ten measurements.

		MC		**HPC**		**NaCMC**	
Line width	***Photolith***	*Screen 1*	*Screen 2*	*Screen 1*	*Screen 2*	*Screen 1*	*Screen 2*
Small (µm)	195 ± 7	206 ± 19 (6%)	206 ± 26 (6%)	183 ± 10 (5%)	211 ± 19 (8%)	202 ± 9 (4%)	212 ± 9 (9%)
Medium(µm)	397 ± 4	400 ± 11 (1%)	402 ± 28 (1%)	364 ± 15 (4%)	397 ± 15 (0%)	418 ± 21 (5%)	422 ± 9 (6%)
Large (µm)	644 ± 8	642 ± 13 (2%)	672 ± 8 (4%)	627 ± 9 (1%)	658 ± 12 (2%)	619 ± 21 (4%)	654 ± 15 (2%)

The surface morphology of the printed lines has been further assessed by SEM to get further information on the cobalt ferrite nanoparticle dispersion onto microporous substrates. **Figure 3.11** reveals SEM images of prints of the prepared inks onto three cellulosic substrates using both screen meshes. Clearly, MC, HPC and NaCMC-based nanocomposite inks images show higher $CoFe_2O_4$ concentration for Screen 2 than Screen 1 due to the larger mesh size. This is accompanied by the presence of larger $CoFe_2O_4$ aggregates for patterns obtained using Screen 2. Attending to the different substrates, the inks based on HPC and NaCMC cover widely the cellulosic microfibers of the substrates in the following increasing order: Substrate 1 < Substrate 2 < Substrate 3. As Substrate 3 presents a lower porosity than the other papers, the ink presents a higher resistance to flow across the substrate. At the same time, when MC-based inks are used, a lower number of magnetic nanoparticles can be observed on the top of the fibres.

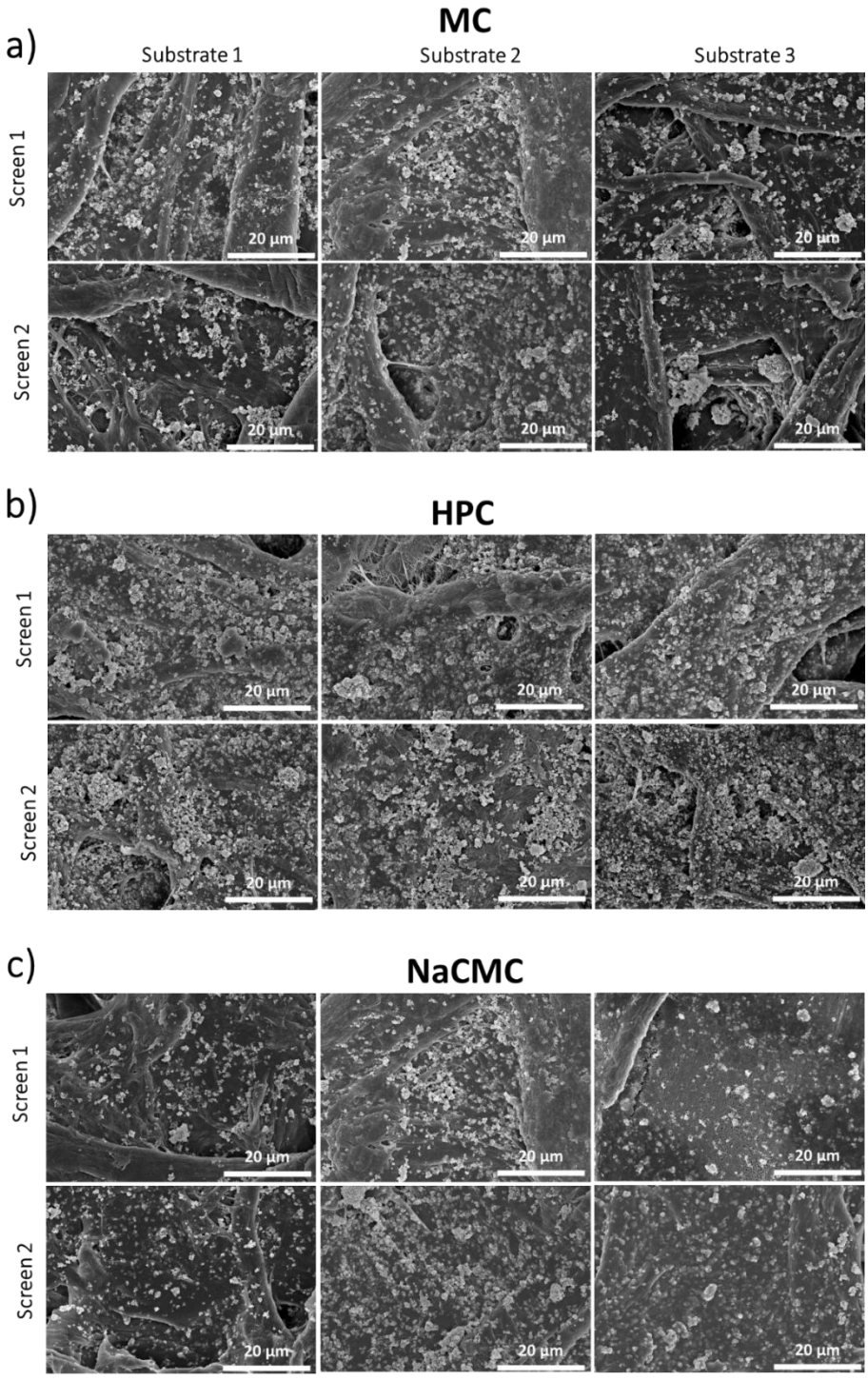

Fig. 3.11. SEM images showing the surface morphology of the screen-printed MC/$CoFe_2O_4$ (a), HPC/$CoFe_2O_4$ (b), and NaCMC/$CoFe_2O_4$ (c) inks onto three different cellulosic substrates for two screen meshes.

Despite its qualitative character, elemental mapping is a very useful technique for further information on the spatial distribution of inorganic nanoparticles onto cellulosic substrates [52]. Accordingly, **Figure 3.12** and **Figure 3.13** show the spatial distribution of screen-printed

patterns using $CoFe_2O_4$–based inks for different processing conditions. In such elemental maps, the cellulosic substrate and the cellulosic derivative were used to prepare the ink to appear as a black background. At the same time, the signal arising from cobalt ferrite nanoparticles is shown in two separate images corresponding to Co and Fe. Overall, images reveal that cobalt ferrite nanoparticles form lines where they remain homogeneously distributed. Coloured dots outside the lines indicate that some nanoparticles manage to cross the screen mesh.

Elemental mapping shows homogenous yellow/green spots displaying higher concentrations, as seen in Fe images, whereas blue colour means lower concentrations, corresponding to the images of Co lines. Based on this colour system, it is observed that the Co:Fe ratio remains approximately at 1:2, which matches the nature of $CoFe_2O_4$. As shown in **Figure 3.12a**, the use of Screen 2 yields notably wider printed patterns with the presence of larger aggregates observed as dispersed yellow regions. This may be due to the increased dot size of Screen 2 compared to Screen 1 (53.33 *vs* 30 µm dot size), allowing the transfer of large agglomerates from the ink formulation into the paper substrate through the mesh. SEM images also support this in **Figure 3.11**, where notably larger aggregates are found when using the larger dot size Screen 2. Regarding the effect of the substrate, **Figure 3.12b**, it can be noticed that cobalt ferrite nanoparticle distribution remains basically unchanged, with a slightly higher quantity of NPs on Substrate 3 than on Substrates 1 and 2.

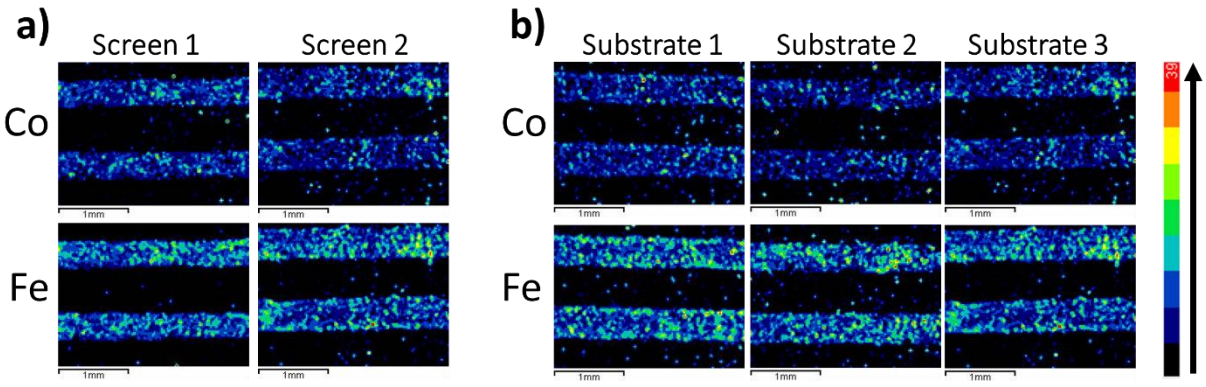

Figure 3.12. Elemental mapping for screen-printed patterns using HPC/$CoFe_2O_4$ inks for a) two different screen meshes (Substrate 3 was used for all printed patterns); b) three different substrates (Screen 2 was used for all printed patterns). The first and second rows correspond to Co and Fe signals, respectively. Scale bars indicate 1 mm.

Figure 3.13 shows the effect of different cellulosic derivatives on the spatial distribution of Co and Fe onto cellulosic substrates (the remaining processing parameters were fixed on: screen 2 and paper 3). It is observed that HPC-based ink presents the largest amount of $CoFe_2O_4$ nanoparticles, whereas MC/$CoFe_2O_4$ and NaCMC/$CoFe_2O_4$ inks display a very similar concentration of Fe and higher of Co. The difference in Co element images may arise from the fact that when MC and NaCMC-based inks are used, nanoparticles can diffuse deeper into the porous structure of the substrate, not allowing the generation of the pixels corresponding to Co and Fe as the penetration depth provided by EDX when analysing biomolecules is generally limited to distances below 1.5 μm [53].

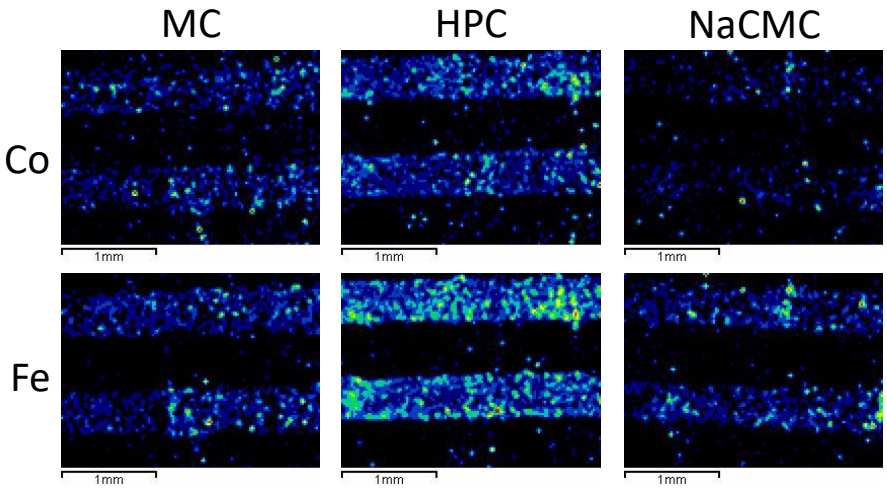

Figure 3.13. Elemental mapping for screen-printed patterns using MC/$CoFe_2O_4$ (left column), HPC/$CoFe_2O_4$ (middle column) and NaCMC/$CoFe_2O_4$ (right column) inks. The first and second rows correspond to Co and Fe signals, respectively. Screen 2 and Substrate 3 were used.

Similarly to previously reported works where water-soluble cellulose derivatives stabilise both organic (cellulose nanocrystals) and inorganic (silver) nanoparticles [54,55], the presence of HPC, MC and NaCMC water-soluble cellulose derivatives serves to efficiently stabilise $CoFe_2O_4$-based magnetic inks, allowing the fabrication of pre-designed patterns with well-dispersed nanoparticles.

3.3.7 Magnetic properties of the printed patterns

The magnetic properties of the printed materials have been quantitatively evaluated using a VSM. **Figure 3.14** displays the magnetic hysteresis loops as a function of the applied magnetic field of the different printed patterns with the same size of 1.17 cm^2 of the printed

area onto the three cellulosic substrates for MC/$CoFe_2O_4$, HPC/$CoFe_2O_4$ and NaCMC/$CoFe_2O_4$ inks. Before the measurements, the printed area was bent into 0.5 x 0.5 cm pieces and tightly attached to the VSM holder with Teflon tape. Measurements were performed by applying a magnetic field from -1.8 to 1.8 T. All three systems present coercivity values of nearly 0.22, similarly to the composite films' values previously shown. The *S* shape of magnetisation hysteresis curves suggests that, despite the squeegee's applied shear stress upon screen-printing, $CoFe_2O_4$ nanoparticles remain randomly distributed on the surface of the cellulosic substrates. Interestingly, HPC/$CoFe_2O_4$ ink shows the largest magnetisation saturation (M_s), reaching a maximum of 0.024 emu (0.021emu·cm^{-2}) when Substrate 1 is used as a substrate, while MC/$CoFe_2O_4$ and NaCMC/$CoFe_2O_4$ inks, present M_s of 0.009 emu each one for the same experimental conditions. The higher M_s value of HPC matrix ink compared with NaCMC ink was obtained since HPC-based ink was fabricated with a higher solid material/water ratio, 10 wt/vol. % vs 2.4 wt/vol. % for NaCMC. Considering the same amount of ink that is transferred to the substrate (both show similar shear stress behaviour), the amount of dry HPC/$CoFe_2O_4$ material will be larger than NaCMC/$CoFe_2O_4$.

On the other hand, there is no direct relationship between the similar M_s values for MC and NaCMC inks. The low viscosity of MC ink favours screen mesh crossing and penetration into the pores, but after drying, both present the same amount of dry material transferred. In any case, it should be taken into account that due to the low amount of magnetic material deposited onto the substrate in comparison with the substrate itself, these values remain well below the M_s obtained for nanocomposite films.

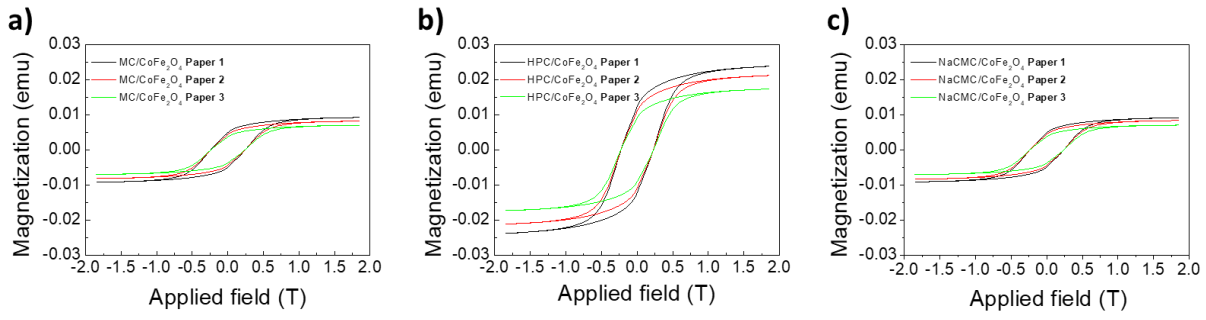

Figure 3.14. Magnetic moment as a function of applied magnetic field of the printed patterns onto 3 cellulosic substrates for MC/$CoFe_2O_4$ (a), HPC/$CoFe_2O_4$ (b) and NaCMC/$CoFe_2O_4$ (c) inks.

To compare obtained VSM results, however, one should consider that the total amount of deposited magnetic ink onto microporous cellulosic substrates depends on the pore-morphology of the substrates; i.e., the larger and more numerous the pores, the larger amount of ink should penetrate the substrate. Based on the maximum magnetisation that the solid nanocomposite films (MC/$CoFe_2O_4$, HPC/$CoFe_2O_4$ and NaCMC/$CoFe_2O_4$) could reach, we have extrapolated the amount of deposited material as:

$$Material\ amount = \frac{[emu]\ of\ printed\ material}{\left[\frac{emu}{g}\right] raw\ material\ film} \tag{3.5}$$

$$Normalized = \frac{material\ amount}{\%\left(\frac{wt.}{V}\right)} \tag{3.6}$$

Accordingly, **Figures 3.15a** and **3.15b** summarise the deposited material weight and normalised material weight as a function of substrate pore size for all the three inks. It is observed that the amount of ink deposited onto the substrates increases with pore size for all the formulations. Additionally, the deviation from the linearity suggests that viscous inks are not well absorbed by the substrates with lower porosity. These results estimate the amount of ink transferred to the paper substrates during the printing process.

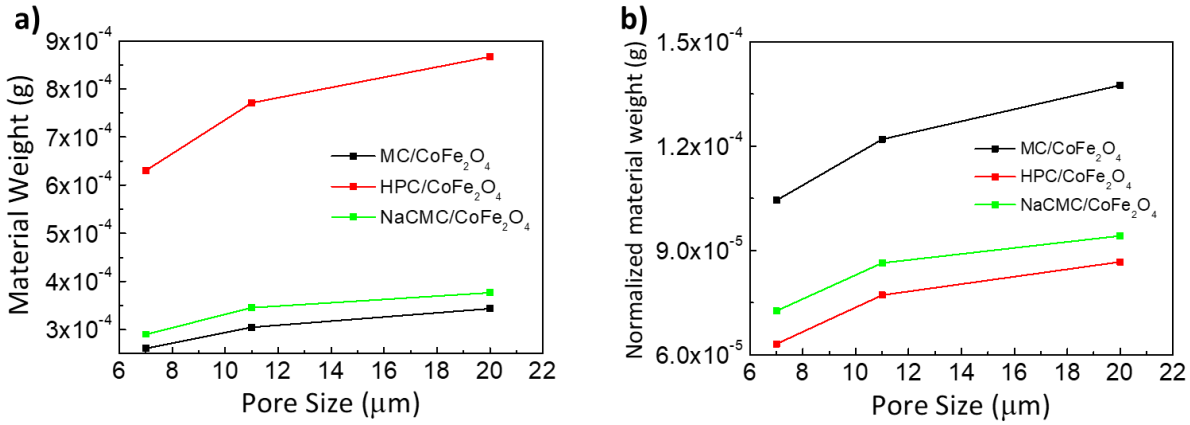

Fig. 3.15. Deposited material weight (a) and normalized material weight (b) as a function of substrate pore size for MC/$CoFe_2O_4$, HPC/$CoFe_2O_4$ and NaCMC/$CoFe_2O_4$ inks.

SEM and elemental mapping results show that the highest amounts of material are obtained for HPC/$CoFe_2O_4$ prints, with values from 6.31 $x10^{-4}$ g to 8.67 $x10^{-4}$ g. When MC/$CoFe_2O_4$ and NaCMC/$CoFe_2O_4$ inks are used, despite their different viscosities, the amount of transferred material remains rather similar (3.44$x10^{-4}$ g and 3.77 $x10^{-4}$ g, respectively). Such differences can be related to the concentration of water in the fabricated inks, which has been optimised to be 2.5, 10, and 4 wt/vol. % for MC, HPC, and NaCMC,

respectively. It should be noticed that when the amount of water in the ink increases (i.e. inks with lower wt/vol. % concentration), a lower amount of cellulosic derivative/magnetic material will be deposited on the microporous substrates upon drying. In this scenario, and in order to shed more light on the amount of transferred material by each ink, the obtained mass was normalised following Equation 3.6. The obtained results are displayed in **Figure 3.15b**, suggesting that lower viscosity MC can host a relatively larger number of magnetic nanoparticles than higher-viscosity HPC and NaCMC.

Given the inherent advantages of screen-printing technology, cellulose-based inks and substrates, and the large amount of magnetically active cobalt ferrite nanoparticles that could be homogeneously embedded into pre-designed shapes, makes the approach here reported promising for the development of sustainable magnetic components [56].

3.4. Conclusions

This chapter has introduced the use of methyl cellulose, hydroxypropyl cellulose and sodium carboxymethyl cellulose as potential matrices to develop multifunctional materials based on renewable resources. Cobalt ferrite nanoparticles with concentrations up to 50 wt.% are homogeneously incorporated within the three cellulose derivatives through simple mechanical stirring followed by doctor blade casting and screen-printing technique. Morphological observations of the prepared crack-free films reveal that nanoparticles remain homogeneously distributed within the cellulosic matrices, both on the surface and through the whole thickness of the films. Overall, mechanical tests reveal an increased Young's modulus for intermediate concentrations, while large amounts of $CoFe_2O_4$ yield aggregation issues, which decrease the effective filler-matrix interactions and create weak points in the material. However, films with loadings as high as 50 wt. % keep a substantial level of flexibility with elongation at break exceeding 5%, which is a crucial property when accounting for flexible electronics applications. A maximum magnetization value of 23.3, 26.6 and 27.0 $emu \cdot g^{-1}$ is obtained for MC/$CoFe_2O_4$, HPC/$CoFe_2O_4$ and NaCMC/$CoFe_2O_4$ nanocomposites containing 50 wt. % cobalt ferrites, respectively. The dielectric constant at room temperature remains in the range of 10-40 for MC and HPC-based nanocomposites, while it dramatically increases for NaCMC films. With respect to the screen-printing approach, it is demonstrated that the shear-thinning behaviour of the inks enables obtaining well-defined patterns with homogeneously distributed nanoparticles. Additionally, the large amount of cobalt ferrite

nanoparticles allows fabricating patterns onto microporous cellulosic substrates, showing enough magnetisation saturation to be used in magnetic sensor applications.

Finally, the homogeneous character of the hybrid films here fabricated together with their magnetically and dielectrically active character highlight the potential of these materials to develop multifunctional materials based on renewable resources. Prepared hybrids match traditional magnetoactive composites' properties but avoid using petroleum-derived matrices and toxic solvents.

3.5. References

1 E. Lizundia, U. Goikuria, J. L. Vilas, F. Cristofaro, G. Bruni, E. Fortunati, I. Armentano, L. Visai and L. Torre, Metal nanoparticles embedded in cellulose nanocrystal based films: material properties and post-use analysis, *Biomacromolecules*, 2018, acs.biomac.8b00243.

2 A. Dufresne, Nanocellulose: A new ageless bionanomaterial, *Mater. Today*, 2013, **16**, 220–227.

3 D. Klemm, B. Heublein, H.-P. Fink and A. Bohn, Cellulose: Fascinating Biopolymer and Sustainable Raw Material, *Angew. Chemie Int. Ed.*, 2005, **44**, 3358–3393.

4 J. Oliveira, V. Correia, H. Castro, P. Martins and S. Lanceros-Mendez, Polymer-based smart materials by printing technologies: Improving application and integration, *Addit. Manuf.*, 2018, **21**, 269–283.

5 I. G. Donhowe and O. Fennema, The Effects of Plasticisers on Crystallinity, Permeability, and Mechanical Properties of Methylcellulose Films, *J. Food Process. Preserv.*, 1993, **17**, 247–257.

6 R. A. Lewis, *Hawley's Condensed Chemical Dictionary*, Sr. John Wiley & Sons, 1997.

7 G. Joshi, V. Rana, S. Naithani, V. K. Varshney, A. Sharma and J. S. Rawat, Chemical modification of waste paper: An optimisation towards hydroxypropyl cellulose synthesis, *Carbohydr. Polym.*, 2019, **223**, 115082.

8 M. S. Yeasmin and M. I. H. Mondal, Synthesis of highly substituted carboxymethyl cellulose depending on cellulose particle size, *Int. J. Biol. Macromol.*, 2015, **80**, 725–731.

9 E. Grządka and S. Chibowski, Adsorption and elektrokinetic properties of the system: carboxymethylcellulose/manganese oxide/surfactant, *Cellulose*, 2012, **19**, 23–36.

10 S. Paunonen, Strength and Barrier Enhancements of Cellophane and Cellulose Derivative Films: A Review, *Bioresour. Vol 8, No 2*.

11 J. F. Luna-Martínez, E. Reyes-Melo, V. González-González, C. Guerrero-Salazar, A. Torres-Castro and S. Sepúlveda-Guzmán, Synthesis and characterization of a magnetic hybrid material consisting of iron oxide in a carboxymethyl cellulose matrix, *J. Appl. Polym. Sci.*, 2013, **127**, 2325–2331.

12 L. Ma, L. Wang, L. Wu, D. Zhuo, Z. Weng and R. Ren, Cellulosic nanocomposite membranes from hydroxypropyl cellulose reinforced by cellulose nanocrystals, *Cellulose*, 2014, **21**, 4443–4454.

13 J. Gao, G. Haidar, X. Lu and Z. Hu, Self-Association of Hydroxypropylcellulose in Water, *Macromolecules*, 2001, **34**, 2242–2247.

14 A. C. Lima, N. Pereira, R. Policia, C. Ribeiro, V. Correia, S. Lanceros-Mendez and P. Martins, All-printed multilayer materials with improved magnetoelectric response, *J. Mater. Chem. C*, 2019, **7**, 5394–5400.

15 E. Lizundia, A. Maceiras, J. L. Vilas, P. Martins and S. Lanceros-Mendez, Magnetic cellulose nanocrystal nanocomposites for the development of green functional materials, *Carbohydr. Polym.*, 2017, **175**, 425–432.

16 S. Tunç, O. Duman and T. G. Polat, Effects of montmorillonite on properties of methyl

cellulose/carvacrol based active antimicrobial nanocomposites, *Carbohydr. Polym.*, 2016, **150**, 259–268.

17 A. Abdulkhani, M. Daliri Sousefi, A. Ashori and G. Ebrahimi, Preparation and characterisation of sodium carboxymethyl cellulose/silk fibroin/graphene oxide nanocomposite films, *Polym. Test.*, 2016, **52**, 218–224.

18 J. F. Luna-Martínez, D. B. Hernández-Uresti, M. E. Reyes-Melo, C. A. Guerrero-Salazar, V. A. González-González and S. Sepúlveda-Guzmán, Synthesis and optical characterization of ZnS–sodium carboxymethyl cellulose nanocomposite films, *Carbohydr. Polym.*, 2011, **84**, 566–570.

19 M. M. Ibrahim, W. K. El-Zawawy and M. A. Nassar, Synthesis and characterisation of polyvinyl alcohol/nanospherical cellulose particle films, *Carbohydr. Polym.*, 2010, **79**, 694–699.

20 M. A. Ashraf, W. Peng, Y. Zare and K. Y. Rhee, Effects of Size and Aggregation/Agglomeration of Nanoparticles on the Interfacial/Interphase Properties and Tensile Strength of Polymer Nanocomposites, *Nanoscale Res. Lett.*, 2018, **13**, 214.

21 J. Silva, S. Lanceros-Mendez and R. Simoes, Effect of cylindrical filler aggregation on the electrical conductivity of composites, *Phys. Lett. A*, 2014, **378**, 2985–2988.

22 G.-X. Qiu, F. Raue and G. W. Ehrenstein, Mechanical properties and morphologies of PP/mPE/filler composites, *J. Appl. Polym. Sci.*, 2002, **83**, 3029–3035.

23 A. International, *ASTM D1746-15, Standard Test Method for Transparency of Plastic Sheeting*, 2015.

24 A. Petritz, A. Wolfberger, A. Fian, T. Griesser, M. Irimia-Vladu and B. Stadlober, Cellulose-Derivative-Based Gate Dielectric for High-Performance Organic Complementary Inverters, *Adv. Mater.*, 2015, **27**, 7645–7656.

25 K. K. Sadasivuni, A. Kafy, L. Zhai, H.-U. Ko, S. Mun and J. Kim, Transparent and Flexible Cellulose Nanocrystal/Reduced Graphene Oxide Film for Proximity Sensing, *Small*, 2015, **11**, 994–1002.

26 E. Lizundia, M. Delgado-Aguilar, P. Mutjé, E. Fernandez, B. Robles-Hernandez, M. Rosario de la Fuente, J. L. Vilas and L. M. Leon, Cu-coated cellulose nanopaper for green and low-cost electronics, *Cellulose*, 2016, 1–14.

27 C. Eyholzer, F. Lopez-Suevos, P. Tingaut, T. Zimmermann and K. Oksman, Reinforcing effect of carboxymethylated nanofibrillated cellulose powder on hydroxypropyl cellulose, *Cellulose*, 2010, **17**, 793–802.

28 M. Yadav, K. Y. Rhee, I. H. Jung and S. J. Park, Eco-friendly synthesis, characterisation and properties of a sodium carboxymethyl cellulose/graphene oxide nanocomposite film, *Cellulose*, 2013, **20**, 687–698.

29 A. Liu and L. A. Berglund, Fire-retardant and ductile clay nanopaper biocomposites based on montmorrilonite in matrix of cellulose nanofibers and carboxymethyl cellulose, *Eur. Polym. J.*, 2013, **49**, 940–949.

30 S. Rimdusit, S. Jingjid, S. Damrongsakkul, S. Tiptipakorn and T. Takeichi, Biodegradability and property characterisations of Methyl Cellulose: Effect of nanocompositing and chemical crosslinking, *Carbohydr. Polym.*, 2008, **72**, 444–455.

31 E. Lizundia, I. Serna, E. Axpe and J. L. Vilas, Free-volume effects on the thermomechanical performance of epoxy–SiO2 nanocomposites, *J. Appl. Polym. Sci.*, 2017, **134**, 45216.

32 K. Suppiah, P. L. Teh, S. Husseinsyah and R. Rahman, Properties and characterisation of carboxymethyl cellulose/halloysite nanotube bio-nanocomposite films: Effect of sodium dodecyl sulfate, *Polym. Bull.*, 2019, **76**, 365–386.

33 S. Ebrahimzadeh, B. Ghanbarzadeh and H. Hamishehkar, Physical properties of carboxymethyl cellulose based nano-biocomposites with Graphene nano-platelets, *Int. J. Biol. Macromol.*, 2016, **84**, 16–23.

34 J. C. H. Affdl and J. L. Kardos, *Polym. Eng. Sci.*, 1976, 16, 344–352.

35 C. Y. Hui and D. Shia, Simple formulae for the effective moduli of unidirectional aligned composites, *Polym. Eng. Sci.*, 1998, **38**, 774–782.

36 M. R. Du, H. W. Jing, W. H. Duan, G. S. Han and S. J. Chen, Methylcellulose stabilised multi-walled carbon nanotubes dispersion for sustainable cement composites, *Constr. Build. Mater.*, 2017, **146**, 76–85.

37 L. M. L. on Erlantz Lizundia, Leyre P erez- Alvarez, M ıriam S aenz-P erez, David Patrocinio, Jos e Luis

Vilas, Physical aging and mechanical performance of Poly (L-lactide)/ZnO nanocomposites, *J. Appl. Polym. Sci.*, 2016, **133**, 43619.

38 Lizundia, E., Fortunati, E., Dominici, F., Vilas, L. J., Le´on, M. L., Armentano, I., Torre, L., K. and and J., PLLA-grafted cellulose nanocrystals: role of the CNC content and grafting on the PLA bionanocomposite film properties, *Carbohydr. Polym.*, , DOI:10.1016/j.carbpol.2016.01.041.

39 B. Zengin Kurt, F. Uckaya and Z. Durmus, Chitosan and carboxymethyl cellulose based magnetic nanocomposites for application of peroxidase purification, *Int. J. Biol. Macromol.*, 2017, **96**, 149–160.

40 P. Martins, C. M. Costa, G. Botelho, S. Lanceros-Mendez, J. M. Barandiaran and J. Gutierrez, Dielectric and magnetic properties of ferrite/poly(vinylidene fluoride) nanocomposites, *Mater. Chem. Phys.*, 2012, **131**, 698–705.

41 J. T.-G. A. Rachocki , E. Markiewicz, Dielectric relaxation in cellulose and its derivatives, *Acta Phys. Pol. A*, 2005, **108**, 137–145.

42 R. I. Nessim, M. G. Botros, G. R. Saad and M. M. Shalaby, Frequency dependence of the complex dielectric constant of sodium carboxymethyl cellulose, *Die Angew. Makromol. Chemie*, 1993, **204**, 51–61.

43 Y. Li, X. Huang, Z. Hu, P. Jiang, S. Li and T. Tanaka, Large Dielectric Constant and High Thermal Conductivity in Poly(vinylidene fluoride)/Barium Titanate/Silicon Carbide Three-Phase Nanocomposites, *ACS Appl. Mater. Interfaces*, 2011, **3**, 4396–4403.

44 R. Kochetov, T. Andritsch, P. H. F. Morshuis and J. J. Smit, Anomalous behaviour of the dielectric spectroscopy response of nanocomposites, *IEEE Trans. Dielectr. Electr. Insul.*, 2012, **19**, 107–117.

45 P. Martins, D. Silva, M. P. Silva and S. Lanceros-Mendez, Improved magnetodielectric coefficient on polymer based composites through enhanced indirect magnetoelectric coupling, *Appl. Phys. Lett.*, 2016, **109**, 112905.

46 M. H. A.-E. Salam, S. El-Gamal, D. M. A. El-Maqsoud and M. Mohsen, Correlation of electrical and swelling properties with nano free-volume structure of conductive silicone rubber composites, *Polym. Compos.*, 2013, **34**, 2105–2115.

47 T. G. Metzger, *The Rheology Handbook: For Users of Rotational and Oscillatory Rheometers*, 2md Editio., 2002.

48 L. Dai, T. Cheng, Y. Wang, H. Lu, S. Nie, H. He, C. Duan and Y. Ni, Injectable all-polysaccharide self-assembling hydrogel: a promising scaffold for localised therapeutic proteins, *Cellulose*, 2019, **26**, 6891–6901.

49 P. L. Nasatto, F. Pignon, J. L. M. Silveira, M. E. R. Duarte, M. D. Noseda and M. Rinaudo, Methylcellulose, a Cellulose Derivative with Original Physical Properties and Extended Applications, *Polymers (Basel).*, 2015, **7**, 777–803.

50 L. Medina-Torres, E. Brito-De La Fuente, B. Torrestiana-Sanchez and R. Katthain, Rheological properties of the mucilage gum (Opuntia ficus indica), *Food Hydrocoll.*, 2000, **14**, 417–424.

51 J. M. McKelvey, *Polymer Processing*, John Wiley & Sons Inc, 1962.

52 W. C. E. Lizundia, M. Jimenez, C. Altorfer, M. Niederberger, Electroless plating of platinum nanoparticles onto mesoporous cellulose films for catalytically active free-standing materials, *Cellulose*.

53 K. SCOTT and N. W. M. RITCHIE, Analysis of 3D elemental mapping artefacts in biological specimens using Monte Carlo simulation, *J. Microsc.*, 2009, **233**, 331–339.

54 Z. Hu, T. Patten, R. Pelton and E. D. Cranston, Synergistic Stabilisation of Emulsions and Emulsion Gels with Water-Soluble Polymers and Cellulose Nanocrystals, *ACS Sustain. Chem. Eng.*, 2015, **3**, 1023–1031.

55 A. T. Qureshi, W. T. Monroe, M. J. Lopez, M. E. Janes, V. Dasa, S. Park, A. Amirsadeghi and D. J. Hayes, Biocompatible/bioabsorbable silver nanocomposite coatings, *J. Appl. Polym. Sci.*, 2011, **120**, 3042–3053.

56 Y. Yan, L. D. Geng, Y. Tan, J. Ma, L. Zhang, M. Sanghadasa, K. Ngo, A. W. Ghosh, Y. U. Wang and S. Priya, Colossal tunability in high frequency magnetoelectric voltage tunable inductors, *Nat. Commun.*, 2018, **9**, 4998.

4. Cellulose-Based Environmentally Sustainable Electro-Mechanical Bending Actuators

In this work, an ionic liquid is employed to develop sustainable electro-mechanical bending actuators. The previously employed water-soluble cellulose derivatives (MC, HPC, and NaCMC) and CNCs were used in the fabrication of hybrid films comprising the ionic liquid 2-hydroxy-ethyl-trimethylammonium dihydrogen phosphate ([Ch][DHP]) for actuator development. The influence of the IL content on the morphology and physico-chemical properties of free-standing composite films was evaluated. Independently of the cellulose derivative, the ductility of the films increases upon [Ch][DHP] incorporation. An increase in the electrical conductivity due to the IL incorporation into cellulosic matrices is found. Based on the obtained electro-mechanical actuation performance and their simple processability and renewable nature, the fabricated materials represent a step forward in developing sustainable soft actuators of high practical relevance.

4.1. Introduction

The development of polymeric composites based on ILs is receiving increasing attention.[1] When an IL is combined with a polymer, it may give rise to composites that possess electroactive functional properties, leading to IL-based electroactive polymers (EAP) with easy processing, low cost, fracture tolerance, low weight and mechanical flexibility.[2] IL-based EAPs are finding applications in many technological fields, particularly for energy harvesting,[1] sensors,[3] and, actuators[4] due to their low operation voltages and large displacement capacity.

Synthetic polymers such as PVDF and its co-polymers and, a variety of ILs such as, 1-ethyl-3-methylimidazolium bis(trifluoromethylsulfonyl)imide [Emim][TFSI][5], 1-butyl-3-methylimidazolium hexafluorophosphate [BMIM][PF_6],[6] (1-hexyl-3-methylimidazolium chloride [C_6mim][Cl],[2] 1-ethyl-3-methylimidazolium bis(trifluoromethylsulfonyl)imide [Emim][TFSI] among others,[7] have been used to develop soft actuators. Results demonstrated that incorporating the [Emim][TFSI] into the PVDF polymeric matrix induces a plasticizing behaviour in the material, strongly influencing its mechanical properties.[5] Moreover, [Emim][TFSI] results in large bending displacement (~ 3 mm) at low voltages. It has also been shown that the bending actuation response of PVDF/IL composites strongly depends on the proper selection of IL anion and cation, the actuation depending on anion and cation size.[8] Besides inducing the PVDF crystallization into the highly polar and electroactive β-phase, the incorporation of IL enhances the electrical conductivity and decreases Young's modulus of the polymer. Similar results were obtained by the incorporation of different ILs with a common anion $[TFSI]^-$ and distinct cations,[9] as well as by the introduction of IL in different polymer matrices such as PLLA,[10] PCL,[11] and poly(ethylene oxide) (PEO).[12]

Despite the obvious interest in environmental concerns and circular economy regulations, few studies have now reported on the development of actuators based on natural polymers. In this framework, cellulose-based materials display promising properties to be used in fields as varied as energy storage,[13] sensing,[14] antimicrobial systems,[15] catalytic,[16] water purification,[17] or tissue engineering.[18] Despite such remarkable efforts, till the date, scarce works have focused their aim on developing cellulose-based materials with actuator properties, an example being the fabrication of a complex bilayer system consisting on mesoporous photonic resins using cellulose nanocrystals (CNCs).[19] CNCs are nanoscale spindle-shaped crystals extracted upon controlled hydrolysis of native cellulose.[20] The ability to form iridescent chiral nematic structures of CNCs was used to obtain materials with

stimuli-responsive actuation behaviour and variation in photonic properties.[19] Similarly, a multi-layered structure using CNCs and polyethylene glycol diacrylate has been developed to obtain actuator properties upon swelling.[21] However, these approaches consist of complex fabrication processes, making their scalability a serious drawback. In order to improve natural polymer-based actuators' performance and processability, the present work reports on CNC-based actuators using simple fabrication technologies: CNCs were mixed through evaporation induced self-assembly (EISA) with a biocompatible ionic liquid, 2-hydroxy-ethyl-trimethylammonium dihydrogen phosphate ([Ch][DHP]).

As CNCs are known to be brittle and the flexibility of the actuator is a key factor determining its performance, the use of other cellulose-based materials is also evaluated. As previously studied (Chapter 3), MC, HPC, and NaCMC have been used, which, apart from presenting an elongation at break exceeding 10 %, have remarkable film forming ability.[22] Therefore, CNC, MC, HPC and NaCMC have been blended with IL contents up to 40 % via solvent casting approach using [Ch][DHP] as a model IL. Film morphology, electrical, mechanical and electro-mechanical properties are evaluated, and the potential of cellulose/[Ch][DHP] films as actuator materials is demonstrated.

4.2. Experimental

4.2.1. Sample preparation and characterisation

CNCs were extracted from microcrystalline cellulose through sulphuric-acid hydrolysis, followed by tip-sonication. Firstly, 20 g of microcrystalline cellulose were subjected to hydrolysis with 64 wt.% sulphuric acid solution (400 mL) at 45 ºC for 30 min (400 rpm). The reaction was then quenched by adding 10-fold excess of cold distilled water. The remaining suspension was washed by centrifugation (4000 rpm) to remove excess aqueous acid. CNCs were obtained by sonication in a Vibracell Sonicator (Sonicsand Materials Inc., Danbury, CT) at 50 % output for 10 min. After further purification by dialysis, aqueous CNC dispersions with a pH of 1.9 and a concentration of 1.46 wt.% were obtained.

Nanocomposites based on CNCs and 2-hydroxyethyl-trimethylammonium dihydrogen phosphate [Ch][DHP] were prepared by a solvent evaporation method, depicted in **Scheme 4.1**). Different contents of [Ch][DHP] (0, 10, 25 and 40 wt.%) were added to an aqueous solution containing CNC and mixed at room temperature under magnetic stirring. After the completely IL dissolution, the CNC/[Ch][DHP] solutions were cast in Petri-dishes and dried

at room temperature for 72h. Similarly, for the water-soluble cellulose derivatives/[Ch][DHP] films, the IL (40 % wt.) was previously dispersed into ultra-pure water, followed by the cellulose derivatives (HPC, MC and NaCMC) dissolution. Similarly to the neat CNC and CNC/[Ch][DHP], the pure cellulose derivatives and cellulose derivatives/[Ch][DHP] films were obtained after the water evaporation at room temperature. The characteristics of the materials used are described in section 2.1 of Chapter 2.

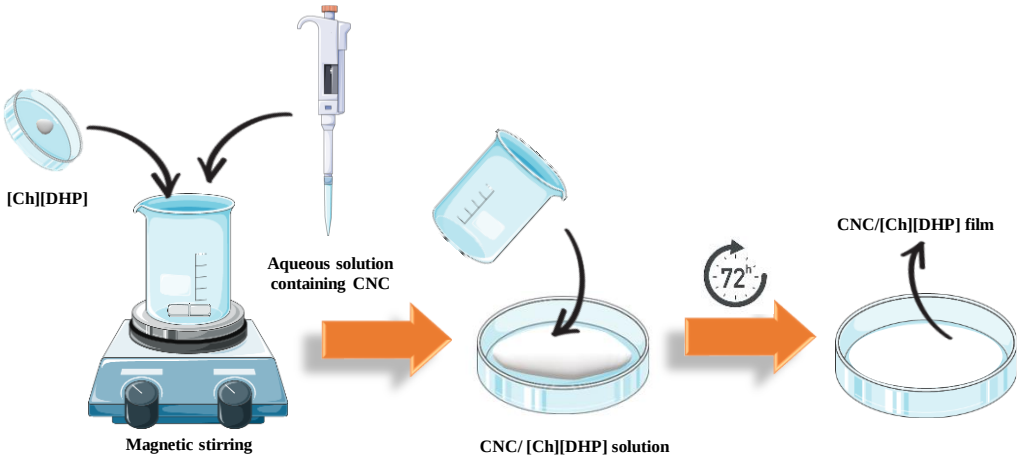

Scheme 4.1. Schematic representation of cellulose-derivatives/[Ch][DHP] composite films prepared by solvent evaporation method.

The samples morphology was evaluated by SEM. FTIR spectroscopy, XRD patterns and uniaxial tensile test were also measured. From the current-voltage characteristic curves was obtained the electrical conductivity applying the Equation (2.6). The bending response was evaluated as indicated in section 2.2.7.

4.3. Results and discussion

4.3.1. Physicochemical and structural characterisation

Fourier transform infrared (FTIR) spectroscopy has been used to study the presence of chemical interactions between CNC, HPC, MC or NaCMC and the [Ch][DHP] ionic liquid. As depicted in **Figure 4.1**, all samples present a broad band located at 3600-3200 cm^{-1} arising from the O−H stretching and a weaker band at 2902 cm^{-1} due to the C−H stretching, which is a characteristic feature of cellulose derivatives.[25,26] More precisely, CNC is characterized by further bands at 1430 cm^{-1} (CH_2 bending), at 1337 cm^{-1} (C-O-H bending), at 1160 cm^{-1} (C-O-C bending) and at 897 cm^{-1} (C-O-C asymmetric stretching).[27] MC shows the 1646 cm^{-1} (C−O stretching), 1455−1251 cm^{-1} (C−H bending), 1065 cm^{-1} (C−O stretching) and 947 cm^{-1}

(O−CH_3 stretching).[28] Finally, NaCMC has bands at 1605 cm^{-1} (asymmetrical stretching of carboxyl methyl ether), 1422 cm^{-1} (symmetrical stretching of carboxyl methyl ether) and 1128 cm^{-1} (>CH−O−CH_2).[29] No band shifting is observed upon IL incorporation, suggesting that no chemical interaction is achieved between the different cellulose types and the [Ch][DHP] ionic liquid.

The FTIR spectra of the CNC/[Ch][DHP] composite films also present the main absorption bands characteristics of the [Ch][DHP] IL, being indicative of the IL incorporation into the CNC and its derivatives. The absorption band at 950 cm^{-1} is attributed to the stretching vibration of the -CCO group, increasing the absorption band intensity with increasing IL content (**Figure 4.1a**). The [Ch][DHP] characteristic absorption bands at 1479 cm^{-1}, ascribed to the CH_3 vibration, and at 1644 cm^{-1}, assigned to the O-H vibration, are identified in the spectra.[30] These absorption bands, except for the NaCMC/[Ch][DHP] composites, overlap with the CNC absorption bands (**Figure 4.1b**).

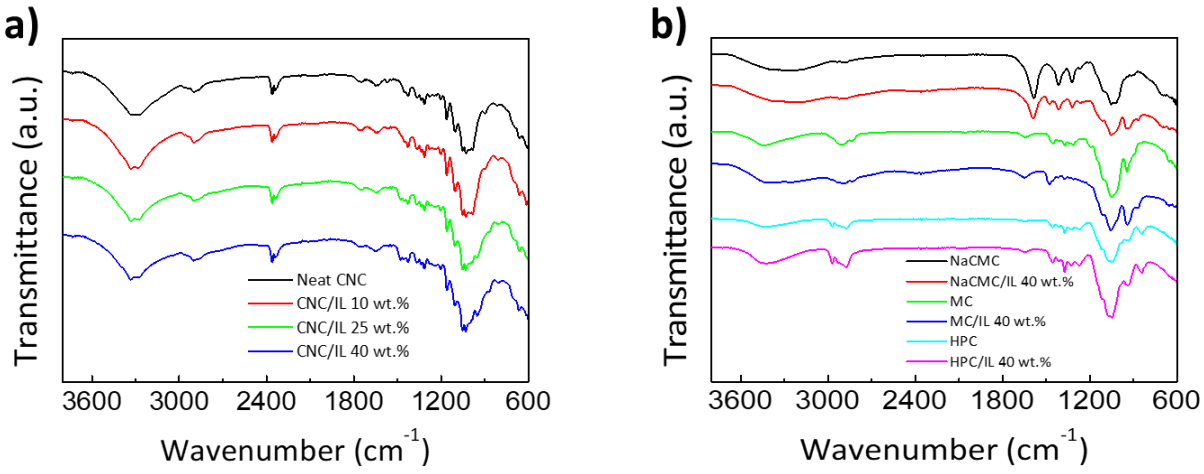

Figure 4.1. FTIR-ATR spectra of a) pure CNC and CNC/[Ch][DHP] composite films and b) cellulose derivative/[Ch][DHP] composites containing 40 wt.% of [Ch][DHP].

XRD analyses were conducted to study the influence of [Ch][DHP] incorporation into the crystalline structure of the resulting films. **Figure 4.2a** depicts XRD patterns for CNC/IL films for [Ch][DHP] concentration up to 40 wt.%. All the films show the characteristic diffraction peaks corresponding to cellulose I, with four main peaks located at 2θ = 14.9, 16.5, 22.7 and 34.4°, corresponding to *(1-10), (101), (200)* and *(004)* planes[31]. Although [Ch][DHP] could form long-range order chlorine crystals,[32] no reflections corresponding to

[Ch][DHP] are noticed irrespectively of its concentration, suggesting that the presence of CNC hinders the formation of such chlorine crystals.

The XRD patterns corresponding to neat and composite water-soluble cellulose derivatives with an IL concentration of 40 wt.% are presented in **Figure 4.2b**. Again, despite the presence of large amounts of [Ch][DHP], no diffraction peaks corresponding to chlorine crystals are observed, indicating that [Ch][DHP] remains in its amorphous state in all the prepared films. HPC and MC present two broad peaks at 2θ = 8.8 and 20.1° and 2θ = 8.2 and 20.3°, respectively, corresponding to *(1-10)* and *(110)* planes, similarly to cellulose II.[33] Interestingly, the crystalline structure of HPC and MC is not disrupted upon [Ch][DHP] incorporation. On the contrary, when [Ch][DHP] is added to NaCMC, its original semi-crystalline character (as evidenced by the two broad diffraction peaks centred at 2θ = 13.0 and 21.1°) is suppressed,[34] suggesting that the presence of ionic liquids limits the ability of NaCMC to form crystalline regions.

HPC and MC maintain the crystalline characteristic of cellulose II as a result of their low degree of substitution (despite their slightly larger *d*-spacing of the *(1-10)* plane). On the contrary, NaCMC presents a more amorphous character due to presence of larger carboxymethyl ether group in the sodium salt form (-O-CH_2-COO^-Na^+). It is also observed that all the films composed of cellulose derivatives (with or without [Ch][DHP]) present broad diffraction peaks, indicating the coexistence of both crystalline and amorphous phases within the films.

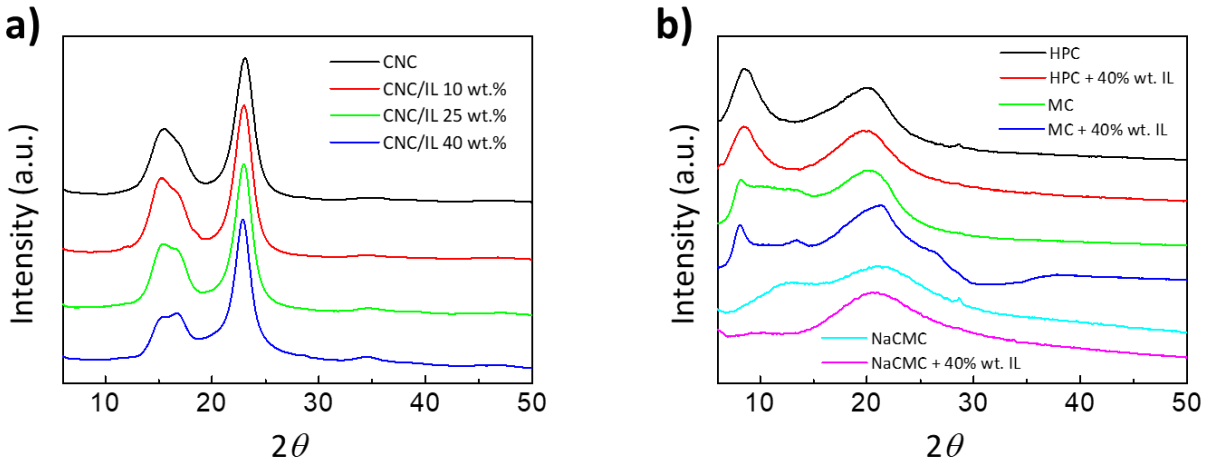

Figure 4.2. XRD patterns of a) pure CNC and CNC/[Ch][DHP] composite films and b) HPC, MC and NaCMC-based composite films.

4.3.2. Morphological characterisation

The morphology of the prepared films has been studied by SEM. **Figure 4.3a** shows the cross-section SEM micrographs of CNC-prepared composites comprising different amounts of IL. In contrast, **Figures 4.3b-d** correspond to neat NaCMC, MC and HPC films, together with their IL composite counterparts, respectively. Neat CNC presents a characteristic parallel arranged layered structure formed upon the EISA of CNCs, which organize into a long-range chiral nematic order.[35–37] Interestingly, although the structure is not entirely homogeneous at large IL loadings, its incorporation does not disrupt the layered structure of CNC film, suggesting a rather homogeneous infiltration of the ionic liquid between individual nanocrystals.[38] The fractured surface of neat NaCMC, MC, and HPC films (**Figures 4.3b, c and d,** respectively) shows homogeneous surfaces with no irregularities, confirming their suitable film-forming properties. Upon IL addition, both MC and NaCMC films still keep a uniform and flat morphology, while HPC/IL films present a non-homogeneous and rough surface. This effect is explained in terms of a poor interaction of the non-ionic HPC with [Ch][DHP], which yields non-uniform films with voids during solvent evaporation. As observed in the micrographs, all the films present a uniform thickness ranging from 15 to 30 μm.

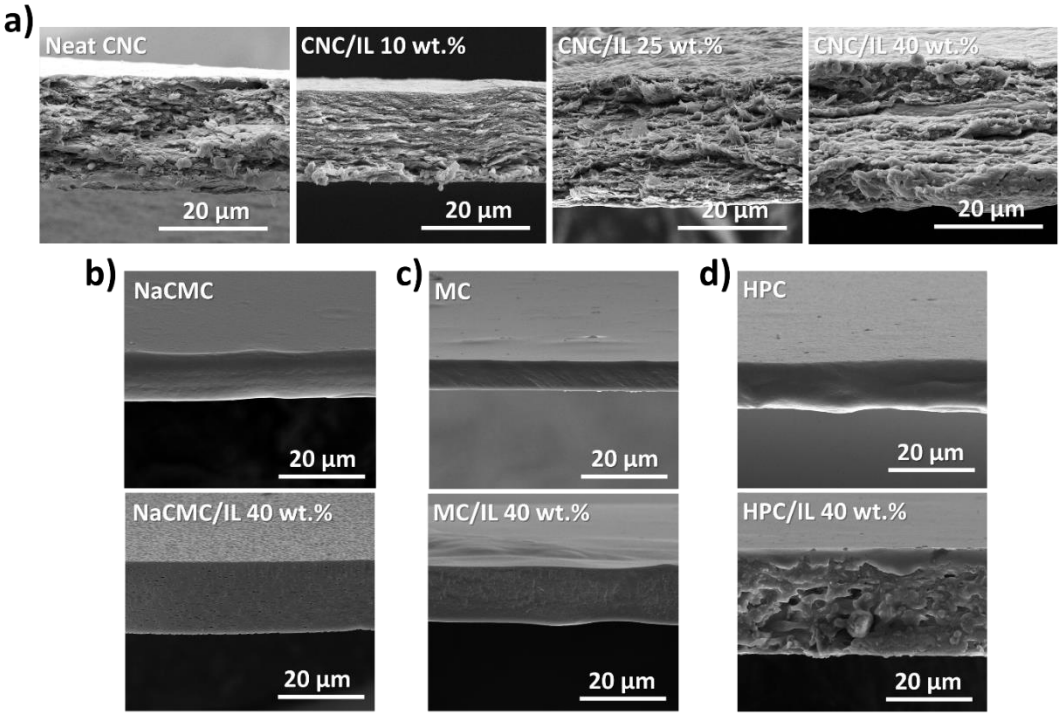

Figure 4.3. SEM images of a) pure CNC and CNC/[Ch][DHP] composites with different IL contents, b) pure NaCMC (up) and NaCMC/IL 40 wt.% (down), c) pure MC (up) and MC/IL 40 wt.% (down), and d) pure HPC (up) and HPC/IL 40 wt.% (down).

4.3.3. Mechanical properties

Determining the mechanical properties of the developed free-standing films is essential for understanding their potential for electro-mechanical actuator applications. Accordingly, as summarized in **Figure 4.4** and **Table 4.1**, room-temperature uniaxial tensile tests have been used to determine Young's modulus (E), elongation at yield (ε_y), yield stress (σ_y), elongation at break (ε_b), and stress at break (ε_b). As observed in **Figure 4.4a**, the neat CNC film shows its characteristic brittle and stiff behaviour with a E, σ_y and ε_b of 2394 ± 215 MPa,[38,39] 11.1 MPa and 0.81 %, respectively. Upon IL addition, films become more ductile with a noticeable plastic deformation region (in contrast with neat CNC film, which only shows a linear section corresponding to elastic deformation), which is accompanied by a marked decrease in E down to 589 ± 290 MPa and in σ_y down to 4.7 MPa for the CNC/IL 25 wt.% sample. This fact is attributed to the plasticizing effect of the IL, which penetrates between adjacent CNCs to reduce their hydrogen bonding-induced entanglement. Despite the observed decrease in E when in the presence of IL, it should be noticed that the modulus of the CNC/IL films still remains above the values reported for some commodity thermoplastics such as polyethylene terephthalate (PET),[40] or polylactide (PLA).[41]

All three cellulose derivatives studied follow a similar trend to the CNC/IL films (**Figure 4.4b**). Neat HPC presents a semi-ductile behaviour with a E and ε_b of 919 ± 71 MPa and 5.62 %, respectively, while MC and NaCMC result semi-brittle with a E and ε_b of 1284 ± 183 MPa and 1889 ± 323 MPa, and 2.80 % and 4.33 %, respectively.[25] IL addition increases the elongation at break and the ductility of the resulting HPC, MC and NaCMC films (**Table 4.1**), inducing the [Ch][DHP] a plasticizing effect and then a thermoplastic role followed by a linear regime.[9] Typically, the IL incorporation limits the hydrogen bonding between cellulosic chains, reducing chain rigidity and increasing the elongation at break of the films, decreasing the Young's Modulus. These experimental results show that it is possible to obtain films with tailored mechanical properties, ranging from stiff and brittle to flexible and ductile, by controlling cellulose type (CNC, HPC, MC or NaCMC) and IL concentration.

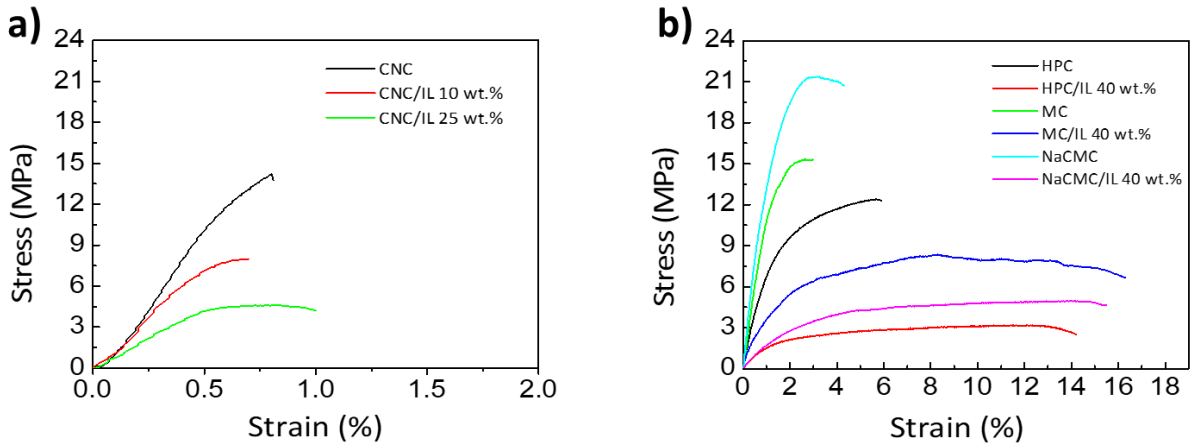

Figure 4.4. Representative stress-strain curves obtained for a) neat CNC and [Ch][DHP]/CNC composites with different [Ch][DHP] contents (10 and 25% wt.) and for neat and cellulose/derivatives/[Ch][DHP] containing 40% wt. of [Ch][DHP].

Table 4.1. Main mechanical parameters obtained after uniaxial tensile test for the prepared free-standing films. *E*: Young's modulus; σ_y: yield stress; ε_y: elongation at yield; σ_b: stress at break; and ε_b: elongation at break.

Sample	*E* (MPa)	σ_y (MPa)	εy (%)	σb (MPa)	ε_b (%)
CNC	2394 ± 215	11.1 ± 1.8	0.55 ± 0.09	14.1 ± 3.1	0.81 ± 0.22
CNC + 10% wt. IL	1461 ± 74	7.4 ± 2.1	0.58 ± 0.10	7.9 ± 1.6	0.71 ± 0.19
CNC + 25% wt. IL	589 ± 290	4.7 ± 0.4	0.54 ± 0.15	4.2 ± 1.0	1.00 ± 0.52
HPC	919 ± 71	10.3 ± 2.3	2.43 ± 0.52	12.4 ± 3.4	5.62 ± 1.11
MC	1284 ± 183	15.1 ± 4.2	2.20 ± 0.21	15.6 ± 1.7	2.80 ± 1.37
NaCMC	1889 ± 323	21.3 ± 2.3	2.91 ± 0.99	20.7 ± 5.3	4.33 ± 2.95
HPC + 40% wt. IL	249 ± 45	2.5 ± 1.0	2.26 ± 0.03	2.6 ± 0.9	14.13 ± 2.15
MC + 40% wt. IL	570 ± 98	6.6 ± 2.7	2.64 ± 0.90	6.9 ± 1.1	16.34 ± 1.50
NaCMC + 40% wt. IL	208 ± 28	5.1 ± 1.5	4.32 ± 0.07	5.3 ± 1.4	15.62 ± 3.12

4.3.4. Electrical properties

The effect of the IL incorporation in the electrical conductivity of the [CH][DHP]/CNC composites and its derivatives was evaluated from the current-voltage curves presented in **Figure 4.5**. For neat CNC non-linear I-V curves were obtained (**Figure 4.5a**), characterized by two regimes: one between -2 V and 2 V and one above those voltages. This behaviour is more noticeable for the CNC/[Ch][DHP] samples indicating a hindrance of IL cation and anion movement within the CNC polymer matrix, attributed to stronger electrostatic interactions between IL and the polymer matrix. For an applied voltage higher than 2 V, the electrical field is strong enough to induce the cation and anion movement, yielding a stronger increase of the electrical conductivity. This effect is also observed for neat NaCMC and NaCMC/[Ch][DHP] composites. For neat HPC and MC and its composites, on the contrary, a linear curve is observed with the applied voltage.

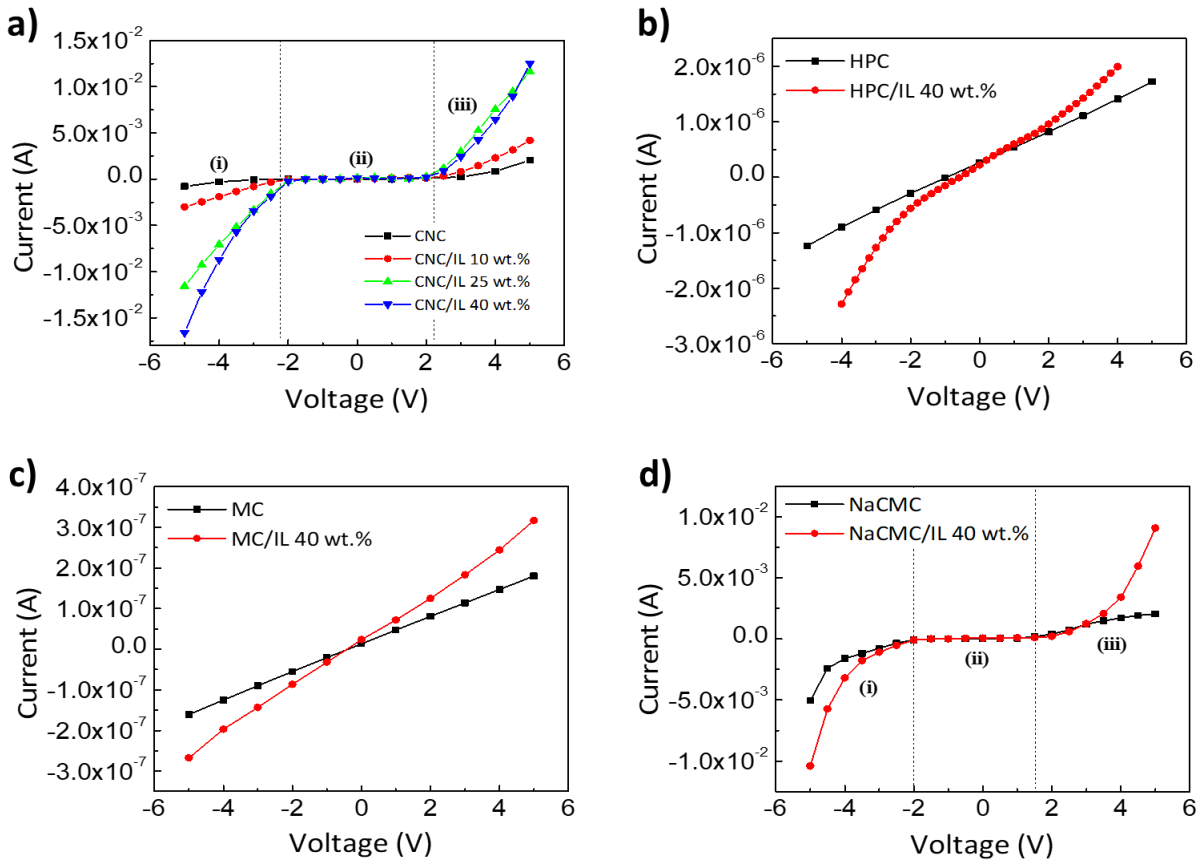

Figure 4.5. a) Representative I-V curves for a) neat CNC and CNC/[Ch][DHP] composite films with different IL contents (10, 25 and 40% wt. IL), b) neat HPC and HPC/IL 40 wt.% IL, c) neat MC and MC/IL 40 wt.% and d) neat NaCMC and NaCMC/IL 40 wt.%.

The effect of the [Ch][DHP] in the electrical conductivity for all developed samples was quantified from the I-V curves of **Figure 4.5**, using Equation (2.6), and the corresponding conductivity values are compiled in **Table 4.2**. Independently of the cellulose derivative, the incorporation of [Ch][DHP] into the polymer matrix improves the electrical conductivity of the composites, increasing the electrical conductivity with increasing IL content. It is notable that this increase occurs in all three regimes studied, but it is particularly relevant for the regime (iii), being therefore determined by the higher content of charges species (anions and cations). On the other hand, a lower increase with filler content is observed for regimes (i) and (ii), being the increase of electrical conductivity attributed to increased mobility of the charge's species. Interestingly, for the CNC and NaCMC, the increase in the electrical conductivity in the regimes (i) and (iii) does not follow a symmetrical behavior, provably due to the polarity of surface interactions. The highest conductivity value is observed for the CNC/[Ch]DHP] samples containing 40 wt.% of IL, showing a conductivity value of 6.43 x $10^{-3} \pm 3.53 \times 10^{-4}$ $S \cdot m^{-1}$ (regime iii).

Table 4.2. Electrical conductivity of CNC and the neat cellulose derivatives and their IL based composites.

Sample	**Electrical conductivity (S m^{-1})**		
	(i)	**(ii)**	**(iii)**
CNC	$1.02 \times 10^{-7} \pm 0.0$	$3.82 \times 10^{-9} \pm 0.0$	$1.40 \times 10^{-7} \pm 0.0$
HPC		$2.42 \times 10^{-7} \pm 0.0$	
MC		$2.22 \times 10^{-8} \pm 0.0$	
NaCMC	$6.52 \times 10^{-4} \pm 0.0$	$2.17 \times 10^{-5} \pm 3.82 \times 10^{-6}$	$4.34 \times 10^{-4} \pm 3.87 \times 10^{-5}$
CNC/IL 10 wt.%	$9.61 \times 10^{-4} \pm 1.40 \times 10^{-4}$	$4.39 \times 10^{-5} \pm 3.87 \times 10^{-6}$	$1.32 \times 10^{-3} \pm 6.53 \times 10^{-5}$
CNC/IL 25 wt.%	$5.50 \times 10^{-3} \pm 1.18 \times 10^{-4}$	$1.29 \times 10^{-4} \pm 1.41 \times 10^{-5}$	$6.09 \times 10^{-3} \pm 1.22 \times 10^{-4}$
CNC/IL 40 wt.%	$8.62 \times 10^{-3} \pm 3.45 \times 10^{-4}$	$1.21 \times 10^{-4} \pm 2.44 \times 10^{-5}$	$6.43 \times 10^{-3} \pm 3.53 \times 10^{-4}$
HPC/IL 40 wt.%		$2.79 \times 10^{-7} \pm 3.99 \times 10^{-8}$	
MC/IL 40 wt.%		$5.75 \times 10^{-8} \pm 1.02 \times 10^{-8}$	
NaCMC/IL 40 wt.%	$1.25 \times 10^{-3} \pm 1.18 \times 10^{-4}$	$4.82 \times 10^{-5} \pm 0.0$	$2.37 \times 10^{-3} \pm 3.15 \times 10^{-4}$

4.3.5. Bending actuation performance

The electro-mechanical properties of the CNC/[Ch][DHP] and cellulose derivatives films were evaluated by measuring the maximum displacement, from the distance of the actuator´s tip in a relaxed position, under an applied electric field (**Figure 4.6** and **Figure 4.7**). For CNC/[Ch][DHP] composites, low displacements were obtained (0.2 mm) (results not shown) due to the mechanical properties of the CNC/[Ch][DHP] composites when compared with the water-soluble cellulose derivatives. As shown in **Figure 4.4** and **Table 4.1**, CNC composites show a brittle and stiff behaviour with a higher Young's Modulus when compared with the CNC derivatives composites, hindering the ions' mobility. **Figure 4.7a** shows the maximum displacement for the water-soluble cellulose derivative/[Ch][DHP] composites with an applied voltage of 5 V at 100 mHz. MC/[Ch][DHP] films developed a maximum displacement of 3.4 mm, larger than the one obtained for the HPC/[Ch][DHP] and NaCMC/[Ch][DHP] composites. On the other hand, this composite does not show bending actuation for applied voltages larger than +5 V, probably due to its lower conductivity values when compared with the HPC and NaCMC/[Ch][DHP] composites. Further, MC/[Ch][DHP] composites show the highest Young's Modulus (570 ± 98 MPa), hindering the bending motion.

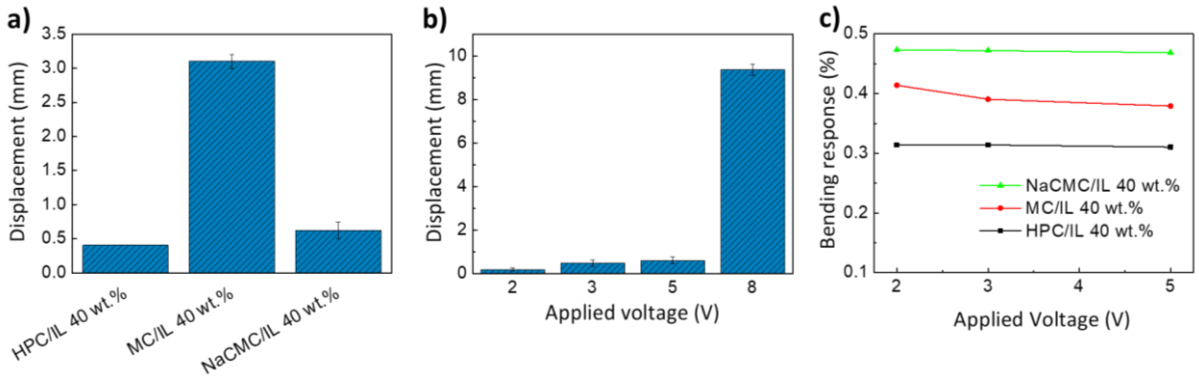

Figure 4.6. a) Displacement of the composites for an applied voltage of 5 V at a frequency of 100 mHz for the HPC, MC and NaCMC composites containing 40% wt. of IL. b), Displacement as a function of the applied voltage for the NaCMC/[Ch[DHP] composite at 100 mHz. c) Bending response as a function of the applied voltage for the cellulose derivatives composites.

The displacement as a function of the applied voltage is shown for the NaCMC/[Ch][DHP] samples (**Figure 4.6b**). An increase of the maximum displacement up to 9.3 mm with increasing applied voltage up to 8 V was observed. The bending response is due

to the presence of anions and cations from the [Ch][DHP], their diffusion and displacement upon an applied voltage to the electrode layers (positive and negative electrode side, respectively), and the different sizes of anion and cation,[8] finally leading to the bending of the film.

Thus, bending actuation is determined by the films' electrical and mechanical properties,[9] as schematized in **Figure 4.7a**. The bending motion as a function of time for the NaCMC/[Ch[DHP] composite for an applied voltage of +8 V at a frequency of 100 mHz is presented in **Figure 4.7b**. The largest displacement is observed for the NaCMC/[Ch][DHP] composites, indicating that the NaCMC matrix favours ion diffusion and mobility as a result of the high ion-dipole interactions between the [Ch][DHP] with the NaCMC polymer chain. The IL-polymer interactions decrease from the NaCMC<MC to the HPC, an indicator of the Na^+ interactions with the IL anions. Further, as expected, the highest bending responses are observed for these types of composites, followed by the MC and HPC composites due to the lowest Young's Modulus (NaCMC<HPC<MC), as demonstrated in **Table 4.1**. It is also to notice that the NaCMC/[Ch][DHP] composites present the highest conductivity values, favouring the movement of IL charge in response to an electric field. Both these parameters favour the bending motion of the films, resulting in higher bending responses.

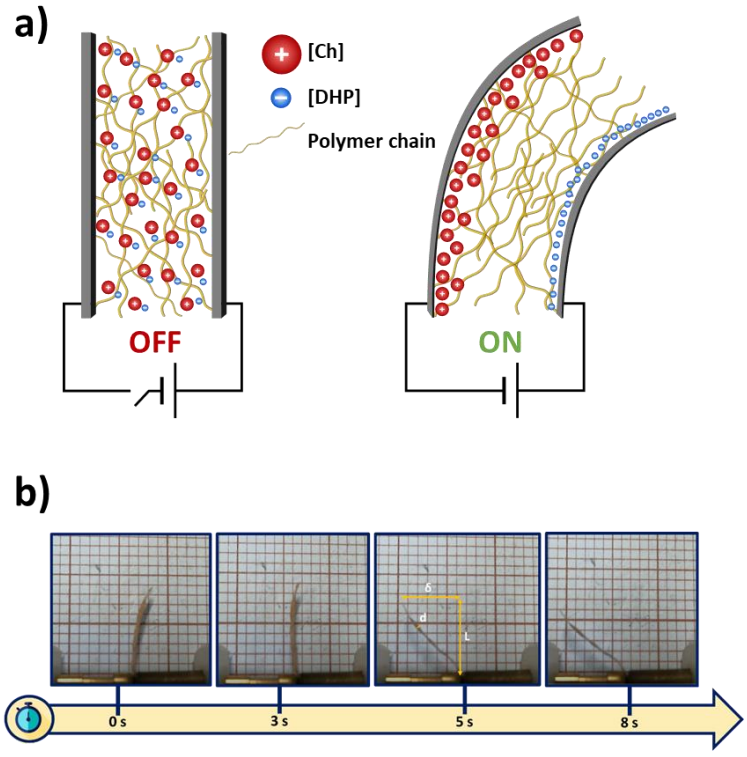

Figure 4.7. a) Schematic representation of the cation and anion migration and b) bending response as a function of time for NaCMC/[Ch][DHP] composite at a 100 mHz frequency and 8 V.

Finally, the bending response (ε) of the HPC/[Ch][DHP], MC/[Ch][DHP] and NaCMC/[Ch][DHP] composites was evaluated for applied voltages between 2 to 10 V through Equation (4.2) where "L" is the sample free length, "d" the thickness and "δ" the displacement along the x-axes (see the schematic representation of **Figure 4.7a**).

$$\varepsilon = \frac{2d\delta}{L^2 + \delta^2} \tag{4.2}$$

It is noteworthy that the highest bending response is observed for the NaCMC-based films, suggesting that NaCMC presents a bright future for developing electro-mechanical materials.

4.4. Conclusions

This work describes the development of cellulose-based bending actuators. CNCs and three water-soluble cellulose derivatives were used to fabricate free-standing films comprising the IL [Ch][DHP] by a solvent casting method. Different contents of [Ch][DHP] (10, 25 and 40 wt.%) were incorporated within the CNC biopolymer matrix. Based on the obtained results, the highest IL content (40 wt.%) was also incorporated into the HPC, MC and NaCMC matrix. No morphological changes were observed for neat and CNC, MC and NaCMC composites upon the IL incorporation, presenting all the samples with a smooth and flat surface. The mechanical properties evaluated from the uniaxial tensile measurements revealed a plasticizing effect due to the IL incorporation into the polymer matrix, resulting in ductile free-standing films. Young's Modulus decreases with the IL incorporation into the matrix for all the samples. The electrical conductivity of the composites increases together with the IL concentration. In the case of CNC and NaCMC, two electrical conductivity regimes based on the increased mobility of anions and cations for applied voltages larger than +/- 2 V. Bending actuators were developed, the highest bending motion of ~9 mm being obtained for the NaCMC/[Ch][DHP] composite at a frequency of 100 mHz and an applied voltage of 8 V. These results highlight the suitability of the developed systems for environmentally-friendly high-performance actuators.

4.5. References

1 S. Ferrari, E. Quartarone, P. Mustarelli, A. Magistris, M. Fagnoni, S. Protti, C. Gerbaldi and A. Spinella, Lithium ion conducting PVdF-HFP composite gel electrolytes based on N-methoxyethyl-N-methylpyrrolidinium bis(trifluoromethanesulfonyl)-imide ionic liquid, *J. Power Sources*, 2010, **195**, 559–566.

2 R. Mejri, J. C. Dias, S. B. Hentati, M. S. Martins, C. M. Costa and S. Lanceros-Mendez, Effect of anion type in the performance of ionic liquid/poly(vinylidene fluoride) electromechanical actuators, *J. Non. Cryst. Solids*, 2016, **453**, 8–15.

3 D. M. Correia, C. M. Costa, E. Lizundia, R. Sabater i Serra, J. A. Gómez-Tejedor, L. T. Biosca, J. M. Meseguer-Dueñas, J. L. Gomez Ribelles and S. Lanceros-Méndez, Influence of Cation and Anion Type on the Formation of the Electroactive β-Phase and Thermal and Dynamic Mechanical Properties of Poly(vinylidene fluoride)/Ionic Liquids Blends, *J. Phys. Chem. C*, 2019, **123**, 27917–27926.

4 Y. Liu, M. Ghaffari, R. Zhao, J.-H. Lin, M. Lin and Q. M. Zhang, Enhanced Electromechanical Response of Ionic Polymer Actuators by Improving Mechanical Coupling between Ions and Polymer Matrix, *Macromolecules*, 2012, **45**, 5128–5133.

5 J. C. Dias, D. M. Correia, C. M. Costa, C. Ribeiro, A. Maceiras, J. L. Vilas, G. Botelho, V. de Zea Bermudez and S. Lanceros-Mendez, Improved response of ionic liquid-based bending actuators by tailored interaction with the polar fluorinated polymer matrix, *Electrochim. Acta*, 2019, **296**, 598–607.

6 C. Xing, M. Zhao, L. Zhao, J. You, X. Cao and Y. Li, Ionic liquid modified poly(vinylidene fluoride): crystalline structures, miscibility, and physical properties, *Polym. Chem.*, 2013, **4**, 5726–5734.

7 J. C. Dias, A. C. Lopes, B. Magalhães, G. Botelho, M. M. Silva, J. M. S. S. Esperança and S. Lanceros-Mendez, High performance electromechanical actuators based on ionic liquid/poly(vinylidene fluoride), *Polym. Test.*, 2015, **48**, 199–205.

8 R. Mejri, J. C. Dias, S. Besbes Hentati, G. Botelho, J. M. S. S. Esperança, C. M. Costa and S. Lanceros-Mendez, Imidazolium-based ionic liquid type dependence of the bending response of polymer actuators, *Eur. Polym. J.*, 2016, **85**, 445–451.

9 D. M. Correia, J. C. Barbosa, C. M. Costa, P. M. Reis, J. M. S. S. Esperança, V. de Zea Bermudez and S. Lanceros-Méndez, Ionic Liquid Cation Size-Dependent Electromechanical Response of Ionic Liquid/Poly(vinylidene fluoride)-Based Soft Actuators, *J. Phys. Chem. C*, 2019, **123**, 12744–12752.

10 P. Xu, Z.-P. Cui, G. Ruan and Y.-S. Ding, Enhanced Crystallization Kinetics of PLLA by Ethoxycarbonyl Ionic Liquid Modified Graphene, *Chinese J. Polym. Sci.*, 2019, **37**, 243–252.

11 Y. Ren, Z. Zhou, G. Yin, G.-X. Chen and Q. Li, Effect of ionic liquid-containing poly(ε-caprolactone) on the dispersion and dielectric properties of polymer/carbon nanotube composites, *RSC Adv.*, 2016, **6**, 31351–31358.

12 K. Elamin, M. Shojaatalhosseini, O. Danyliv, A. Martinelli and J. Swenson, Conduction mechanism in polymeric membranes based on PEO or PVdF-HFP and containing a piperidinium ionic liquid, *Electrochim. Acta*, 2019, **299**, 979–986.

13 and D. K. Hadrien Glatz, Erlantz Lizundia, Fiona Pacifico, An Organic Cathode Based Dual-Ion Aqueous Zinc Battery Enabled by a Cellulose Membrane, *ACS Appl. Energy Mater.*, 2019, **2**, 1288–1294.

14 O. Kose, A. Tran, L. Lewis, W. Y. Hamad and M. J. MacLachlan, Unwinding a spiral of cellulose nanocrystals for stimuli-responsive stretchable optics, *Nat. Commun.*, 2019, **10**, 510.

15 P. Tyagi, R. Mathew, C. Opperman, H. Jameel, R. Gonzalez, L. Lucia, M. Hubbe and L. Pal, High-Strength Antibacterial Chitosan–Cellulose Nanocrystal Composite Tissue Paper, *Langmuir*, 2019, **35**, 104–112.

16 W. C. E. Lizundia, M. Jimenez, C. Altorfer, M. Niederberger, Electroless plating of platinum nanoparticles onto mesoporous cellulose films for catalytically active free-standing materials, *Cellulose*.

17 M. Lucchini, E. Lizundia, S. Moser, M. Niederberger and G. Nystrom, Titania-cellulose hybrid monolith for in-flow purification of water under solar illumination, *ACS Appl. Mater. Interfaces*, , DOI:10.1021/acsami.8b09735.

18 D. A. Osorio, B. E. J. Lee, J. M. Kwiecien, X. Wang, I. Shahid, A. L. Hurley, E. D. Cranston and K. Grandfield, Cross-linked cellulose nanocrystal aerogels as viable bone tissue scaffolds, *Acta Biomater.*, 2019, **87**, 152–165.

19 M. K. Khan, W. Y. Hamad and M. J. MacLachlan, Tunable Mesoporous Bilayer Photonic Resins with Chiral Nematic Structures and Actuator Properties, *Adv. Mater.*, 2014, **26**, 2323–2328.

20 A. Dufresne, Nanocellulose: A new ageless bionanomaterial, *Mater. Today*, 2013, **16**, 220–227.

21 T. Wu, J. Li, J. Li, S. Ye, J. Wei and J. Guo, A bio-inspired cellulose nanocrystal-based nanocomposite photonic film with hyper-reflection and humidity-responsive actuator properties, *J. Mater. Chem. C*, 2016, **4**, 9687–9696.

22 I. G. DONHOWE and O. FENNEMA, THE EFFECTS of PLASTICIZERS ON CRYSTALLINITY, PERMEABILITY, and MECHANICAL PROPERTIES of METHYLCELLULOSE FILMS, *J. Food Process. Preserv.*, 1993, **17**, 247–257.

23 L. C. Fernandes, D. M. Correia, N. Pereira, C. R. Tubio and S. Lanceros-Méndez, Highly Sensitive Humidity Sensor Based on Ionic Liquid–Polymer Composites, *ACS Appl. Polym. Mater.*, 2019, **1**, 2723–2730.

24 J. C. Dias, M. S. Martins, S. Ribeiro, M. M. Silva, J. M. S. S. Esperança, C. Ribeiro, G. Botelho, C. M. Costa and S. Lanceros-Mendez, Electromechanical actuators based on poly(vinylidene fluoride) with [N1 1 1 2(OH)][NTf2] and [C2mim] [C2SO4], *J. Mater. Sci.*, 2016, **51**, 9490–9503.

25 M. Rincon-Iglesias, E. Lizundia and S. Lanceros-Mendez, Water-soluble cellulose derivatives as suitable matrices for multifunctional materials, *Biomacromolecules*, , DOI:10.1021/acs.biomac.9b00574.

26 E. Lizundia, J. L. Vilas and L. M. León, Crystallization, structural relaxation and thermal degradation in Poly(l-lactide)/cellulose nanocrystal renewable nanocomposites., *Carbohydr. Polym.*, , DOI:10.1016/j.carbpol.2015.01.054.

27 Lizundia, E., Fortunati, E., Dominici, F., Vilas, L. J., Le´on, M. L., Armentano, I., Torre, L., K. and and J., PLLA-grafted cellulose nanocrystals: role of the CNC content and grafting on the PLA bionanocomposite film properties, *Carbohydr. Polym.*, , DOI:10.1016/j.carbpol.2016.01.041.

28 S. Tunç, O. Duman and T. G. Polat, Effects of montmorillonite on properties of methyl cellulose/carvacrol based active antimicrobial nanocomposites, *Carbohydr. Polym.*, 2016, **150**, 259–268.

29 J. F. Luna-Martínez, D. B. Hernández-Uresti, M. E. Reyes-Melo, C. A. Guerrero-Salazar, V. A. González-González and S. Sepúlveda-Guzmán, Synthesis and optical characterization of ZnS–sodium carboxymethyl cellulose nanocomposite films, *Carbohydr. Polym.*, 2011, **84**, 566–570.

30 R. M. Meira, D. M. Correia, S. Ribeiro, P. Costa, A. C. Gomes, F. M. Gama, S. Lanceros-Méndez and C. Ribeiro, Ionic-Liquid-Based Electroactive Polymer Composites for Muscle Tissue Engineering, *ACS Appl. Polym. Mater.*, 2019, **1**, 2649–2658.

31 N. Lin, C. Bruzzese and A. Dufresne, TEMPO-oxidized nanocellulose participating as crosslinking aid for alginate-based sponges, *ACS Appl. Mater. Interfaces*, 2012, **4**, 4948–4959.

32 P. Barbosa, J. Campos, A. Turygin, V. Y. Shur, A. Kholkin, A. Barros-Timmons and F. M. Figueiredo, Piezoelectric poly(lactide) stereocomplexes with a cholinium organic ionic plastic crystal, *J. Mater. Chem. C*, 2017, **5**, 12134–12142.

33 M. Kiyose, E. Yamamoto, C. Yamane, T. Midorikawa and T. Takahashi, Structure and Properties of Low-Substituted Hydroxypropylcellulose Films and Fibers Regenerated from Aqueous Sodium Hydroxide Solution, *Polym. J.*, 2007, **39**, 703–711.

34 I. Gulati, J. Park, S. Maken and M.-G. Lee, Production of carboxymethylcellulose fibers from waste lignocellulosic sawdust using NaOH/NaClO2 pretreatment, *Fibers Polym.*, 2014, **15**, 680–686.

35 T.-D. Nguyen, E. Sierra, H. Eguiraun and E. Lizundia, Iridescent cellulose nanocrystal films: the link between structural colour and Bragg's law, *Eur. J. Phys.*, 2018, **39**, 045803.

36 M. J. M. E. Lizundia, T. D. Nguyen, J. L. Vilas, Wadood Y. Hamad, Chiroptical luminescent nanostructured cellulose films, *Mater. Chem. Front.*

37 E. Lizundia, T.-D. Nguyen, J. L. Vilas, W. Y. Hamad and M. J. Maclachlan, Chiroptical, morphological and conducting properties of chiral nematic mesoporous cellulose/polypyrrole composite films, *J. Mater. Chem. A*, , DOI:10.1039/C7TA05684B.

38 P. Liu, X. Guo, F. Nan, Y. Duan and J. Zhang, Modifying Mechanical, Optical Properties and Thermal Processability of Iridescent Cellulose Nanocrystal Films Using Ionic Liquid, *ACS Appl. Mater. Interfaces*, 2017, **9**, 3085–3092.

39 E. Lizundia, A. Urruchi, J. L. Vilas and L. M. León, Increased functional properties and thermal stability of flexible cellulose nanocrystal/ZnO films, *Carbohydr. Polym.*, , DOI:10.1016/j.carbpol.2015.09.041.

40 A. M. Torres-Huerta, D. Del Angel-López, M. A. Domínguez-Crespo, D. Palma-Ramírez, M. E. Perales-Castro and A. Flores-Vela, Morphological and Mechanical Properties Dependence of PLA Amount in PET Matrix Processed by Single-Screw Extrusion, *Polym. Plast. Technol. Eng.*, 2016, **55**, 672–683.

41 E. Lizundia, S. Petisco and J.-R. Sarasua, Phase-structure and mechanical properties of isothermally melt-and cold-crystallized poly (L-lactide), *J. Mech. Behav. Biomed. Mater.*, 2012, **17**, 242–251.

5. Cellulose Nanocrystals-Based Magnetically Active and Electrically Conducting Mesoporous Nanocomposites

Free-standing mesoporous membranes based on CNCs are fabricated upon the incorporation of $CoFe_2O_4$ and graphite nanoparticles at concentrations up to 20 wt.% through a soft-templating process. Scanning electron microscopy (SEM) and N_2 adsorption-desorption isotherms reveal the development of the highly-porous interconnected random 3D structure. Thermogravimetric analysis (TGA) shows enhanced thermal stability. Vibrating sample magnetometer (VSM) measurements reveal a maximum magnetisation saturation of 8.77 $emu \cdot g^{-1}$ with materials having either ferromagnetic behaviour upon incorporating $CoFe_2O_4$. Four-point-probe measurements display a maximum electrical conductivity of 9.26 ± 0.04 $S \cdot m^{-1}$ when graphite is incorporated into CNCs. Obtained magnetically active or electrically conducting nanohybrids are suitable for fabricating sensors/actuators from natural origin where porous structures can be taken to advantage.

5.1. Introduction

The use of CNCs as a matrix phase instead of a reinforcing phase is a relatively recent strategy which pursues the development of novel materials with improved functionalities. Accordingly, CNCs dispersed in aqueous solutions can be mixed with various inorganic nanoparticles to obtain nanohybrids for flexible electronics, sensors, actuators or antibacterial applications.[1–4] Interestingly, nanoparticle aggregation effects, arising from their high surface energy,[5] are prevented as the electrostatic repulsion forces between CNCs maintain nanohybrid constituents well-dispersed in solution at the nanoscale level.[2] Moreover, using CNCs enables keeping the individual composite constituents homogeneously distributed at the molecular level. This 3D homogeneous dispersion can then be captured into solid-state after a self-assembly process, which is especially interesting to develop percolated conducting networks.[6]

The incorporation of active nanoparticles (either magnetically active or electrically conducting) into cellulosic hosting matrices further allows obtaining organic-inorganic hybrid materials with upgraded functional properties. Ferrites, and more specifically cobalt ferrite, have been used to develop magnetic materials for bio-separation devices, electromagnetic wave absorption or diagnostics,[7] among others. On the other side, thanks to their low density and cost, carbonaceous materials such as graphite are being used as additives to develop electrically-conducting polymer-based composites, enabling their use as electromagnetic interference (EMI) shielding materials or flexible electronics.[8–10] Overall, these materials present the attractive feature of allowing external operation through applied external fields, allowing a non-invasive approach to the remote control.[11]

Additionally, and in comparison with dense solid films, high-surface-area mesoporous membranes show enhanced accessibility to the active sites of the material,[12,13] providing improved performance for magnetic-assisted separation, purification or shielding, for instance.[12,14,15] In 2010, it was reported that alkoxysilane precursors such as tetramethyl orthosilicate (TMOS) are compatible with CNC self-assembly.[16] They showed that the evaporation induced self-assembly (EISA) of aqueous CNCs with TMOS yielded solid CNC/silica materials due to the concomitant $Si(OMe)_4$ hydrolysis and condensation as water evaporates.[17] The silica phase could be removed by alkaline or acid treatment to give access to mesoporous cellulosic structures, where the mesoporosity can be controlled by simply modifying the silica-to-CNC ratio.[18]

Accordingly, this work aims to fabricate high specific surface area cellulosic films with magnetic/electric properties. The combination of structural stability, high specific surface area, and good thermal stability provided by the cellulosic structure, together with the magnetic/electric performance provided by the well-dispersed cobalt ferrite/graphite particles, results in nanohybrid materials with potential applicability in the fields of sensors, energy storage, recoverable catalysts for water purification and actuators, among others.

5.2. Experimental

5.2.1. Sample preparation and characterisation

Mesoporous CNC-based nanohybrids (MCNC) were obtained by self-assembly CNC/graphite/glucose or CNC/$CoFe_2O_4$/glucose with TMOS and subsequent silica removal (**Scheme 5.1**; **Table 5.1** gives a summary of the obtained samples and their codes).[18] To prevent the film cracking during the last stages of EISA into centimetre-sized pieces due to the formation of capillary pressure gradients and to allow the fabrication of large membranes, and glucose has been added to the aqueous CNC dispersion.[19]

As shown in **Table 5.1**, the required amount of $CoFe_2O_4$ or graphite was firstly dispersed in distilled water via ultrasonication for 60 min to get nanohybrids with final concentrations ranging from 1 to 20 wt.%. Subsequently, water-dispersed CNCs were added to obtain 0, 1, 5, 10 and 20 wt.% nanohybrids and the dispersion was further ultrasonicated. Then, 100 mg of glucose was added and the mixture was ultrasonicated for 60 min. Aqueous CNC/graphite/glucose or CNC/$CoFe_2O_4$/glucose dispersions were subsequently mixed with TMOS at a concentration of 1 μL TMOS per 1 mg of CNC/graphite/glucose or CNC/$CoFe_2O_4$/glucose and they were vigorously stirred for 1 h. The suspensions having $Si(OMe)_4$ were cast into polystyrene weighing boats and were allowed to dry for 48 h under ambient conditions. After EISA, CNC/graphite/glucose/silica and CNC/$CoFe_2O_4$/glucose/silica films were obtained. Mesoporous films were obtained after removing silica and glucose with 2 M NaOH (1 mL per 10 mg of the composite film) for 48 h. The resulting films were washed three times with distilled water and four times with ethanol before drying them with supercritical carbon dioxide (s-CO_2). Non-porous CNC films were also obtained for comparison. As shown in the optical image of **Scheme 5.1**, large mesoporous hybrid films with tailored geometries are obtained.

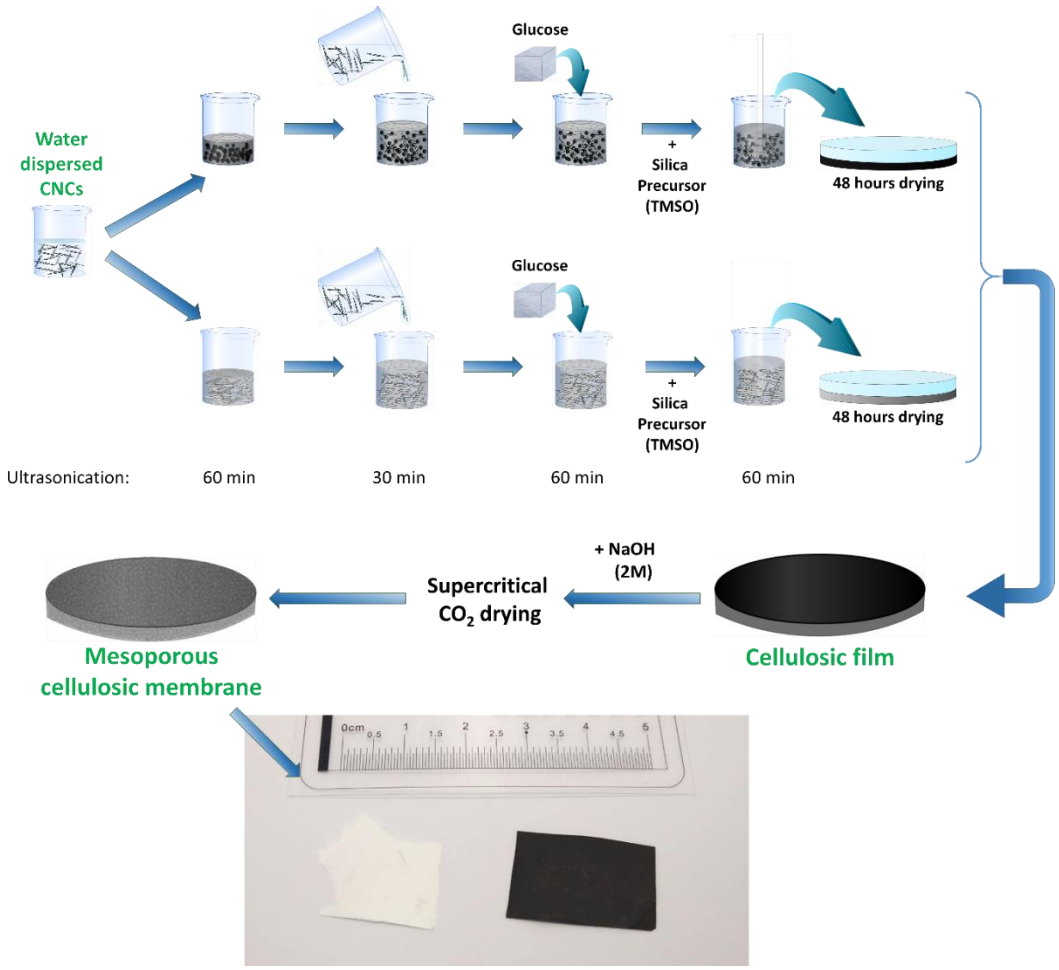

Scheme 5.1. Schematic diagram displaying the fabrication of mesoporous cellulose nanocrystal nanohybrids based on cobalt ferrite nanoparticles and graphite with optical photograph showing the macroscopic appearance of neat MCNC membrane and the 20 wt.% $CoFe_2O_4$ nanocomposite.

Table 5.1. Synthesis parameters of the prepared films.

Sample	CNC (mg)	Nanoparticle (mg)	Glucose (mg)	TMOS (µL)
CNC	100	-	-	-
MCNC	100	-	100	100
MCNC/$CoFe_2O_4$-1	99	1	100	100
MCNC/$CoFe_2O_4$-5	95	5	100	100
MCNC/$CoFe_2O_4$-10	90	10	100	100
MCNC/$CoFe_2O_4$-20	80	20	100	100
MCNC/graphite -1	99	1	100	100
MCNC/graphite -5	95	5	100	100
MCNC/graphite -10	90	10	100	100
MCNC/graphite -20	80	20	100	100

Similarly to previous experimental chapters, XRD patterns, FTIR measurements and SEM images were collected. In addition, Nitrogen sorption experiments were carried out to determine the surface area via the BET method. Thermal stability was evaluated by TGA measurements. Magnetic hysteresis loops were measured using a VSM. Electrical conductivity was measured using the four-point probe method, applying Equation 2.6.

5.3. Results and discussion

5.3.1. Physicochemical and structural characterisation

FTIR spectra in **Figure 5.1a** show the characteristic conformational features of cellulose nanocrystals for CNC and MCNC films. As explained in previous chapters, cellulose presents its characteristic peaks in the 3650–3200 cm^{-1} and 1800–800 cm^{-1} regions. Graphite presents a broad band corresponding to the -OH stretching at 3600–3000 cm^{-1} region, with other bands due to the carboxyl C=O, C-C, O-H, and C-O groups in the fingerprint 1800–600 cm^{-1} region. [20] Finally, a relatively weak IR signal is observed for cobalt ferrite nanoparticles, excluding the intense peak at 575 cm^{-1} due to the stretching of Fe^{3+}–O^{2-}.[21] Overall, the spectra obtained for fabricated nanohybrids are a superposition of the spectra of each individual component and no band displacement is observed. However, the presence of a new weak peak at 894 cm^{-1} is observed for the MCNC/$CoFe_2O_4$ 20 wt.% sample. This band arises from the O-H bond in ferrites, suggesting an interaction between the surface hydroxyl groups of CNCs with the cobalt ferrite nanoparticles.[22]

Besides, the XRD pattern in **Figure 5.1b** for the CNC film presents three prominent peaks at 2θ angles of 14.9, 16.5 and 22.7º, which can be ascribed to the *(1-10)*, *(101)* and *(200)* planes of the cellulose I structure.[23,24] MCNC film shows virtually the same XRD pattern, indicating that no damage was impaired to the crystalline structure of CNCs during the silica removal by alkali treatment. Conversely, graphite presents a sharp diffraction peak at 2θ = 26.6º corresponding to the *(002)* plane, indicating a *d* spacing of 0.34 nm.[25] Cobalt ferrite nanoparticles display narrow diffraction peaks at 2θ angles 30.1, 35.5, 43.1, 56.9 and 62.6º corresponding to *(220)*, *(311)*, *(400)*, *(511)* and *(440)* planes of the inverse cubic spinel structure with space group F*d*-3$_m$.[26]

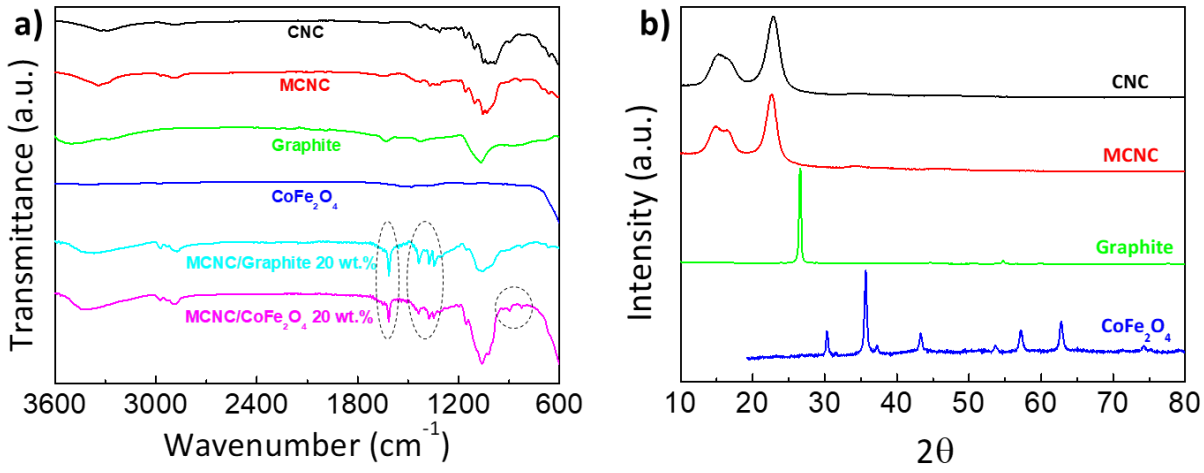

Figure 5.1. FTIR spectra of synthesised cellulose nanocrystals, (a) and XRD patterns (b) of CNC, graphite and $CoFe_2O_4$.

5.3.2. Porous structure of the nanohybrids

SEM analyses of the prepared films' cross-sections were performed to get insights into the porous structure of the fabricated nanohybrids. As depicted in **Figure 5.2**, mesoporous films display a highly porous structure compared to neat CNC film, which is composed of tightly packed CNC layers, forming a dense structure (**Figure 5.2a**). A higher magnification image shown as an inset in **Figure 5.2b** denotes the presence of randomly and loosely packed CNCs within the neat mesoporous MCNC film.[27] The images shown for 5 wt.% filler content are representative of the remainder concentrations allowing to conclude that no morphological changes are observed in the polymer matrix after the incorporation of nanoparticles, which remain well dispersed in the CNC microstructure (either cobalt ferrite in **Figure 5.2c** or graphite in **Figure 5.2d**), confirming that the fabrication approach here followed allows obtaining highly porous nanohybrids which may show large specific surface areas.

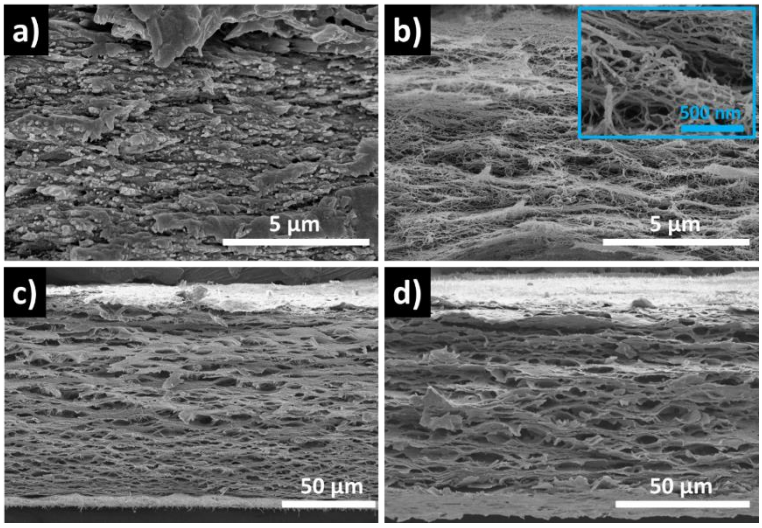

Figure 5.2. Representative SEM micrographs showing the synthesised materials cross-sections: a) non-porous CNC film; b) mesoporous MCNC film with higher magnification inset; c) MCNC/$CoFe_2O_4$ 5 wt.% and d) MCNC/graphite 5 wt.%.

The porous character of the fabricated structures was further analysed by N_2 adsorption-desorption isotherms. N_2 adsorption-desorption isotherms of synthesised cobalt ferrite and graphite nanohybrids in **Figure 5.3a** present the classical type IV isotherm shape. The observed hysteresis loop is ascribed to the capillary process linked to the mesopore filling, indicating that the structures present pores within the 2-50 nm range.[28] The specific surface area (S_{BET}) of mesoporous nanohybrids, calculated according to the BET method, is found to be in the 162-196 $m^2 \cdot g^{-1}$ range depending on the composition, which is in contrast with the S_{BET} of 11.2 $m^2 \cdot g^{-1}$ obtained for neat CNC film fabricated after the simple self-assembly of aqueous CNC dispersion (**Figure 5.3b**). It is also observed that nanohybrids keep the high surface area of pure MCNC film, indicating that the presence of inorganic particles (graphite and $CoFe_2O_4$) does not substantially modify the self-assembly process of CNCs and TMOS during EISA. Actually, in spite of the low S_{BET} of 26.7 and 33.6 $m^2 \cdot g^{-1}$ achieved for $CoFe_2O_4$ and graphite, respectively (**Figure 5.3c**), these particles provide additional surface area to the mesoporous cellulosic structure, resulting in increased BET surface areas by up to 20 %. More interestingly, the obtained S_{BET} results remain well above the 63.5 $m^2 \cdot g^{-1}$ reported for other magnetic systems such as nanofibrillated cellulose/Fe_3O_4 aerogels,[29] suggesting that such mesoporous structures are a suitable alternative for the fabrication of highly-porous magnetic materials.

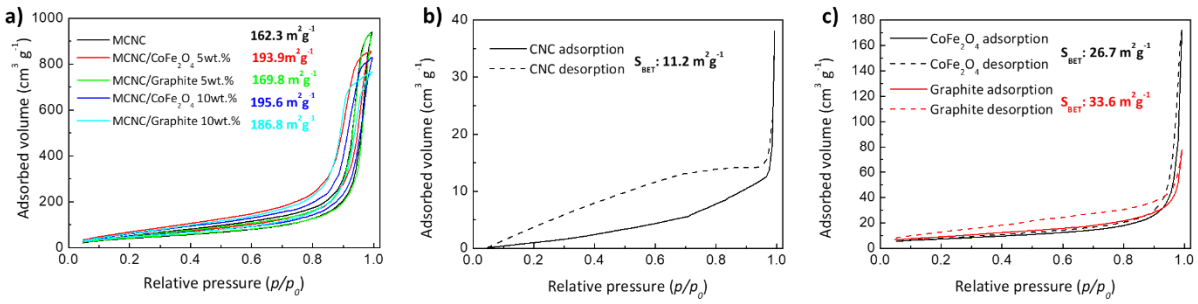

Figure 5.3. N_2 adsorption-desorption isotherms of mesoporous nanohybrids (a) and DFT pore size analysis on the desorption branch of the BET isotherm for the MCNC film.

5.3.3. Thermal properties

The thermal degradation behaviour of mesoporous nanohybrids has been evaluated by thermogravimetric analysis (TGA). **Figure 5.4** shows the TGA traces and their corresponding weight loss rates (represented as the first derivative of the TGA curve, the DTG) for the non-porous CNC film, the raw MCNC membrane and the 20 wt.% composites containing $CoFe_2O_4$ and graphite. The main representative thermodegradation parameters, including the onset of thermal degradation temperature, $T_{10\%}$, defined as the temperature at 10 % mass loss, the temperature at which the maximum degradation rate is obtained, T_{peak}, and maximum degradation rate, α_{max}, are summarised in **Table 5.2**. It is observed that the non-porous CNC films begin to degrade at relatively low temperatures, with a $T_{10\%}$ of 166.1 ºC attaining its maximum degradation rate (T_{peak}) at 173.1 ºC as a result of the depolymerisation, dehydration and decomposition of cellulosic glycosyl units upon heating.[30] The onset of the degradation process is notably delayed up to 218.3 ºC (and T_{peak} up to 326.9 ºC) for the neat MCNC membrane.

Moreover, the two-stage thermodegradation process suffered by CNC film, indicated by the two well-resolved peaks in **Figure 5.4b**, is shifted to a single-stage process, as noticed by the presence of one maximum in the DTG curve. These differences suggest that the thermodegradation process of both CNC and MCNC samples is different. Lin and Dufresne concluded that this enhanced thermal stability and the shift from one-stage to two-stage thermodegradation originates from the removal of negative $–OSO_3^-$ charges onto CNC surfaces, which is here accomplished during the silica dissolution step with 2M NaOH.[31]

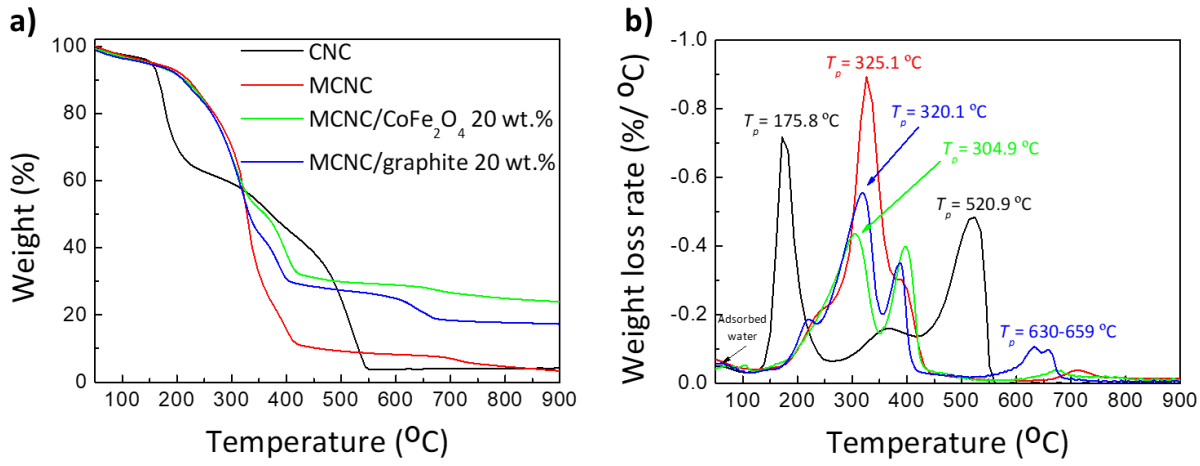

Figure 5.4. Thermogravimetric traces (a) and weight loss rates (b) of neat CNC, MCNC and MCNC nanohybrids containing 20 wt.% of $CoFe_2O_4$ and graphite.

Regarding the nanohybrids, it is observed that the presence of low amounts (1 wt.%) of both $CoFe_2O_4$ and graphite boost thermal degradation reactions of cellulose as indicated by the decrease in the onset of thermal degradation of neat MCNC membranes by 79.4 and 67.3 °C respectively.

Table 5.2. Characteristic thermodegradation temperatures ($T_{10\%}$ and T_{peak}) and maximum degradation rates (α_{max}) of MCNC nanohybrids.

Sample	$T_{10\%}$ (°C)	T_{peak} (°C)	α_{max} (%/°C)
CNC	166	173	- 0.71
MCNC	218	327	- 1.03
MCNC/CoFe₂O₄-1	139	269	- 0.59
MCNC/CoFe₂O₄-5	155	296	- 0.41
MCNC/CoFe₂O₄-10	165	293	- 0.36
MCNC/CoFe₂O₄-20	211	316	- 0.54
MCNC/graphite -1	151	262	- 0.49
MCNC/graphite -5	207	322	- 0.71
MCNC/graphite -10	214	323	- 0.54
MCNC/graphite -20	213	307	- 0.43

This behaviour has been observed in several cellulose/nanoparticle composite systems and is ascribed to the high susceptibility of cellulose to undergo thermally-induced degradation events in the presence of certain inorganic particles which act as catalysing agents.[4,32] It is worth noting that the char residue at 800 ºC matches with the initial weight fraction of the inorganic phase (it increases from 4 wt.% for neat CNC or MCNC to 24.5 and 29.1 wt.% for the graphite and $CoFe_2O_4$ nanohybrids having 20 wt.%).

Interestingly, the thermal stability is continuously increased with increasing inorganic phase content, reaching T_{peak} values of 315.8 and 307.1 ºC for MCNC/$CoFe_2O_4$ and MCNC/graphite nanocomposites bearing 20 wt.% in comparison with 173.1 ºC for CNC film. At the same time, α_{max} values drop with increasing inorganic phase concentration. The increased resistance to the thermodegradation process upon particle addition arises from the concomitant flame-retardant behaviour of cobalt ferrite and graphite,[33] and their influential role as barriers to the permeation of combustion products during degradation.[34,35] Therefore, two competitive and overlapping effects can be found upon cobalt ferrite/graphite addition into the MCNC matrix. At low concentrations, cobalt ferrite and graphite remain well-dispersed within the porous cellulosic network, and their catalysing effect dominates the degradation process (see **Figure 5.2** for representative morphological images). However, as the filler concentration increases, they may form a tortuous network of particles that serve as barriers to the degradation by-products' hindrance.[36]

5.3.5. Magnetic and electrical properties

To explore the potential of the synthesised nanohybrids for porous sensor and actuator applications, their room temperature magnetic properties have been evaluated using a vibrating sample magnetometer (VSM). The M-H measurements of MCNC/$CoFe_2O_4$ nanohybrids shown in **Figure 5.5a** within the −1.8 to 1.8 T range are characterised by a marked hysteresis loop due to the ferromagnetic nature of cobalt ferrite nanoparticles.[37] It is also observed that the magnetisation increases with increasing applied field until it reaches the M_s. Such M_s increases linearly with $CoFe_2O_4$ concentration to yield a maximum value of 8.77 emu·g^{-1} for the 20 wt.% nanohybrid (as a matter of fact, $CoFe_2O_4$ presents a M_s of 53 emu·g^{-1} at 1.5 T).[38] The coercivity (H_c) arising from the ferromagnetic behaviour of $CoFe_2O_4$ nanoparticles remains barely unchanged at 0.21 T for all the compositions. The fact that M_s increases linearly with $CoFe_2O_4$ concentration and the magnetisation curve shape suggests that ferromagnetic nanoparticles remain randomly oriented and well-distributed within the

porous cellulosic structure. Indeed, the obtained M_s values remain slightly above previously reported works dealing with biopolymer-based magnetic nanocomposites such as the ~10 emu·g^{-1} achieved for carboxymethyl cellulose/Fe_3O_4 with nanoparticle concentration of 30 wt.%, [39] or 6.2 emu·g^{-1} for cellulose/Fe_2O_3/Ag with a Fe content of 45.1 wt.%,[40] and match the performance of petroleum-based magnetoactive composites such as poly(vinylidene fluoride) (PVDF).[41,42]

The electrical conductivity of porous nanohybrids has been measured through the 4-point probe method. Results in **Figure 5.5b** show that, similarly to other fibrous cellulosic materials, [43] porous MCNC film presents a low electrical conductivity of 8 ± 5 x 10^{-6} S·m^{-1}. Upon graphite incorporation, the conductivity rises to a maximum value of 9.26 ± 0.04 S·m^{-1} for the nanohybrid containing 10 wt.%, which remains slightly above the conductivity values reported for cellulose/carbon nanotube aerogels,[44,45] but bearing the advantage of using cheap fillers. This increase of several orders of magnitude arises from the formation of a continuous three-dimensional structure of conducting fillers known as a percolative network, providing efficient routes for electron flow.[46] Interestingly, obtained conductivities are appropriate to develop EMI shielding materials.[10] It is to notice that a larger graphite concentration yield markedly lower conductivity values after percolation. This is explained in terms of poorer graphite distribution within the electrically insulating cellulosic network, which reduces the number of percolation paths through the sample.[47] As expected, the hybrids containing cobalt ferrite nanoparticles are characterised by concentration-independent electrical conductivity, with conductivities similar to that of neat MCNC film.

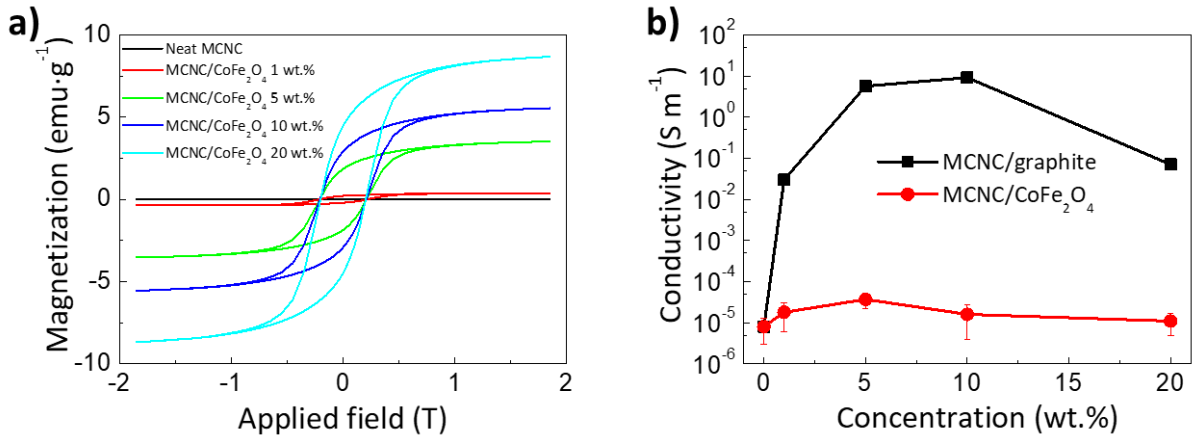

Figure 5.5. (a) Room-temperature hysteresis loops for mesoporous cellulosic films containing $CoFe_2O_4$ and (b) electrical conductivity values of MCNC-based nanohybrids as a function of filler concentration.

The large specific surface area of the MCNC matrix and the hydrophilic character of cellulose make these materials especially interesting for the removal of pollutants from water. Interestingly, the presence of $CoFe_2O_4$ nanoparticles within the nanohybrid may enable easy removal of the material from water through the application of external magnetic fields. Accordingly, as a proof of concept, MCNC/$CoFe_2O_4$ 20 wt.% nanohybrid was considered for removing methylene blue (MB) from an aqueous solution, as shown in **Figure 5.6a**. During the experiment, the absorbance of the solution was measured at regular time intervals, and the amount of the removed dye with respect to the nanohybrid ($\mu g \cdot g^{-1}$) was obtained. These results shown in **Figure 5.6b** indicate a nearly linear MB removal from the aqueous solution in the time investigated (3 h). 2365 µg of MB were removed per gram of MCNC/CoFe2O4 at 20 wt.% after 3 h, accounting for 30 % of the total MB present in the solution. Such efficient removal of MB through adsorption arises from the electrostatic interactions between the cationic MB and the negatively charged CNC surfaces. In contrast to many batch processes, where freely dispersed powder systems are used, this purification material can be quickly recovered via external magnetic fields. Overall, these results highlight the potential of synthesised mesoporous cellulosic magnetic materials for environmental remediation applications where having the chance of an easy recovery is of the utmost importance.

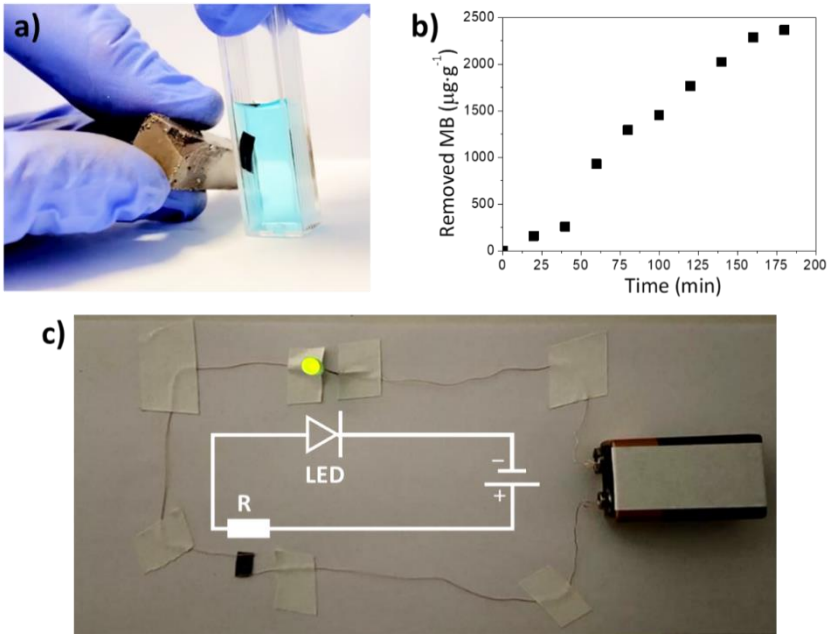

Figure 5.6. (a) Photograph showing the recovery of MCNC/CoFe2O4 20 wt.% sample from an aqueous methylene blue dissolution with a magnet; (b) plot showing the removal of methylene blue from the aqueous dissolution using the mesoporous membrane and (c) photograph highlighting the use of MCNC/graphite 20 wt.% as an electrically conducting material into a simple electrical circuit (the equivalent electrical circuit is shown in white).

MCNC/graphite materials can be used in electrical circuits thanks to their electrical conducting character. **Figure 5.6c** displays a simple electrical circuit composed of a battery (9 V), a green light-emitting diode (LED) and a piece of MCNC/graphite 20 wt.% sample (black square, identified as "R"). Soon, these materials can be applied as sensors where the presence of a given analyte could change the resistance (and thus, conductivity) of the mesoporous nanohybrid. This change will be reflected in differences in the electrical current, yielding different light intensities.

5.4. Conclusions

Magnetically and electrically active porous structures based on renewable resources and having large specific surface areas are presented here. Based on a soft-templating approach, water-dispersed CNCs are mixed with an alkoxysilane precursor to obtaining a solid nanostructured composite upon an evaporation induced self-assembly process. Subsequently, the silica phase is selectively removed through a mild alkaline treatment to yield a mesoporous structure with a large specific surface area. $CoFe_2O_4$ nanoparticles and graphite particles have been introduced during this process to provide functional properties to the membranes. Morphological observations reveal that the original three-dimensional porous structure composed of randomly and loosely entangled CNCs is not modified in the presence of inorganic particles, allowing to obtain specific surface areas as large as 193.9 $m^2 \cdot g^{-1}$. Interestingly, nanohybrids display an enhanced thermal stability thanks to the tortuous path provided by $CoFe_2O_4$ and graphite. At the same time, a maximum magnetisation value of 8.77 $emu \cdot g^{-1}$ and a conductivity of 9.26 ± 0.04 $S \cdot m^{-1}$ were obtained for samples comprising 20 wt.% of $CoFe_2O_4$ and 10 wt.% of graphite, respectively. Interestingly, such nanohybrids match the properties of traditional petroleum-based magnetoactive composites. Hence, this work provides a means for developing bio-based magnetically-active or electrically-conducting free-standing composite membranes with large surface areas, suitable for applications in the fields of sensors and actuators.

5.5. References

1 M. Giese and M. Spengler, Cellulose nanocrystals in nanoarchitectonics – towards photonic functional materials, *Mol. Syst. Des. Eng.*, 2019, **4**, 29–48.

2 E. Lizundia, T.-D. Nguyen, J. L. Vilas, W. Y. Hamad and M. J. MacLachlan, Chiroptical luminescent nanostructured cellulose films, *Mater. Chem. Front.*, 2017, **1**, 979–987.

3 X. Xu, J. Zhou, L. Jiang, G. Lubineau, T. Ng, B. S. Ooi, H.-Y. Liao, C. Shen, L. Chen and J. Y. Zhu, Highly transparent, low-haze, hybrid cellulose nanopaper as electrodes for flexible electronics, *Nanoscale*, 2016, **8**, 12294–12306.

4 E. Lizundia, U. Goikuria, J. L. Vilas, F. Cristofaro, G. Bruni, E. Fortunati, I. Armentano, L. Visai and L. Torre, Metal nanoparticles embedded in cellulose nanocrystal based films: material properties and post-use analysis, *Biomacromolecules*, 2018, acs.biomac.8b00243.

5 M. Grzelczak, J. Vermant, E. M. Furst and L. M. Liz-Marzán, *ACS Nano*, 2010, 4, 3591–3605.

6 W. Bauhofer and J. Z. Kovacs, A review and analysis of electrical percolation in carbon nanotube polymer composites, *Compos. Sci. Technol.*, 2009, **69**, 1486–1498.

7 P. Martins and S. Lanceros-Méndez, Polymer-Based Magnetoelectric Materials, *Adv. Funct. Mater.*, 2013, **23**, 3371–3385.

8 H. Huang, P. He, T. Huang, S. Hu, T. Xu, H. Gu, S. Yang, L. Song, X. Xie and G. Ding, Electrochemical Strategy for Flexible and Highly Conductive Carbon Films: The Role of 3-Dimensional Graphene/Graphite Aggregates, *ACS Appl. Mater. Interfaces*, 2019, **11**, 1239–1246.

9 Y. Mamunya, L. Matzui, L. Vovchenko, O. Maruzhenko, V. Oliynyk, S. Pusz, B. Kumanek and U. Szeluga, Influence of conductive nano- and microfiller distribution on electrical conductivity and EMI shielding properties of polymer/carbon composites, *Compos. Sci. Technol.*, 2019, **170**, 51–59.

10 J. Tolvanen, J. Hannu, M. Hietala, K. Kordas and H. Jantunen, Biodegradable multiphase poly(lactic acid)/biochar/graphite composites for electromagnetic interference shielding, *Compos. Sci. Technol.*, 2019, **181**, 107704.

11 J. Thévenot, H. Oliveira, O. Sandre and S. Lecommandoux, Magnetic responsive polymer composite materials, *Chem. Soc. Rev.*, 2013, **42**, 7099–7116.

12 Y. Zhan, Y. Meng, W. Li, Z. Chen, N. Yan, Y. Li and M. Teng, Magnetic recoverable MnFe2O4/cellulose nanocrystal composites as an efficient catalyst for decomposition of methylene blue, *Ind. Crops Prod.*, 2018, **122**, 422–429.

13 W. C. E. Lizundia, M. Jimenez, C. Altorfer, M. Niederberger, Electroless plating of platinum nanoparticles onto mesoporous cellulose films for catalytically active free-standing materials, *Cellulose*.

14 J. Guo, I. Filpponen, L. S. Johansson, P. Mohammadi, M. Latikka, M. B. Linder, R. H. A. Ras and O. J. Rojas, Complexes of Magnetic Nanoparticles with Cellulose Nanocrystals as Regenerable, Highly Efficient, and Selective Platform for Protein Separation, *Biomacromolecules*, 2017, **18**, 898–905.

15 M. Giese, L. K. Blusch, M. Schlesinger, G. R. Meseck, W. Y. Hamad, M. Arjmand, U. Sundararaj and M. J. MacLachlan, Magnetic Mesoporous Photonic Cellulose Films, *Langmuir*, 2016, **32**, 9329–9334.

16 K. E. Shopsowitz, H. Qi, W. Y. Hamad and M. J. Maclachlan, Free-standing mesoporous silica films with tunable chiral nematic structures., *Nature*, 2010, **468**, 422–425.

17 J. A. Kelly, M. Giese, K. E. Shopsowitz, W. Y. Hamad and M. J. MacLachlan, The development of chiral nematic mesoporous materials, *Acc. Chem. Res.*, 2014, **47**, 1088–1096.

18 E. Lizundia, T.-D. Nguyen, J. L. Vilas, W. Y. Hamad and M. J. Maclachlan, Chiroptical, morphological and conducting properties of chiral nematic mesoporous cellulose/polypyrrole composite films, *J. Mater. Chem. A*, , DOI:10.1039/C7TA05684B.

19 J. A. Kelly, M. Yu, W. Y. Hamad and M. J. Maclachlan, Large, Crack-Free Freestanding Films with Chiral Nematic Structures, *Adv. Opt. Mater.*, 2013, **1**, 295–299.

20 R. Gao, N. Hu, Z. Yang, Q. Zhu, J. Chai, Y. Su, L. Zhang and Y. Zhang, Paper-like graphene-Ag composite films with enhanced mechanical and electrical properties, *Nanoscale Res. Lett.*, 2013, **8**, 32.

21 R. A. Bohara, N. D. Thorat, H. M. Yadav and S. H. Pawar, One-step synthesis of uniform and biocompatible amine functionalised cobalt ferrite nanoparticles: a potential carrier for biomedical applications, *New J. Chem.*, 2014, **38**, 2979.

22 U. Klekotka, M. Rogowska, D. Satuła and B. Kalska-Szostko, Characterisation of ferrite nanoparticles for preparation of biocomposites, *Beilstein J. Nanotechnol.*, 2017, **8**, 1257–1265.

23 D. Liu, T. Zhong, P. R. Chang, K. Li and Q. Wu, Starch composites reinforced by bamboo cellulosic crystals, *Bioresour. Technol.*, 2010, **101**, 2529–2536.

24 N. Lin, C. Bruzzese and A. Dufresne, TEMPO-oxidized nanocellulose participating as crosslinking aid for alginate-based sponges, *ACS Appl. Mater. Interfaces*, 2012, **4**, 4948–4959.

25 Y. Wen, K. He, Y. Zhu, F. Han, Y. Xu, I. Matsuda, Y. Ishii, J. Cumings and C. Wang, Expanded graphite as superior anode for sodium-ion batteries, *Nat. Commun.*, , DOI:10.1038/ncomms5033.

26 E. Lizundia, A. Maceiras, J. L. Vilas, P. Martins and S. Lanceros-Mendez, Magnetic cellulose nanocrystal nanocomposites for the development of green functional materials, *Carbohydr. Polym.*, 2017, **175**, 425–432.

27 D. K. C. Hänsel, E. Lizundia, A Single Li-Ion Conductor Based on Cellulose, *ACS Appl. Energy Mater.*

28 C. G. Sonwane and S. K. Bhatia, Characterisation of pore size distributions of mesoporous materials from adsorption isotherms, *J. Phys. Chem. B*, 2000, **104**, 9099–9110.

29 R. Xiong, C. Lu, Y. Wang, Z. Zhou and X. Zhang, Nanofibrillated cellulose as the support and reductant for the facile synthesis of Fe3O4/Ag nanocomposites with catalytic and antibacterial activity, *J. Mater. Chem. A*, 2013, **1**, 14910–14918.

30 M. Roman and W. T. Winter, Effect of sulfate groups from sulfuric acid hydrolysis on the thermal degradation behavior of bacterial cellulose, *Biomacromolecules*, 2004, **5**, 1671–1677.

31 N. Lin and A. Dufresne, Surface chemistry, morphological analysis and properties of cellulose nanocrystals with gradiented sulfation degrees, *Nanoscale*, 2014, **6**, 5384–5393.

32 U. Goikuria, A. Larrañaga, J. L. Vilas and E. Lizundia, Thermal stability increase in metallic nanoparticles-loaded cellulose nanocrystal nanocomposites, *Carbohydr. Polym.*, 2017, **171**, 193–201.

33 M. Ul-Islam, W. A. Khattak, M. W. Ullah, S. Khan and J. K. Park, Synthesis of regenerated bacterial cellulose-zinc oxide nanocomposite films for biomedical applications, *Cellulose*, 2014, **21**, 433–447.

34 A. Liu, A. Walther, O. Ikkala, L. Belova and L. A. Berglund, Clay nanopaper with tough cellulose nanofiber matrix for fire retardancy and gas barrier functions, *Biomacromolecules*, 2011, **12**, 633–641.

35 L. Medina, F. Carosio and L. A. Berglund, Recyclable nanocomposite foams of Poly(vinyl alcohol), clay and cellulose nanofibrils – Mechanical properties and flame retardancy, *Compos. Sci. Technol.*, 2019, **182**, 107762.

36 F. Carosio, J. Kochumalayil, F. Cuttica, G. Camino and L. Berglund, Oriented Clay Nanopaper from Biobased Components—Mechanisms for Superior Fire Protection Properties, *ACS Appl. Mater. Interfaces*, 2015, **7**, 5847–5856.

37 M. Rincon-Iglesias, E. Lizundia and S. Lanceros-Mendez, Water-soluble cellulose derivatives as suitable matrices for multifunctional materials, *Biomacromolecules*, , DOI:10.1021/acs.biomac.9b00574.

38 P. Martins, C. M. Costa, G. Botelho, S. Lanceros-Mendez, J. M. Barandiaran and J. Gutierrez, Dielectric and magnetic properties of ferrite/poly(vinylidene fluoride) nanocomposites, *Mater. Chem. Phys.*, 2012, **131**, 698–705.

39 B. Zengin Kurt, F. Uckaya and Z. Durmus, Chitosan and carboxymethyl cellulose based magnetic nanocomposites for application of peroxidase purification, *Int. J. Biol. Macromol.*, 2017, **96**, 149–160.

40 A. Maleki, H. Movahed and P. Ravaghi, Magnetic cellulose/Ag as a novel eco-friendly nanobiocomposite to catalyse synthesis of chromene-linked nicotinonitriles, *Carbohydr. Polym.*, 2017, **156**, 259–267.

41 P. Martins, A. Lasheras, J. Gutierrez, J. M. Barandiaran, I. Orue and S. Lanceros-Mendez, Optimising piezoelectric and magnetoelectric responses on CoFe2O4/P(VDF-TrFE) nanocomposites, *J. Phys. D. Appl. Phys.*, 2011, **44**, 495303.

42 J. Kim, J.-S. Choi, H. Yang, F. K. Ko and K. H. Kim, Alternating magnetic field heat behaviors of PVDF fibrous mats filled with iron oxide nanoparticles, *AIP Adv.*, 2016, **6**, 55907.

43 T. Ardyani, A. Mohamed, S. Abu Bakar, M. Sagisaka, Y. Umetsu, M. Hafiz Mamat, M. Khairul Ahmad, H. P. S. Abdul Khalil, S. M. King, S. E. Rogers and J. Eastoe, Electrochemical exfoliation of graphite in nanofibrillated kenaf cellulose (NFC)/surfactant mixture for the development of conductive paper, *Carbohydr. Polym.*, 2020, **228**, 115376.

44 H. Qi, E. Mäder and J. Liu, Electrically conductive aerogels composed of cellulose and carbon nanotubes, *J. Mater. Chem. A*, 2013, **1**, 9714–9720.

45 H.-D. Huang, C.-Y. Liu, D. Zhou, X. Jiang, G.-J. Zhong, D.-X. Yan and Z.-M. Li, Cellulose composite aerogel for highly efficient electromagnetic interference shielding, *J. Mater. Chem. A*, 2015, **3**, 4983–4991.

46 E. Lizundia, R. Sarasua, F. D 'angelo, A. Orlacchio, S. Martino, M. Kenny Josè and I. Armentano, Biocompatible Poly(L-lactide)/MWCNT Nanocomposites: Morphological Characterisation, Electrical Properties, and Stem Cell Interaction, *Macromol. Biosci.*, 2012, **12**, 870–881.

47 S. Khan, M. Ul-Islam, M. W. Ullah, M. Israr, J. H. Jang and J. K. Park, Nano-gold assisted highly conducting and biocompatible bacterial cellulose-PEDOT:PSS films for biology-device interface applications, *Int. J. Biol. Macromol.*, 2018, **107**, 865–873.

6. All-Natural Polymer Composites Based on ι-Carrageenan and Cellulose Nanocrystals as Environmentally Friendlier Electroactive Materials

Contrary to the previous chapters, CNCs have been employed as fillers to enhance the mechanical and dielectric properties of ι-carrageenan, a polysaccharide obtained from algae. Free-standing nanocomposites with a CNC concentration up to 20 wt.% were fabricated using water solely as a solvent by doctor blade casting. Uniaxial tensile testing shows a marked increase of Young's modulus for the 5 wt.% counterparts with no remarkable loss in ductility. Such increase, which remains well above the theoretical prediction obtained from Halpin-Tsai equations, indicates that CNCs are homogeneously dispersed within the matrix, as well as the presence of a strong carrageenan-CNC interface. Finally, the CNC incorporation enhances the real dielectric constant ε' and the AC conductivity values thanks to the additional carrageenan-CNC interfacial contributions to the dielectric response.

6.1. Introduction

A less known than cellulose but worthy of attention group of polysaccharides are carrageenans. Carrageenans are a group of polysaccharides which can be extracted from the cell walls of red algae (*Rhodophyta*).[1] Interestingly, the use of algae can valorise agricultural waste streams into higher-value bio-products, providing circular economy solutions for waste management.[2] These polymers present a linear chain structure composed of D-galactose and D-anhydrogalactose units, where galactans are partially sulfated ($-OSO_3^-$ groups).[1] Depending on the degree of sulfation on the disaccharide, three main types are found: kappa (κ), iota (ι), and lambda (λ), where their sulfate content is 20, 33 and 41 wt.%, respectively.[3] Similarly to HPC or NaCMC,[4] carrageenans present good film-forming properties. Because of their ability to develop water-based thermoresponsive gels when cooling below the critical temperature,[5] carrageenans have been mainly used as thickening/gelation additives for the food industry,[6] drug delivery,[7] and pharmaceutical fields.[8] They have also been used as edible materials for the packaging industry to form a protective barrier against flavours, gases, UV-light or moisture.

Among the three types of carrageenans, most of the efforts carried out so far have been focused on κ-carrageenan-based materials for food packaging and biomedical applications.[9–11] However, with an elongation at break of 1.9 ± 0.5 %, κ-carrageenan films show the limited possibility of developing flexible materials. On the contrary, native ι-carrageenan presents an elongation at break of 11.3 ± 1.3,[12] encouraging its use as a matrix for developing flexible, foldable and rollable multifunctional materials. In this sense, it is interesting to note that, compared with other carrageenan classes, scarce works have been devoted to using multifunctional materials based on ι-carrageenan. Possible reasons may arise from the fact that while κ-carrageenan forms strong thermo-reversible gels useful in the biomedical field and λ-carrageenan functions as a very efficient thickening agent in dairy products, ι-carrageenan gives soft elastic gels which can break apart during mechanical action.[1,7]

One strategy to expand the applicability of polymer-based materials is to tune their dielectric response, which allows implementation in electronics,[13] including flexible and stretchable electronics.[14] This has been typically achieved by incorporating inorganic fillers such as graphene oxide,[15] zinc oxide,[16] zeolites,[17] or barium titanate ($BaTiO_3$),[18]. In contrast, the incorporation of natural organic nanofillers may represent a new approach to develop all-renewable green multifunctional nanocomposites. In order to follow this strategy, CNCs result

a proper selection as they are naturally occurring piezoelectric materials.[19,20]

Instead of using cellulose as a matrix, smooth and free-standing ι-carrageenan nanocomposite films were developed through doctor blade casting using water solely as a solvent. CNCs up to a concentration of 20 wt.% were introduced to upgrade the thermal and mechanical properties and to tune the dielectric properties of native ι-carrageenan. The hydroxyl (-OH) groups of ι-carrageenan interact with the oxygen-containing groups onto CNC surfaces to provide well-dispersed nanoparticles with strong interfacial interaction. Overall, obtained results provide a proof of concept for developing dielectric materials using biomass residues as raw materials with strong applicability in electronics, including energy harvesters, wearable sensors or flexible/foldable displays.

6.2. Experimental

6.2.1. Sample preparation and characterisation

The fabrication of nanocomposite films follows the same route as the cellulose derivatives films, as shown in **Scheme 6.1**:

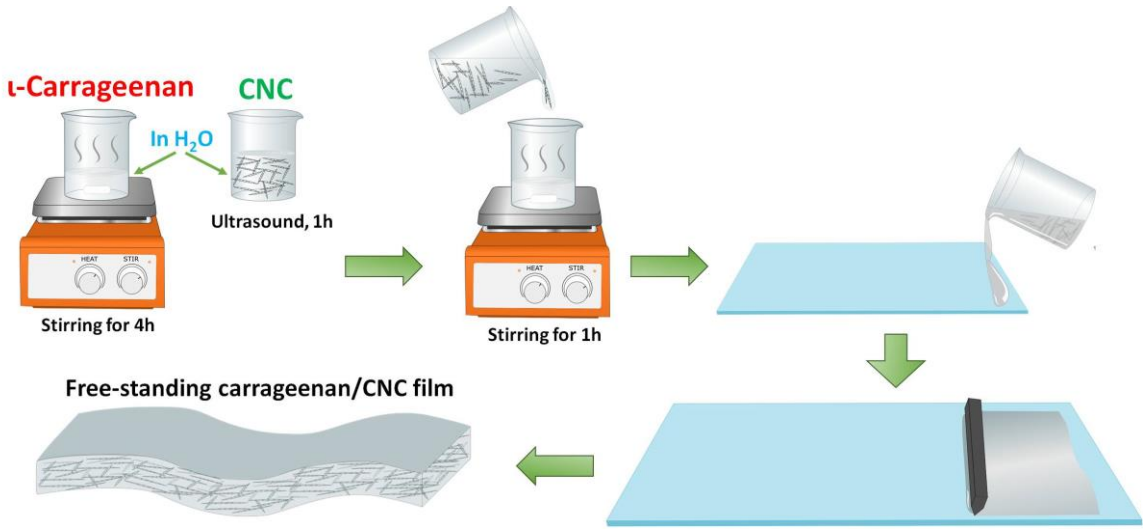

Scheme 6.1. Schematic diagram depicting ι-carrageenan/CNC nanocomposite film preparation.

First, ι-carrageenan was dissolved in distilled water at 80ºC by a magnetic stirrer for 4h to achieve a liquid solution instead of a gel, while CNCs (pH of 1.9 and a concentration of 1.5 wt.%), obtained as explained in Chapter 5, were dispersed in water using an ultrasound bath during 1h. Then, dispersed CNCs were incorporated into the aqueous ι-carrageenan solution,

and the resulting mixture was magnetically stirred for 1 h. Finally, single-layer films were cast onto clean glass substrates with a doctor blade. The process was carried out at a constant rate of approximately 4 $cm \cdot s^{-1}$ (equivalent to a simple shear rate of 0.6 s^{-1}), where the gap between the blade and the substrate was set at 800 μm. The substrate was previously heated at 80 ºC to avoid a lower solubility of ι–carrageenan from a quick cooling of the solution. After room temperature drying for 24 h, 25 ± 5 μm thick films were obtained.

The morphology of individual CNCs was analysed by a TEM. The cross-section morphology of the samples was evaluated by FESEM. Total transmittance experiments were analyzed with UV−vis spectrophotometer. FTIR measurements in ATR mode were performed. XRD patterns were collected. Thermal transitions of the nanocomposites were analyzed by DSC. Further, the thermodegradation behavior of the nanocomposites was determined by TGA. The mechanical properties of the nanocomposites were evaluated by tensile testing. Dielectric properties and AC conductivity were obtained by measuring the capacity and the dielectric losses following Equations (2.3), (2.4), and (2.5).

6.3. Results and discussion

6.3.1. Morphology and optical properties

Figure 6.1a shows that CNCs present the commonly obtained rod-shaped morphology for CNCs extracted through the sulfuric acid hydrolysis process, having diameters of about 12 nm and lengths of 140 ± 37 nm (statistics based on 60 counts from 4 TEM images). Furthermore, the corresponding cross-section SEM images of the carrageenan/CNC composite films are shown in **Figure 6.1** for a CNC concentration up to 20 wt.%. Pure carrageenan in **Figure 6.1b** shows a rough and compact surface with no pores. Increased surface roughness is observed when increasing CNC concentration from 1 wt.% to 20 wt.% (**Figure 6.1c** and **6.1d**, respectively), as shown in other works containing CNCs.[21] Interestingly, no voids are observed, suggesting good interfacial compatibility between the hosting carrageenan matrix and the reinforcing CNCs. It is also important to note that no CNC aggregates are observed in those SEM images, indicating that CNCs remain well distributed within the carrageenan matrix.

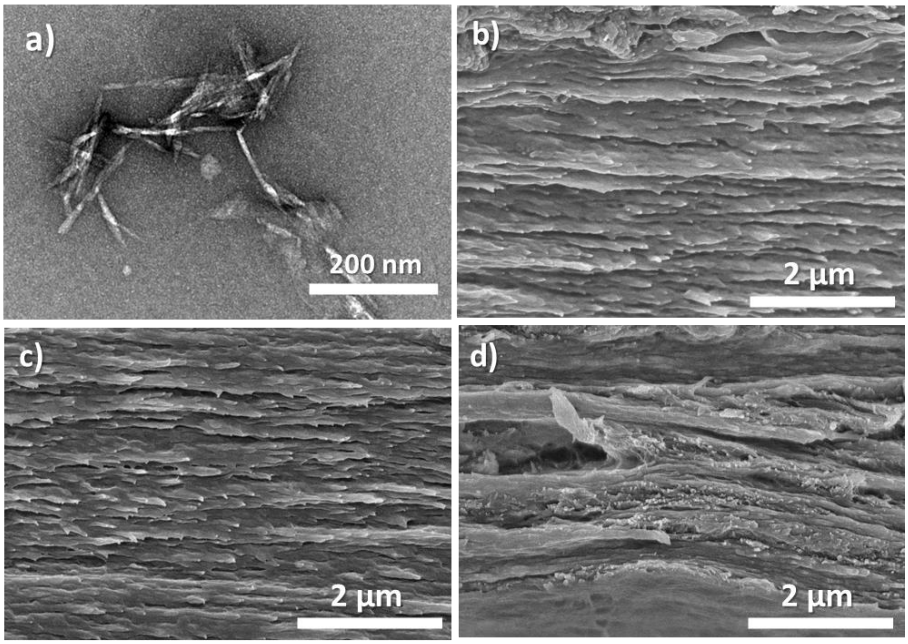

Figure 6.1. a) Representative TEM image of synthesised CNCs. Representative cross-section SEM images of carrageenan/CNC nanocomposite films with concentrations of: b) 0 wt.%; c) 1 wt.% and d) 20 wt.%.

The transmittance of the nanocomposite films within the λ = 200 - 800 nm region is depicted in **Figure 6.2**. The optical transparency of neat carrageenan in the λ = 540 – 560 nm region ((ASTM D1746−15 standard; Standard Test Method for Transparency of Plastic Sheeting) is about 69 %. This optical transparency continuously decreases to a minimum value of 34 % for the 20 wt.% counterpart, due to the heterogeneous nature of the material and higher nanocrystals agglomeration at high loadings.[22]

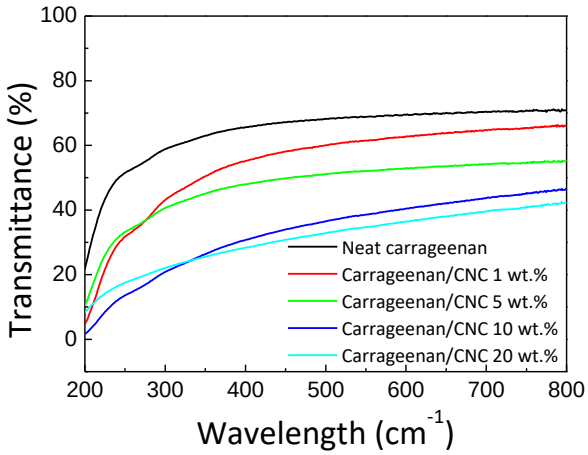

Figure 6.2. UV-vis transmittance spectroscopy for carrageenan/CNC composite films with concentrations of: 0 wt.%, 1 wt.%, 5 wt.%, 10 wt.% and 20 wt.%.

6.3.2. Physicochemical and structural characterisation

FTIR was conducted to investigate the interaction between the two components in the carrageenan/CNC composites. Accordingly, **Figure 6.3a** shows the FTIR spectra of carrageenan/CNC nanocomposite films containing up to 20 wt.% CNCs. The bands at 3600-3000 and 2949 cm^{-1} are related to the –OH and –CH stretching vibration, respectively, as commonly found in many other polysaccharides, while other narrower bands at 1261 cm^{-1} (arising from the O=S=O symmetric vibration), 1159 cm^{-1} (due to the C-O bridge), 1070 cm^{-1} (C-O stretch), 930 cm^{-1} (C-O-C linkage in 3,6-anhydro-D-galactose) and 850 cm^{-1} (C_4-O-S stretching vibration) are found.[23,24] It is observed that CNC incorporation slightly modifies the characteristic carrageenan vibration bands, where a small but continuous band displacement is achieved for the 3600-3000 cm^{-1} band. More precisely, as shown in **Figure 6.3b**, the maximum of this band is shifted from 3410 to 3371 cm^{-1} after adding 20 wt.% CNC. This shifting indicates the presence of hydrogen bonding interactions between these two polysaccharides as previously found for other CNC-reinforced nanocomposites.[21,25]

Figure 6.3c displays the XRD patterns corresponding to carrageenan/CNC nanocomposites. Neat carrageenan presents a broad peak centred at 2θ = 22.5º, which is ascribed to the amorphous ι-carrageenan.[23] New diffraction peaks arise upon CNC addition, especially for nanocomposites with concentrations larger than 5 wt.%. These peaks are found at 2θ = 14.9, 16.5 and 22.7º and correspond respectively to the *(1−10)*, *(110)* and *(200)* planes of cellulose I_β,[26,27] which consist of a monoclinic structure with two chains per unit cell.[28] The fact that the obtained XRD patterns result from a superposition between the patterns corresponding to neat carrageenan and CNC indicates that no crystallinity changes occur during nanocomposite preparation; i.e. no new crystalline regions are developed, and the crystalline integrity of CNCs keeps unchanged.

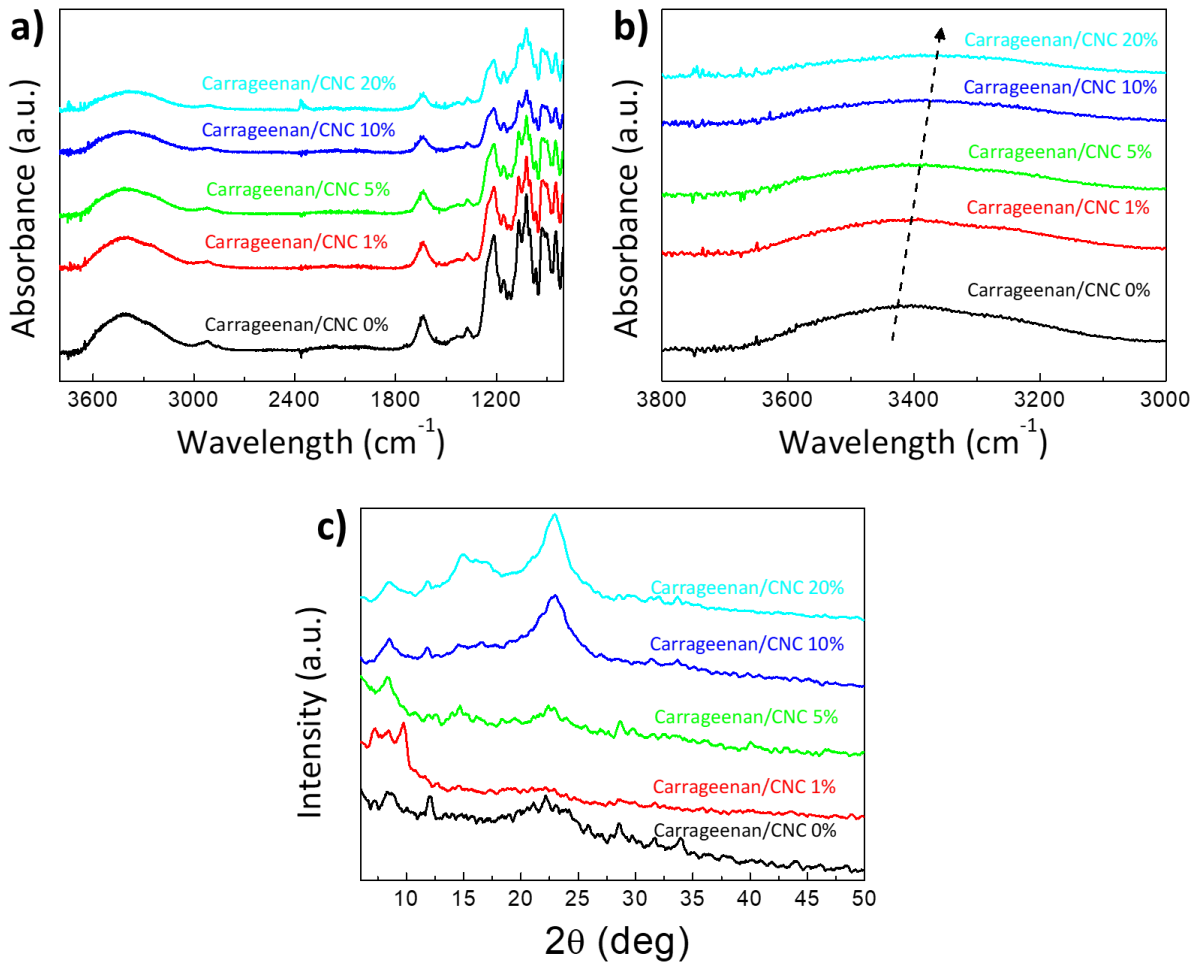

Figure 6.3. a) FTIR spectra and b) the enlarged spectra in the 3800 to 3000 cm^{-1} region; c) XRD patterns of carrageenan/CNC composites.

6.3.3. Thermal properties

Thermal transitions and thermodegradation behaviour of the nanocomposites have been evaluated by DSC and TGA, respectively. **Figure 6.4a** displays the DSC heating curves of ι-carrageenan/CNC nanocomposite films, where a broad endothermic curve centred at ~126 ºC associated with the melting of neat ι-carrageenan is seen. The melting temperature (T_m) of the nanocomposites is markedly enhanced up to 142-145 ºC upon CNC incorporation. These results are in line with the data shown by Savadekar et al., where an increase in T_m of ι-carrageenan from 125 to 132 with the addition of 1 wt.% of nanofibrillated cellulose was observed.[29] They indicate the strong interaction between the ι-carrageenan matrix and CNC fillers.

TGA traces in **Figure 6.4b** show the presence of three degradation steps. The first weight loss at temperatures below 150 ºC arises from water removal due to the characteristic high-

water affinity of polysaccharides. A second marked thermodegradation step in the range of 185-215 ºC comprising a weight loss of nearly 20 wt.% followed by a less substantial degradation process at temperatures above 225 ºC is observed due to the thermally induced ι-carrageenan degradation, where the sulphur dioxide in the polymeric backbone is degraded.[30] The presence of CNCs slightly decreases the thermal stability of ι-carrageenan films as T_{peak} (the temperature at which the maximum degradation rate occurs) is lowered from 214 ºC for the neat film to a minimum of 189 ºC for the nanocomposite containing 10 wt.% CNCs. This decreased thermal stability arises from the presence of sulphate groups on CNC surfaces, which catalyse thermodegradation events. However, when CNCs are incorporated at 20 wt.%, the thermal stability is comparable to that of neat polymer, thanks to the fact that CNCs act as barriers which reduce the permeation of combustion gases upon heating.[31]

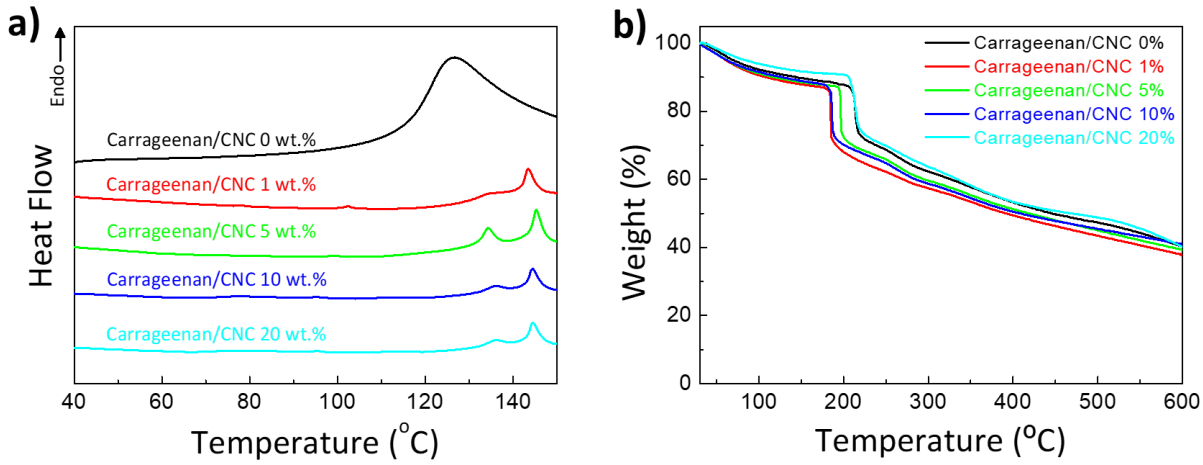

Figure 6.4. Thermal results of a) DSC analysis and b) TGA degradation of prepared carrageenan/CNC composites.

6.3.4. Mechanical properties

The representative stress-strain curves for the fabricated carrageenan/CNC nanocomposite films, depicted in **Figure 6.5a**, show a semiductile behaviour characteristic of many thermoplastic materials, comprising two regions corresponding to both elastic and plastic deformation. In addition, the average values and standard deviation of the most representative mechanical parameters (E, ε_y, σ_y, ε_b, and σ_b) are summarised in **Table 6.1**. It is observed that Young's modulus increases with the addition of CNCs from 231 ± 24 MPa for neat carrageenan up to a maximum of 1724 ± 50 MPa for the carrageenan/CNC 5 wt.% nanocomposite. This marked modulus increase, which can be observed in more detail in **Figure 6.5b**, is ascribed to the large-aspect ratio of CNCs and suggest a strong interfacial

adhesion between the carrageenan matrix and the reinforcing CNC phase as previously found for CNC-reinforced hydrogels.[32] Increasing the CNC concentration up to 5 wt.% slightly enhances σ_y, and the maximum elongation remains above 10 %. Then, ε_b values markedly decrease to a minimum of 4.7 ± 1.6 % for the nanocomposites having 20 wt.% CNCs. This ductility decrease is related to the presence of stress concentration regions in CNC-rich regions, which result in premature fracture of the film.[33] Similar behaviour was observed in κ-carrageenan/CNC composites,[21] where an E of 1300 MPa and an ε_b of 16% for samples containing 4 wt.% CNCs were shown, which is comparable to this work (E of 1724 ± 50 MPa and ε_b of 11.0 ± 2.6 % for 5 wt.% of CNC).

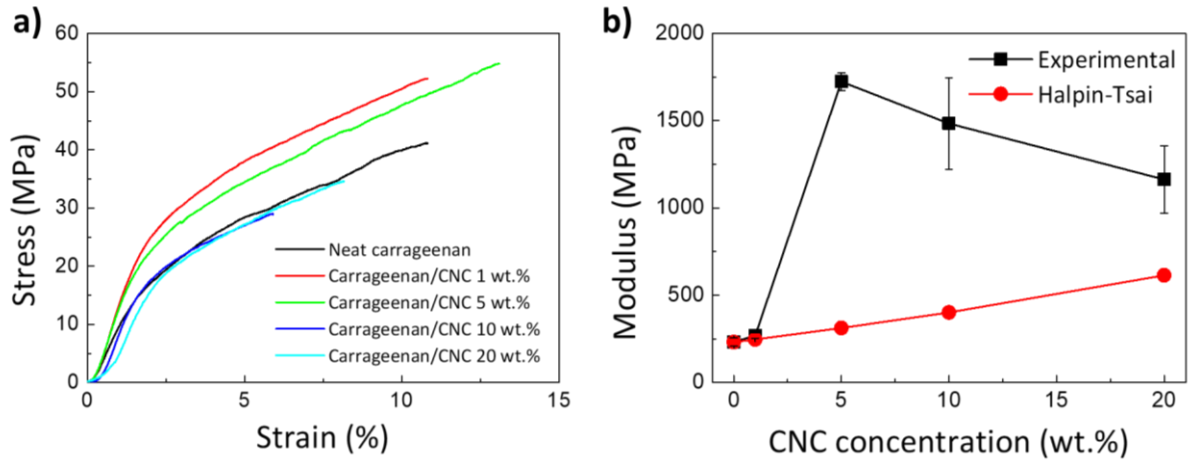

Figure 6.5. a) Representative stress-strain curves for carrageenan/CNC composite films and b) experimental data and fitting results according to the modified Halpin-Tsai model.

Yadav, M., et al., recently reported tensile strength values of 40.07 ± 2.80 MPa for κ-carrageenan/CNC composites comprising 5 wt.%, slightly below the 50.1 ± 5.3 MPa here obtained. However, the elongation at break value was much higher than observed for ι-carrageenan (24.33 ± 3.00 % vs 11.0 ± 2.6).[34] Overall, the largest CNC concentration leads to strong intermolecular interactions between CNCs, making them behave as a macroscopic fiber. Additionally, the fact that the composite comprising 5 wt.% of CNCs shows lower stress at break than obtained for 10 and 20 wt.% suggests that larger aggregates of CNCs were formed during casting, inducing local defects in the film.

Table 6.1. Table displaying the main representative parameters of tensile test for the fabricated nanocomposite films. *E*: Young's modulus; ε_y: elongation at yield; σ_y: stress at yield; ε_b: elongation at break; and σ_b: stress at break.

CNC (wt. %)	E (MPa)	ε_y (%)	σ_y (MPa)	ε_b (%)	σ_b (MPa)
0	231 ± 24	2.0 ± 0.4	17.4 ± 1.9	10.8 ± 1.2	40.1 ± 1.6
1	269 ± 15	2.1 ± 0.1	24.3 ± 2.4	12.3 ± 2.4	54.3 ± 8.4
5	1724 ± 50	1.8 ± 0.1	21.3 ± 0.7	11.0 ± 2.6	50.1 ± 5.3
10	1484 ± 263	2.5 ± 0.3	22.8 ± 5.1	7.0 ± 1.8	27.8 ± 8.0
20	1163 ± 193	2.3 ± 0.1	19.6 ± 1.4	4.7 ± 1.6	34.7 ± 5.5

Theoretical models are gaining importance in materials science as a tool for saving time and making approaches to the final composite properties. Among all the available models, the modified Halpin–Tsai is a semi-empirical model widely used to predict the elastic modulus of nanocomposites. Many works could be found on using this model for mechanical reinforcement predictions. Halpin-Tsai equations have been used to model as a function of the fibre length reinforcement degree of CNC-based nanocomposites.[34] Recently, Li, V. et al. used the modelling for reinforcement predictions of digital light processing 3D printable polymer using CNCs as fillers, obtaining accurate fitting values.[35] Also, this model was used to compare experimental values in PVA/CNC nanocomposites, where CNCs having two different lengths were studied.[36] Accordingly, to get further insights into the marked increase shown by Young's modulus, the experimentally obtained results are compared with the theoretical results according to a modified Halpin-Tsai model in Equation (3.3) in Chapter 3. In this case, the CNCs aspect ratio (set at 11 from the TEM images of individual CNCs). The CNC volume fraction within the nanocomposite (V_{CNC}) was extracted from the weight fraction of both components and their densities, assuming a density of 1.55 g·cm^{-3} for CNC,[37] and 1.37 g·cm^{-3} for carrageenan (taken from the manufacturer) and E_R value, defined as the ratio between Young's modulus of the filler and the matrix, was of 592 MPa, assuming an elastic modulus of CNC of 137 GPa.[38]

Figure 6.5b compares the experimental results with the theoretical values obtained following the modified Halpin-Tsai model. It is worthy to note that this model assumes the presence of a homogeneously distributed reinforcement phase within the hosting matrix with favourable matrix-filler interactions between the hydroxyls onto CNC surfaces and the hydroxyls pending from the ι-carrageenan.[39] Theoretical values are not in agreement with the

experimental values (except up to 1 wt.% of CNCs), remaining well-bellow obtained empirical results. The significant deviation observed, with a predicted modulus of 312 MPa *vs* the experimentally obtained 1724 ± 50 MPa for the 5 wt.% nanocomposite, suggests a strong interaction between the surface hydroxyl groups of cellulosic reinforcements with the sulfate groups of ι-carrageenan.

6.3.5. Electrical properties

The dielectric response of the samples was analysed to understand the relaxation processes of carrageenan/CNC nanocomposites as a function of CNC concentration.[40] Accordingly, **Figures 6.6a** and **6.6b** show the real dielectric constant (ε') and dielectric loss ($tan\ \delta$) as a function of frequency for all carrageenan/CNC composite films. All the samples present a similar behaviour independently of the CNC concentration. A high value of dielectric permittivity at low frequencies is observed in **Figure 6.6a**, which occurs due to the fluctuation of bound counterions.[41] ε' decreases when the frequency increases due to the limited dipolar mobility and the accumulation of charge carriers at the electrode–sample (Maxwell-Wagner-Sillars effect).[42] The high value of the dielectric constant is similar to the results reported in the literature for ι-carrageenan.[43] On the contrary, $tan\ \delta$ increases with increasing frequency for all samples as a result of relaxation processes within the amorphous carrageenan phases.[44] As summarised in **Figure 6.6d**, the dielectric constant ε' at 1 kHz increases at low CNC contents from 144.7 ± 7.1 x 10^5 for pure carrageenan to 369.5 ± 18.5 x 10^5 for the 10 wt.% nanocomposites, and then further decreases for higher CNC concentration. This dual effect can be ascribed to a poorer CNC dispersion and aggregation at high concentrations, where the nanofillers fail to provide available surfaces for conduction as similarly found in related polymer nanocomposite systems.[45]

Figure 6.6c shows the AC conductivity values as a function of frequency for all carrageenan/CNC nanocomposite films. As occurs in other polymeric systems, AC conductivity increases with increasing frequency up to 10^4 Hz due to high ion concentration and motion of carrageenan chains and space charge polarisation occurring at the electrode-sample interface.[46] For frequency above 10^4 Hz, the AC conductivity remains practically constant, showing a plateau upon frequency increase. Additionally, the presence of CNC increases the AC conductivity values up to a concentration of 10 wt.%. This behaviour is due to the presence of charge carriers in localised sites, mainly at the CNC/carrageenan interfaces, as further pathways for ion conduction are provided by CNC surfaces within the

nanocomposite.[46] The charge carrier movement takes place through hopping transport and can be described by the Jonscher law:[47]

$$\sigma'(\omega) \propto \omega^n \tag{6.1}$$

where ω is the angular frequency and the n parameter characterises a thermally activated hopping across an energy barrier ($0 < n < 1$). For all composite films, n ranges between 0.9 and 1, further confirming that the hopping conduction is responsible of the displacement of the charge carriers.

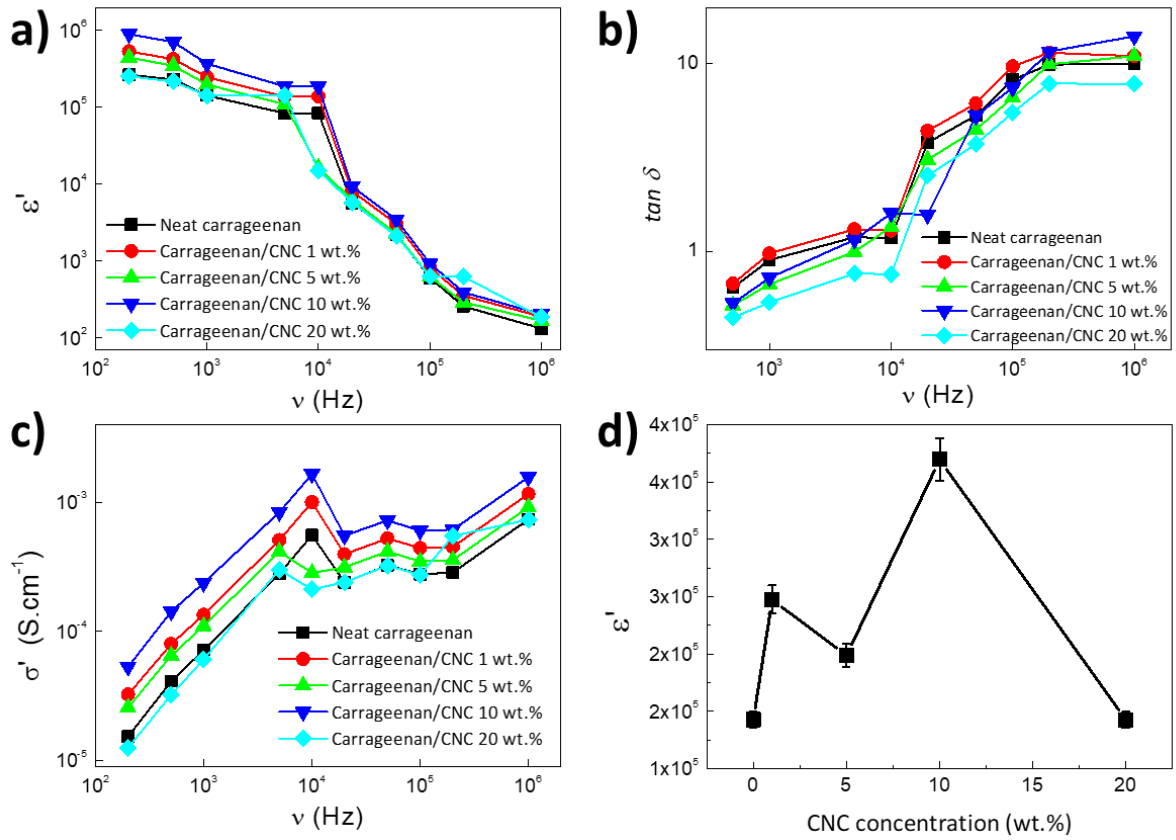

Figure 6.6. a) Real part of the dielectric constant; b) *tan δ* dielectric loss values; and c) AC conductivity values as a function of frequency for carrageenan/CNC nanocomposites. d) Dielectric constant values measured at 1 kHz for the studied compositions.

Finally, I-V curves were also analysed to get further insights into the conduction mechanism in carrageenan/CNC nanocomposite films. **Figure 6.7** shows the I–V curves for all composite films, where CNC content barely changes the DC conducting behaviour, indicating that CNC presence affects more efficiently the AC conductivity of carrageenan/CNC nanocomposites, mainly at high frequencies, due to the local contributions of interface effects and localised ion movement to the conduction processes. Further, it is to

notice the existence of two regimes of DC electrical conductivity: a lower conductivity regime up to approximately 2.0 V and a higher conductivity one above this voltage, which ascribed to the increase of charge carriers contributing to the conductivity process, related to the release of trapped charges from interface states.

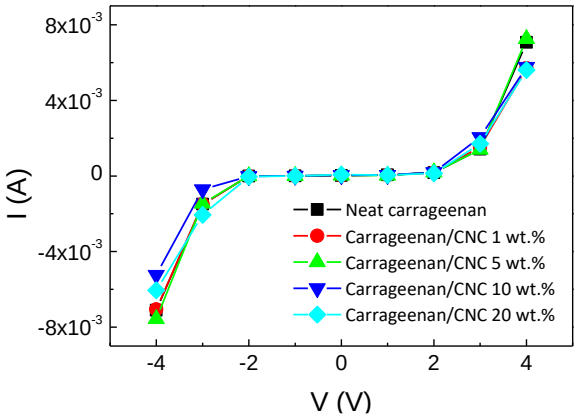

Figure 6.7. Characteristic I-V curves for carrageenan/CNC composite films with concentrations of 0 wt.%, 1 wt.%, 5 wt.%, 10 wt.% and 20 wt.%.

6.4. Conclusions

Free-standing mechanically tough films based on renewable resources have been obtained with a tailored electrical response. A polysaccharide from marine origin, ι-carrageenan, has been reinforced with CNCs. Morphological analysis reveals that doctor blade casting yields free-standing films where CNCs remain distributed within the matrix. The presence of CNCs lowers the transmitted visible light from 69% for neat ι-carrageenan to a minimum value of 34 % for the 20 wt.% nanocomposite film. On the other hand, incorporating CNCs into the ι-carrageenan matrix markedly improves the mechanical characteristics of the hosting matrix, with a 7-fold increase in Young's modulus with no ductility loss at a CNC concentration of 5 wt.%. Such increase, which largely exceeds the modified Halpin-Tsai model for the theoretical determination of the modulus, is ascribed to the strong and favourable CNC-carrageenan interfacial interaction achieved. Dielectric spectroscopy results show an increase in the real dielectric constant and AC conductivity with CNC concentration as a result of both charge carrier concentration and ionic conductivity increase arising from CNC interfaces. Finally, DC conductivity is characterised by two regimes with an increase of the electrical conductivity at a 2.0 V threshold. These results demonstrate the design of multifunctional materials from both marine and plant origin with tailored mechanical and dielectric performance.

6.5. References

1 V. L. Campo, D. F. Kawano, D. B. da Silva and I. Carvalho, Carrageenans: Biological properties, chemical modifications and structural analysis – A review, *Carbohydr. Polym.*, 2009, **77**, 167–180.

2 W. A. V. Stiles, D. Styles, S. P. Chapman, S. Esteves, A. Bywater, L. Melville, A. Silkina, I. Lupatsch, C. Fuentes Grünewald, R. Lovitt, T. Chaloner, A. Bull, C. Morris and C. A. Llewellyn, Using microalgae in the circular economy to valorise anaerobic digestate: challenges and opportunities, *Bioresour. Technol.*, 2018, **267**, 732–742.

3 T. Karbowiak, H. Hervet, L. Léger, D. Champion, F. Debeaufort and A. Voilley, Effect of plasticisers (water and glycerol) on the diffusion of a small molecule in iota-carrageenan biopolymer films for edible coating application, *Biomacromolecules*, 2006, **7**, 2011–2019.

4 M. Rincon-Iglesias, E. Lizundia and S. Lanceros-Mendez, Water-soluble cellulose derivatives as suitable matrices for multifunctional materials, *Biomacromolecules*, , DOI:10.1021/acs.biomac.9b00574.

5 D. J. Maciel, I. L. D. M. Ferreira, G. M. Da Costa and M. R. Da Silva, Nanocomposite hydrogels based on iota-carrageenan and maghemite: Morphological, thermal and magnetic properties, *Eur. Polym. J.*, 2016, **76**, 147–155.

6 S. Mabeau and J. Fleurence, Seaweed in food products: biochemical and nutritional aspects, *Trends Food Sci. Technol.*, 1993, **4**, 103–107.

7 L. Li, R. Ni, Y. Shao and S. Mao, Carrageenan and its applications in drug delivery, *Carbohydr. Polym.*, 2014, **103**, 1–11.

8 P. Laurienzo, Marine Polysaccharides in Pharmaceutical Applications: An Overview, *Mar. Drugs 2010, Vol. 8, Pages 2435-2465*, 2010, **8**, 2435–2465.

9 A. A. Oun and J. W. Rhim, Carrageenan-based hydrogels and films: Effect of ZnO and CuO nanoparticles on the physical, mechanical, and antimicrobial properties, *Food Hydrocoll.*, 2017, **67**, 45–53.

10 J. W. Rhim and L. F. Wang, Preparation and characterisation of carrageenan-based nanocomposite films reinforced with clay mineral and silver nanoparticles, *Appl. Clay Sci.*, 2014, **97**–**98**, 174–181.

11 J. W. Rhim, Physical-Mechanical Properties of Agar/κ-Carrageenan Blend Film and Derived Clay Nanocomposite Film, *J. Food Sci.*, 2012, **77**, N66–N73.

12 T. Barahona, H. J. Prado, P. R. Bonelli, A. L. Cukierman, E. L. Fissore, L. N. Gerschenson and M. C. Matulewicz, Cationization of kappa- and iota-carrageenan - Characterisation and properties of amphoteric polysaccharides, *Carbohydr. Polym.*, 2015, **126**, 70–77.

13 Y. Zhang, C. Ellingford, R. Zhang, J. Roscow, M. Hopkins, P. Keogh, T. McNally, C. Bowen and C. Wan, Electrical and Mechanical Self-Healing in High-Performance Dielectric Elastomer Actuator Materials, *Adv. Funct. Mater.*, 2019, **29**, 1808431.

14 S. K. Sinha, Y. Noh, N. Reljin, G. M. Treich, S. Hajeb-Mohammadalipour, Y. Guo, K. H. Chon and G. A. Sotzing, Screen-Printed PEDOT:PSS Electrodes on Commercial Finished Textiles for Electrocardiography, *ACS Appl. Mater. Interfaces*, 2017, **9**, 37524–37528.

15 J. Guan, C. Xing, Y. Wang, Y. Li and J. Li, Poly (vinylidene fluoride) dielectric composites with both ionic nanoclusters and well dispersed graphene oxide, *Compos. Sci. Technol.*, 2017, **138**, 98–105.

16 C. Mendes-Felipe, J. Oliveira, I. Etxebarria, J. L. Vilas-Vilela and S. Lanceros-Mendez, State-of-the-Art and Future Challenges of UV Curable Polymer-Based Smart Materials for Printing Technologies, *Adv. Mater. Technol.*, 2019, **4**, 1800618.

17 M. Lakhane, K. Bogle, R. Khairnar, S. Dahiwale, R. Sharma, V. Mokale and M. Mahabole, Dielectric properties of zeolite based metal oxide nanocomposites, *Nano-Structures & Nano-Objects*, 2019, **17**, 248–258.

18 H. Luo, D. Zhang, C. Jiang, X. Yuan, C. Chen and K. Zhou, Improved dielectric properties and energy storage density of poly(vinylidene fluoride-co-hexafluoropropylene) nanocomposite with hydantoin

epoxy resin coated BaTiO3, *ACS Appl. Mater. Interfaces*, 2015, **7**, 8061–8069.

19 Y. Zong, T. Zheng, P. Martins, S. Lanceros-Mendez, Z. Yue and M. J. Higgins, Cellulose-based magnetoelectric composites, *Nat. Commun. 2017 81*, 2017, **8**, 1–8.

20 Y. Calahorra, A. Datta, J. Famelton, D. Kam, O. Shoseyov and S. Kar-Narayan, Nanoscale electromechanical properties of template-assisted hierarchical self-assembled cellulose nanofibers, *Nanoscale*, 2018, **10**, 16812–16821.

21 S. Zarina and I. Ahmad, Biodegradable composite films based on κ-carrageenan reinforced by cellulose nanocrystal from kenaf fibers, *BioResources*, 2015, **10**, 256–271.

22 H. Liu, D. Liu, F. Yao and Q. Wu, Fabrication and properties of transparent polymethylmethacrylate/cellulose nanocrystals composites, *Bioresour. Technol.*, 2010, **101**, 5685–5692.

23 V. Moniha, M. Alagar, S. Selvasekarapandian, B. Sundaresan and G. Boopathi, Conductive bio-polymer electrolyte iota-carrageenan with ammonium nitrate for application in electrochemical devices, *J. Non. Cryst. Solids*, 2018, **481**, 424–434.

24 L. Pereira, A. M. Amado, A. T. Critchley, F. van de Velde and P. J. A. Ribeiro-Claro, Identification of selected seaweed polysaccharides (phycocolloids) by vibrational spectroscopy (FTIR-ATR and FT-Raman), *Food Hydrocoll.*, 2009, **23**, 1903–1909.

25 L. Urbina, A. Alonso-Varona, A. Saralegi, T. Palomares, A. Eceiza, M. Á. Corcuera and A. Retegi, Hybrid and biocompatible cellulose/polyurethane nanocomposites with water-activated shape memory properties, *Carbohydr. Polym.*, 2019, **216**, 86–96.

26 M. Wada, J. Sugiyama and T. Okano, Native celluloses on the basis of two crystalline phase (Iα/Iβ) system, *J. Appl. Polym. Sci.*, 1993, **49**, 1491–1496.

27 A. Thygesen, J. Oddershede, H. Lilholt, A. B. Thomsen and K. Ståhl, On the determination of crystallinity and cellulose content in plant fibres, *Cellul. 2005 126*, 2005, **12**, 563–576.

28 Y. Nishiyama, P. Langan and H. Chanzy, Crystal structure and hydrogen-bonding system in cellulose Iβ from synchrotron X-ray and neutron fiber diffraction, *J. Am. Chem. Soc.*, 2002, **124**, 9074–9082.

29 N. R. Savadekar, V. S. Karande, N. Vigneshwaran, A. K. Bharimalla and S. T. Mhaske, Preparation of nano cellulose fibers and its application in kappa-carrageenan based film, *Int. J. Biol. Macromol.*, 2012, **51**, 1008–1013.

30 F. N. Jumaah, N. N. Mobarak, A. Ahmad, M. A. Ghani and M. Y. A. Rahman, Derivative of iota-carrageenan as solid polymer electrolyte, *Ionics (Kiel).*, 2015, **21**, 1311–1320.

31 E. Lizundia, J. L. Vilas and L. M. León, Crystallization, structural relaxation and thermal degradation in Poly(l-lactide)/cellulose nanocrystal renewable nanocomposites, *Carbohydr. Polym.*, 2015, **123**, 256–265.

32 M. Shir Mohammadi, C. Hammerquist, J. Simonsen and J. A. Nairn, The fracture toughness of polymer cellulose nanocomposites using the essential work of fracture method, *J. Mater. Sci.*, 2016, **51**, 8916–8927.

33 M. Yadav and F. C. Chiu, Cellulose nanocrystals reinforced κ-carrageenan based UV resistant transparent bionanocomposite films for sustainable packaging applications, *Carbohydr. Polym.*, 2019, **211**, 181–194.

34 M. Yadav and F. C. Chiu, Cellulose nanocrystals reinforced κ-carrageenan based UV resistant transparent bionanocomposite films for sustainable packaging applications, *Carbohydr. Polym.*, 2019, **211**, 181–194.

35 V. C. F. Li, X. Kuang, A. Mulyadi, C. M. Hamel, Y. Deng and H. J. Qi, 3D printed cellulose nanocrystal composites through digital light processing, *Cellulose*, 2019, **26**, 3973–3985.

36 M. J. Dunlop, B. Acharya and R. Bissessur, Study of plant and tunicate based nanocrystalline cellulose in hybrid polymeric nanocomposites, *Cellulose*, 2020, **27**, 249–261.

37 E. J. Foster, R. J. Moon, U. P. Agarwal, M. J. Bortner, J. Bras, S. Camarero-Espinosa, K. J. Chan, M. J. D. Clift, E. D. Cranston, S. J. Eichhorn, D. M. Fox, W. Y. Hamad, L. Heux, B. Jean, M. Korey, W. Nieh, K. J. Ong, M. S. Reid, S. Renneckar, R. Roberts, J. A. Shatkin, J. Simonsen, K. Stinson-Bagby, N. Wanasekara and J. Youngblood, Current characterisation methods for cellulose nanomaterials, *Chem. Soc. Rev.*, 2018, **47**, 2609–2679.

38 M. Mariano, N. El Kissi and A. Dufresne, Cellulose nanocrystals and related nanocomposites: Review of some properties and challenges, *J. Polym. Sci. Part B Polym. Phys.*, 2014, **52**, 791–806.

39 M. R. Loos and I. Manas-Zloczower, Reinforcement Efficiency of Carbon Nanotubes – Myth and Reality, *Macromol. Theory Simulations*, 2012, **21**, 130–137.

40 R. N. Haward, *The physics of glassy polymers;*, Applied Science Publishers, 1973.

41 S. Ikeda and H. Kumagai, Scaling Behavior of Physical Properties of Food Polysaccharide Solutions: Dielectric Properties and Viscosity of Sodium Alginate Aqueous Solutions, *J. Agric. Food Chem.*, 1997, **45**, 3452–3458.

42 M. Samet, V. Levchenko, G. Boiteux, G. Seytre, A. Kallel and A. Serghei, Electrode polarisation vs. Maxwell-Wagner-Sillars interfacial polarisation in dielectric spectra of materials: Characteristic frequencies and scaling laws, *J. Chem. Phys.*, 2015, **142**, 194703.

43 M. Takemasa, A. Chiba and M. Date, Counterion dynamics of κ- and ι-carrageenan aqueous solutions investigated by the dielectric properties, *Macromolecules*, 2002, **35**, 5595–5600.

44 V. Saminatha Kumaran, H. M. Ng, S. Ramesh, K. Ramesh, B. Vengadaesvaran and A. Numan, The conductivity and dielectric studies of solid polymer electrolytes based on poly (acrylamide-co-acrylic acid) doped with sodium iodide, *Bioresources*, 2019, **14**, 7494–7542.

45 H. Zhang, C. Dou, L. Pal and M. A. Hubbe, Review of Electrically Conductive Composites and Films Containing Cellulosic Fibers or Nanocellulose.

46 S. Ramesh and A. K. Arof, Structural, thermal and electrochemical cell characteristics of poly(vinyl chloride)-based polymer electrolytes, *J. Power Sources*, 2001, **99**, 41–47.

47 A. K. Jonscher, The 'universal' dielectric response, *Nat. 1977 2675613*, 1977, **267**, 673–679.

7. Magnetically Active Nanocomposites Based on Biodegradable Synthetic Polyesters

This chapter reports on biodegradable magnetic nanocomposites. In contrast to the previous chapters, the prepared nanocomposites are based on a series of biodegradable polyesters. Thus, PLLA, PCL, PBSu, and PBAT have been blended with Fe_3O_4 nanoparticles up to 10 wt.%. Nanocomposite films with tunable mechanical properties ranging from stiff and brittle to soft and ductile are obtained. Furthermore, the influence in the crystallinity by the inclusion of Fe_3O_4 is analysed by DSC. Adding magnetic character to biodegradable polymers in a fabrication method based on solution mixture opens new venues for developing functional devices. These aimed to replace the short and medium-term durable conventional systems based on petroleum-derived materials.

7.1. Introduction

Magnetite is one of the most common naturally occurring iron oxides and is a prominent magnetic material with recognised non-toxicity and environmentally friendly characteristics.[1,2] Fe_3O_4 shows a saturation magnetisation of 92 $emu \cdot g^{-1}$ (when in bulk) at room temperature,[3] low coercivity, and is potentially biodegradable.[1] So far, Fe_3O_4 nanoparticles have often been incorporated into non-degradable matrices such as PVDF,[4] poly(diphenylamine),[5] or polyurethane.[6] As most plastic waste ends up in landfills and, ultimately, in the environment, its durable character is a severe threat to terrestrial or marine ecosystems.[7]

According to the "reuse, recycle, or biodegrade" model, substituting these long-lasting materials with biodegradable choices offers a circular economy approach to address the environmental issues originating from the inadequate disposal of traditional magnetoactive polymer-based composites.[8] In fact, several works have pointed out the relevant role of biodegradable plastics in the scope of the circular economy.[9,10] In previous chapters, the use of degradable water-soluble cellulose derivatives as suitable matrices to develop magnetically active free-standing materials is shown. However, with a maximum elongation at break of ~15%, their mechanical performance can be further improved upon selecting appropriate biodegradable matrices.

In this approach, biodegradable polyesters represent a group of polymers with tailored physico-mechanical properties.[11] The ester linkage between monomer units is highly susceptible to hydrolytic attack, so these materials are widely applied in environmentally friendly applications.[12] Traditionally, biodegradable polymers have been mainly limited to aliphatic polyesters such as PLLA,[13] or PCL.[14] Accordingly, research efforts have been directed to synthesising novel degradable polymers with enhanced functionalities. Among them, the aliphatic PBSu[15] and aliphatic-aromatic PBAT show a promising future.[16] The introduction of aromatic rings into the polymer structure, as in the case of PBAT, allows the fabrication of novel biodegradable polyesters with reported properties equivalent or even superior to conventional polymers.[17]

In spite of the notable advances in the field of magnetically active polymer nanocomposites, little attention has been paid to developing hydrolytically degradable materials bearing Fe_3O_4. Accordingly, here we explore the suitability of four relevant biodegradable polyesters to fabricate magnetically active free-standing materials with tailored mechanical and degradation performance. Obtained results highlight the potential of PLLA,

PCL, PBSu and PBAT for developing degradable magnetic materials for sustainable electronics, limiting the environmental impacts due to the uncontrolled accumulation of waste in aqueous and terrestrial environments.

7.2. Experimental

7.2.1. Sample preparation and characterisation

Biodegradable nanocomposites were prepared by a doctor blade technique. First, 1 g of polymer pellets was dissolved in 5 mL chloroform at RT using a Thinky ARE-250 (Nordson EFD, Japan) planetary mixer at 2000 rpm for 5 minutes. Closed polyethylene containers were employed to prevent the evaporation of the solvent. Fe_3O_4 nanoparticles were added to obtain concentrations of 1, 5, and 10 wt.% (with respect to the polymer) and mixed at 2000 rpm for another 5 minutes. Then, the mixture was cast by a doctor blade set at 600 µm on a flat glass substrate. After the evaporation of the solvent, the films were further dried at 40 ºC for 24 h to remove the remaining solvent and water. Free-standing films with a thickness of 70 µm were obtained. Materials specifications are explained in section 2.1 of Chapter 2.

As polysaccharides-based materials previously analysed, these nanomaterials have been characterised by FTIR, XRD, FESEM, DSC, uniaxial tensile test, and VSM. equipment specifications and measurement conditions are collected in section 2.2 of Chapter 2.

In addition, a hydrolytic degradation test of neat polymers and their composites containing a 10 wt.% of Fe_3O_4 was performed by immersing square-shaped films of 1 cm^2 in a phosphate-buffered saline (PBS) solution (pH = 7.4) with a surface area to volume ratio of 0.2 cm^{-1} and placed in an oven at 80 ºC for 360h. Afterwards, the films were removed from the PBS solution, rinsed with deionised water and dried at 40 ºC for 24 h. Then, was measured the pH of the remaining PBS solution. The dried films were weighted before and after hydrolytic degradation to calculate the mass loss percentage according to Equation 7.1:

$$weight\ loss\ (\%) = \frac{m_0 - m_f}{m_0} * 100 \qquad (7.1)$$

where m_0 and m_f are the initial and final mass of the films, respectively.

7.3. Results and discussion

7.3.1. Physicochemical and morphological characterisation

The occurrence of chemical interactions between degradable polyester matrices and magnetite nanoparticles was first evaluated. **Figure 7.1** shows the FTIR spectra in the range 600–3600 cm^{-1} for the neat polymers and the ones after incorporating 10 wt.% of Fe_3O_4 into the matrix. Neat polymers are characterised by intense absorption bands in the carbonyl region at 1700 and 1750 cm^{-1}, attributed to the C=O stretching. As typically evidenced in semicrystalline polyesters, the carbonyl group region (−C=O) is composed of several overlapping peaks, which arise from the stretching of the amorphous and crystalline domains of ester carbonyl groups.[18] Specifically, for PLLA and PCL, the absorption peaks at 2998 cm^{-1} and ~2886 cm^{-1} are assigned to the CH_3 and CH stretching, while the ester linkage C-O and C-C stretching in the crystalline phase are identified at 1293 cm^{-1}. The bands at 1184 cm^{-1} and 1088 cm^{-1} are attributed to the asymmetric and symmetric stretching vibrations of the C–O–C group. Finally, peaks observed at ~962 cm^{-1} and ~843 cm^{-1} correspond to the characteristic vibrations of the helical backbone with CH_3 rocking modes.[19]

Regarding PBSu, the weak absorption band of around 3410 cm^{-1} and the peak at 956 cm^{-1} are assigned to the bending of the –C–OH terminal hydroxyl groups. In addition, the absorption band at about 1044 cm^{-1} is ascribed to the –O–C–C– stretching vibration. As the only aliphatic/aromatic polyester in this study, PBAT exhibits additional vibration bands compared with the previous polymers. Thus, besides the absorption band corresponding to C=O stretching mentioned above, the peak at 1715 cm^{-1} is associated with site-specific interactions, given the conjugative effect between the phenylene aromatic groups and the carbonyl groups of PBAT terephthalate residues. Moreover, these phenylene aromatic groups can also be identified by the stretching peaks of the C=C phenylene group at 1505 cm^{-1} and 1459 cm^{-1} and by the out-of-plane bending vibration of the phenylene ring identified at 873 cm^{-1} and 727 cm^{-1}. Concerning the different polymer nanocomposites, when Fe_3O_4 nanoparticles are incorporated (**Figure 7.1b**), no band displacement or intensity changes are observed, suggesting a lack of interaction between the NPs and the polymers used.

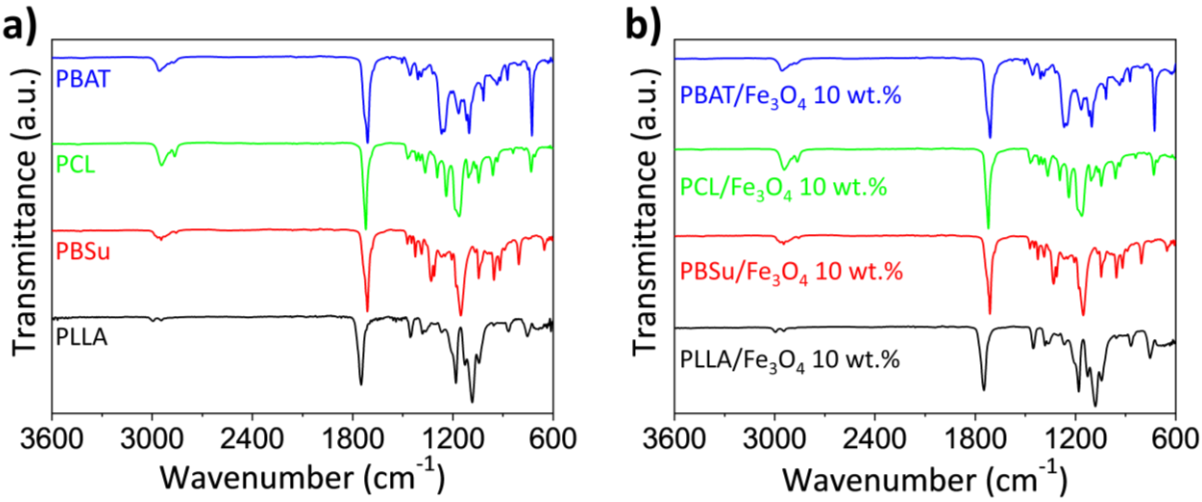

Figure 7.1. a) FTIR spectra in the 3600-600 cm^{-1} region for neat PLLA, PCL, PBSu and PBAT and b) for the corresponding nanocomposites with 10 wt% Fe_3O_4 content.

Further, the morphological characteristics of the samples, as well as nanoparticle dispersion within its hosting matrix in the composites, have been analysed by FESEM. **Figure 7.2** depicts representative FESEM cross-sectional images of the samples. Generally, for neat polymers, rough surfaces are observed for PCL, PBAT and PBSu, characteristic of a ductile fracture, while PLLA exhibits a plane section commonly found in brittle materials. In the case of PLLA composites, randomly dispersed bright spots are observed across the film thickness, corresponding to Fe_3O_4 nanoparticle aggregates. The absence of voids indicates good physical compatibility between the polymer and the nanoparticles.[20] Regarding PCL-based nanocomposites, oriented non-spherical aggregates are observed at loadings of 10 wt.% parallel to the casting direction as a result of their irregular planar shape when the blade is applied during casting. Interestingly, in the case of PBAT, an absence of aggregation effects can be observed. For PBSu, the formation of the films was conditioned by its faster crystallisation when combined with nanostructured fillers.[15,21] It is worth to mention that, as in the case of PCL/Fe_3O_4 at loadings of 10 wt.%, the aggregation of particles occurs parallel to the planes (**Figure 7.2k**). This can explain the mechanical behaviour of this polymer that shows discontinuous stress-strain curves, which is attributed to the film's local breaking as deformation increases (**Figure 7.5c**).[22]

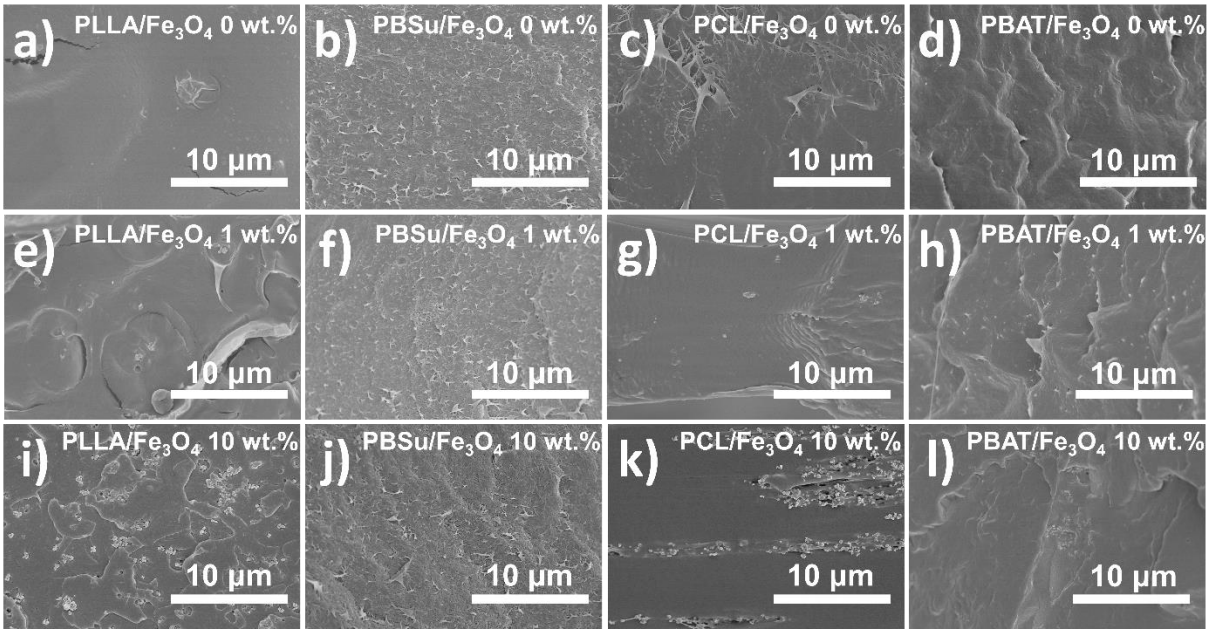

Figure 7.2. Representative field-emission scanning electron microscopy (FESEM) images of fractured surfaces for PLLA, PBSu, PCL, and PBAT pristine samples and nanocomposite films: a-d) 0 wt. %, e-h) 1 wt.% and i-l) 10 wt.% Fe_3O_4 contents.

7.3.2. Structural characterisation

X-ray diffraction experiments have been applied to determine the nanocomposites' crystalline structure and the nanoparticles' presence in the matrix. As shown in **Figure 7.3a**, the neat polymers present a semicrystalline structure. In the case of pure PLLA, it shows a broad diffraction peak centred at 16.6º, which indicates the predominant amorphous microstructure.[23] The characteristic peaks of PBSu at 2θ = 19.7°, 22°, and 22.6° correspond to the diffractions from (020), (021) and (110) planes.[24] Contrary to the rest of the polymers, PCL homopolymer crystallises quickly. The diffraction pattern reveals the presence of significant crystallinity with peaks at 2θ= 21.9º and 24.2º corresponding to the (110) and (200) planes of the orthorhombic crystal structure.[25] Concerning PBAT films, diffraction peaks can be observed at 2θ= 16.2º, 17.3º, 20.4º, 23.2º, 24.8º, related to (011), (010), (101), (100) and (111), crystalline planes, respectively.[26] However, the majority of the characteristic diffraction peaks were not clear and with low-intensity values. As represented in **Figure 7.3b**, the presence of the nanoparticles in the polymer is noticed by the diffraction peaks at 30.2º, 35.52º, 43.54º, 54.21º, 56.85º that correspond to the (220), (311), (400), (422), and (511) crystal planes of magnetite, respectively.[27]

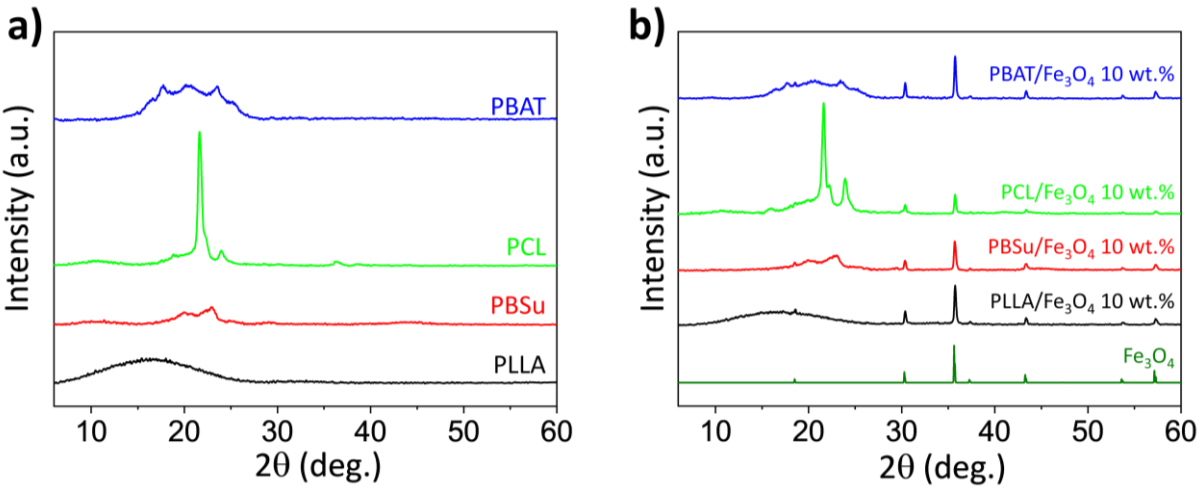

Figure 7.3. a) X-ray diffraction (XRD) spectra for neat PLLA, PCL, PBSu and PBAT and b) for the corresponding nanocomposites with 10 wt.% Fe_3O_4 content (the XRD corresponding to neat Fe_3O_4 is also included).

7.3.3. Thermal transitions

Typically, the crystallisation process in polymeric nanocomposites is more complex than that of the neat polymer,[28] ending in three different scenarios: the filler can speed up the crystallisation, the filler impedes the diffusion of polymeric molecular chains to the surface, or the filler has no effect on the crystallisation process.[29] **Figure 7.4** shows the DSC thermograms of neat polymers and nanocomposites. Neat PLLA exhibited a glass transition (T_g) at 52 ºC, lower values than obtained by the melting film forming process, probably due to a higher free volume as a consequence of the rapid solvent evaporation, allowing higher mobility of amorphous chains. In addition, a double endothermic peak (melting temperature) entered at 150 °C and 159 °C. This double peak is expected in aged polyesters and is attributed to a melt/recrystallisation/re-melt ageing mechanism.[30] In the case of PBSu, the double melting behaviour observed at 104 °C and 113 °C is ascribed to the melting and recrystallisation mechanism, similar to PLLA. According to Yasuniwa et al.[31] the low-temperature peak is attributed to the recrystallisation of the melt of the crystallites with high thermal stability. The peak at higher temperature is attributed to the reorganisation of the crystallites with high thermal stability. Only an endothermic melting peak is observed for PCL at 60 °C, while no signs of its T_g (located around -60 ºC) could be observed, probably due to the presence of rigid-amorphous fraction rather than the mobile amorphous fraction.[32] The PBAT film showed two endothermic peaks at 52 °C and 120 °C, the lower peak attributed to the melting of the crystalline phase of soft aliphatic domains in the sample.[33] On the other hand, there is no variation in the prepared nanocomposites' melting temperatures (±2

°C). Only in the case of PBSu/Fe_3O_4 10 wt.%, a slightly increased thermal resistance in the lower temperature peak at 104 °C can be observed, where the two peaks overlap.

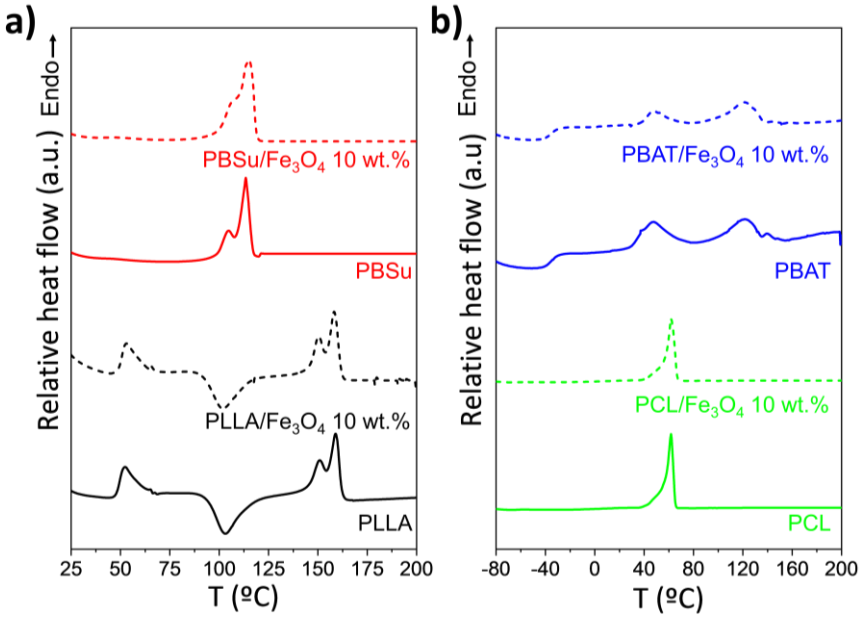

Figure 7.4. DSC thermograms for a) neat PBSu and PLLA in the temperature range from 25 to 200 ºC and b) PBAT and PCL in the temperature range from -80 to 200 ºC as well as for the corresponding nanocomposites with 10 wt.% Fe_3O_4 content.

To get further insights into the crystalline structure of the prepared samples, the degree of crystallinity (X_{cc}) was quantified according to Equation 7.2:[34]

$$X_{CC} = \frac{\Delta H_m - \Delta H_{cc}}{\Delta H_m^0 * (1 - m_f)} * 100 \qquad (7.2)$$

where ΔH_m and ΔH_{cc} are respectively the enthalpies of melting and cold crystallisation of the samples determined by DSC, and ΔH_m^0 is the heat of melting of an infinitely thick crystal, computed as 110.3 J·g^{-1} for PBSu,[35] 106 J·g^{-1} for PLLA,[36] 114 J·g^{-1} for PBAT,[37] and 139.5 J·g^{-1} for PCL.[38] The results are normalised based on the sample's matrix weight fraction (1-m_f). **Table 7.1** summarises the cold crystallisation temperature (T_{cc}), melting temperature (T_m), ΔH_m, ΔH_{cc}, and X_{cc} of the samples related to the first heating scan. The addition of the Fe_3O_4 notably increases the degree of crystallinity of PBSu. It barely affects the crystalline fraction of PLLA and PCL and notably reduces the crystallinity in PBAT. For PBSu, Fe_3O_4 acts as nucleation surfaces to boost the development of more abundant and thicker crystals, which are then melted at higher temperatures, while introduced magnetic nanoparticles act as a physical barrier preventing the reorganisation of the PBAT chains into crystalline phases.[39] Neither the crystallinity degree nor the T_m (directly related to the thickness of crystalline lamellae) of PLLA and PCL are affected by the presence of Fe_3O_4. The pronounced cold

crystallisation peak of PLLA (at 103 ºC for the neat sample and 102 ºC for the 10 wt.% nanocomposite) is related to the two different crystal structures (α-crystals >120 ºC and α´-crystals <100 ºC) that are being formed during heating.[40]

Table 7.1. Thermal transitions of neat PLLA, PBSu, PCL and PBAT films and their nanocomposites 10 wt.% Fe_3O_4 content.

Formulation	T_g (°C)	T_{cc} (°C)	ΔH_{cc} (J·g^{-1})	T_m (°C)	ΔH_m (J·g^{-1})	Xcc (%)
PLLA	52	103	3	150/159	10	7.9
PLLA/Fe_3O_4 10 wt.%	53	101	2	150/158	8	6.3
PBSu	-	-	-	104/113	37	34
PBSu /Fe_3O_4 10 wt.%	-	-	-	115	75	75.6
PCL	- 60	-	-	60	61	43.6
PCL/Fe_3O_4 10 wt.%	- 60	-	-	61	61	48.8
PBAT	- 30	-	-	52/120	56	54.7
PBAT/Fe_3O_4 10 wt.%	- 30	-	-	53/120	40	35.1

7.3.4. Mechanical properties

The capacity of fabricated materials to withstand external mechanical forces upon prospective use in sensors, actuators and biomedical applications is assessed by uniaxial tensile testing. Representative stress-strain curves for neat polymers and nanocomposites comprising 1, 5 and 10 wt.% of Fe_3O_4 nanoparticles are depicted in **Figure 7.5,** and the main mechanical properties values are summarised in **Table 7.2**. Neat PLLA shows a brittle behaviour, breaking right after yielding, with ε_b values of 3.2 ± 0.2 % and E of 2019 ± 21 MPa, while PBSu presents semiductile behaviour with an ε_b of 10.1 ± 1.1 % and a modulus of 704 ± 119 MPa. In both cases, a slight mechanical reinforcement effect is observed for samples comprising 1 wt.% of nanoparticles, increasing the modulus to 2147 ± 174 MPa for PLLA and 902 ± 70 MPa for PBSu, due to the higher modulus of the filler, its homogeneous dispersion in the matrix and the wettability of the filler by the polymer. However, larger concentrations produce a constraining effect on the polymeric chains by the filler-rich regions and result in more extensive NP aggregates, creating zones of weak mechanical strength in the material resulting in a negligible effect on the overall mechanical response concerning the

pristine polymer. Furthermore, this effect is enhanced given the lack of chemical filler-matrix interaction as indicated by FTIR results. Similar mechanical behaviour was observed for composites of both polymers forming bionanocomposites with cellulose nanocrystals (CNC),[34,42] processed by extrusion method.[43] Even so, PLLA and PBSu nanocomposites loaded at 10 wt.% maintain enough mechanical flexibility to develop magnetic sensors and actuators.

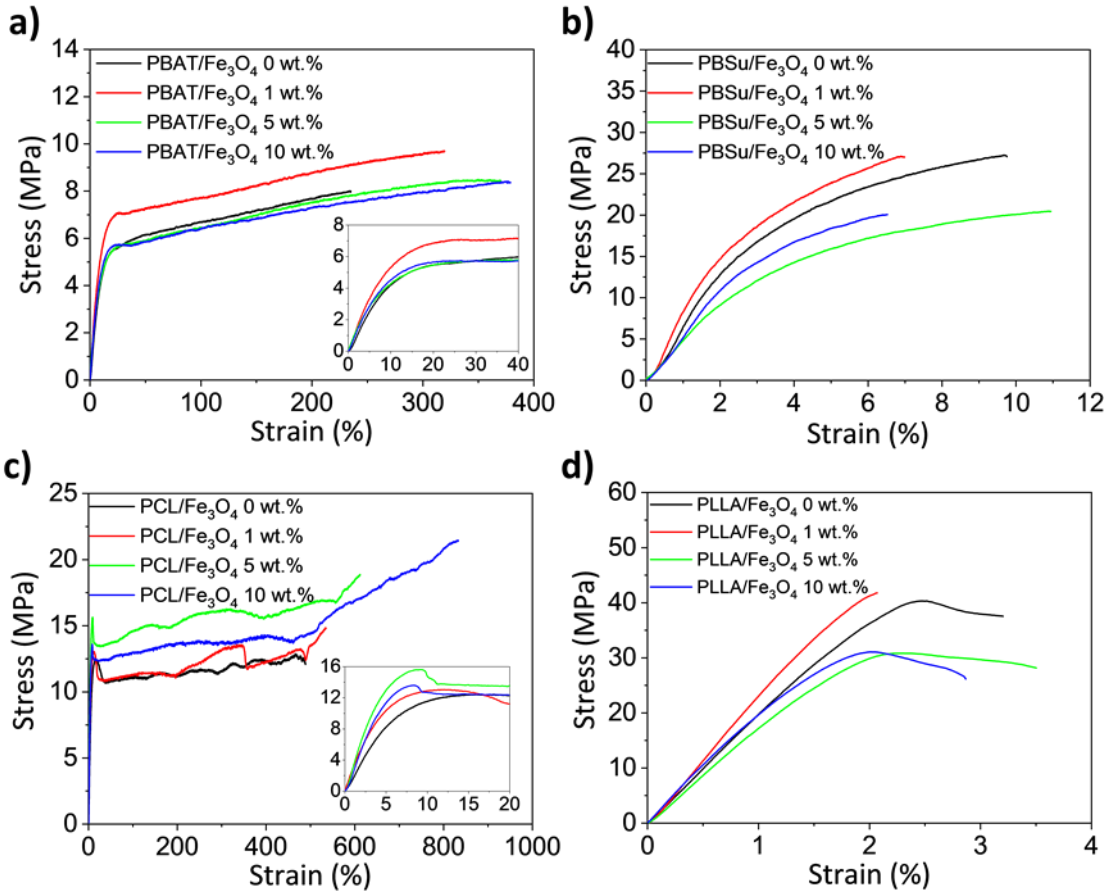

Figure 7.5. Representative stress−strain curves for the pristine polymers and composites with different Fe_3O_4 compositions: a) PLLA, b) PBSu, c) PCL, and d) PBAT.

On the other hand, PCL and PBAT-based films show remarkable ductile behaviour, with lower moduli of 190 ± 17 and 57 ± 2 MPa, and larger elongations at break of 493 ± 52 and 236 ± 31 %, respectively. In contrast to PLLA and PBSu, incorporating Fe_3O_4 can potentially reduce the molecular mobility at the interface, mechanically reinforcing the composite materials.[44] As a result, ε_b and E increase up to 833 ± 42 % and 358 ± 56 MPa (PCL) and 379 ± 126% and 80 ± 13 MPa (PBAT), respectively, when a 10 wt.% filler is added.[45] The improvement of the mechanical properties of PBAT and PCL-based composites at large loadings indicated the compatibility of these matrices with Fe_3O_4 nanoparticles. These

characteristics, together with their soft surface (non- sticky surface), make their manipulation suitable for sensing and actuator applications. In the case of PCL, discontinuous stress−strain curves are observed, probably due to mechanical micro-crashes within the film triggered by the oriented aggregates observed in the SEM images (**Figure 7.2k**). On the contrary, the more favourable dispersion of the nanoparticles within the PBAT matrix results in nanocomposites with improved mechanical properties.

Table 7.2. Main tensile parameters. *E*: Young´s modulus; ε_y: elongation at yield; σ_y: yield stress; ε_b: elongation at break; σ_b: stress at break. Mean average value and standard deviation over five specimens are reported for each composition.

Sample	wt.%	*E* (MPa)	ε_Y (%)	σ_y (MPa)	ε_b (%)	σ_b (MPa)
PLLA	0	2019 ± 21	2.3 ± 0.2	39 ± 2	3.2 ± 0.2	38 ± 2
	1	2147 ± 174	2.0 ± 0.3	38 ± 3	2.3 ± 0.4	40 ± 3
	5	1541 ± 194	2.2 ± 0.1	25 ± 5	3.5 ± 0.3	24 ± 4
	10	1829 ± 60	2.0 ± 0.3	31 ± 1	3.3 ± 0.5	27 ± 1
PBSu	0	704 ± 119	2.0 ± 0.2	11.8 ± 0.5	10.1 ± 1.1	27 ± 2
	1	902 ± 70	1.4 ± 0.2	11.7 ± 0.9	7.4 ± 0.4	27 ± 2
	5	319 ± 137	4.2 ± 1.3	12.0 ± 0.6	9.5 ± 1.2	17 ± 4
	10	649 ± 40	2.9 ± 0.2	12.3 ± 0.9	7.5 ± 0.5	22 ± 2
PCL	0	190 ± 17	16.3 ± 1.5	12.8 ± 1.0	493 ± 52	13 ± 2
	1	232 ± 37	11.2 ± 0.4	14.1 ± 0.5	534 ± 107	17 ± 2
	5	303 ± 43	9.8 ± 0.4	15.8 ± 0.3	611 ± 47	19 ± 1
	10	358 ± 56	9.4 ± 0.8	14.8 ± 1.2	833 ± 42	22 ± 1
PBAT	0	57 ± 2	11.1 ± 0.1	4.4 ± 0.2	236 ± 31	7.5 ± 0.5
	1	81 ± 2	12.8 ± 0.1	5.8 ± 0.1	320 ± 43	9.6 ± 0.3
	5	59 ± 3	14.2 ± 0.4	4.9 ± 0.1	370 ± 53	8.0 ± 0.6
	10	80 ± 13	4.9 ± 0.40	3.2 ± 0.1	379 ± 126	8.6 ± 1.4

7.3.5. Magnetic properties

The magnetic properties at room temperature of the prepared nanocomposites have been assessed by VSM. Characteristic ferrimagnetic behaviour is observed for pure Fe_3O_4

nanoparticles in the mass normalised hysteresis loops in the −1.0 to 1.0 T range, depicted in **Figure 7.6**. The magnetisation increases with the applied magnetic field until it reaches H_s at ~0.2 T with a M_s value of 70 ± 1 emu·g^{-1} with a H_c of 0.014 T.

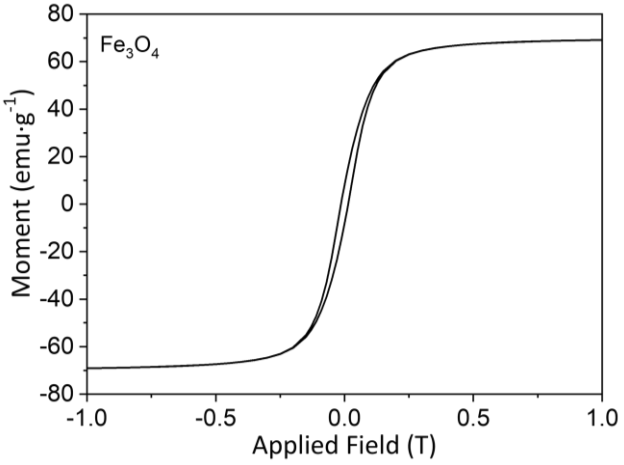

Figure 7.6. Room-temperature magnetic hysteresis loop of Fe_3O_4 nanoparticles measured from -1 to 1 T.

Figure 7.7a-c shows magnetic hysteresis loops corresponding to nanocomposites of PLLA, PBSu, PCL and PBAT, respectively. Nearly all the measured samples comprising 1, 5 and 10 wt.% of Fe_3O_4 present M_s values of 0.70 ± 0.1 emu·g^{-1}, 3.6 ± 0.2 emu·g^{-1}, and 7.1 ± 0.1 emu g^{-1}, while maintaining a similar value of coercive field (H_c = 0.014 T) as pure magnetite. The linear increase of saturation magnetisation and the constant coercivity indicates that NPs are generally randomly distributed within the polymeric matrices.[46] Although some aggregates are observed, they do not disturb the magnetic behaviour. Particularly for PCL composites, magnetic hysteresis loops were measured in the parallel and perpendicular casting directions (**Figure 7.7e**) to test the orientation degree of the nanoparticles.

However, the absence of changes in the characteristic parameters suggests that the directionality only affects flattened aggregates parallel to the film surface but maintains the random dispersion. Interestingly, the M_s values obtained for 10 wt.% of Fe_3O_4 loaded nanocomposites are comparable with other non-degradable nanocomposites loaded with larger NP content (measured under similar conditions), such as Poly(dimethylsiloxane) (PDMS) nanocomposites loaded with 20 wt.% of Fe_3O_4 (6.3 emu·g^{-1}),[47] which is used as a magnetic membrane in an electromagnetic microactuator. Regarding biobased or biodegradable magnetic nanocomposites, similar M_s results have been obtained for CNC/$CoFe_2O_4$ nanocomposites (8.47 emu·g^{-1} at 20 wt.%).[48] However, it is important to note that the materials shown here rely on biodegradable polymers and biocompatible and

potentially degradable magnetic nanoparticles. The polymeric matrices show improved mechanical properties, and their synthesis does not require extensive harmful chemicals.

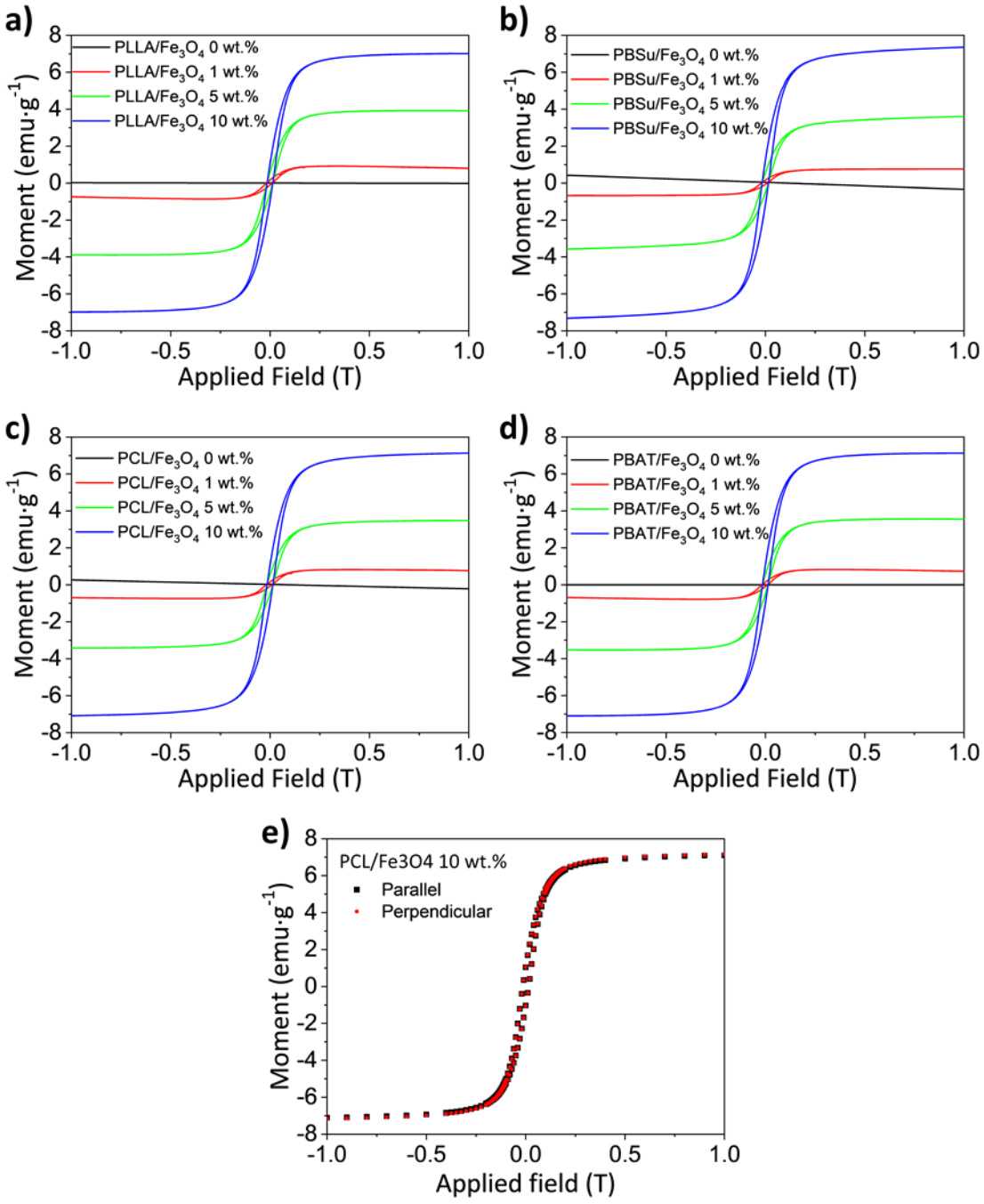

Figure 7.7. Room-temperature magnetic hysteresis loops of the prepared nanocomposites of a) PLLA, b) PBSu, c) PCL, and d) PBAT, measured from -1.0 to 1.0 T. And e) composite PCL/Fe3O4 at 10 wt.%, measured both, in parallel and perpendicular to the casting directions.

7.3.6. Nanocomposite hydrolytic degradation

Polyester-based nanocomposites are known to have a high degree of degradability, making them suitable to be used in biomedical or environmentally friendly applications.[49] In the case of aliphatic polyesters, hydrolysis rate is affected by different factors such as temperature, crystallinity, molecular structure, ester group density and type of degradation media (hydrolytic, soil burial, pH media, in vivo).[50] Generally, the degradation of biopolymers consists of two sequential processes: first, diffusion of an aqueous solution within the polymer, and then hydrolytic degradation mediated either by water and/or enzymes. A general consequence of the degradation process is the dropping of the plastic flow ability of the polymer, thus causing an increase in brittleness.[14] Specifically, PCL and PLLA degradation was studied for medical applications as it is initially degraded by hydrolysis of ester bonds and the subsequent solubilisation of its oligomers.[51,52] As an example, Rangel et al.[53] studied the degradation of PCL *in vitro* incubation, confirming that the degradation has no impact on the biological response. PBSu has been reported to be biodegradable in soil burial tests due to the presence of bacteria and fungi with degradation in terms of weight loss of 31.7 % in 180 days,[54] and 13 % in 80 days in a compost soil[55] and approximately 5 % in a natural soil.[56] On the other hand, when PBSu is exposed to hydrolytic degradation in PBS solution, there is a dramatic decrease in mass after the 9th week, reaching a maximum mass loss of 87.5% in the 15th week.[15,57] Finally, PBAT is a completely compostable material, certificated from Australia TUV (Belgium), DIN-CERTCO (Germany) and BPI (USA).[16] However, it has good resistance to hydrolysis, mainly due to its steric hindrance coming from the aromatic part.[58] To evaluate the degradability of the synthesised nanocomposites, an accelerated hydrolytic degradation at 70 ºC in PBS was carried out as the rate of this hydrolytic degradation is primarily temperature- and humidity-dependent. **Figure 7.9a** shows the physical aspect of polymer/Fe_3O_4 nanocomposites once they were removed from PBS solution (after 360 h immersion) and after being completely dried.

Crystallinity influences hydrolytic degradation due to the different chain-packing arrangements of each polymer. Typically, PLLA and PBSu tend to absorb water that initiates the hydrolysis.[59,60] First, the ester linkages of the amorphous regions are broken, where the macromolecules are more flexible and, thus, easier to be attacked by water. This reduces the entanglement of the amorphous region and increases chain mobility. Finally, the degradation of the crystalline regions that are less susceptible to being attacked due to their higher-ordered structure begins.[61] As consequence, PLLA and PBSu after degradation (**Figure 7.9b**) result in small brittle pieces with a considerable weight loss (27 and 26%, respectively).

Regarding the evolution of the pH in the degradation media (**Figure 7.9c**), a substantial drop in the pH of PLLA (from 7.5 to 3.0) has been observed due to the migration of the monomeric degradation product lactic acid. The degradation products of PBSu are butyric acid and succinic acid. However, a slight drop in pH values is observed compared to PLLA. In contrast, for PCL and PBAT, barely any weight loss and pH value changes were observed. However, the presence of fillers increases the degradation rate as they increase the surface area of the polymer in contact with water, increasing the polymer matrix's hydrophilicity. Nevertheless, there were no observed differences in the behaviour of the nanocomposites (with or w/o filler) when they suffered from fast degradation.

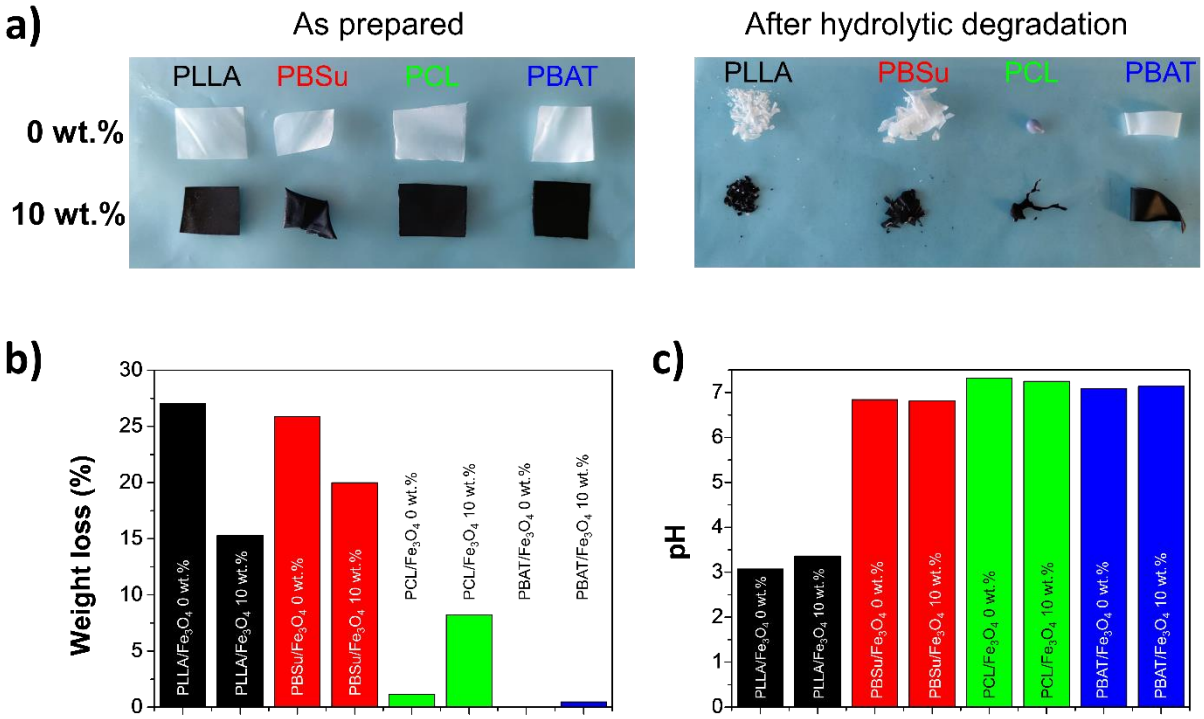

Figure 7.9. a) Physical changes of polymer/Fe_3O_4 nanocomposites with concentrations 0 and 10 wt.% as prepared and after 360 h in PBS medium at 70 ºC; b) weight loss percentage of the nanocomposites and c) pH evolution of PBS after the degradation process.

7.4. Conclusions

Magnetically active biodegradable nanocomposite materials have been prepared. The biodegradable magnetically-active nanocomposites have been developed based on polyesters combined with Fe_3O_4 nanoparticles with concentrations up to 10 wt.%, cast by a doctor blade approach. Although no chemical interactions between nanocomposite partners are observed, Fe_3O_4 nanoparticles can markedly affect the thermal and mechanical properties of the studied materials. For instance, PLLA and PCL crystallisation ability remain barely unchanged, while

Fe_3O_4 surfaces act as nucleation points to boost the crystallisation of PBSu. On the contrary, the degree of crystallinity of PBAT is reduced by the presence of the inorganic nanoparticles. Additionally, mechanically tuneable characteristics ranging from stiff and brittle to soft and ductile are obtained. Interestingly, the lack of specific interactions between the polymeric matrices and the inorganic nanoparticles will facilitate the biodegradation of the materials after their use, smoothing the end-of-life scenario. After exposing the samples to an accelerated hydrolytic degradation at 70 ºC for 15 days in PBS medium, weight losses up to 30% were observed. The combination of ductility (reaching elongations at break up to 833 ± 42 % for PCL) and magnetical response (magnetisation values up to 7.1 ± 0.1 $emu \cdot g^{-1}$) for the samples comprising a 10 wt.% of Fe_3O_4 makes these biodegradable materials attractive to develop a new generation of sustainable and multifunctional materials for electronic applications.

7.5. References

1 L. Zhang, W.-F. Dong and H.-B. Sun, Multifunctional superparamagnetic iron oxide nanoparticles: design, synthesis and biomedical photonic applications, *Nanoscale*, 2013, **5**, 7664–7684.

2 P. H. Nam, L. T. Lu, P. H. Linh, D. H. Manh, L. T. Thanh Tam, N. X. Phuc, P. T. Phong and I.-J. Lee, Polymer-coated cobalt ferrite nanoparticles: synthesis, characterisation, and toxicity for hyperthermia applications, *New J. Chem.*, 2018, **42**, 14530–14541.

3 P. Hu, L. Kang, T. Chang, F. Yang, H. Wang, Y. Zhang, J. Yang, K. Wang, J. Du and Z. Yang, High saturation magnetisation Fe3O4 nanoparticles prepared by one-step reduction method in autoclave, *J. Alloys Compd.*, 2017, **728**, 88–92.

4 J.-S. Im and I.-K. Park, Mechanically Robust Magnetic Fe3O4 Nanoparticle/Polyvinylidene Fluoride Composite Nanofiber and Its Application in a Triboelectric Nanogenerator, *ACS Appl. Mater. Interfaces*, 2018, **10**, 25660–25665.

5 S. Z. Ozkan, E. L. Dzidziguri, G. P. Karpacheva, P. A. Chernavskii, M. N. Efimov and G. N. Bondarenko, A magnetic metal/polymer nanocomposite material based on poly(diphenylamine) and Fe3O4 nanoparticles, *Russ. Chem. Bull.*, 2015, **64**, 196–201.

6 H. Zou, C. Weder and Y. C. Simon, Shape-Memory Polyurethane Nanocomposites with Single Layer or Bilayer Oleic Acid-Coated Fe3O4 Nanoparticles, *Macromol. Mater. Eng.*, 2015, **300**, 885–892.

7 Y. Su, Z. Zhang, D. Wu, L. Zhan, H. Shi and B. Xie, Occurrence of microplastics in landfill systems and their fate with landfill age, *Water Res.*, 2019, **164**, 114968.

8 Bio-based Industries Consortium (BIC), The European circular economy package: Position of the Bio-based Industries Consortium.

9 A. Di Bartolo, G. Infurna and N. T. Dintcheva, *Polym.* , 2021, 13.

10 S. Spierling, C. Röttger, V. Venkatachalam, M. Mudersbach, C. Herrmann and H.-J. Endres, Bio-based Plastics - A Building Block for the Circular Economy?, *Procedia CIRP*, 2018, **69**, 573–578.

11 L. N. Woodard and M. A. Grunlan, Hydrolytic Degradation and Erosion of Polyester Biomaterials, *ACS Macro Lett.*, 2018, **7**, 976–982.

12 J. Rydz, W. Sikorska, M. Kyulavska and D. Christova, *Int. J. Mol. Sci.* , 2015, 16.

13 E. Fortunati, F. Luzi, D. Puglia, R. Petrucci, J. M. Kenny and L. Torre, Processing of PLA nanocomposites with cellulose nanocrystals extracted from Posidonia oceanica waste: Innovative reuse

of coastal plant, *Ind. Crops Prod.*, 2015, **67**, 439–447.

14 M. Bartnikowski, T. R. Dargaville, S. Ivanovski and D. W. Hutmacher, *Prog. Polym. Sci.*, 2019, 96, 1–20.

15 S. A. Rafiqah, A. Khalina, A. S. Harmaen, I. A. Tawakkal, K. Zaman, M. Asim, M. N. Nurrazi and C. H. Lee, *Polym.* , 2021, 13.

16 J. Jian, Z. Xiangbin and H. Xianbo, An overview on synthesis, properties and applications of poly(butylene-adipate-co-terephthalate)–PBAT, *Adv. Ind. Eng. Polym. Res.*, 2020, **3**, 19–26.

17 E. Lizundia, V. A. Makwana, A. Larrañaga, J. L. Vilas and M. P. Shaver, Thermal, structural and degradation properties of an aromatic–aliphatic polyester built through ring- opening polymerisation, *Polym. Chem.*, 2017, **8**, 3530–3538.

18 S. Mallardo, V. De Vito, M. Malinconico, M. G. Volpe, G. Santagata and M. L. Di Lorenzo, Poly(butylene succinate)-based composites containing β-cyclodextrin/d-limonene inclusion complex, *Eur. Polym. J.*, 2016, **79**, 82–96.

19 E. Lizundia, L. Ruiz-Rubio, L. Vilas J and M. León L, Towards the development of eco-friendly disposable polymers: ZnO-initiated thermal and hydrolytic degradation in Poly (L- lactide)/ZnO nanocomposites, *RSC Adv.*, 2016, **00**, 1–3.

20 G.-X. Qiu, F. Raue and G. W. Ehrenstein, Mechanical properties and morphologies of PP/mPE/filler composites, *J. Appl. Polym. Sci.*, 2002, **83**, 3029–3035.

21 Y. J. Phua, W. S. Chow and Z. A. Mohd Ishak, The hydrolytic effect of moisture and hygrothermal aging on poly(butylene succinate)/organo-montmorillonite nanocomposites, *Polym. Degrad. Stab.*, 2011, **96**, 1194–1203.

22 G. Sparks, Y. Cui, G. Po, Q. Rizzardi, J. Marian and R. Maaß, Avalanche statistics and the intermittent-to-smooth transition in microplasticity, *Phys. Rev. Mater.*, 2019, **3**, 80601.

23 W. Siriprom, N. Sangwaranatee, Herman, K. Chantarasunthon, K. Teanchai and N. Chamchoi, Characterisation and analysation of the poly (L-lactic acid) (PLA) films, *Mater. Today Proc.*, 2018, **5**, 14803–14806.

24 Q. Jiao, J. Shen, L. Ye, Y. Li and H. Chen, Poly(oxymethylene)/poly(butylene succinate) blends: Miscibility, crystallisation behaviors and mechanical properties, *Polymer (Guildf).*, 2019, **167**, 40–47.

25 I. Castilla-Cortázar, A. Vidaurre, B. Marí and A. J. Campillo-Fernández, *Polym.* , 2019, 11.

26 H. Zhao, H. Liu, Y. Liu and Y. Yang, Blends of poly(butylene adipate-co-terephthalate) (PBAT) and stereocomplex polylactide with improved rheological and mechanical properties, *RSC Adv.*, 2020, **10**, 10482–10490.

27 L. Mohammed, H. G. Gomaa, D. Ragab and J. Zhu, Magnetic nanoparticles for environmental and biomedical applications: A review, *Particuology*, 2017, **30**, 1–14.

28 R. M. Michell and A. J. Müller, Confined crystallisation of polymeric materials, *Prog. Polym. Sci.*, 2016, **54**–**55**, 183–213.

29 S. Iannace, A. Maffezzoli, G. Leo and L. Nicolais, Influence of crystal and amorphous phase morphology on hydrolytic degradation of PLLA subjected to different processing conditions, *Polymer (Guildf).*, 2001, **42**, 3799–3807.

30 S. V Borges, M. L. Dias, V. J. R. R. Pita, C. Azuma and M. V Dias, Processability, morphology and thermal behavior of poly(lactic acid)/synthetic mica nanocomposites obtained by melt blending, *J. Compos. Mater.*, 2013, **48**, 1429–1440.

31 M. Yasuniwa and T. Satou, Multiple melting behavior of poly(butylene succinate). I. Thermal analysis of melt-crystallised samples, *J. Polym. Sci. Part B Polym. Phys.*, 2002, **40**, 2411–2420.

32 M. Rizzuto, L. Marinetti, D. Caretti, A. Mugica, M. Zubitur and A. J. Müller, Can poly(ε-caprolactone) crystals nucleate glassy polylactide?, *CrystEngComm*, 2017, **19**, 3178–3191.

33 L. C. Arruda, M. Magaton, R. E. S. Bretas and M. M. Ueki, Influence of chain extender on mechanical, thermal and morphological properties of blown films of PLA/PBAT blends, *Polym. Test.*, 2015, **43**, 27–37.

34 E. Lizundia, E. Fortunati, F. Dominici, J. L. Vilas, L. M. León, I. Armentano, L. Torre and J. M. Kenny,

PLLA-grafted cellulose nanocrystals: Role of the CNC content and grafting on the PLA bionanocomposite film properties, *Carbohydr. Polym.*, 2016, **142**, 105–113.

35 Z. Qiu and W. Yang, Crystallisation kinetics and morphology of poly(butylene succinate)/poly(vinyl phenol) blend, *Polymer (Guildf).*, 2006, **47**, 6429–6437.

36 M. C. Righetti, M. Gazzano, M. L. Di Lorenzo and R. Androsch, Enthalpy of melting of α′- and α-crystals of poly(l-lactic acid), *Eur. Polym. J.*, 2015, **70**, 215–220.

37 D. Mondal, B. Bhowmick, M. M. R. Mollick, D. Maity, N. Ranjan Saha, V. Rangarajan, D. Rana, R. Sen and D. Chattopadhyay, Antimicrobial activity and biodegradation behavior of poly(butylene adipate-co-terephthalate)/clay nanocomposites, *J. Appl. Polym. Sci.*, , DOI:https://doi.org/10.1002/app.40079.

38 M. A. Woodruff and D. W. Hutmacher, The return of a forgotten polymer—Polycaprolactone in the 21st century, *Prog. Polym. Sci.*, 2010, **35**, 1217–1256.

39 C. Wolf, H. Angellier-Coussy, N. Gontard, F. Doghieri and V. Guillard, How the shape of fillers affects the barrier properties of polymer/non-porous particles nanocomposites: A review, *J. Memb. Sci.*, 2018, **556**, 393–418.

40 R. Androsch, C. Schick and M. L. Di Lorenzo, eds. M. L. Di Lorenzo and R. Androsch, Springer International Publishing, Cham, 2018, pp. 235–272.

41 S. Fu, Z. Sun, P. Huang, Y. Li and N. Hu, Some basic aspects of polymer nanocomposites: A critical review, *Nano Mater. Sci.*, 2019, **1**, 2–30.

42 J. Xu, P. H. Manepalli, L. Zhu, S. Narayan-Sarathy and S. Alavi, Morphological, barrier and mechanical properties of films from poly (butylene succinate) reinforced with nanocrystalline cellulose and chitin whiskers using melt extrusion, *J. Polym. Res.*, 2019, **26**, 188.

43 E. Fortunati, D. Puglia, A. Iannoni, A. Terenzi, J. M. Kenny and L. Torre, *Mater.* , 2017, 10.

44 E. Senses, A. Faraone and P. Akcora, Microscopic Chain Motion in Polymer Nanocomposites with Dynamically Asymmetric Interphases, *Sci. Reports 2016 61*, 2016, **6**, 1–11.

45 B. Mensah, K. C. Gupta, H. Kim, W. Wang, K. U. Jeong and C. Nah, Graphene-reinforced elastomeric nanocomposites: A review, *Polym. Test.*, 2018, **68**, 160–184.

46 M. Rincon-Iglesias, E. Lizundia and S. Lanceros-Mendez, Water-soluble cellulose derivatives as suitable matrices for multifunctional materials, *Biomacromolecules*, , DOI:10.1021/acs.biomac.9b00574.

47 A. A. Paknahad and M. Tahmasebipour, An electromagnetic micro-actuator with PDMS-Fe3O4 nanocomposite magnetic membrane, *Microelectron. Eng.*, 2019, **216**, 111031.

48 E. Lizundia, A. Maceiras, J. L. Vilas, P. Martins and S. Lanceros-Mendez, Magnetic cellulose nanocrystal nanocomposites for the development of green functional materials, *Carbohydr. Polym.*, 2017, **175**, 425–432.

49 N. Mittal, A. Ojanguren, M. Niederberger and E. Lizundia, Degradation Behavior, Biocompatibility, Electrochemical Performance, and Circularity Potential of Transient Batteries, *Adv. Sci.*, 2021, **8**, 2004814.

50 S. Gai, J. Xu, H. Zhang, R. Yin and W. Zhang, Effects of nanofillers on the hydrolytic degradation of polyesters, *Tissue Eng. - Part B Rev.*, 2020, **26**, 484–495.

51 S.-D. Yoon, Y.-S. Kwon and K.-S. Lee, Biodegradation and Biocompatibility of Poly L-lactic Acid Implantable Mesh, *Int. Neurourol. J.*, 2017, **21**, S48–S54.

52 L. N. Woodard and M. A. Grunlan, Hydrolytic Degradation of PCL–PLLA Semi-IPNs Exhibiting Rapid, Tunable Degradation, *ACS Biomater. Sci. Eng.*, 2019, **5**, 498–508.

53 A. Rangel, T. N. Nguyen, C. Egles and V. Migonney, Different real-time degradation scenarios of functionalised poly(ε-caprolactone) for biomedical applications, *J. Appl. Polym. Sci.*, 2021, **138**, 50479.

54 L. Liu, J. Yu, L. Cheng and X. Yang, Biodegradability of poly(butylene succinate) (PBS) composite reinforced with jute fibre, *Polym. Degrad. Stab.*, 2009, **94**, 90–94.

55 H.-S. Kim, H.-J. Kim, J.-W. Lee and I.-G. Choi, Biodegradability of bio-flour filled biodegradable poly(butylene succinate) bio-composites in natural and compost soil, *Polym. Degrad. Stab.*, 2006, **91**, 1117–1127.

56 H.-S. Kim, H.-S. Yang and H.-J. Kim, Biodegradability and mechanical properties of agro-flour–filled

polybutylene succinate biocomposites, *J. Appl. Polym. Sci.*, 2005, **97**, 1513–1521.

57 H. Li, J. Chang, A. Cao and J. Wang, In vitro evaluation of biodegradable poly(butylene succinate) as a novel biomaterial., *Macromol. Biosci.*, 2005, **5**, 433–440.

58 S. Girdthep, P. Worajittiphon, T. Leejarkpai, R. Molloy and W. Punyodom, Effect of silver-loaded kaolinite on real ageing, hydrolytic degradation, and biodegradation of composite blown films based on poly(lactic acid) and poly(butylene adipate-co-terephthalate), *Eur. Polym. J.*, 2016, **82**, 244–259.

59 M. Puchalski, G. Szparaga, T. Biela, A. Gutowska, S. Sztajnowski and I. Krucińska, Molecular and Supramolecular Changes in Polybutylene Succinate (PBS) and Polybutylene Succinate Adipate (PBSA) Copolymer during Degradation in Various Environmental Conditions, *Polym. 2018, Vol. 10, Page 251*, 2018, **10**, 251.

60 X. Yuan, A. F. T. Mak and K. Yao, Comparative observation of accelerated degradation of poly(L-lactic acid) fibres in phosphate buffered saline and a dilute alkaline solution, *Polym. Degrad. Stab.*, 2002, **75**, 45–53.

61 M. C. Araque-Monrós, A. Vidaurre, L. Gil-Santos, S. Gironés Bernabé, M. Monleón-Pradas and J. Más-Estellés, Study of the degradation of a new PLA braided biomaterial in buffer phosphate saline, basic and acid media, intended for the regeneration of tendons and ligaments, *Polym. Degrad. Stab.*, 2013, **98**, 1563–1570.

8. Anisotropic Gels Based on Core-shell Fe_3O_4@Au Nanorods with Magnetic and Optical Functionalities

Here is reported the synthesis of Fe_3O_4@Au core-shell nanorods and their subsequent incorporation into an agarose hydrogel to obtain anisotropic magnetic and optical properties for magneto- and photo-thermal anisotropic transductions. Highly monodisperse ferrimagnetic Fe_3O_4 nanorods with tunable size were synthesized by a solvothermal method by varying the amount of hexadecylamine capping ligand. A gold shell was coated onto Fe_3O_4 nanorods by the intermediate formation of core-satellite structures and a subsequent controlled growth process, leading to an optical response variation from the visible to the near IR region. The nanorods were oriented within an agarose hydrogel to fabricate free-standing anisotropic materials, providing a proof of concept for the applicability of these materials for anisotropic magneto- and photo-thermia applications. The strongly gelling upon cooling and shear-thinning behavior of agarose enables the fabrication of magnetically active continuous hydrogel filaments upon injection. These developed multifunctional nanohybrid materials represent a base for advanced sensing, biomedical, or actuator applications with an anisotropic response.

8.1. Introduction

Hybrid core-shell nanoparticles offer unique characteristics, including high thermal/chemical stabilities, low toxicity, or improved solubility.[1] These nanoparticles generally consist of a core (inner material) and a shell (outer layer material).[1] In addition, introducing anisotropic characteristic represents a further step as it results in a novel functional response. Thus, anisotropic nanoparticles having asymmetric axes are particularly attractive as they show varying and controlled physical properties along the different orientations.[2] In this context, Au nanorods (Au NRs) are considered a good example where two distinct localized surface plasmon resonances (LSPR) can be obtained in the longitudinal and transverse directions.[3] Thus, combining a Au NR shell with a magnetic core can result in optically and magnetically active hybrid nanoparticles with high tunability and anisotropy.[4] Particularly, Fe_3O_4 can offer high saturation magnetization, translated into easier magnetic manipulation and magneto-thermal transduction while offering high biocompatibility. The versatility of hybrid Fe_3O_4-Au nanoparticles has been demonstrated by their many different applications, including the subattomole detection of cancer-associated biomarkers, targeted drug delivery, contaminants sensing, multimodal imaging, or hyperthermal therapy of cancer cells, among others.[5,6]

Unfortunately, nanoparticles have a strong tendency to aggregate when dispersed in aqueous media when a magnetic field is applied,[7] decreasing the effectiveness in photo- and magneto-activity.[8] A possible approach to overcome this bottleneck is the effective immobilization of nanoparticles within a soft matrix. On this basis, hydrogels emerge as a suitable host candidate due to their mechanically-soft character, compatibility with nanoparticles, biocompatibility, and ease of fabrication.[9] Thanks to their versatility, both chemically and physically crosslinked hydrogels show many applications in a large variety of fields, including catalysis,[10] biomedicine,[11] photonics,[12] or energy storage.[13] Implementing nanocomposite hydrogels with permanent anisotropy will also impart additional features to classical isotropic hydrogels as the physico-chemical properties will vary depending on the orientation. In this sense, dispersing anisotropic materials within a hydrogel precursor and orienting those particles through external electric or magnetic fields results in an attractive approach given its versatility, simplicity, and effectiveness.[14,15] Moreover, magnetic orientation can be uniformly applied throughout the whole sample, and it is a non-contact approach.[15] In comparison to hydrogels containing self-assembled nanoparticles forming filaments,[16] NRs, having intrinsic anisotropy, can be easily oriented inside uniform magnetic

fields without the necessity of high nanoparticle concentration and translation of nanoparticles in its interior.[17,18]

This work demonstrates the fabrication of Au-coated rod-shaped magnetite nanoparticles (Fe_3O_4-NR@Au) exhibiting optical and magnetic properties and their use to form anisotropic hydrogels and, as the first application, have been studied their hyperthermia properties (**Scheme 8.1**). Fe_3O_4 NRs were synthesized with controlled geometrical features (length and width). NRs were hybridized with Au nanoclusters, which were further modified to grow a Au shell. The morphological and optical properties of the nanoparticles were characterised as a function of the shell formation. The magnetically and optically active Fe_3O_4-NR@Au were then embedded and subsequently oriented within an agarose hydrogel to fabricate free-standing anisotropic materials, enabling the understanding of the effect of orientation on the photo- and magneto-thermia. Besides, the nanoparticle' synthetic route employed can also be applied to other materials, expanding the horizons of anisotropic materials such as filamentous hydrogels.

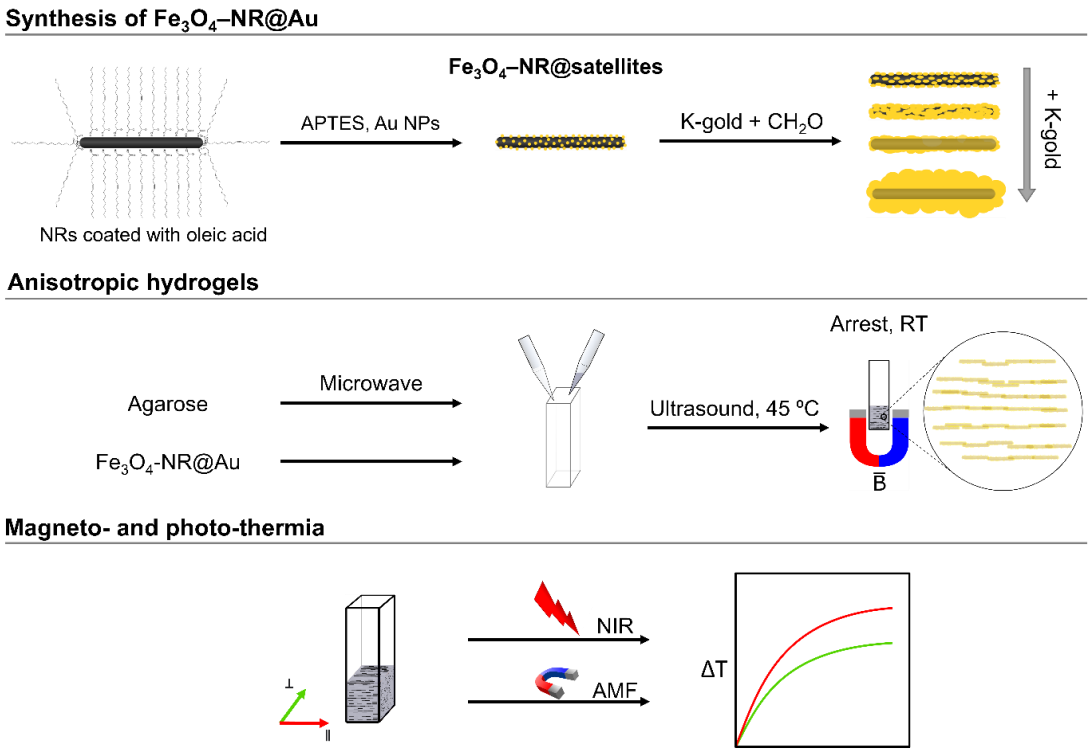

Scheme 1. Representation of the different steps followed to achieve the anisotropic gel and its use in magnetothermia. From top to down: Synthesis of the hybrid nanoparticles Fe_3O_4-NR@Au. Preparation of the nanoparticle-loaded anisotropic agarose hydrogel. Use of the loaded hydrogel in magneto- and photothermia with directional characteristics.

8.2. Experimental section

8.2.1. Synthesis of Fe_3O_4 NRs

Magnetite NRs were synthesized by solvothermal method as reported by Si et al.[19] in a 50 mL Teflon-lined autoclave. First, 0.47 g of hexadecylamine and 5.33 mL of oleic acid were dissolved in 21.33 mL of 1-octanol at 45 ºC under magnetic stirring until a homogenous liquid was obtained. Then, the solution was cooled to room temperature, and 5.33 mL of $Fe(CO)_5$ were added and stirred for 2 min. Finally, the mixture was poured into the Teflon autoclave, sealed with its stainless steel shell, and heated at 200 ºC for 6 h, without a heating ramp and after preheating the oven. After cooling to room temperature, the product was washed three times with ethanol and dispersed in 5 mL of chloroform (28.9 $mg \cdot mL^{-1}$).

8.2.2. Fe_3O_4-NRs-satellite synthesis

Before the decoration of NRs with Au-satellites, NRs were functionalized with aminopropyltriethoxysilane (APTES), an aminosilane that substitutes oleic acid on NRs' surface, providing an amine-rich coating. Typically, 100 µL of well dispersed NRs' solution were poured dropwise into a solution of 600 µL APTES: 5 mL ethanol and mixed using a rotary tube mixer overnight. Then, the NRs were washed twice with ethanol and further dispersed in 3 mL ethanol.

Besides, spherical Au nanoparticles of 2-3 nm in diameter were synthesized. First, 0.9013 g of PVP were dissolved in 50 mL of ultrapure H_2O. Then, 429 µL of a solution of $HAuCl_4$ (50 mM) were added, and the NPs were formed by reducing the Au^{+3} with 15 mL of $NaBH_4$ solution of 5.24 mM.

Finally, 3 mL of APTES functionalized NRs were added dropwise into 30 mL of Au-nanoparticles solution and mixed with a rotary tube mixer for 2 h. The core-satellite NRs were purified by centrifugation and the decoration process was repeated once more to improve the satellite-coating of the NRs. Repeated cycles have been shown to improve the coating with satellites.[20] However, based on the TEM images in our case, further improvement is not observed after two cycles.

8.2.3. Fe_3O_4-NR@Au synthesis

A basic growth solution, k-gold, was initially prepared: 5 mg of K_2CO_3 were dissolved in 19.7 mL of ultrapure H_2O for 15 minutes under magnetic stirring. Then, 150 µL of $HAuCl_4$ solution 50 mM were added and mixed for 30 minutes, where the solution got colourless due to the reduction of Au^{+3} to Au^{+}. 25 - 400 µL of the solution of Fe_3O_4-NR-satellites (Fe_3O_4 = 1.26 mM; Au = 2.22 mM) were added under orbital stirring (see **Table 8.1**) to 1.6 mL of K-gold solution. After one minute, 2.6 µL of formaldehyde was added to reduce the Au^{+} to metallic Au, where the surface of satellites acted as autocatalytic growing sites until a shell was formed by fusion of the growing satellites, completely covering the NRs. After 2 h, the reaction was complete and no change was further observed in the UV-Vis spectrum. The nanoparticles were then centrifuged and cleaned in two extra centrifugation cycles with ultrapure water and finally dispersed with 5 mL of water.

Table 8.1. Conditions of added NR-satellites and Au growth solution of the prepared samples. The concentration values of satellites and magnetite are separately expressed. In addition, the $HAuCl_4$ /Fe_3O_4 molar ratio is indicated.

Sample	Fe_3O_4 (mM)	Au-satellites (mM)	$HAuCl_4$ (mM)/ Fe_3O_4 (mM)
1	3.41	6.07	0.08
2	1.97	3.51	0.16
3	1.07	1.91	0.32
4	0.56	1.00	0.64
5	0.29	0.51	1.27

8.2.4. Agarose hydrogel nanocomposites

To develop the hydrogels, firstly, a dispersion of agarose in water at 2 wt.% was heated by using a microwave at 800 W for 30 seconds (80-90 ºC), and it was allowed to cool down. Then the solution of Fe_3O_4-NR@Au dispersed at 45 ºC was poured within the agarose solution and homogenized in an ultrasound bath. The composite hydrogel was finally poured into a mould (typically polystyrene cuvettes are employed) where the physical crosslinking occurs at room temperature between two magnets, as shown in **Scheme 8.1**.

8.2.5. Characterisation methods

Images of the nanoparticles were acquired by using TEM and HRTEM. At the same time, XRD and XPS measurements were employed to elucidate the structure and composition of the nanorods, thereby the anisotropy of the hydrogels. Then, the ratio between magnetite and gold was determined by ICP. Au-shell growth was followed by UV-Vis measurements of the absorbance of the solutions. Magnetic parameters were obtained with the VSM.

For AC magnetothermia measurements, a hydrogel solution containing 100 μL of 2 % agarose and the NRs at 3 $mg \cdot mL^{-1}$ was introduced into a plastic capsule and left to gel in the presence of a DC magnetic field. Then, the AC hysteresis loops were measured at 133 kHz frequency and field intensities up to 90 mT. The measurements were carried out in NR and Fe_3O_4-NR@Au of different sizes (L=52 ± 7 nm, L= 140 ± 11 nm and L= 397 ± 49 nm) oriented parallel, perpendicular and random to the applied magnetic field. The SAR was extracted applying Equation (2.2).

In the case of photothermia: 1 mL of the Fe_3O_4-NR@Au solution (2 wt.% of agarose, NRs at a 0.5 mM of Au) was passed to a spectroscopic fluorescence cuvette and irradiated with a LED light (see Section 2.2.4 of Chapter 2). The temperature variation was measured as a function of time (dT / dt) at the initial linear slope ($t \approx 1$ min) in order to evaluate power dissipation, i.e. the SAR ($W \cdot g^{-1}$) per mass of the active element Au. The SAR was then calculated using the following Equation (2.1) of Chapter 2.

8.3. Results and discussion

8.3.1. Magnetite nanorods

Iron oxide NRs were initially synthesized by a solvothermal method in octanol using iron pentacarbonyl as an iron source and oleic acid and HDA as capping ligands. **Figures 8.1a-e** show representative TEM images of synthesized NRs at different sizes. In general, highly monodisperse single-crystal NRs with well–defined shapes were obtained. **Figure 8.1f** shows a HR-TEM image of a single NR. The lattice fringes corresponding to the (220) planes of magnetite can be observed, with a spacing of nearly 0.29 nm, as expected for a NR growing in the [110] direction.[21,22] The different sizes were achieved by varying the amount of HDA capping ligand (**Figure 1g**). Both length and width of the NRs decrease when the amount of HDA increases with a similar linear trend in the HDA range from 0.18 to 0.53 g. The shortest

NRs were obtained at 0.53 g of HDA, exhibiting a length of 52 ± 7 nm and a width of 6.2 ± 0.9 nm (aspect ratio, A.R. = 8.4 ± 1.7). Within this region, the longest rods were obtained at 0.18 g of HDA, presenting a length of 275 ± 23 nm and a width of 39.4 ± 3.9 nm (A.R. = 7.0 ± 0.9). Nevertheless, a change in the growth kinetic was observed when 0.70 g of HDA were added, obtaining the largest NRs (length = 397 ± 49 nm, width = 45. 2 ± 6.1 nm), probably due to the complex interplay between nucleation and growth.

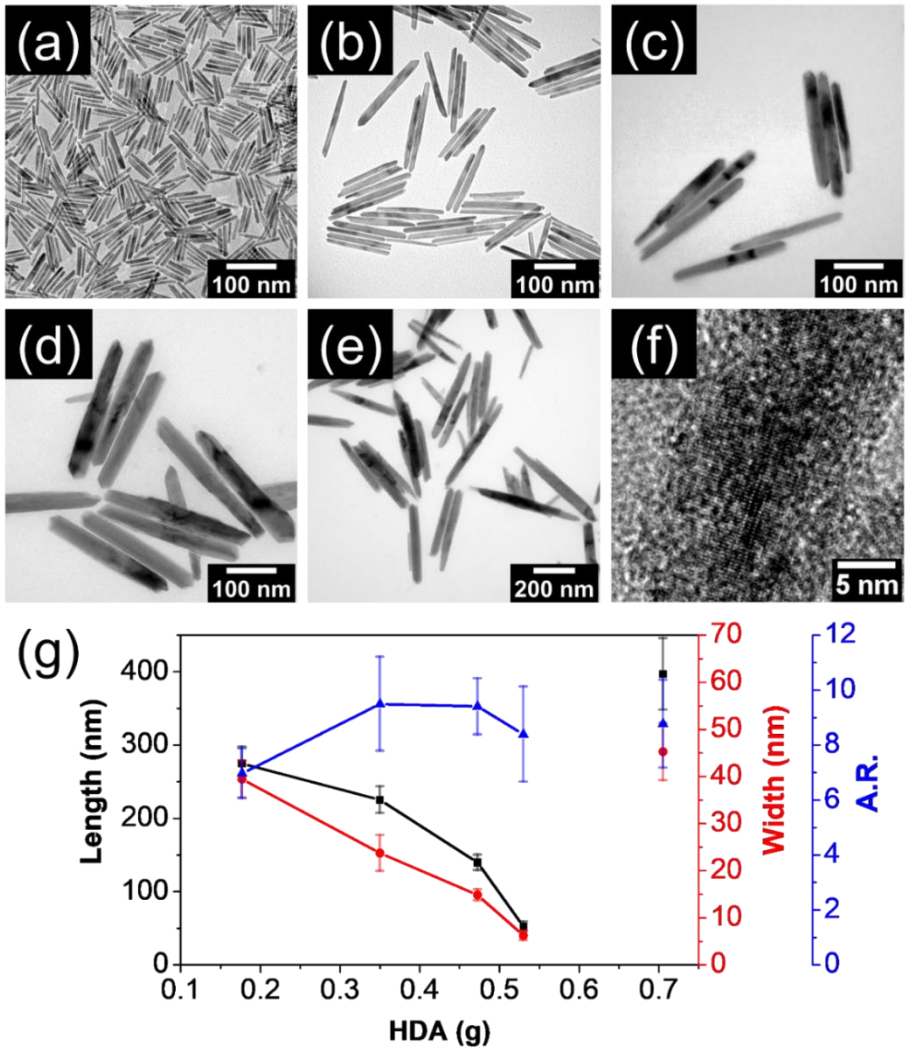

Figure 8.1. TEM images of the synthesized NRs at different amounts of the capping ligand HDA: (a) 0.53 g, (b) 0.47 g, (c) 0.35 g (d) 0.18 g (e) 0.70 g. Error bars correspond to the standard deviation of an average of 50 measured nanoparticles. (f) HRTEM of a NR from Figure 1(b). (g) Average sizes of the NRs in a-e (black squares: length, red circles: width, and blue triangles: aspect ratio (A.R.)) representing their evolution with the HDA and maintaining the rest of the parameters constant.

The formation of iron oxide NRs can be explained as competing effects between the decomposition of iron pentacarbonyl and the hydrolysis of iron oleate. Firstly, HDA and oleic

acid condense, forming water and iron oleate. The oleic acid also acts as a capping ligand, which attached to nucleation points of magnetite avoids the growth of the crystals on determined planes and results in rod-shaped nanoparticles expanding into the [110] direction.[22,23] Also, oleic acid avoids the oxidation of Fe^{+2} to Fe^{+3} and circumvents nanoparticle aggregation. To verify the crystalline structure of NRs, XRD experiments were conducted. As shown in **Figure 8.2a**, the characteristic crystalline structure of an inverse spinel is achieved. No peaks corresponding to any other phases were observed, indicating the high purity of the material. Since the XRD patterns of magnetite (Fe_3O_4) and maghemite (γ-Fe_2O_3) are very similar,[24] it is necessary to consider additional characterisation so the oxidation state of iron can be distinguished (Fe^{2+} and Fe^{3+} for magnetite and solely Fe^{2+} for maghemite). The XPS results in **Figures 8.2b** and **8.2c** confirm the magnetite composition, with binding energies of $2p_{3/2}$ and $2p_{1/2}$ and at 709.7 eV and 724.1 eV, respectively, and absence of satellite peak.[25]

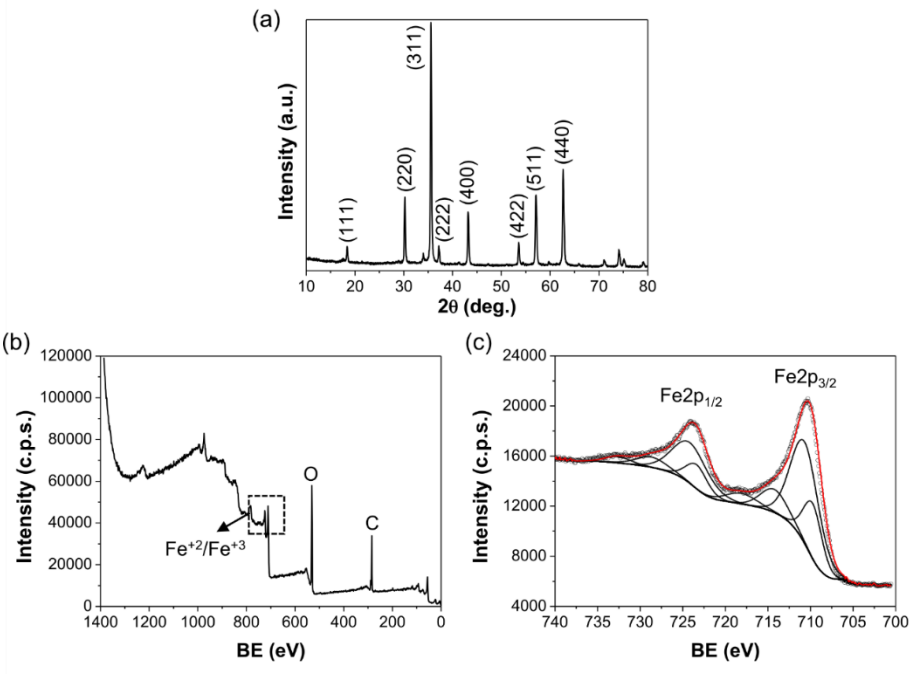

Figure 8.2. a) X-Ray diffraction pattern of NRs (140 ± 11 nm (length) and 14.8 ± 1.2 nm (width)) and X-Ray photoelectron spectrometry (XPS) spectra: (b) wide scan and (c) Fe 2p region.

8.3.2. Au-coated Fe_3O_4 nanorods (Fe_3O_4-NR@Au)

Then, Fe_3O_4 were hybridized with Au nanoshell to impart, together with the magnetic, also optical properties to the nanoparticles. To that end, Fe_3O_4 NRs were coated with a Au shell through a multi-step process consisting of: i) silanization of the surface of magnetite

NRs with APTES and transfer to water; ii) anchoring small Au nanoclusters, < 3 nm, (Au-seeds) on the surface of NRs to form a NR core-satellite (Fe_3O_4-NR-satellite) structure; iii) grow the Au-seeds until a complete shell is obtained. This coating strategy has been previously used to coat different types of nanoparticles such as silica,[20,26,27] or iron oxide,[28,29] and avoids the formation of patches generated by the slightly different lattice parameter between metallic Au and the double lattice fringe of iron oxide preventing a good epitaxial growth along the whole NR.[30,31]. Hereafter, results will focus on the medium-sized NRs with 140 ± 11 nm (length) and 14.8 ± 1.2 nm (width). This NR size was selected as a good compromise to exhibit a suitable magnetothermal effect, a relatively small size to avoid sedimentation, and for being big enough for a good formation of a thick Au shell layer around while maintaining a rod shape. This synthesis uses formaldehyde, a well-known toxic compound, that ideally would need to be replaced in the pursuit of a greener and less toxic chemistry. However, replacing it by greener reducing agents such as ascorbic acid or citrate gives rise to the formation of patches at the surface and/or secondary nucleation that form new gold nanoparticles. This is probably due to the highly autocatalytic reduction of K-gold by formaldehyde in which the gold is reduced mainly at the nanorods-satellite surface. Despite its use, formaldehyde is applied in very low concentrations, partially oxidized during the reaction, and removed in the successive cleaning steps giving rise to ppb and sub-ppb remaining concentrations, below its cytotoxic threshold,[32] and making the nanoparticles safe for biomedical applications.

During the first step, silane groups are bound selectively to magnetite and a 2D polymerization of the silanes is produced at its surface. As a result, the nanoparticles exhibit exposed amine groups that make them dispersible in water and a positive Zeta-potential of 14.5 ± 1.3 mV in ultrapure water. This leaves the NR surfaces available for Au-seeds linkage. In the next step, negatively charged Au-seeds and positively charged silanized NRs are mixed in an aqueous solution to form a new intermediate structure of NRs with Au-seeds attached to the surface amine functional groups, resulting in the so-called NR-satellites. Negative Zeta-potential values of -14.3 ± 1.7 mV indicated the successful attachment of Au-seeds. Finally, a complete shell was obtained upon the reduction of the extra amount of Au, from a Au growth solution (K-gold) of $HAuCl_4$ and K_2CO_3 on the NR-satellites and by using formaldehyde as a reducing agent. Au-satellites act as growing sites so metallic Au is formed on their surface finally merging and forming a complete shell. **Figure 8.3a** schematically shows the TEM images of NRs at different degrees of Au-coating, starting with Fe_3O_4-NR-satellites (Fe_3O_4 =

1.26 mM; Au = 2.22 mM) until a thick shell of Au is obtained. The differences in the shell formation were obtained by adjusting the ratio between Fe_3O_4-NR-satellites and $HAuCl_4$, (see **Table 8.1** in the experimental section of this chapter).

UV-Vis was conducted to get further insights into the state of the shell. As shown in **Figure 8.3b**, the Fe_3O_4-NR-satellite solution presents a dark-brown color (sample 0; left vial in the photograph) without a peak in the visible spectrum. On the contrary, sample 1, having a small ratio of Au growth solution/NR-satellites ($HAuCl_4$ (mM)/ Fe_3O_4 (mM) = 0.08), turns into a lilac (or pale violet) color with a maximum absorbance peak at 543 nm. This effect is ascribed to the growth of the Au satellites onto Fe_3O_4 surfaces. In samples 2 and 3, satellites are big enough to touch and start merging each other, although a complete shell is not formed. They present bluish color, where the maximum absorbance shifts to higher wavelengths of 556 and 568 nm, respectively, and a high increase of the absorbance at the near Infrared (NIR) (Au layer in sample 3 is 12.7 ± 4.6 nm thick) is observed. A complete lumpy shell (Fe_3O_4-NR@Au) of 16.6 ± 3.6 nm thick was obtained for sample 4, where two maximum absorbance peaks appear at 537 and 613 nm and a large tail that extends up to the NIR region are observed. This is somehow similar to previously reported Au coated hematite spindles,[28] however in this case a very broad peak from the reds to the near IR region was obtained. This broad peak could be interpreted as a mixture between the expected peak of the nanoshell-rod hybridization mode and the modes of the bumpy rough surface of the NR, somehow similar to a quasy-nanostar morphology. Finally, a 25.0 ± 4.5 nm thick Au shell can be observed for sample 5, which presents only one narrower peak at 538 nm with additional absorption in the infrared region. Based on this, samples with the thinnest but complete shells are optimal for a photothermal therapy using NIR light.

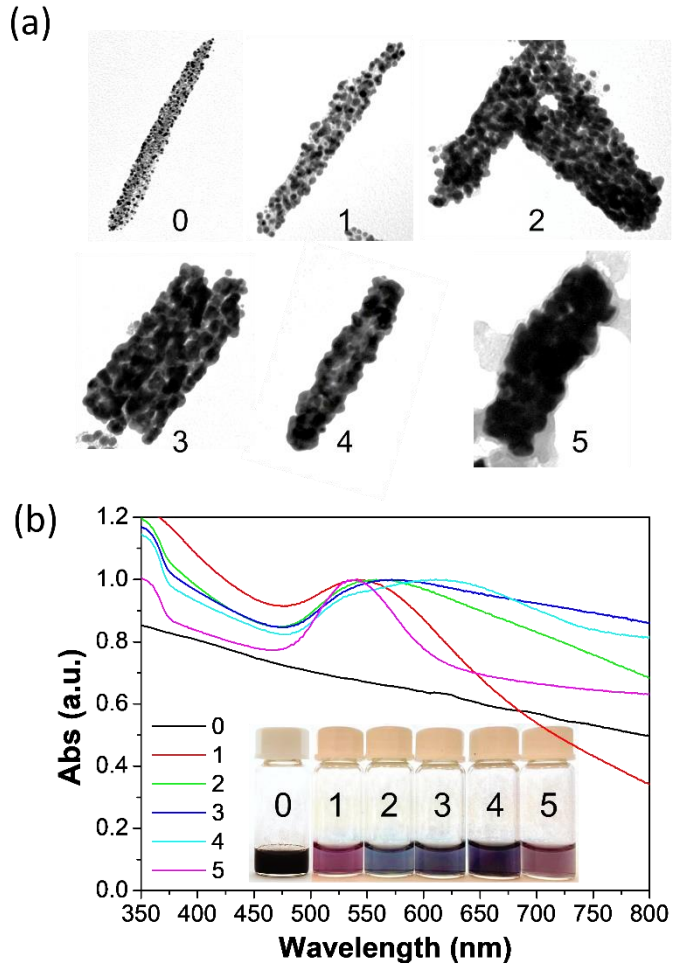

Figure 8.3. a) TEM image of the rods at different growth conditions. Sample 0 corresponds to Fe_3O_4-NR-satellites structure, and the subsequent samples (1-5) were prepared increasing the amount of the ratio [K-gold]/[NR-satellite seeds], generating different degrees of core-satellites until a complete core-shell is obtained. b) UV-Vis spectra of the solution of the different nanoparticles and their pictures showing the differences in the optical properties (a).

The complete shell is required as a protective layer for the magnetite to help maintain its properties during therapeutic use. On the other hand, thicker shells produce undesired shifts of the plasmonic bands to lower wavelengths. Therefore sample 4 shows the most desirable characteristics for photothermia, and although the maximum absorbance is still around 613 nm, the broad band at the NIR covers the whole first transparency window of biological tissue with a relatively high extinction coefficient, which is, as shown below, more than enough to drive an effective photothermal effect. Note here that this absorption is mainly due to the absorption of the gold part as iron oxide shows a limited extinction coefficient at these wavelengths and would require several orders of magnitude higher concentration to achieve photothermia.[33,34]

8.3.3. Agarose/NR and agarose/Fe_3O_4-NR@Au composite hydrogels

Fe_3O_4-NR@Au were then incorporated into a polymeric matrix to obtain a free-standing material with magnetic and optical properties. Anisotropic hydrogels were prepared by dispersing NRs into aqueous agarose solutions (previously dissolved in water by microwave) at 45 ºC in an ultrasonic bath and then placing the mixture between the gap of two magnets at 0.32 T (see **Scheme 8.1**). In these conditions, the NRs orientate according to the applied magnetic fields due to magnetic dipolar interactions and the relatively low viscosity of the media. Once the temperature decreases below the gel point, the gelation process arrests the structure. In other words, the gelation traps the nanoparticles into the oriented condition. The mechanical properties of the agarose hydrogels at different NPs concentrations were measured to determine their capacity to withstand externally applied compressive forces. **Figure 8.4a** shows representative uniaxial compressive stress–strain curves of neat agarose hydrogels at concentrations ranging from 0.5 to 3 wt.%. The curves are characterised by an elastic behavior at strains up to 20 % where the compressive stress increases linearly with strain, followed by a plastic deformation region (20 to 60 % strain) and a final stiffening region at strains exceeding 60 %.[35] Generally, all the gels show good deformability as they are able to accommodate strains without breaking. Compressive modulus values of 7.9-180.9 kPa were achieved for the 0.5-3 wt.% compositions. Those values are similar to hydrogels formed by other biopolymers, including cellulose nanocrystal hydrogels (7 kPa),[36] or the 25-85 kPa for cellulose nanofibers.[37] The increased modulus with agarose concentration results from the formation of extensive physical crosslinks between agarose chains through weak interactions, yielding a mechanically robust three-dimensional structure.[38] In addition, agarose hydrogels comprising a 0.1 wt.% of Fe_3O_4-NR@Au were tested to study the effect of the Fe_3O_4-NR@Au at different orientations inside the hydrogel matrix. The parameters of hydrogel, at this concentration, remain very similar and comparable to the neat agarose hydrogel. When using agarose at 1 wt.%, however, a displacement of the NRs inside the hydrogel during the magnetic characterisation curves was observed. This displacement/rotation was not visualized magnetically at concentrations of 2 wt.% and above, where the nanorods were arrested inside of the hydrogel and no changes were observed in the magnetic behavior after exposing them to magnetic fields. Based on mechanical and magnetic results, we decided to prepare the composite hydrogels at 2 wt.% of agarose due to its fabrication simplicity by microwave heating, its suitable mechanical strength, easiness to

manipulate, and the adequate entrapment of NRs (**Figure 8.4b**). Both magnetite NRs and Fe_3O_4-NR@Au were prepared in this way and characterised magnetically and optically.

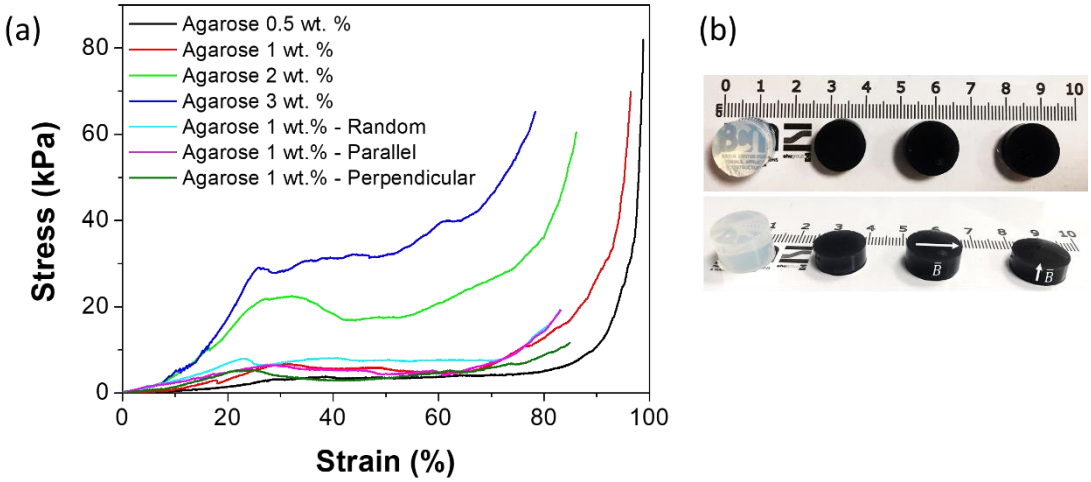

Figure 8.4. (a) Representative stress−strain curves of compression test for agarose hydrogels of 0.5 wt.%, 1 wt.%, 2 wt.%, 3 wt.% and agarose hydrogels of 1 wt.% comprising 0.1 wt.% of NR@Au in random parallel and perpendicular orientations. (b) Images of neat and NR@Au loaded Agarose hydrogels, with indication of the direction of the applied magnetic field.

Besides, the strong and fast gelling character upon cooling the dispersion to temperatures below the gelling point offers an interesting platform to incorporate synthesized nanoparticles.[39] More interestingly, like many other polysaccharides, agarose dispersions show a characteristic shear-thinning behavior.[40] This property encourages us to also fabricate magnetically active injectable hydrogels, where water-based agarose/NR hybrids are injected by application of shear stresses and quickly self-heal after the removal of shear forces.[41] As shown in **Figure 8.5**, after a 45ºC water-based agarose/Fe_3O_4-NRs@Au dispersion was injected into an aqueous solution with a retracting movement, they form smooth and continuous hydrogel filaments with a dark color as a result of the optically and magnetically active core-shell nanoparticles. The combination of such magnetic-optic properties and their injectable character makes these materials suitable for localized cancer therapies, outperforming traditional cancer treatments.[42] The ability to obtain filaments is also interesting for biomedical applications where large surface areas are preferred,[43] as well as the generation of novel avenues for the development of (magnetically) externally-triggered drug delivery applications, allowing a new family of minimally invasive on-demand drug delivery systems.[44]

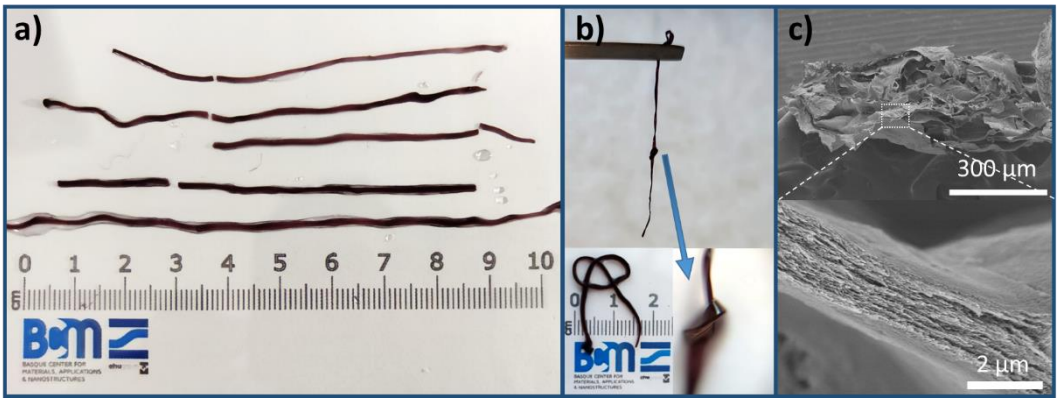

Figure 8.5. Injected Fe_3O_4-NR@Au/hydrogel filaments obtained with a syringe (gelification occurs at room temperature). a) Optical photographs of the formed filaments having several centimeters in length and uniform thickness. b) The knot shows the malleability of the produced hydrogel filaments that can adapt to the desired shape. c) SEM images of the crossed section of the filament (aprox. 1.2 x 0.25 mm^2) after freeze-drying and the fracture surface showing the macroporosity of the structure (upper image) and sub-mircroporosity on the cell walls.

8.3.4. Magnetic properties of hydrogels

With the aim to determine the magnetic properties of the NRs, a powder of NRs, prepared by evaporating the solvent overnight in vacuum conditions, was analyzed through VSM. A saturation magnetization (M_S) of 83.1 emu·g^{-1}, a remanence (M_R) of 16.8 emu·g^{-1} and a coercive field (H_C) of 8.0 mT were obtained as shown in **Figure 8.6**). The obtained M_S showed low values in comparison with the bulk value of 92 Am^2kg^{-1}.[45] This could be ascribed to a combination of the coating of a non-magnetic oleic acid/HDA monolayer, coated surface's electrostatic interactions, and the formation of aggregates that quench the saturation magnetization.[46,47]

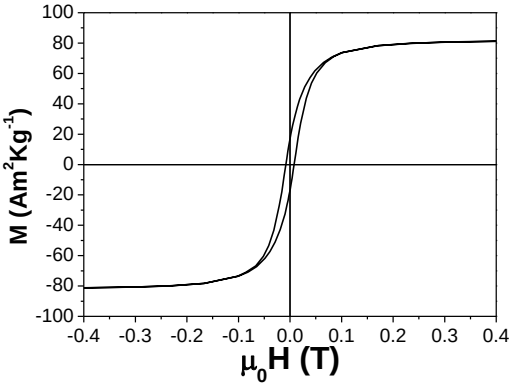

Figure 8.6. Magnetic hysteresis loops of magnetite NRs with a length of 140 ± 11 nm.

When 0.065 mg of the NRs were incorporated into the hydrogel under a magnetic field, the NRs got oriented inside it. In fact, as observed in optical microscopy pictures of the prepared hydrogels in **Figure 8.7a**, the field-directed assembly process induced the formation of linear NR assemblies, with microscopic NR lines parallel to the observed external magnetic field, and dark points in the perpendicular direction. This orientation is obtained thanks to the elongated shape of the NRs which confers a marked shape anisotropy, where the long axis is considered as the easy magnetization axis and a dipole-dipole interaction between the NRs takes place. On the contrary, for samples of non-oriented NRs, a homogenous color of the sample, without the presence of any darker spot, was observed.

M-H hysteresis loops of the NR-loaded hydrogels were measured in a random, parallel, and perpendicular direction and represented in **Figure 8.7b.** The marked differences in the hysteresis loops demonstrate the anisotropy with respect to the composite hydrogel in the random orientation of loaded NRs. Both the random and parallel oriented samples exhibit a similar coercive field of 10.2 and 10.6 mT, respectively, which is slightly higher in comparison with the powder sample. Interestingly, the loop measured in the parallel direction reaches faster saturation at a field (H_S, indicated with dashed lines) of 155 mT as compared to the random orientation loop (H_S = 242 mT). In addition, larger M_R (13.7 $Am^2 \cdot kg^{-1}$) was measured for parallel orientation than for randomly distributed NRs (M_R = 8.05 $x10^{-4}$ $Am^2 \cdot kg^{-1}$). As expected, the opposite effect was observed for perpendicularly oriented NRs, where lower values of H_C = 76 mT and M_R = 5.77 $x10^{-4}$ $Am^2 \cdot kg^{-1}$ and slower curve with H_S = 320 mT were measured. These results demonstrate that synthesized magnetite NRs presented enough magnetic susceptibility to be aligned within the hydrogel. The anisotropy of the gel containing oriented NRs was further demonstrated using X-ray Azimuthal angle plots. As seen in **Figure 8.8** for the *in plane* [311] peak, a high angular variation is observed. The separation of 180 degrees between both maximum intensities is indicative of the single-crystal NRs orientation inside of the gel. Finally, **Figure 8.7c** shows the magnetic behavior of Fe_3O_4-NR@Au (0.6 mg) within a hydrogel under a magnetic field. Similar differences between parallel, perpendicular and random to those of the pure NRs are achieved, indicating that even with the additional weight and volume of the non-magnetic material, the NRs were still able to orientate and assemble prior to the gelation of agarose. Despite this, higher slightly higher values of remanence and coercitivity are observed for the three configurations, which, as discussed below, can improve the magnetothermal effect.

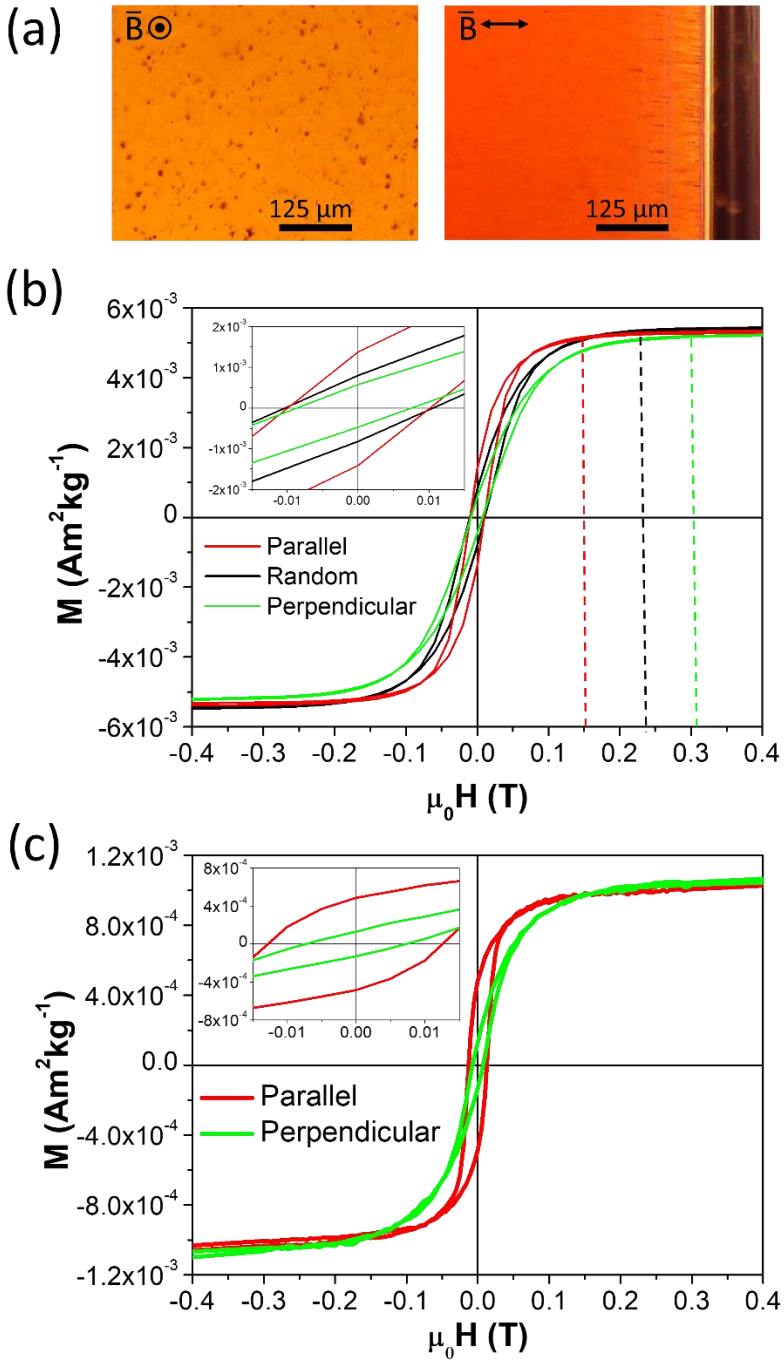

Figure 8.7. a) Optical microscopy pictures of the gel at agarose 2 wt.% and loaded with 0.065 mg of NR, taken parallel to the magnetic field applied (left) and in a perpendicular direction (right) where alignment of elongated structures can be observed. b) Corresponding magnetic hysteresis loops of gels, measured in VSM, for non-oriented NRs, perpendicular, and parallel-oriented NRs. Dashed lines indicate the magnetic field applied when the M_s is reached (H_S) for each orientation. The inset shows a magnified view of the hysteresis loops. c) Magnetic hysteresis loops of the gels at 2 wt.%, measured in VSM, for perpendicular, and parallel-oriented, comprising 0.6 mg of Fe_3O_4-NR@Au. The inset shows a magnified view of the hysteresis loops.

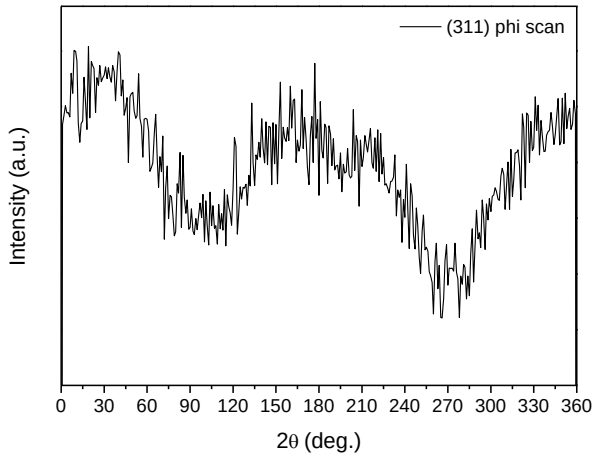

Figure 8.8. X-Ray diffraction pattern of (311) plane in Azimuthal angle plots for 2 wt.% agarose hydrogels loaded with silanized 140 ± 11 nm NRs.

8.3.5. Magnetic hyperthermia

Magnetic hyperthermia offers a non-toxic, local and selective solution for the treatment of tumors by producing local heating through the application of external magnetic fields.[48] Accordingly, the magnetothermal capabilities of the hydrogel containing NRs of three different sizes, with lengths of 52, 140, and 397 nm, were tested with different configurations: with the alignment parallel to the magnetic field, perpendicular to the magnetic field, and without a preferential orientation, i.e. random. In this case, relatively large amounts of NRs (3mg·mL^{-1}) were needed due to the sensibility of the equipment. To characterise the magnetothermal effect of the NR, their AC hysteresis loops were measured and the SAR was directed obtained from the area of the loops using an AC magnetometer previously described.[49] These measurements allow precise quantification of the power generated by integrating the area of the hysteresis loops. At first view, a high difference is appreciated in AC hysteresis loops shape when comparing the three different configurations (see **Figure 8.9a-c** for 140 ± 11 nm NRs). The perpendicular configuration shows narrow and elongated hysteresis loops while the parallel configuration shows a more square shape with a higher area. The case of the random configuration remains in between both configurations. Similar shapes have been reported for instance in magnetotactic bacteria dispersed in agar, somehow similar to a rod shapes, under random and parallel orientation.[50] The SAR was calculated as a function of the applied magnetic field for the three NR lengths and the three configurations (**Figure 8.9d-f**). The results show a sigmoidal shape, and for the case of

parallel oriented configuration, the increase in SAR begins at much lower magnetic fields than for the perpendicular configuration. In fact, the sigmoidal middle point (magnetic field at half maximum of the sigmoid) is 20-30 mT lower for the perpendicular than for the parallel case (20, 26 and 30 mT for the 52, 140, and 357 nm NRs respectively). For the case of randomly oriented NRs it shows intermediate values. Additionally, the maximum SAR value, obtained at high magnetic fields, was also dependent on the orientation, achieving the highest values for the case of parallel configuration and the lowest ones for the perpendicular case. Therefore, the use of oriented NRs seems an efficient strategy for achieving an enhanced SAR that allows the use of lower quantities of nanoparticles or alternatively the decrease of magnetic field and frequencies, to achieve similar effects to other non-anisotropic iron oxides nanoparticles. Additionally, the high difference between parallel and perpendicular configurations opens the door to a fine-tuning of the magnetothermal effect by varying the angle of application of magnetic fields.

The change of NR length did not seem to produce a big variation in the measured SAR value, the small differences could be on the other hand due to small differences in the NRs concentration or small portions of aggregation. To see the influence of the Au shell on the magnetothermal effect, the 140 nm length NRs were coated with Au. This NR size (140 ± 11 nm length) was chosen as a compromise to have a NR big enough to have a relatively homogenous coating, while not too big to have nanoparticle sedimentation. The SAR for the three configurations of Fe_3O_4-NRs@Au (3mg·mL^{-1} of Fe_3O_4, 150 mg·mL^{-1} of Fe_3O_4-NRs@Au) can be observed in **Figure 8.9g**. This graph shows very similar results to the non-coated nanoparticles, with the parallel configuration showing a higher maximum SAR at high fields but interestingly, unlike the case of non-coated NRs, it shows that the beginning of SAR increases at similar magnetic fields for the three different configurations. The values are higher than the non-coated nanoparticles, attributed to a dipolar decoupling due to the Au shell spacer between the nanoparticles, similar to what has been seen to other coated magnetic nanoparticles.[51] This dipolar decoupling produces a more squared hysteresis loop with higher remanence and coercivity which is translated into a higher heat generated per magnetic cycle.

8.3.6. Plasmonic hyperthermia

The same Fe_3O_4-NRs@Au were used to form a gel for photothermal transduction. In this case, due to the much higher efficiency of plasmonic photothermia, a much lower concentration was used (0.1 $mg \cdot mL^{-1}$ instead of 3 $mg \cdot mL^{-1}$ for magnetothermia). The gel was formed inside a fluorescence cuvette and oriented in one of the directions (parallel to the cuvette base). The gel was irradiated with NIR (735 nm) light from one side of the cuvette either parallel or perpendicular to the NRs@Au inside the cuvette using an LED light and being the temperature monitored from above with a thermal camera. LED light was chosen as a simple, cheap, and highly available illumination source, while 735 nm is located at the middle of the first transparency window where minimum absorption by leaving tissue takes place. The gel showed high photothermal efficiency, with an increment of the temperature of more than 20 °C for a low light power of 0.2 W (**Figure 8.9h**), which is harmless for tissues such skin or other internal tissues,[52,53] and a low nanoparticle concentration. When comparing the two configurations, however, very similar results were obtained, only marginally superior for the case of parallel configuration. This unexpected result is probably due to the complexity of the plasmonic modes of the nanoparticles that produce a very broad plasmonic band that comprises the nanoshell modes plus the additional modes of the bumpy surface of the nanoparticles, which makes it difficult to excite uniquely the longitudinal and transversal hybridized modes.

The photothermal SAR was calculated for this sample in terms of the Au mass as the photothermal active element. Values of 2.18 and 2.36 KW g^{-1} for parallel and perpendicular configuration respectively were obtained for the given setup conditions (0.2 $W \cdot cm^{-2}$, 735 nm). These values are one order of magnitude higher than the ones obtained in magnetothermia and in the same order of magnitude that other reported plasmonic structures,[54,55] in particular after considering the low power used here (corresponding to a SAR of 11.8 KW g^{-1} per watt of irradiating light).

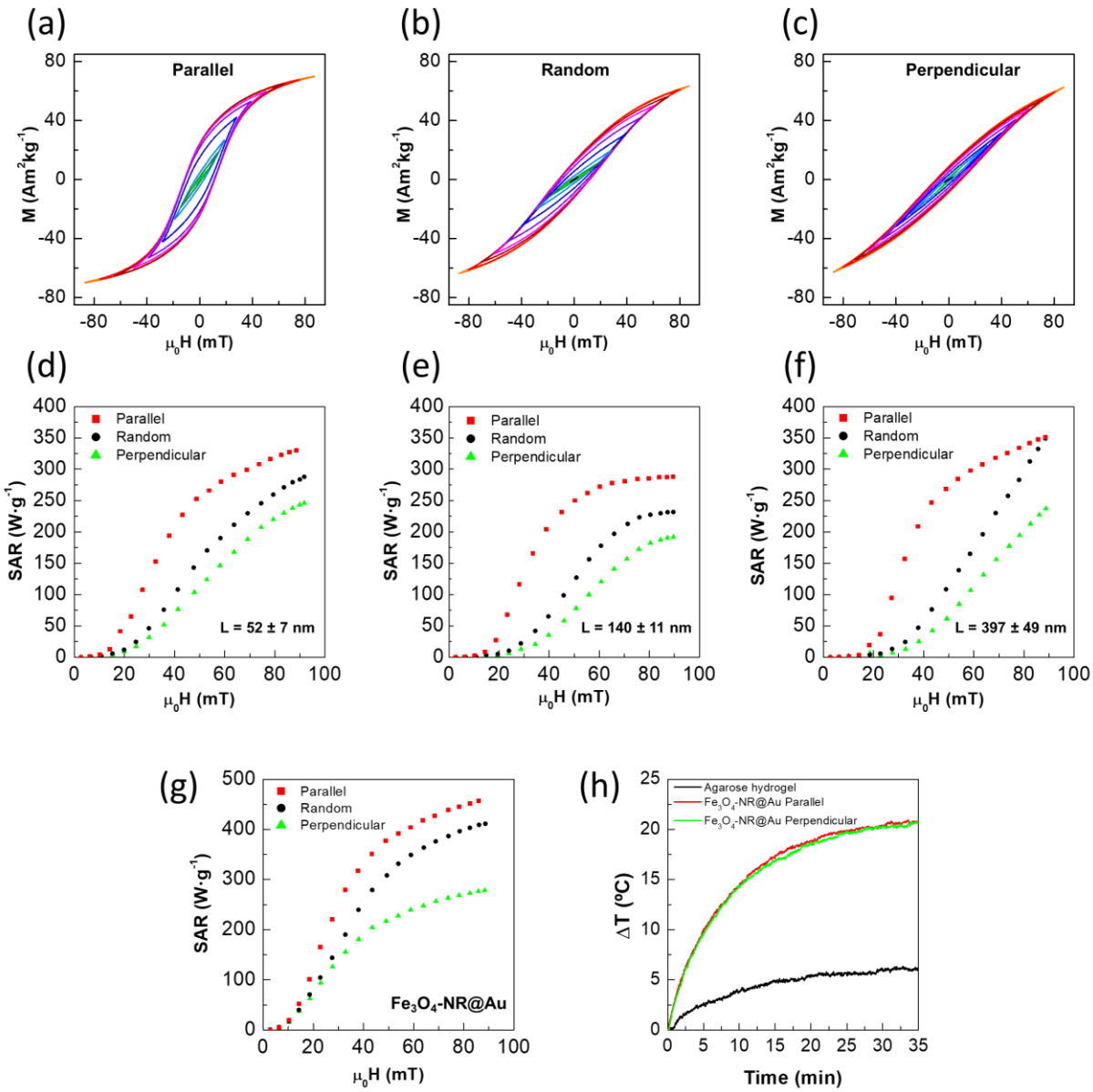

Figure 8.9. AC magnetometry measurements of agarose hydrogel at 2 wt.% loaded with 3 mg·mL^{-1} of magnetite NRs of a length of 140 nm in (a) parallel, (b) random, and (c) perpendicular orientations measured at 133 kHz. SAR dependent of the applied magnetic field of different sized NRs: (d) L= 52 ± 7 nm, (e) L= 140 ± 11 nm and (f) L= 397 ± 49 nm. Magnetothermia (g) and photothermia (h) of Fe_3O_4-NR@Au were also measured.

8.4. Conclusions

The synthesis of novel Fe_3O_4@Au NRs and their tunability in both nanoparticle dimension and shell thickness has been demonstrated by varying the HDA capping ligand and the ratio of seeds to Au, respectively. Developed core-shell materials show magnetic and photonic properties and tailored sizes for magneto- and photo-thermal anisotropic transductions. The

NRs were aligned within a hydrogel upon cooling in the presence of a magnetic field. The gel showed a clear anisotropy, as demonstrated by magnetical and XRD experiments. This gel offers the possibility to produce simultaneous magneto- and photo-thermia which can be used as dual therapy either in regenerative medicine or in cancer ablation, in which the synergistic effect and the possibility to induce anisotropic response can help to lower the therapeutic doses in terms of nanoparticles, light irradiation, or magnetic field applied. Moreover, obtained magnetic filament hydrogels upon injection offer suitable characteristics to be applied in localized therapies. Its use also opens the door to further technological applications where directionality and dual magnetic and optical properties are required, such as sensors or actuators, among others.

8.5. References

1 R. Ghosh Chaudhuri and S. Paria, Core/Shell Nanoparticles: Classes, Properties, Synthesis Mechanisms, Characterization, and Applications, *Chem. Rev.*, 2012, **112**, 2373–2433.

2 N. D. Burrows, A. M. Vartanian, N. S. Abadeer, E. M. Grzincic, L. M. Jacob, W. Lin, J. Li, J. M. Dennison, J. G. Hinman and C. J. Murphy, Anisotropic Nanoparticles and Anisotropic Surface Chemistry, *J. Phys. Chem. Lett.*, 2016, **7**, 632–641.

3 S. Link, M. B. Mohamed and M. A. El-Sayed, Simulation of the Optical Absorption Spectra of Gold Nanorods as a Function of Their Aspect Ratio and the Effect of the Medium Dielectric Constant, *J. Phys. Chem. B*, 1999, **103**, 3073–3077.

4 E. Cazares-Cortes, S. Cabana, C. Boitard, E. Nehlig, N. Griffete, J. Fresnais, C. Wilhelm, A. Abou-Hassan and C. Ménager, Recent insights in magnetic hyperthermia: From the "hot-spot" effect for local delivery to combined magneto-photo-thermia using magneto-plasmonic hybrids, *Adv. Drug Deliv. Rev.*, 2019, **138**, 233–246.

5 T. A. Larson, J. Bankson, J. Aaron and K. Sokolov, Hybrid plasmonic magnetic nanoparticles as molecular specific agents for MRI/optical imaging and photothermal therapy of cancer cells, *Nanotechnology*, 2007, **18**, 325101.

6 J. Reguera, D. de Aberasturi, M. Henriksen-Lacey, J. Langer, A. Espinosa, B. Szczupak, C. Wilhelm and L. M. Liz-Marzán, Janus plasmonic-magnetic gold-iron oxide nanoparticles as contrast agents for multimodal imaging, *Nanoscale*, 2017, **9**, 9467–9480.

7 M. Grzelczak, J. Vermant, E. M. Furst and L. M. Liz-Marzán, *ACS Nano*, 2010, 4, 3591–3605.

8 I. Castellanos-Rubio, I. Rodrigo, A. Olazagoitia-Garmendia, O. Arriortua, I. Gil de Muro, J. S. Garitaonandia, J. R. Bilbao, M. L. Fdez-Gubieda, F. Plazaola, I. Orue, A. Castellanos-Rubio and M. Insausti, Highly Reproducible Hyperthermia Response in Water, Agar and Cellular Environment by Discretely PEGylated Magnetite Nanoparticles., *ACS Appl. Mater. Interfaces*, 2020, **12**, 27917–27929.

9 R. Vo, H. H. Hsu and X. Jiang, Hydrogel facilitated bioelectronic integration, *Biomater. Sci.*, 2021, **9**, 23–37.

10 H. Seto, H. Matsumoto and Y. Miura, Preparation of palladium-loaded polymer hydrogel catalysts with high durability and recyclability, *Polym. J.*, 2020, **52**, 671–679.

11 K. J. De France, T. Hoare and E. D. Cranston, Review of Hydrogels and Aerogels Containing Nanocellulose, *Chem. Mater.*, 2017, **29**, 4609–4631.

12 M. Umar, K. Min and S. Kim, Advances in hydrogel photonics and their applications, *APL Photonics*, 2019, **4**, 120901.

13 E. Lizundia and D. Kundu, Advances in Natural Biopolymer-Based Electrolytes and Separators for Battery Applications, *Adv. Funct. Mater.*, 2021, **31**, 2005646.

14 K. Sano, Y. Ishida and T. Aida, Synthesis of Anisotropic Hydrogels and Their Applications, *Angew. Chemie Int. Ed.*, 2018, **57**, 2532–2543.

15 S. Yook, S. Shams Es-haghi, A. Yildirim, Z. Mutlu and M. Cakmak, Anisotropic hydrogels formed by magnetically-oriented nanoclay suspensions for wound dressings, *Soft Matter*, 2019, **15**, 9733–9741.

16 K. Hu, J. Sun, Z. Guo, P. Wang, Q. Chen, M. Ma and N. Gu, A Novel Magnetic Hydrogel with Aligned Magnetic Colloidal Assemblies Showing Controllable Enhancement of Magnetothermal Effect in the Presence of Alternating Magnetic Field, *Adv. Mater.*, 2015, **27**, 2507–2514.

17 S. Monz, A. Tschöpe and R. Birringer, Magnetic properties of isotropic and anisotropic CoFe2O4 -based ferrogels and their application as torsional and rotational actuators, *Phys. Rev. E - Stat. Nonlinear, Soft Matter Phys.*, 2008, **78**, 021404.

18 Y. Gu and K. G. Kornev, Alignment of Magnetic Nanorods in Solidifying Films, *Part. Part. Syst. Charact.*, 2013, **30**, 958–963.

19 J.-C. Si, Y. Xing, M.-L. Peng, C. Zhang, N. Buske, C. Chen and Y.-L. Cui, Solvothermal synthesis of tunable iron oxide nanorods and their transfer from organic phase to water phase, *CrystEngComm*, 2014, **16**, 512–516.

20 A. M. Brito-Silva, R. G. Sobral-Filho, R. Barbosa-Silva, C. B. de Araújo, A. Galembeck and A. G. Brolo, Improved Synthesis of Gold and Silver Nanoshells, *Langmuir*, 2013, **29**, 4366–4372.

21 N. Li, G.-W. Huang, X.-J. Shen, H.-M. Xiao and S.-Y. Fu, Controllable fabrication and magnetic-field assisted alignment of Fe3O4-coated Ag nanowires via a facile co-precipitation method, *J. Mater. Chem. C*, 2013, **1**, 4879–4884.

22 H. Sun, B. Chen, X. Jiao, Z. Jiang, Z. Qin and D. Chen, Solvothermal synthesis of tunable electroactive magnetite nanorods by controlling the side reaction, *J. Phys. Chem. C*, 2012, **116**, 5476–5481.

23 R. Das, J. Alonso, Z. Nemati Porshokouh, V. Kalappattil, D. Torres, M.-H. Phan, E. Garaio, J. Á. García, J. L. Sanchez Llamazares and H. Srikanth, Tunable High Aspect Ratio Iron Oxide Nanorods for Enhanced Hyperthermia, *J. Phys. Chem. C*, 2016, **120**, 10086–10093.

24 M. I. Dar and S. A. Shivashankar, Single crystalline magnetite, maghemite, and hematite nanoparticles with rich coercivity, *RSC Adv.*, 2014, **4**, 4105–4113.

25 S. P. Schwaminger, D. Bauer, P. Fraga-García, F. E. Wagner and S. Berensmeier, Oxidation of magnetite nanoparticles: impact on surface and crystal properties, *CrystEngComm*, 2017, **19**, 246–255.

26 N. Phonthammachai, J. C. Y. Kah, G. Jun, C. J. R. Sheppard, M. C. Olivo, S. G. Mhaisalkar and T. J. White, Synthesis of contiguous silica-gold core-shell structures: Critical parameters and processes, *Langmuir*, 2008, **24**, 5109–5112.

27 M. K. Otoufi, N. Shahtahmasebebi, A. Kompany and E. Goharshadi, A systematic growth of Gold nanoseeds on Silica for Silica@Gold core-shell nanoparticles and investigation of optical properties, *Int. J. Nano Dimens.*, 2014, **5**, 525–531.

28 Hui Wang, Daniel W Brandl, Fei Le, Peter Nordlander and and Naomi J Halas, Nanorice: A Hybrid Plasmonic Nanostructure, *Nano Lett.*, 2006, **6**, 827–832.

29 M. Spuch-Calvar, J. Pérez-Juste and L. M. Liz-Marzán, Hematite spindles with optical functionalities: Growth of gold nanoshells and assembly of gold nanorods, *J. Colloid Interface Sci.*, 2007, **310**, 297–301.

30 H. Yu, M. Chen, P. M. Rice, S. X. Wang, R. L. White and S. H. Sun, Dumbbell-like bifunctional Au-Fe3O4 nanoparticles, *Nano Lett.*, 2005, **5**, 379–382.

31 C. Gatel and E. Snoeck, Epitaxial growth of Au and Pt on Fe3O4(1 1 1) surface, *Surf. Sci.*, 2007, **601**, 1031–1039.

32 Y. J. Ke, X. D. Qin, Y. C. Zhang, H. Li, R. Li, J. L. Yuan, X. Yang and S. M. Ding, In vitro study on cytotoxicity and intracellular formaldehyde concentration changes after exposure to formaldehyde and its derivatives, *Hum. Exp. Toxicol.*, 2014, **33**, 822–830.

33 B. Lesiak, N. Rangam, P. Jiricek, I. Gordeev, J. Tóth, L. Kövér, M. Mohai and P. Borowicz, Surface

Study of Fe3O4 Nanoparticles Functionalized With Biocompatible Adsorbed Molecules, *Front. Chem.*, 2019, **7**, 642.

34 E. Alphandéry, Light-Interacting iron-based nanomaterials for localized cancer detection and treatment, *Acta Biomater.*, 2021, **124**, 50–71.

35 B. Wicklein, A. Kocjan, G. Salazar-Alvarez, F. Carosio, G. Camino, M. Antonietti and L. Bergström, Thermally insulating and fire-retardant lightweight anisotropic foams based on nanocellulose and graphene oxide, *Nat. Nanotechnol.*, 2015, **10**, 277–283.

36 C. M. Walters, G. K. Matharu, W. Y. Hamad, E. Lizundia and M. J. MacLachlan, Chiral Nematic Cellulose Nanocrystal/Germania and Carbon/Germania Composite Aerogels as Supercapacitor Materials, *Chem. Mater.*, 2021, **33**, 5197–5209.

37 Y. Liu, Y. Sui, C. Liu, C. Liu, M. Wu, B. Li and Y. Li, A physically crosslinked polydopamine/nanocellulose hydrogel as potential versatile vehicles for drug delivery and wound healing, *Carbohydr. Polym.*, 2018, **188**, 27–36.

38 K. Rotjanasuworapong, N. Thummarungsan, W. Lerdwijitjarud and A. Sirivat, Facile formation of agarose hydrogel and electromechanical responses as electro-responsive hydrogel materials in actuator applications, *Carbohydr. Polym.*, 2020, **247**, 116709.

39 M. Ghebremedhin, S. Seiffert and T. A. Vilgis, Physics of agarose fluid gels: Rheological properties and microstructure, *Curr. Res. Food Sci.*, 2021, **4**, 436–448.

40 F. Cuomo, M. Cofelice and F. Lopez, Rheological Characterization of Hydrogels from Alginate-Based Nanodispersion, *Polymers (Basel).*, 2019, **11**, 259.

41 M. Guvendiren, H. D. Lu and J. A. Burdick, Shear-thinning hydrogels for biomedical applications, *Soft Matter*, 2012, **8**, 260–272.

42 D.-Y. Fan, Y. Tian and Z.-J. Liu, Injectable Hydrogels for Localized Cancer Therapy, *Front. Chem.*, 2019, **7**, 675.

43 M. Shin, K. H. Song, J. C. Burrell, D. K. Cullen and J. A. Burdick, Injectable and Conductive Granular Hydrogels for 3D Printing and Electroactive Tissue Support, *Adv. Sci.*, 2019, **6**, 1901229.

44 R. Dimatteo, N. J. Darling and T. Segura, In situ forming injectable hydrogels for drug delivery and wound repair, *Adv. Drug Deliv. Rev.*, 2018, **127**, 167–184.

45 J. Watt, G. C. Bleier, Z. W. Romero, B. G. Hance, J. A. Bierner, T. C. Monson and D. L. Huber, Gram scale synthesis of Fe/FexOy core–shell nanoparticles and their incorporation into matrix-free superparamagnetic nanocomposites, *J. Mater. Res.*, 2018, **33**, 2156–2167.

46 B. Feng, R. Y. Hong, L. S. Wang, L. Guo, H. Z. Li, J. Ding, Y. Zheng and D. G. Wei, Synthesis of Fe3O4/APTES/PEG diacid functionalized magnetic nanoparticles for MR imaging, *Colloids Surfaces A Physicochem. Eng. Asp.*, 2008, **328**, 52–59.

47 G. F. Goya, T. S. Berquó, F. C. Fonseca and M. P. Morales, Static and dynamic magnetic properties of spherical magnetite nanoparticles, *J. Appl. Phys.*, 2003, **94**, 3520–3528.

48 C. Mandawala, I. Chebbi, M. Durand-Dubief, R. Le Fèvre, Y. Hamdous, F. Guyot and E. Alphandéry, Biocompatible and stable magnetosome minerals coated with poly-l-lysine, citric acid, oleic acid, and carboxy-methyl-dextran for application in the magnetic hyperthermia treatment of tumors, *J. Mater. Chem. B*, 2017, **5**, 7644–7660.

49 I. Rodrigo, I. Castellanos-Rubio, E. Garaio, O. K. Arriortua, M. Insausti, I. Orue, J. Á. García and F. Plazaola, Exploring the potential of the dynamic hysteresis loops via high field, high frequency and temperature adjustable AC magnetometer for magnetic hyperthermia characterization, *Int. J. Hyperth.*, 2020, **37**, 976–991.

50 D. Gandia, L. Gandarias, I. Rodrigo, J. Robles-García, R. Das, E. Garaio, J. Á. García, M.-H. Phan, H. Srikanth, I. Orue, J. Alonso, A. Muela and M. L. Fdez-Gubieda, Unlocking the Potential of Magnetotactic Bacteria as Magnetic Hyperthermia Agents, *Small*, 2019, **15**, 1902626.

51 A. K. Boal, B. L. Frankamp, O. Uzun, M. T. Tuominen and V. M. Rotello, Modulation of Spacing and Magnetic Properties of Iron Oxide Nanoparticles through Polymer-Mediated 'Bricks and Mortar' Self-assembly, *J. Phys. Chem B*, 2003, **107**, 3252–3256.

52 X. Ding, C. H. Liow, M. Zhang, R. Huang, C. Li, H. Shen, M. Liu, Y. Zou, N. Gao, Z. Zhang, Y. Li, Q. Wang, S. Li and J. Jiang, Surface plasmon resonance enhanced light absorption and photothermal therapy in the second near-infrared window., *J. Am. Chem. Soc.*, 2014, **136**, 15684–15693.

53 A. N. Bashkatov, E. A. Genina, V. I. Kochubey and V. V. Tuchin, Optical properties of human skin, subcutaneous and mucous tissues in the wavelength range from 400 to 2000 nm, *J. Phys. D. Appl. Phys.*, 2005, **38**, 2543–2555.

54 A. Espinosa, A. K. A. Silva, A. Sánchez-Iglesias, M. Grzelczak, C. Péchoux, K. Desboeufs, L. M. Liz-Marzán and C. Wilhelm, Cancer Cell Internalization of Gold Nanostars Impacts Their Photothermal Efficiency In Vitro and In Vivo: Toward a Plasmonic Thermal Fingerprint in Tumoral Environment, *Adv. Healthc. Mater.*, 2016, **5**, 1040–1048.

55 S. Freddi, L. Sironi, R. D'Antuono, D. Morone, A. Donà, E. Cabrini, L. D'Alfonso, M. Collini, P. Pallavicini, G. Baldi, D. Maggioni and G. Chirico, A Molecular Thermometer for Nanoparticles for Optical Hyperthermia, *Nano Lett.*, 2013, **13**, 2004–2010.

9. Conclusions

In the scope of the technological transition driven by the increased digitalisation of the society and the economy, there is an urgent need for highly efficient materials suitable for sensors and actuators, also comprising sustainability paradigms.

In this scope, advanced multifunctional, biodegradable composites based on natural or synthetic polymers have been developed. These materials were processed in dissolution with the aim of making them suitable for solvent-based additive manufacturing printing technologies. The physico-chemical and mechanical properties of these materials have been characterised, as well as their functional properties relative to their concentration. Overall, materials presenting magnetic and electrical functionalities have been prepared for sensor and actuator applications. The magnetic activity was introduced by incorporating cobalt ferrite ($CoFe_2O_3$) and magnetite (Fe_3O_4). Both are ferrites with high saturation magnetisation and relatively low coercive fields, interesting for developing non-contact magnetic sensors and actuators. Regarding composites with electrical properties, the functionality is tailored by fillers and additives of different nature: graphite, cellulose nanocrystals (CNCs), and the ionic liquid (IL) 2-hydroxy-ethyl-trimethylammonium dihydrogen phosphate [Ch][DHP].

First, composite materials with matrices sourced from cellulose were studied to develop multifunctional materials based on renewable resources. Three water-soluble cellulose derivatives, methyl cellulose, hydroxypropyl cellulose, and sodium carboxymethyl cellulose, were combined with cobalt ferrite nanoparticles with concentrations up to 50 wt.%, and [Ch][DHP] to a maximum concentration of 40 wt.% using water solely as solvent.

The magnetic samples were cast by doctor blade technique, obtaining free-standing films with $CoFe_2O_4$ nanoparticles homogeneously distributed through the whole thickness of the films. The mechanical tests showed an increase in Young's modulus and elongation at break for intermediate concentrations. Nevertheless, amounts ≥25 wt.% of $CoFe_2O_4$ tend to form aggregates, creating defective structures in the material when the effective filler-matrix interactions are decreased. Ultimately, films comprising a 50 wt. % present an elongation at break exceeding 5 %. Regarding functional characterisation, a maximum saturation magnetisation value of 27.0 $emu \cdot g^{-1}$ was obtained for a nanocomposite containing 50 wt. % of cobalt ferrite and a dielectric constant ranging between 10 and 40 for MC and HPC-based nanocomposites, while it substantially increases for NaCMC films. Furthermore, the solutions were employed as inks for screen-printing due to the demonstrated shear-thinning behaviour of the nanocomposites based on cellulose derivatives and CoFe2O4. Well-defined printed

patterns were obtained onto microporous cellulosic substrates with homogeneously distributed nanoparticles. Additionally, the large amount of $CoFe_2O_4$ incorporated showed enough magnetisation saturation to be used in magnetic sensor applications.

The films based on the three water-soluble cellulose derivatives and comprising the IL [Ch][DHP] were cast by a solvent casting method. Additionally, cellulose nanocrystals have also been employed as matrix and [Ch][DHP] as functional additives. No morphological changes were observed for neat CNC, MC, HPC, and NaCMC composites upon the IL incorporation, presenting all the samples a smooth and flat surface. HPC and NaCMC prepared by solvent casting show higher Young's moduli in the uniaxial tensile test than those observed by doctor blade casting. In contrast, MC Young's modulus values remain below half compared to doctor blade fabricated film. In fact, neat MC films cast by doctor blade (E=2620 ± 390 MPa) show similar values to CNC films (E= 2394 ± 215 Mpa). Incorporating the IL into the studied matrices has a plasticising effect resulting in more ductile films, which present lower Young's modulus values. In general, the electrical conductivity of the composites increased with increasing IL concentration. Besides, CNC and NaCMC showed two electrical conductivity regimes as a result of the increased mobility of anions and cations. These materials, based on ILs, were employed for developing bending actuators, where NaCMC/[Ch][DHP] performed the highest bending displacement of ~9 mm.

Continuing with cellulose as a matrix, CNCs were employed for developing porous structures by soft-templating approach, having large surface areas with magnetic and electrical activity. Water-dispersed CNCs were mixed with an alkoxysilane precursor. After the evaporation-induced self-assembly process, solid nanostructured composites were obtained. Subsequently, the silica phase was removed, leading to a mesoporous structure. The functional properties were provided by the inclusion of $CoFe_2O_4$ nanoparticles and graphite particles during processing. The three-dimensional porous structure of randomly entangled CNCs was not modified after the incorporation of inorganic particles, allowing to obtain specific surface areas of 193.9 $m^2 \cdot g^{-1}$. Besides, $CoFe_2O_4$ and graphite enhanced the thermal stability of the hybrids due to their tortuous path. At the same time, the samples comprising 20 wt.% of $CoFe_2O_4$ showed a maximum saturation magnetisation value of 8.77 $emu \cdot g^{-1}$, a similar value estimated for the same concentration of magnetic films based on cellulose derivatives ($M_{s\ (20\ wt.\%)}$ = 10.25 $emu \cdot g^{-1}$). On the other hand, the samples comprising 10 wt.% of graphite reached an electrical conductivity of 9.26 ± 0.04 $S \cdot m^{-1}$.

Then, the role of CNCs was changed, employing them as filler and ι-carrageenan, another polysaccharide sourced from seaweed, as a matrix. Thus, free-standing films made of fully renewable materials have been prepared with a tailored electrical response. The samples were cast by doctor blade yielding films with CNCs homogeneously distributed within the matrix with a maximum CNC concentration of 20 wt.%. The uniaxial tensile test revealed a marked reinforcing effect of the CNCs in the ι-carrageenan matrix. Interestingly, Young's modulus of the samples with a concentration of 5 wt.% of CNC increased 7-times without loss in ductility. Although Young's modulus values are generally lower than those obtained for cellulose derivatives and CoFe2O4 composites, the reinforcing effect of CNC is much higher than that of $CoFe_2O_4$. Actually, such increase vastly exceeds the theoretical determination of the modulus, ascribed to a strong CNC-carrageenan interfacial interaction. Also, elongation at break values of ι-carrageenan composites are more stable than the ones observed for cellulose derivative composites cast by a doctor blade. Dielectric spectroscopy results show a strong influence of the CNC surface on electrical properties. The real dielectric constant and AC conductivity increase with CNC concentration due to the charge carrier's concentration and ionic conductivity from CNC interfaces. Concerning DC electrical conductivity, there two regimes were observed where the electrical conductivity increased at a 2.0 V threshold.

Apart from naturally sourced polymers, the suitability of biodegradable synthetic polyesters has been explored for developing sustainable magnetically active materials prepared by solvent casting. As $CoFe_2O_4$ is a critical raw material due to the presence of Co, and in order to decrease the environmental footprint, we used magnetite Fe_3O_4 with similar magnetic properties. Hence, magnetically active biodegradable nanocomposites based on PLLA, PCL, PBSu, and PBAT combined with Fe_3O_4 up to a 10 wt.% were fabricated by a doctor blade. The presence of Fe_3O_4 nanoparticles can substantially affect the thermal and mechanical properties of these materials. For instance, the inclusion of Fe_3O_4 fillers increases the crystallinity degree of PBSu, decreases the crystallinity degree of PBAT, and barely affects the crystallinity of PLLA and PCL. Additionally, mechanically tunable characteristics ranged from stiff and brittle (PLLA and PBSu) to soft and ductile (PCL and PBAT). After exposing the samples to accelerated hydrolytic degradation, weight losses up to 27 % at 70 ºC for 15 days in PBS medium were observed for PLLA. A maximum saturation magnetisation of 7.1 ± 0.1 emu·g^{-1} was observed for the samples comprising a 10 wt.% of Fe_3O_4, comparable values for those obtained with cellulose derivates/CNC and $CoFe_2O_4$ nanocomposites at the same concentration.

Finally, anisotropic core-shell hybrid rod-shaped nanoparticles made of magnetite and gold were synthesised, named Fe_3O_4@Au NRs. Thus, the multifunctionality of the material comes from a single particle with different functional properties: magnetic and photonic properties. Furthermore, they allow directionality of the magnetic response with the orientation and tunability in both nanoparticle dimension and shell thickness. In this sense, developed Fe_3O_4@Au NRs show magnetic and photonic properties and tailored sizes for magneto- and photo-thermal anisotropic transductions. Aiming to study the properties of the nanorods in the different orientations, they were aligned within agarose hydrogels upon cooling in the presence of a magnetic field. It has been demonstrated that this gel offers the possibility to produce simultaneous magneto- and photo-thermia, which can be used in regenerative medicine or in cancer ablation, among others, where the anisotropic response can help to lower the therapeutic doses in terms of nanoparticles, light irradiation, or magnetic field applied. Moreover, filaments of the hydrogels were prepared by injection. This offer suitable characteristics to be involved in localised therapies and foresee their ability to be printed, for example, by direct ink writing. Hence, they can be further explored for their application in technological applications where directionality and dual magnetic and optical properties are required, such as sensors or actuators, among others.

As a general conclusion, these biodegradable materials are attractive for developing a new generation of sustainable and multifunctional materials for printed electronic applications. Interestingly, the properties of the composites based on biodegradable polymers here showed, most of them from renewable resources, are comparable with the ones of traditional petroleum-based magneto- and electro-active composites. Hence, some paths have been shown for developing bio-based magnetically-active or electrically-conducting free-standing composites suitable for applications in the fields of sensors and actuators.